NNT : 2016SACLS178

THESE DE DOCTORAT
DE
L'UNIVERSITE PARIS-SACLAY
PREPAREE A
UNIVERSITE PARIS-SUD

ECOLE DOCTORALE N°575

ÉCOLE DOCTORALE
Physique et ingénierie : électrons, photons, sciences du vivant (EOBE)

Doctorat en Physique
Par

Pedro Alberto Lúcio de Sales Damas

Effet Pockels dans les guides d'onde en silicium contraint

Vers la modulation optique à haute vitesse et faible consommation d'énergie dans le silicium

Thèse présentée et soutenue le 19/07/2016 au Centre Scientifique d'Orsay

Composition du Jury :

Mme. VÉNIARD, Valérie	Professeur, École Polytechnique, U. Paris-Saclay	Président
M. PAVESI, Lorenzo	Professeur, University of Trento	Rapporteur
M. WITZENS, Jeremy	Professeur, Aachen University	Rapporteur
M. BŒUF, Frédéric	Docteur, STMicroelectronics	Examinateur
VIVIEN, Laurent	Professeur, Université Paris-Sud, U. Paris-Saclay	Directeur de thèse

université PARIS-SACLAY

ÉCOLE DOCTORALE
Physique et ingénierie : électrons, photons, sciences du vivant (EOBE)

Titre : Effet Pockels dans les guides d'onde en silicium contraint

Mots clés : Photonique, Silicium, Contraint, Modulateur Optique, Optique non-linéaire

Résumé : Ce travail est centré sur l'étude des non-linéarités de deuxiéme ordre dans le silicium vers une modulation optique à faible puissance et haute vitesse. Étant un cristal centro-symétrique, le silicium ne possède pas une susceptibilité non linéaire de deuxiéme ordre (X2), ce qui inhibe l'effet Pockels, un effet électro-optique linéaire couramment utilisé dans la modulation de la lumière dans les communications optiques. Une solution possible pour vaincre cette limitation est par application de contraint et déformation de la maille cristalline, ce qui rompt localement la centro-symétrie du cristal et génère X2.

Dans cette thèse, nous abordons le problème de la génération de X2 dans le silicium par l'utilisation de la contrainte, couvrant toutes les étapes de la recherche:nous partons de bases théoriques développées par nous, on simule l'ensemble des effets de contraints, optiques et électriques, on décrit la fabrication des dispositifs et finalement on présent la caractérisation expérimentale de ces dispositifs.

Dans ce travail de recherche, nous avons pu détecter des effets très particuliers qui sont attribués au effet Pockels, comme par example une dépendance claire de l'orientation du cristal sur l'efficacité de la modulation et aussi la modulation à haute fréquences, plus élevées que celles attendues par autres contributions. Ces résultats sont très prometteurs et se composent d'une nouvelle étape vers la mise en œuvre, dans un avenir proche, de la modulation à grande vitesse et à faible puissance dans les dispositifs de silicium.

Title : Pockels effect in strained silicon waveguides

Keywords : Photonics, Silicon, Strain, Optical Modulator, Nonlinear Optics

Abstract : This work is devoted to the study of second order nonlinearities in silicon towards low power, high speed modulation. Being a centro-symmetric crystal, silicon does not possess a second order nonlinear susceptibility (X2), which inhibits Pockels effect, a linear electro-optic effect commonly used in the modulation of light in high speed communications. A possible solution to overcome this limitation is by straining/deforming the crystal lattice, which locally breaks the centro-symmetry of the crystal and generates X2.

In this thesis, we approach the problem of generating X2 in silicon through the use of strain, covering all the research stages: we depart from newly developed theoretical grounds, simulate together the strain, optical and electrical effects together, describe the fabrication of the devices and present the experimental characterization.

In our research work, we were able to detect very particular effects which are attributed to Pockels effect, such as a clear dependence of the crystal orientation on the modulation efficiency and high speed modulation, at frequencies higher than those expected from other contributions. This results are very promising and consist on a step further towards the possible implementation of high speed, low power modulation in silicon devices in the near future.

Université Paris-Saclay
Espace Technologique / Immeuble Discovery
Route de l'Orme aux Merisiers RD 128 / 91190 Saint-Aubin, France

Pockels effect in strained silicon waveguides

Pedro Damas

La photonique silicium a généré un vif intérêt au cours des dernières années, principalement pour les communications optiques dans les circuits intégrés. Les principales motivations du développement dela photonique silicium sont la réduction des coûts des circuits, l'augmentation de la fréquence, l'augmentation du nombre de fonctionnalités sur puce en combinant la photonique et l'électronique et une forte réduction de la consommation énergétique des circuits. Cependant, une des plus grandes contraintes du silicium comme matériau optique est l'absence de $\chi^{(2)}$, la susceptibilité optique du deuxième ordre, à cause de la centro-symétrie du cristal. Sans phénomènes optiques non linéaires du deuxième ordre, l'effet Pockels, qui permet la modulation optique très rapide et à faible consommation d'énergie, n'est pas possible. D'autres solutions ont donc été développées pour pallier ce manque, en particulier, basées soit sur des effets de variation de porteurs dans le silicium ou d'effet d'électro-absorption dans le germanium massif ou dans les puits quantiques Ge/SiGe. Aujourd'hui, les différentes approches explorées souffrent encore d'une trop forte puissance électrique consommée.

Pour surmonter ce problème, la génération de contraintes dans le silicium ($\overline{\boldsymbol{\varepsilon}}$) a été exploitée comme un moyen de déformer le cristal et briser la centrosymétrie qui inhibe $\chi^{(2)}$. Lors des dernières années, l'effet Pockels a été démontré dans des dispositifs où le silicium était déformé par une couche contrainte déposée au dessus du guide d'onde, généralement en nitrure de silicium (SiN). Une des plus grandes motivations d'étudier le silicium contraint pour développer des dispositifs de modulation optique est la suivante: la perspective d'un modulateur optique à vitesse élevée, compact, faible consommation d'énergie, avec une grande bande-passante et compatible avec la technologie silicium serait un des Graal de la photonique silicium. Le présent manuscrit porte sur l'effet Pockels dans lesilicium contraint en allant de la discussion de son origine fondamentale jusqu'à sa mise en œuvre dans un dispositif réel.

Dans la première partie, nous étudions l'effet dela déformation sur la structure cristalline de silicium pour comprendre comment un coefficient $\chi^{(2)}$ peut être généré. Pour ça, nous avons développé un modèle théorique original basé sur le *Bond-Orbital Model*, incluant les bases de mécanique quantique et qui décrit les électrons dans les liaisons entre les atomes de silicium. En utilisant cette approche avec des arguments de symétrie, on a réussi à montrer que la distribution spatiale de $\chi^{(2)}$ dans le cristal peut être donnée par

$$\chi^{(2)}_{ijk} = \Gamma_{ijk,lmn}\eta_{lmn} \ , \tag{1}$$

où η_{lmn} est la component de *gradient de deformation*, défini par

$$\eta_{ijk} \equiv \frac{\partial \varepsilon_{ij}}{\partial x_k} \,. \tag{2}$$

Cela signifie que le coefficient $\chi^{(2)}$ peut être définie par la contribution de tous les gradients de déformation, pondérée par les coefficients Γ. Les valeurs de Γ sont déterminées par notre modèle quantique, où Γ est une fonction de seulement deux paramètres: α et β qui dépendent seulement du matériel. De plus, étant un tenseur caractéristique du cristal, Γ dépend également de l'orientation cristalline. Ce coefficient Γ en fonction de l'angle φ ($\varphi = 0$ correspond à [110] et $\varphi = \pi/4$ correspond à [100]) s'écrit sous la forme:

$$\Gamma_{xxy,xxy}(\varphi) = \frac{d^6 K}{27\epsilon_0} \left[(5\beta - 3\alpha - (\alpha+\beta)\cos(4\varphi))\right] \tag{3}$$

$$\Gamma_{xxy,yyy}(\varphi) = -\frac{d^6 K}{27\epsilon_0} \left[2(\alpha - 3\beta)\right] \,. \tag{4}$$

Les deux seules inconnues dans la précédente série d'équations sont les constantes α et β, à déterminer expérimentalement.

Les deux seules inconnues dans les précédentes équations sont les constantes α et β, qui seront à déterminer expérimentalement.

Suite à ces résultats théoriques sur l'influence du coefficient $\chi^{(2)}$ dans le silicium avec les contraintes, nous nous sommes concentrés sur la conception d'un dispositif pour la modulation de la lumière sous champ électrique, en utilisant l'effet Pockels. Une couche contrainte, le nitrure de silicium, est utilisée pour générer un gradient de contrainte dans le silicium. Cette couche SiN est déposée par PECVD dont $\sigma_0 = SI1.2GPa$, en compression. Le champ électrostatique est créé en plaçant des électrodes au-dessus du guide d'onde. La section transversale de la structure que nous avons conçu est représentéedans la Fig. 1. Pour faire varier la contrainte et les propriétés électroniques de toute la structure photonique, nous avons fabriqué trois échantillons avec trois épaisseurs de la couche de SiO_2, $t_{SiO_2} = 0\,\text{nm}$, 250 nm and 500 nm (correspondant aux Dispositifs 0, 250 et 500) .

Cependant, le silicium est un semiconducteur et la densité et la distribution des porteurs libres (électrons et trous) varient en fonction du champ électrique appliqué ($\boldsymbol{F}$). Par conséquent, deux effets électro-optiques sont induits lorsqu'un champ électrique est appliqué sur le guide d'onde: le *plasma dispersion effect*, qui correspond à la variation de l'indice de réfraction du silicium avec la variation de la concentration des porteurs; et l'effet Pockels, un effet qui dépend de l'interaction du champ électrique à l'intérieur du guide d'onde et les

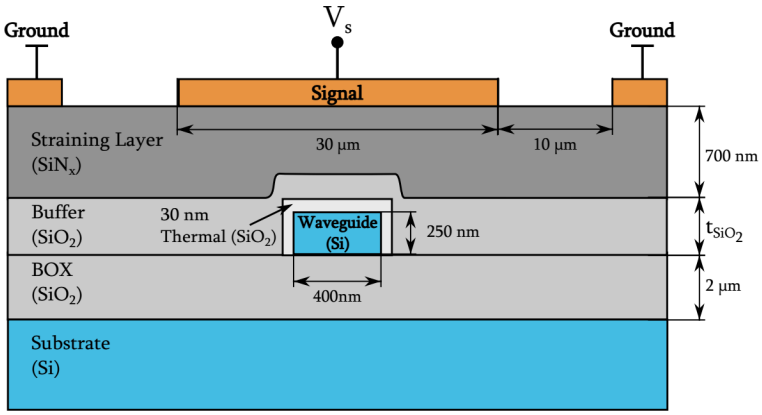

Fig. 1 Structure finale du dispositif, oú $t_{\mathrm{SiO}_2} = 0$ nm, 250 nm and 500 nm.

gradients de déformation dans le silicium. Ces deux effets, cependant, sont profondément liés: l'application d'un champ électrique induit un changement dans la distribution des porteurs libres, que à son tour affecte la distribution du champ électrique à l'intérieur du guide d'onde, résultant en un changement de l'effet Pockels. En outre, la couche de SiN, nécessaire pour induire la déformation dans le silicium, est généralement caractérisée par une grande quantité de charge positif (Q_f) qui affecte également la concentration de porteurs libres dans le guide d'onde ainsi que le champ électrique. Par conséquent, afin d'étudier d façon rigoureuse l'effet Pockels dans le silicium contraint, nous devons inclure l'étude des porteurs à l'intérieur du guide d'onde silicium ainsi que les effets de charge aux interfaces, avec les effets de déformation.

En utilisant toutes ces considérations, nous avons déduit que la variation d'indice effectif (n_{eff}) d'un mode optique guidé sous un champ électrique $\boldsymbol{E}$ peut être écrite comme une somme de *gradients de deformation effectives*:

$$\Delta n_{eff_P} = \Gamma_{ijk,mnl} \widehat{\eta_{mnl}^{ijk}} \,, \tag{5}$$

où les *gradients de deformation effectives* ($\widehat{\eta_{mnl}^{ijk}}$), tenant en comptede la distribution du champ électrostatique appliqué, du mode optique et des gradients de déformation, sont définis par

$$\widehat{\eta_{mnl}^{ijk}} = \frac{2}{N} \int_{wg} \eta_{mnl} E_i E_j F_k \, dS \,, \tag{6}$$

avec N la puissance actif du mode optique. L'effet electro-optique final est donc la combinaison du *plasma dispersion effect* (Δn_{eff_c}) et l'effet Pockels, qui peut être réduite à:

$$\Delta n_{eff} = \Delta n_{eff_c} + \Delta n_{eff_P} = \tag{7}$$

$$= \Delta n_{eff_c} + \Gamma_{xxy,xxy}\left(\widehat{\eta_{xxy}^{xxy}} + \zeta\widehat{\eta_{yyy}^{xxy}}\right) , \tag{8}$$

où $\zeta = \Gamma_{xxy,xxy}/\Gamma_{xxy,yyy}$.

Les deux effets électro-optiques Δn_{eff_c} et Δn_{eff_P} dépendent de la tension appliquée et leurs valeurs en fonction de V_s ont été déterminées en simulant la structure avec le logiciel COMSOL Multyphysics, où on peut combiner la physique des contrainte, les effets optiques et la physique des semi-conducteurs dans une seule simulation. Les dimensions présentées dans la Fig. 1 ont été obtenues par des simulations en vue d'une optimization de Δn_{eff_P}. Les courbes de Δn_{eff_c} et $\widehat{\eta_{xxy}^{xxy}}$ dépendants de la tension pour les dispositifs représentés dans la Fig. 1 sont présentés dans la Fig. 2. L'effet électro-optique final sera donc une combinaison de ces courbes (Fig. 2a et Fig. 2b) et dépend de la valeur des deux coefficients $\Gamma_{xxy,xxy}$ et ζ, qui ne peuvent qu'être déterminées expérimentalement.

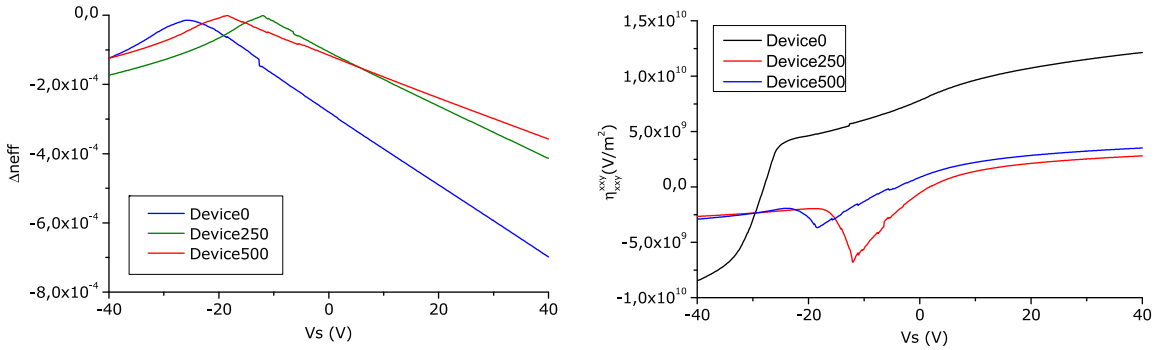

(a) (b)

Fig. 2 Le *plasma dispersion effect* (a) et la component $\widehat{\eta_{xxy}^{xxy}}$ du gradient de déformation effective (b) en fonction de la tension V_s appliqué dans les trois Devices.

Il y a deux grandes différences entre les deux effets électro-optiques: l'effet Pockels est un effet très rapide limitée seulement à la gamme de fréquences de THz, alors que l'effet de porteurs est limitée à des fréquences autour du GHz; l'effet Pockels dépend de l'orientation cristalline tandis que les porteurs dans silicium ne sont pas sensibles aux directions cristallographiques. Pour détecter ces deux différences expérimentalement, nous avons conçu des interféromètres de Mach-Zehnder (MZI) pour obtenir une modulation électro-optique rapideavec différentes orientations cristallographiquesdes guides d'ondecaractérisées par l'angle φ (Fig. 3). La fabrication des trois dispositifs a été réalisée dans la Centrale

Technologique Universitaire (CTU) de l'IEF en utilisant un large éventail de techniques: lithographie électronique, gravure ICP, oxydation thermique, PECVD, l'évaporation par faisceau électronique, entre autres.

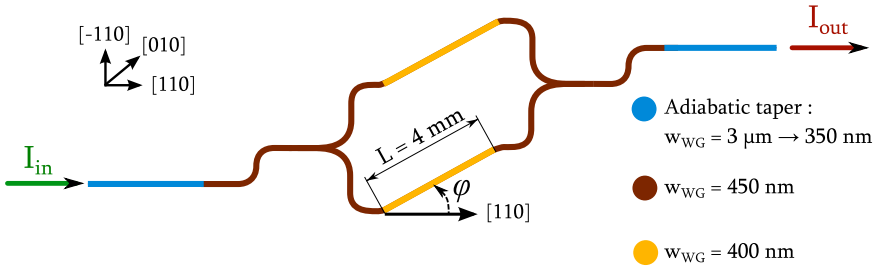

Fig. 3 Disposition du dispostif complète quand un angle de rotation est inclus.

Enfin, nous avons caractérisé les dispositifs fabriqués dans deux régimes différents: sous champ électrostatique statique DC et en modulation RF à haute vitesse. Sous champ électrique DC, l'objectif était de comparer les résultats expérimentaux avec le modèle développées pendant dans la thèse, en particulier ceux avec la dépendance à l'orientation du cristal. L'objectif final était de trouver un seul ensemble de paramètres α et β qui pourrait décrire les résultats expérimentaux. Nous avons ainsi pu déterminer les valeurs des coefficients α et β en ajustant les courbes expérimentales obtenues en fonction de l'orientation cristallographique :

$$\alpha = 4.31 \times 10^7\,\mathrm{J/m^2} \quad \text{et} \quad \beta = -6.45 \times 10^7\,\mathrm{J/m^2}\,. \tag{9}$$

Les valeurs obtenues sont élevées, et conduisent à un coefficient $\chi^{(2)}$ moyen de $\sim$120 pm/V à l'intérieur du guide d'onde. Des études sont encore à menées pour consolider cette valeur.

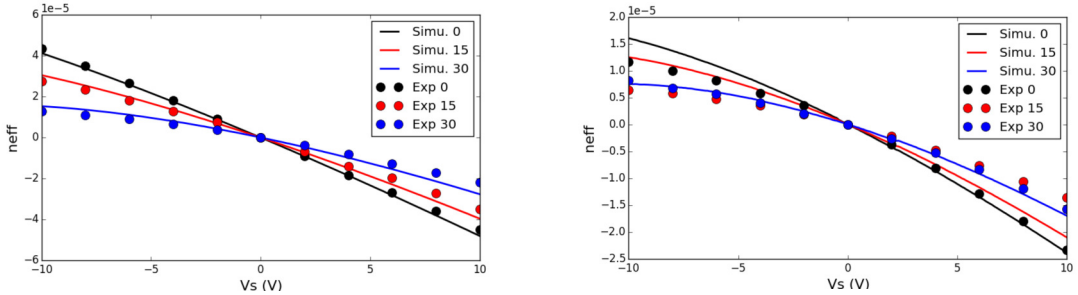

(a) (b)

Fig. 4 Comparaison entre les resultats experimentaux et les simulations pour $\alpha = 4.31 \times 10^7\,\mathrm{J/m^2}$ et $\beta = -6.45 \times 10^7\,\mathrm{J/m^2}$ pour trois orientations angulaires différentes et pour Device 250 (a) et Device 500 (b).

Pour la caractérisation à haute vitesse, nous avons détecté une faible modulation électro-optique jusqu'à 20 GHz, qui ne peutpas être expliquée par les effets de porteurs, limitée au-dessus de 5 GHz. La bande passante de modulation mesurée est de 1.7 GHz. Cette fréquence de coupure correspond à la bande passante des électrodes métalliques, comme illustré dans la Fig. 5. Par conséquent, la modulation est limitée par la propagation du signal RF et non par l'effet électro-optique. Des améliorations de la réponse RF des électrodes sont en cours pour améliorer la bande passante et avoir sans ambiguïté une démonstration de l'existence d'effet Pockels.

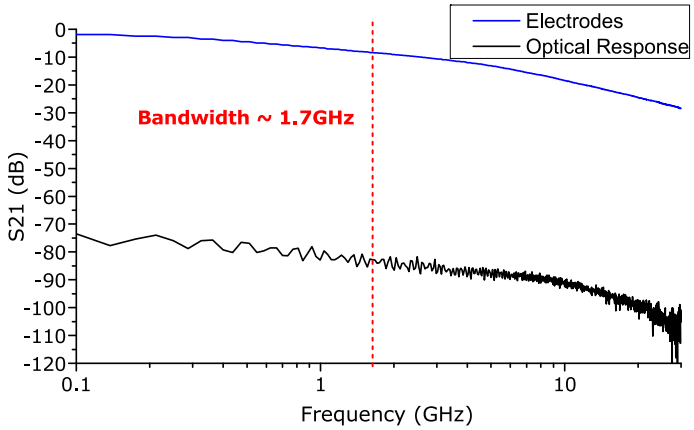

Fig. 5 La comparaison entre la réponse électrique des électrodes et de la réponse du dispositif opto-électronique. La ligne rouge verticale représente la bande passante des deux réponses.

Pour conclure, nous avons développé un nouveau modèle théorique pour expliquer les origines de $\chi^{(2)}$ dans le silicium en appliquant des contraintes dans le cristal de silicium. Nous avons utilisé ces concepts pour simuler les effets électro-optiques dans une approche incluant la physique des semi-conducteurs, la contraint et les effets optiques. Enfin, nous avons montré expérimentalement une dépendance claire de l'effet electro-optiqueen fonction dela direction cristalline du silicium et une modulation optique à haute vitesse. Ces résultats prometteurs, ne peuvent pas être expliqués qu'en considérant la contribution de l'effet Pockels dans le guide d'onde silicium contraint.

Pockels effect in strained silicon waveguides

Towards high-speed and low power consumption optical modulation in silicon

Pedro Damas

Supervisor: Prof. Laurent Vivien

Physics and engineering: electrons, photons and living sciences
Université Paris-Saclay

This dissertation is submitted for the degree of
Doctor of Philosophy

September 2016

To my mother, to my father and to my brother, for everything.

Declaration

I hereby declare that except where specific reference is made to the work of others, the contents of this dissertation are original and have not been submitted in whole or in part for consideration for any other degree or qualification in this, or any other university. This dissertation is my own work and contains nothing which is the outcome of work done in collaboration with others, except as specified in the text and Acknowledgements.

Pedro Damas
September 2016

Acknowledgements

This thesis would not be possible without the continuous support of my supervisor, Professor Laurent Vivien, for his enthusiasm, optimism and encouragement. I am extremely grateful for the positive energy he always brought to our research, for having given me enough space to do the research on my own and for always having time to help, despite being one of busiest persons I know.

I would like to express by deepest gratitude to Xavier Leroux, for the endless hours spent in the clean room, for all the support demonstrated the many times the fabrication did not go well and the patience to deal with another PhD student. I am also particularly grateful to Prof. Delphine Marris-Morini, Prof. Eric Cassan and Prof. Paul Crozat for all the guidance and fruitful discussions throughout this thesis.

I am thankful for the assistance by all my colleagues, in particular to Mathias Berciano and Guillaume Marcaud for their support in creating and measuring samples when my time was scarcer, and also to Carlos, Diego, Joan, Samuel, Weiwei, Elena and Daniel for contributing for such a pleasant working environment. I would also like to express my gratitude to STMicroelectronics and Frédéric Boeuf for the financial support.

I cannot express how much I owe to my parents and brother for all the support given during the ups and downs, in every step along the way. All their efforts to provide the best education, all the dinner time discussions and all the answered questions since the very beginning were the main contribution for this academic milestone. Thank you.

A special word to all my closest friends (they know who they are) for helping me in the darkest periods during the development of this thesis and for having always given the best support someone could possibly ask. Finally, I am thankful to the dozens of people I met in the Maison du Portugal of Cité International Universitaire de Paris for having made the last four years of my life the most magical experience, particularly to Rita, Nuno, José, Serôdio, Castro, Porya, Emanuele, Joana, Gerson, Mariana, Mário, Jorge, Manuel and Madalena, for all her support and patience during the writing of this manuscript.

Abstract

Silicon-based photonics has generated a strong interest in recent years, mainly for optical communications and optical interconnects in CMOS circuits. The main motivations for silicon photonics are the reduction of photonic system costs and the increase of the number of functionalities on the same integrated chip by combining photonics and electronics, along with a strong reduction of power consumption. However, one of the biggest constraints of silicon as an active photonic material is its vanishing second order optical susceptibility, the so called $\chi^{(2)}$, due to the centrosymmety of the silicon crystal. Without any second order nonlinear phenomena, fast and low power consumption optical modulation based on Pockels effect and wavelength conversions based on Second Harmonic Generation (SHG) are not possible in bulk Si. This is a very limiting factor when we expect silicon to be part of a solution to high performances and highly energy efficient devices.

To overcome this problem, strain ($\overline{\boldsymbol{\varepsilon}}$) has been used as a way to deform the crystal and destroy the centrosymmetry which inhibits $\chi^{(2)}$. In fact, over the last few years Pockels electro-optic modulation and SHG have been claimed to be demonstrated in devices where the silicon active region is strained by a stress overlayer, usually made of SiN. This is the very motivation to the development of *strained silicon* devices for optical modulation: the prospect of a high speed, low loss, compact, low power consumption, with large optical bandwidth and silicon compatible modulator. The present manuscript is all about Pockels effect in strained silicon. The focus will be on discussing it from its very fundamental origin until its implementation in a real device.

We start our analysis to strained silicon by studying how strain affects the silicon crystal structure to understand how $\chi^{(2)}$ effects can be generated. To achieve that, we developed an original theoretical model based on the *Bond Orbital Model*, which is a quantum mechanical theory that describes the electrons in the bonds between the silicon. By using that approach together with symmetry arguments, we found that the spatial distribution of $\chi^{(2)}$ in the crystal can be given by

$$\chi^{(2)}_{ijk} = \Gamma_{ijk,lmn}\eta lmn \,, \tag{1}$$

where ηlmn is a *strain gradient* component defined by

$$\eta_{ijk} \equiv \frac{\partial \varepsilon_{ij}}{\partial x_k} \,. \tag{2}$$

This means that $\chi^{(2)}$ is defined by the contribution of all strain gradients, weighted by the Γ coefficients. The values of Γ can be uniquely determined by our Bond Orbital description, which defines Γ as a function of only two parameters α and β. In fact, being a tensor characteristic of the crystal, Γ depends on the crystal orientation and from our model, we could deduce the most relevant components of Γ in a [010] silicon wafer as a function of the angle φ ($\varphi = 0$ corresponds to [110] and $\varphi = \pi/4$ corresponds to [100] directions) as follows:

$$\Gamma_{xxy,xxy}(\varphi) = \frac{d^6 K}{27\epsilon_0}\left[(5\beta - 3\alpha - (\alpha+\beta)\cos(4\varphi))\right] \tag{3}$$

$$\Gamma_{xxy,yyy}(\varphi) = -\frac{d^6 K}{27\epsilon_0}\left[2(\alpha - 3\beta)\right] \,. \tag{4}$$

The only two unknowns in the previous set of equations are the constants α and β to be determined experimentally.

Once we got a better understanding of how strain affects $\chi^{(2)}$, we focused on designing a device that could modulate light using Pockels effect, i.e. a strained silicon waveguide under a variable electric field. For it to happen, the silicon waveguide requires two main features: a source of strain and a source of electrostatic field. The former is achieved by placing a layer of straining material, under high internal stress (σ_0), on top of the waveguide. This highly stressed layer strains the waveguide underneath, creating the strain gradients required to generate $\chi^{(2)}$ in the waveguide. The stress layer we used was a SiN thin film, deposited by PECVD whose internal stress $\sigma_0 = 1.2\,\text{GPa}$ compressive stress. The electrostatic field is created by placing electrodes on top of the waveguide which are activated by the application of a voltage difference V_s. The cross-section of the final structure we designed is shown in Fig. 1, where a layer of SiO_2 with three different thicknesses $t_{SiO_2} = 0\,\text{nm}$, 250 nm and 500 nm (corresponding to Devices 0, 250 and 500) was added to vary both the stress and the electronic properties.

However, silicon is a semiconductor and its free-carrier concentration and distribution is dependent on the applied electric field ($\boldsymbol{F}$). Therefore, there are two electro-optic effects that take place in the waveguide when an electric field is applied to the waveguide: the plasma-dispersion effect, an effect that corresponds to a variation of refractive index of silicon due to a variation of free-carrier concentration; and the Pockels effect, an effect that depends on

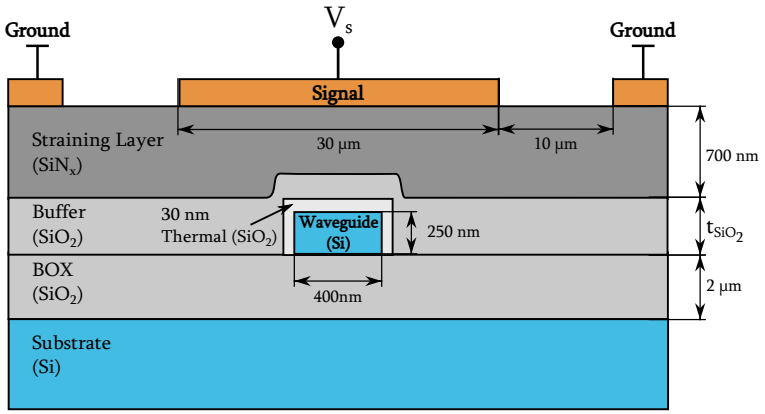

Fig. 1 Final layout of the device, where $t_{\mathrm{SiO}_2} = 0$ nm, 250 nm and 500 nm.

the interaction of the electric field inside the waveguide and the strain gradients. These two effects, however, are deeply connected: the application of an electric field induces a change in free-carrier distribution, that in turn affects the electric field distribution inside the waveguide, which influences the Pockels effect. Furthermore, the SiN stress layer required to induce strain in the waveguide, is usually characterized by a considerable positive charge distribution (Q_f) which also affects the free carrier concentration in the waveguide. Therefore, in order to study Pockels effect in strained silicon, we must include the study of the free-carriers inside the silicon waveguide together with the charging effects of the cladding and the strain effects.

By using all these considerations, we deduced that the effective index variation of an optical mode with electric field $\boldsymbol{E}$ propagating in the waveguide due to Pockels effect (Δn_{eff_P}) can be written as a sum of *effective strain gradients* so that

$$\Delta n_{eff_P} = \Gamma_{ijk,mnl} \widehat{\eta^{ijk}_{mnl}} \,, \tag{5}$$

where the *effective strain gradients* ($\widehat{\eta^{ijk}_{mnl}}$), which include the electrostatic field, the optical mode and the strain gradients, are defined by

$$\widehat{\eta^{ijk}_{mnl}} = \frac{2}{N} \int_{wg} \eta_{mnl} E_i E_j F_k \, dS \,. \tag{6}$$

and N is the active power of the optical mode. The final electro-optic effect is a combination of the plasma dispersion effect (Δn_{eff_c}) and Pockels effect, which can be reduced to:

$$\Delta n_{eff} = \Delta n_{eff_c} + \Delta n_{eff_P} = \tag{7}$$

$$= \Delta n_{eff_c} + \Gamma_{xxy,xxy} \left(\widehat{\eta^{xxy}_{xxy}} + \zeta \widehat{\eta^{xxy}_{yyy}} \right) \,, \tag{8}$$

where $\zeta = \Gamma_{xxy,xxy}/\Gamma_{xxy,yyy}$.

Both Δn_{eff_c} and Δn_{eff_P} are voltage dependent and the their value as a function of V_s is determined by simulating the structure using COMSOL multiphysics, which combines elasticity, optical and semiconductor effects in a single simulation. The dimensions presented in Fig. 1 were determined by simulations towards a maximization of Δn_{eff_P}. The voltage dependent curves of both Δn_{eff_c} and $\widehat{\eta_{xxy}^{xxy}}$ for the devices shown in Fig. 1 are presented in Fig. 2. The final electro-optic effect will be a combination of these curves dependent on the value of both $\Gamma_{xxy,xxy}$ and ζ, to be determined experimentally.

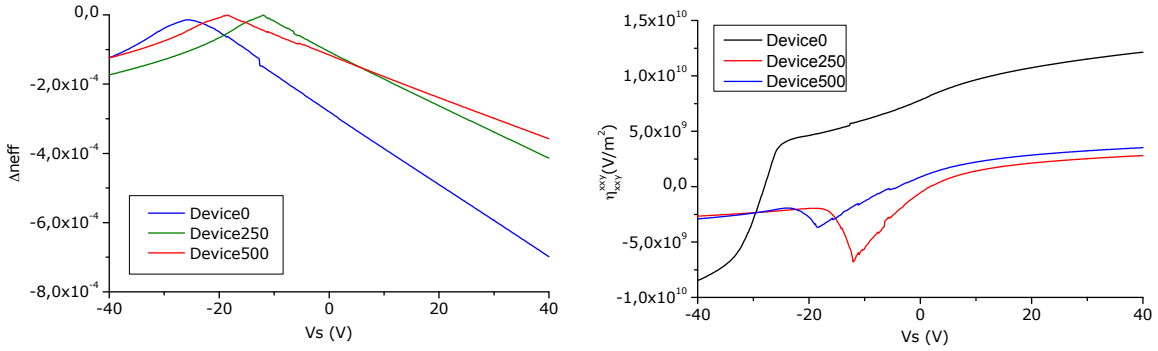

(a) (b)

Fig. 2 The plasma dispersion effect (a) and the effective gradient component $\widehat{\eta_{xxy}^{xxy}}$ (b) as a function of V_s for the three Devices.

There are two main differences between the two electro-optic effects: Pockels effect is a very fast effect limited only at the THz range, whereas plasma-dispersion effect can be limited at the GHz range; Pockels depends on the crystal orientation whereas carriers are not sensitive to crystallographic directions. To detect these two differences experimentally, we designed Mach-Zehnder Interferometers compatible with RF electro-optical modulation and with the waveguides oriented with different angles φ. The fabrication of the three Devices was successfully performed in the Centre Technologique Universitaire (CTU) by using a wide range of techniques: e-beam lithography, ICP etching, silicon thermal oxidation, PECVD, e-beam evaporation, among others. The results were in line with the desired layout.

Finally, we characterized the fabricated devices in two different regimes: DC electrostatic field and RF high speed modulation. The goal of the former was to characterize the electro-optic effect and compare the experimental results with the theory and simulations developed before, particularly with the crystal orientation dependence. The final goal was to find a single set of α and β that could describe all the experimental results. In fact, we found that

$$\alpha = 4.31 \times 10^7\,\mathrm{J/m^2} \quad \text{and} \quad \beta = -6.45 \times 10^7\,\mathrm{J/m^2}\,. \tag{9}$$

could fit the data for the angle dependence of the Devices 250 and 500 quite well, as shown in Fig. 3. These α et β parameters correspond, for $\varphi = 0°$, to

$$\Gamma_{xxy,xxy} = -2.2 \times 10^{-13}\,\mathrm{m}^2/\mathrm{V} \quad \text{and} \quad \zeta = 1.18\,, \tag{10}$$

which are very high values and lead to an average $\chi^{(2)}$ inside the waveguide of $\sim$120 pm/V. Further studies are still being development to understand the achieve a better understanding on the origins of this value.

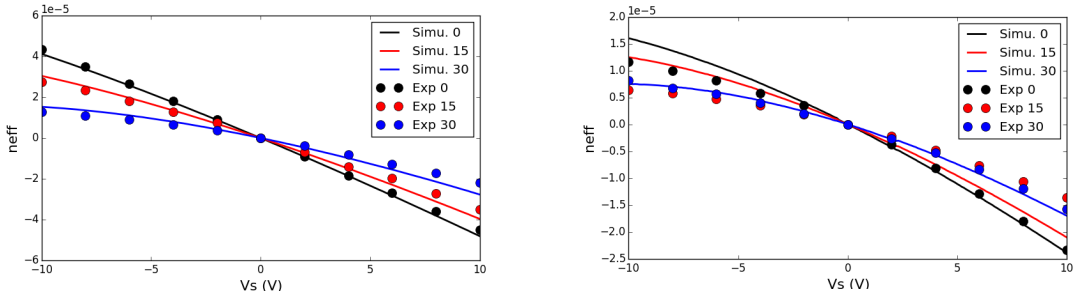

(a) (b)

Fig. 3 Comparison between experiment and simulations for $\alpha = 4.31 \times 10^7\,\mathrm{J/m^2}$ and $\beta = -6.45 \times 10^7\,\mathrm{J/m^2}$ for the three different angle orientations and for Devices 250 (a) and Device 500 (b).

For the high speed characterization, we detected a weak electro-optical modulation up to 20 GHz, which could not be explained by the plasma-dispersion effect, which should be highly limited above 5 GHz. Furthermore, the modulation bandwidth was 1.7 GHz and this cut-off frequency corresponds to the measured electrical bandwidth of the metallic electrodes as shown in Fig. 4. Therefore, the modulation is limited by the propagation of the RF signal in the electrical system and not by the electro-optic effect and with an improvement of the electrodes response we could achieve high speed modulation with a wide bandwidth, just like Pockels effect.

To sum up, we developed a new theoretical model to explain the origins of strain-induced $\chi^{(2)}$ in silicon which related the electro-optic effect with strain gradients. We used these concepts to simulate the electro-optic effects in an approach that includes semiconductor, strain and optical effects. Lastly, we measured the samples fabricated under these considerations and we measured a clear angle dependence of the structure and weak optical modulation at very high speeds. We could only explain these results by considering a contribution from Pockels effect in the strained silicon waveguide.

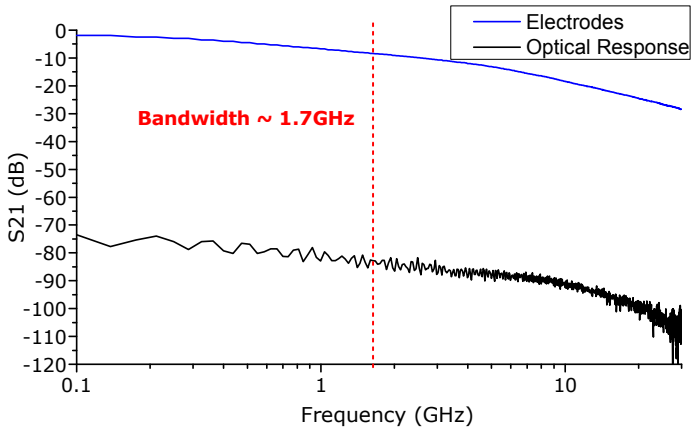

Fig. 4 Comparison between the electrical response of the electrodes and the optoelectronic response. The vertical red line represents the bandwidth of both responses.

Table of contents

Chapter 1

Introduction

Silicon is one of those materials that changed the world as we know it. Ever since the invention of the transistor by Bell Labs in 1947 [1], the world has witnessed a fantastic growth of semiconductor electronics. The dramatic shrinkage in feature size and a corresponding increase in transistor numbers led to the invention of integrated circuits (IC) [2], which are now the undisputed backbone of microelectronics. Since then, the development of the electronics industry towards cheaper, smaller and faster electronic devices has been driven by the so-called Moore's law, announced by Gordon Moore in 1965 which predicts an exponential increase of the number of transistors per chip [3].

Transistors are made of semiconductors and silicon (Si) is unbeatably the preferred material for the semiconductor industry. This can be explained by its very particular advantageous characteristics: it is the second most abundant element on earth after oxygen, making it a very cheap material; its energy bandgap of 1.1 eV allows for efficient devices at room temperature; it presents higher processing temperature than other common semiconductors; and also the ease of growing silicon dioxide and related materials on Si, allowing for fabrication techniques such as parallel and planar processing [4].

The silicon-based transistors and microprocessors in an integrated circuit communicate with each other commonly by metallic wires that propagate the electrical signals throughout the different layers of the chip. However, metal based *electrical interconnects* (EI) are reaching its limit of performance and have faced difficulties to keep up with the surge in the data rate demand over the last decade. The communications bottleneck is identified as one of the grand challenges in the progress of silicon computation and can be stated as: while individual logic elements have become significantly faster, computational speed is limited by the communication between different parts of a processor [5]. The main limitations of EI's are, among others, the constraint interconnect shrinkage, high energy consumption, signal delay and limited bandwidth and datarate [5–7]. Particularly, power consumption in data

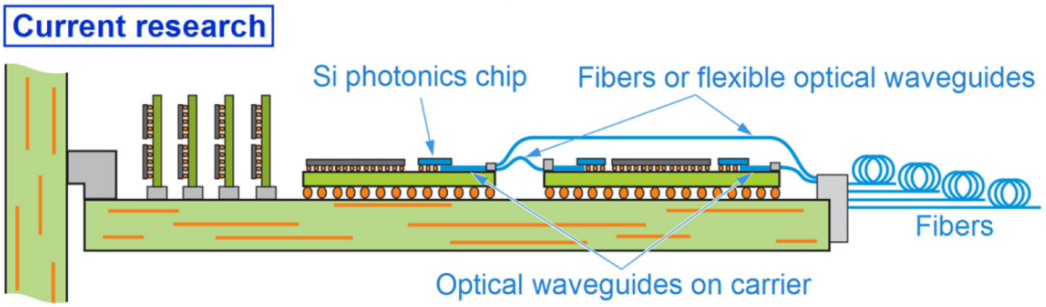

Fig. 1.1 Different interconnects levels on a board. Source IBM [9].

processing is now so large that it is starting to be environmentally significant. In 2013, data centres alone were estimated to consume 91 billion kWh, equivalent to the annual output of 34 large (500-megawatt) coal-fired power plants in the USA [8]. Power dissipation in interconnects, estimated to correspond to 25% of the total energy consumed by the CPU [7], is therefore a problem that directly limits the performance of chips and increasingly is a significant factor in system economics and the environmental impact of information technology.

Optical interconnects (OIs), where an optical signal is used instead of an electrical one, can provide a solution to the communication bottleneck and to energy consumption by replacing electrical wires with faster and less lossy optical waveguides [9]. The small wavelength of light (on the order of $300-1500$ nm in free space corresponding to carrier frequency of 1000 THz to 200 THz) means that dielectric waveguides (which can have very low loss) can be used to guide the waves. Moreover, optical interconnects are seen as the solution to increase the bandwidth of data transmission, retain very precise timing in clocks among the circuit and signals in ICs, boost the signal propagation speed with little distortion and reduce the total power consumption in the interconnect, to name a few [5, 7, 10]. For its wide range of applications and promising advantages, target application areas for optical interconnects range from high-performance computing and data centres down to mobile-to-server interconnects and desktop computers.

Different levels of interconnects can be identified, as shown in Fig. 1.1. While optical interconnects on the backplane levels of a board are already being implemented through the use of optical fibres, the integration of on-chip OIs are only feasible if they can be monolithically fabricated using the same manufacturing technology being employed for producing electronic integrated circuits: the Complementary Metal-Oxide-Semiconductor (CMOS) fabrication process. This is the main rationale of silicon photonics: apply the paradigm of microelectronics to photonics by manufacturing various devices in a single material (silicon) and using a single manufacturing process (the CMOS) [11]. The reason is very simple and

appealing: economics. By using the existing technology and vast infrastructures of CMOS manufacturing, silicon photonics offers the desirable features of photonics technologies, such as high performance, low heat and power dissipation, at the same low cost of silicon microelectronics [11].

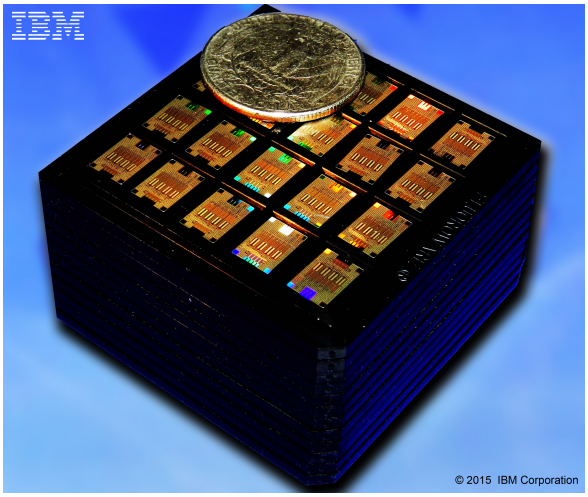

Fig. 1.2 First fully integrated monolithic silicon photonics chip demonstrated by IBM [12].

However, silicon is not the perfect optical material. Its indirect bandgap makes silicon-based light-emitting devices very challenging to achieve and the symmetry of its crystal structure is not compatible with linear electro-optic effects. Nonetheless, silicon has some excelent properties for photonics applications namely its high third order nonlinearity and its wavelength transparency windows from 1.1 μm to nearly 7 μm [13]. Pioneering work in investigating silicon as an optical material was performed by Soref and co-workers in the late 1980's [14, 15] and the development of silicon-on-insulator (SOI) platform for optical device development has sparked renewed interest in silicon photonics technology. The large refractive index contrast between silicon ($n_{\mathrm{Si}} \sim 3.47$) and SiO_2 ($n_{\mathrm{SiO_2}} \sim 1.45$), and their optical transparency at the IR main datacom band enables ultra-compact device dimensions suitable for large-scale, high density integration on a chip. This culminated in 2015 with the first fully integrated monolithic silicon photonics chip demonstrated by IBM [12] and shown in Fig. 1.2, confirming it as one of the most promising emerging platforms for a new generation of optical interconnects.

1.1 Silicon-based optical interconnects and optical modulation

An optical interconnect is generally formed by 3 main elements, as represented in Fig. 1.3: the Transmitter, responsible for the electrical-optical conversion of the signal; the optical channel, that guides the light into the different elements of the photonic IC; and the Receiver, where the optical signal is converted back to an electrical one. To compete with existing EI technologies, the energy consumption of an OI should be $50-200\,\mathrm{fJ/bit}$ and to meet the global demands in the near future, this value should be lowered to $10\,\mathrm{fJ/bit}$, according to an analysis presented by Miller [7]. Therefore, each one of the main elements of the OI must be implemented so that its overall speed and energy consumption satisfies the required limits. Deep overviews on the state of the art of the silicon-based elements of an optical interconnect have been done recently and the interested reader is referred to Refs. [11, 16]. For the purposes of this thesis, the most relevant element is the Transmitter and we will focus primarily on it.

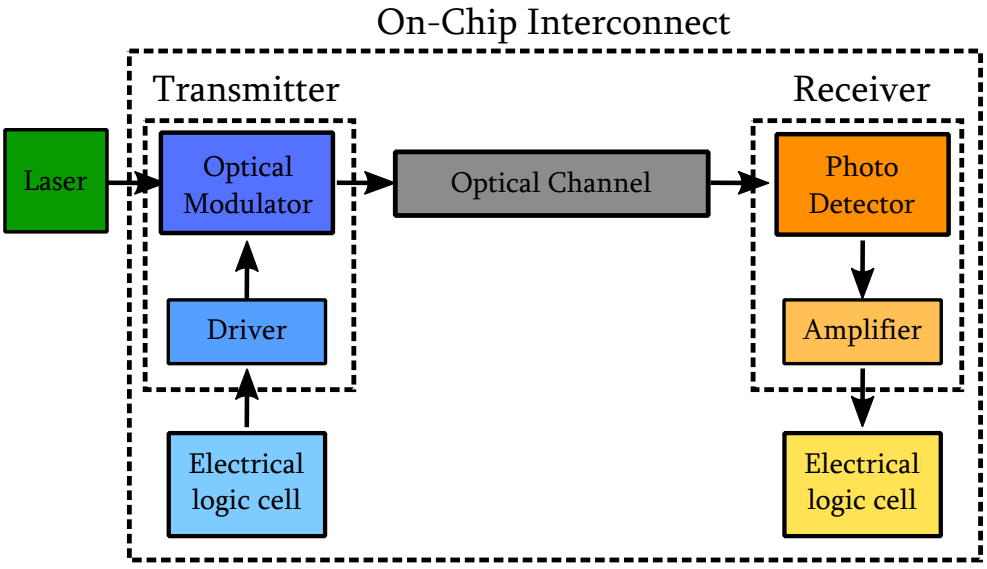

Fig. 1.3 The composition of an on-chip interconnect.

The job of a Transmitter is simply convert an electrical signal into a corresponding optical one. This can in principle be achieved by directly modulating the light source, but this method is not an efficient method and it is not considered as a viable solution for high speed low loss transmission [7]. The alternative and most accepted method to achieve electrical/optical signal conversion is my externally modulating a continuous light beam. The result is a Transmitter consisting of an *optical modulator* and driver circuits, as represented in Fig. 1.3.

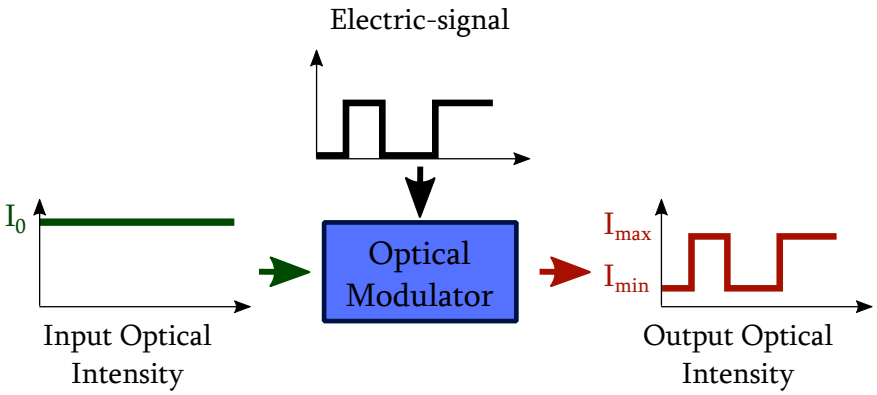

Fig. 1.4 Schematic representation of the working principle of a optical modulator, converting an electrical signal into an equivalent optical signal.

Next we concentrate on the optical modulation in silicon, presenting its performance metrics and how it can be achieved in silicon-based devices.

An optical modulator is an optoelectronic device that provides modulated optical signal at the output driven by an electric command when a continuous beam is provided at the input, as shown in Fig. 1.4 [11]. The performance of an optical modulator can be evaluated by defining performance metrics such as extinction ratio, insertion loss, optical bandwidth, footprint and power consumption. The *Extinction Ratio* (ER) is defined by the ratio between the "on" and "off" states

$$ER = 10\log\left(\frac{I_{max}}{I_{min}}\right) \tag{1.1}$$

where the I_{max} is the intensity of the on state and I_{min} is the intensity of the off state, represented in Fig. 1.4. A large ER is useful for long transmission distances, good bit error rates and high receiver sensitivity. The *Insertion Loss* (IL), takes into account the optical power that is lost when the modulator is added to a photonic circuit and is defined by

$$IL = 10\log\left(\frac{I_{max}}{I_0}\right), \tag{1.2}$$

with I_0 being the optical intensity at the modulator input.

The power consumption of a modulator is also known as the energy per bit and the target energy per bit of on-chip optical modulation for it to be a solution for the high energy expenditure in interconnects is $2-10\,\mathrm{fJ/bit}$ [7]. Finally, the footprint corresponds to the physical space required by the modulator and its optical bandwidth refers to the useful operational wavelength range of the device.

Generally, optical modulation involves an *electro-optic* (EO) effect that alters the light beam with the application of an electric field. Electro-optic effects can be separated into two

main categories: *electro-absorption* and *electro-refraction*. The primary electric field effects that are traditionally used in semiconductor materials for causing either electro-absorption or electro-refraction are the Pockels effect, the Kerr effect, the Franz–Keldysh effect and the Quantum Confined Stark Effect [11, 17]. Unfortunately, it has been shown that these are very weak in pure silicon at the telecommunications wavelengths of 1.3 μm and 1.55 μm [15, 18]. Consequently, alternative methods must be developed to achieve light modulation in silicon. An extensive review on silicon-based optical modulators and methods was performed by Diego Galacho approximately at the same time of the writing of the present thesis and reported in [19]. The interested reader is referred to this work where a detailed overview on the devices, processes to modulate light in silicon and the comparison between different approaches can be found. In this manuscript we will focus on the general lines about silicon optical modulators for the comprehensive understanding and motivations of the present thesis.

Electro-absorption modulation

Electro-absorption (EA) modulators are a class of modulators that employ an electric field to induce a variation of the absorption coefficient (α) of the material which changes the intensity of light propagating in it. In this class of devices, direct modulation of the optical intensity is obtained and the performance metrics depend on the absorption coefficient variation and the working spectral range. There are two main mechanisms used in EA modulators in silicon photonics: the Franz-Keldysh effect and the (QCSE). Both of these effects have been demonstrated in Germanium [20–22], thus providing a platform for silicon-compatible high speed, low power and compact modulators. The biggest challenge is the efficient integration of these devices on a silicon platform [17] because it requires the introduction of a second material (Ge), even though very recently, big progress has been made in the integration with the SOI platform [23].

Electro-refraction modulation

In Electro-refraction (ER) modulators an applied electric field induces a change of the real part of the refractive index (n), making a phase shift in the light wave. Electro-refraction by itself does not alter the intensity of light but only its phase. Then, to achieve light modulation a *resonator* or an *interferometer* is required. These devices share the property that the light output intensity depends on the light wave phase conditions and they are capable of converting a phase shift into a change of intensity.

Since silicon does not possess relevant Pockels and Kerr electro-optic effects, where the refractive index is directly affected by the application of an electric field (these effects will be covered in Chapter 2), alternative methods to induce electric field dependent phase shifts have be explored. One option is thermal modulation owing to the large thermo-optic coefficient of silicon, where the temperature of the silicon lattice is simply controlled by an electric current. However, this is too slow for the high frequencies required by modern telecommunications applications [15].

The most common method to achieve electro-refraction in silicon, though, involves the change of free-carriers density. In 1987 Soref and Bennett [15] shown that a change in concentration of free carriers in silicon has a direct effect on the optical properties of silicon, the so-called *plasma-dispersion effect*. They found a semi-empirical expression relating the change in both real and imaginary parts of refractive index of silicon (Δn_{Si} and α_{Si} respectively) with the concentration of free carriers n and p. These formulas, commonly known as Soref-Bennet equations are wavelength dependent and for $\lambda = 1.55\,\mu$m are given by [17]

$$\Delta n_{\mathrm{Si}} = -\left(8.8\times10^{-22}\Delta n + 8.5\times10^{-18}\Delta p^{0.8}\right) \tag{1.3}$$

$$\Delta \alpha_{\mathrm{Si}} = 8.5\times10^{-18}\Delta n + 6.0\times10^{-18}\Delta p \tag{1.4}$$

whereas for $\lambda = 1.3\,\mu$m take the form

$$\Delta n_{\mathrm{Si}} = -\left(6.2\times10^{-22}\Delta n + 6.0\times10^{-18}\Delta p^{0.8}\right) \tag{1.5}$$

$$\Delta \alpha_{\mathrm{Si}} = 6.0\times10^{-18}\Delta n + 4.0\times10^{-18}\Delta p\,, \tag{1.6}$$

where n and p are given in cm^{-3} units. This is the main method used for electro-optic modulation in silicon. It shows that any change in free carrier concentration can induce a change in refractive index which can be used to modulate light in silicon.

The electrical manipulation of the free carrier is achieved through three main mechanisms: injection, accumulation or depletion [17]. The first monolithic silicon-based modulator operating at speeds higher than 1 GHz was based on carrier-accumulation and it was experimentally demonstrated in 2004 by Intel [24]. Since then, tremendous developments took place, with demonstrations of modulators working in both carrier depletion and carrier injection [25, 26]. Despite these mechanisms are able to modulate light in silicon, their speed and efficiency are intrinsically limited by carrier mobility and recombination, which introduces constraints on the performances the modulators. Each one of these methods has its advantages and disadvantages and the challenge remains to improve efficiency while maintaining other performance metrics, such as the speed. For instance, carrier-depletion

achieves high modulation bandwidth at the expense of modulation efficiency, whereas the opposite situation occurs in carrier-injection devices.

Again, a deep analysis of these processes with the presentation of advantages and disadvantages can be found in the review work performed by Diego Galacho in [19].

To sum up, among the different possibilities to get high performance modulators, carrier-depletion silicon modulator and Ge-based electroabsorption devices deserve special attention. In the first case, large extinction ratio modulators were recently demonstrated at 40 Gbit/s data rate [26], while tor the second case, compact 45 μm long waveguides with 30 GHz bandwidth have shown high speed modulation requiring only 100 fJ/bit [21]. Although these are very promising results, some challenges are still ahead for the modulators to meet the requirements for telecommunications or data communications. Carrier depletion modulators suffer from high driving voltage which increases the power consumption beyond the energy requirements referred above (< 10 fJ/bit). On the other hand Ge-based EA modulators still require the development of an efficient waveguide integration scheme in the silicon platform. Obtaining simultaneously low-loss, high-speed, compact, low power-consumption and large optical bandwidth modulators in silicon is still a challenge and for that to be achieved, innovative approaches must be developed.

1.2 Pockels effect in strained silicon

Imagine for a second that Pockels effect was possible in silicon, i.e. its refractive index was affected by the application of an electric field. What characteristics would a Pockels-based silicon-modulator have? Firstly, Pockels effect mechanism does not involve physical displacement of charged carriers and thus it has an inherent temporal response down to the femtosecond range which enables ultrafast modulation beyond 1 THz [27]. Secondly, it is inherently low power consumption, as it does not involve any movement of carriers or currents and thus the only theoretical energy requirement involved is in the application of a driving voltage. Thirdly, its optical bandwidth would depend on the modulator itself and it would not be limited by the physical effect because Pockels effect is not expected to have a considerable wavelength dependence. Finally, no doping regions in silicon would be required because carriers do not play a role and thus the insertion loss of the modulator would be minimal and the fabrication of the devices and its integration with the silicon photonics platform would not be a problem. Essentially, the advantageous would be numerous.

However, silicon is a centro-symmetric crystal and an immediate consequence is the non-existence of second-order optical susceptibility ($\chi^{(2)}$) in the material, which is the material property behind the origin of Pockels effect. This will be discussed in high detail over the

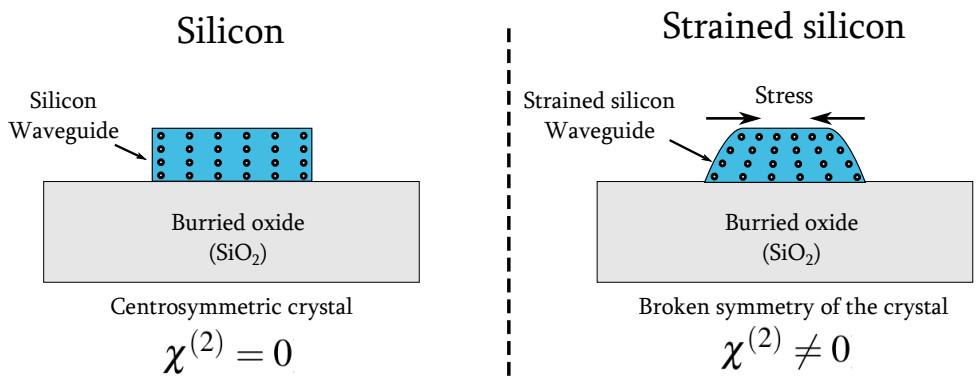

Fig. 1.5 The process of straining silicon to break the symmetry and induce $\chi^{(2)}$ dependent phenomena.

next chapters. As a result, such "ideal" Pockels-based otpical modulator is not feasible in silicon.

Nevertheless, it has been suggested that strain can be used to break the symmetry of the silicon crystal, as represented in Fig. 1.5. This process is capable of generating the normally inhibited second-order susceptibility ($\chi^{(2)} \neq 0$) and enable nonlinear phenomena like Pockels effect [28–34]. This is the very motivation to the development of *strained silicon* devices for optical modulation: the prospect of a high speed, low loss, compact, low power consumption, with large optical bandwidth and silicon compatible modulator. Such type of device could possibly meet the requirements discussed above for on-chip optical interconnects: large bandwidth, high-speed, energy per bit lower than $10\,\mathrm{fJ/bit}$ and easy integration with silicon, thus putting us one step closer for the possible monolithic integration of silicon photonics at the chip level.

1.3 Presentation of the thesis

The present manuscript is all about Pockels effect in strained silicon. The focus will be on discussing it from its very fundamental origin until its implementation in a real device. Our goal is to develop a methodical work that takes into consideration the strain dependence of Pockels effect in strained silicon, puts it together with the electro-optic response towards a consistent description of the strain-induced electro-optic Pockels effect in strained silicon.

The organization of the thesis is as follows. In Chapter 2 we present the physics of Pockels effect and its relationship with the fundamental characteristics of nonlinear optics. Next, we present the state of the art of strained silicon devices for photonic applications and the evolution of the context during the development of this thesis.

In Chapter 3 we approach the physical origin of Pockels effect in strain silicon, by describing its relation with the symmetries of the crystal and how strain may affect it. Moreover, we develop an original theoretical model to describe the relation between the strain-induced $\chi^{(2)}$ and the strain applied to the crystal. This model is fundamental to understand the source of $\chi^{(2)}$ in strained silicon devices and how we can engineer the strained structure to optimize its Pockels effect.

Chapter 4 deals with strain in micro-structures. We cover how strain is induced in real devices, compare sources of stress, materials and ways of measuring it. This study is important to have a clear idea of how a real silicon device is strained and how we can implement those conditions for proper simulation of the device strain state.

In Chapter 5 we analyse free-carrier effects in silicon. The presence of this chapter may seem a little odd in a work concerned about Pockels effect in strained silicon where carriers do not have a direct role to play. However, as we will see, by applying an electric field to the strained silicon structure, which is required to activate Pockels effect, the carrier concentration and the distribution of the electric field distribution in the silicon waveguide will be strongly affected by it. Therefore, this chapter is very important because we describe the carrier variations occurring in the waveguide whilst the application of a voltage and how the electric field is modified by it, which strongly influences Pockels effect.

In Chapter 6 the developments of the previous three chapters are merged together with the optical phenomena towards the description of the strain-induced Pockels electro-optic effect. This will be done in the following way: we use the model developed in Chapter 3 that relates $\chi^{(2)}$ with strain and put it together with the strain distribution, which was simulated based on the considerations made in Chapter 4. This will give us a clearer idea on the $\chi^{(2)}$ distribution inside the waveguide. Then, the carriers effects analysed in 5 are simulated together with the $\chi^{(2)}$ distribution and the optics to describe the final electro-optic effect. This information is then used to design the device with the best feasible characteristics for an enhanced strain-induced Pockels effect and for the simulation of the electro-optic effect.

The design and fabrication of the strained silicon chip is discussed in Chapter 7. We present the methodology used to develop a strained silicon device on the SOI platform and the fabrication procedure to make such device for it to be characterized.

In Chapter 8 we put the experiment and modelling together. We present the characterization methods of DC and high-speed Pockels effect in the structures fabricated and the corresponding experimental results. Then we attempt a match between the experimental results and the models developed in chapter 6, in an effort to make an experimental validation of the considerations made before.

Finally, in Chapter 9 we conclude with the perspectives and future work to continue this research work. We present different approaches to validate the theory developed in this thesis and possible routes for optimization and enhancement of Pockels effect in strained silicon devices.

Chapter 2

Pockels effect and strained silicon devices: state of the art

Classical optics is based on the linear properties of light. In other fields of electricity and magnetism, yet, *nonlinearities* have been studied by scientists for a long time. Electrical nonlinearities are behind the working mechanisms of the most important electronic devices such as semiconductor diodes and transistors. In the field of optics, however, the study of nonlinear effects was only possible after the invention of the laser in 1960 [35]. To measure a nonlinear response of matter to electromagnetic waves, in general high fields are necessary which was not possible to achieve before the laser. Since that moment, *nonlinear optics* has been a rapidly growing field in physics [36].

Presently, many nonlinear optical materials play a fundamental role in photonics devices and nonlinearities are found everywhere in optical applications. Pockels effect in particular, is a second order nonlinear phenomenon where the refractive index of a material changes linearly with an applied electric field. This effect, however, is not present in materials possessing an inversion symmetry, which is the case of silicon. In order to overcome this limitation, strain may be applied to the crystal in order to break its symmetry and induce second order nonlinear effects

The interest of strained silicon for nonlinear photonics applications has been growing rapidly for the past few years and great developments have been achieved since the first experimental demonstration of Pockels effect in a strained silicon waveguide in 2006 [28]. In this chapter we introduce the fundamental physics of nonlinear optics and the most relevant nonlinear effects for photonics applications. In the process, we discuss the *second order nonlinear susceptibility* or $\chi^{(2)}$ and its fundamental role in this subject. After that introductory part to Pockels effect, we concentrate on the description of the state of the art of

strained silicon devices for photonics applications, showing its evolution during the period of development of this thesis.

2.1 Fundamental principles of nonlinear optics

All electromagnetic phenomena are governed by the Maxwell equations for both the electric ($\boldsymbol{E}(\boldsymbol{r},t)$) and magnetic ($\boldsymbol{B}(\boldsymbol{r},t)$) fields:

$$\nabla \cdot \boldsymbol{D} = \rho \tag{2.1}$$

$$\nabla \cdot \boldsymbol{B} = 0 \tag{2.2}$$

$$\nabla \times \boldsymbol{E} = -\frac{\partial \boldsymbol{B}}{\partial t} \tag{2.3}$$

$$\nabla \times \boldsymbol{H} = \boldsymbol{J} + \frac{\partial \boldsymbol{D}}{\partial t} \, , \tag{2.4}$$

where ρ and $\boldsymbol{J}$ are the free charge and free current in the material, respectively. The *displacement field* $\boldsymbol{D}$ relates the electric field $\boldsymbol{E}$ with the *macroscopic polarization* $\boldsymbol{P}$ of the material by

$$\boldsymbol{D}(\boldsymbol{r},t) = \epsilon_0 \boldsymbol{E}(\boldsymbol{r},t) + \boldsymbol{P}(\boldsymbol{r},t) \, , \tag{2.5}$$

The constant $\epsilon_0 = 8.854 \times 10^{-12}\,\mathrm{F/m}$ is the *vacuum permittivity*. In non-magnetic materials, which is the case of all materials discussed throughout this thesis, the *magnetizing field* $\boldsymbol{H}$, is simply given by

$$\boldsymbol{H}(\boldsymbol{r},t) = \frac{\boldsymbol{B}(\boldsymbol{r},t)}{\mu_0} \, , \tag{2.6}$$

where $\mu_0 = 4\pi \times 10^{-7}\,\mathrm{H/m}$ is the *vacuum permeability*.

The nonlinear optics arise from the macroscopic polarization. An exhaustive and generalized analysis of the nonlinear effects can be found in other texts [37, 38] and it is not in the scope of this thesis. Here, we will only consider the nonlinear optics in lossless materials with no dispersion through the Kramers-Kronig relations. In this case, the nonlinear phenomena in the frequency domain, can be described by a series expansion of the macroscopic polarization $\boldsymbol{P}(\omega)$ in terms of the electrical field $\boldsymbol{E}(\boldsymbol{r},t)$ [37, 38] [1]:

$$\boldsymbol{P}(\omega) = \boldsymbol{P}^{(1)}(\omega) + \boldsymbol{P}^{(2)}(\omega) + \boldsymbol{P}^{(3)}(\omega) + \cdots \tag{2.7}$$

[1] More generally, we can also include $\boldsymbol{P}^{(0)}$, which is the polarization of a material in the absence of any external electric field. However, it is usually zero in the most common semiconductors and we do not include it here. However, it will be considered later when we study the effect of strain on $\boldsymbol{P}$, in Chapter 3, to study effects like piezoelectricity.

where the i^{th} component of the polarization orders are given by[2]:

$$P_i^{(1)}(\omega) = \epsilon_0 \chi_{ij}^{(1)}(\omega) E_j(\omega) \tag{2.8}$$

$$P_i^{(2)}(\omega) = \epsilon_0 \chi_{ijk}^{(2)}(\omega = \omega_n + \omega_m) E_j(\omega_n) E_k(\omega_m) \tag{2.9}$$

$$P_i^{(3)}(\omega) = \epsilon_0 \chi_{ijkl}^{(3)}(\omega = \omega_m + \omega_n + \omega_l) E_j(\omega_m) E_k(\omega_n) E_l(\omega_l) \tag{2.10}$$

$$\cdots .$$

The $\boldsymbol{P}^{(1)}$ term is called the *linear polarization* and all the others consist on the *nonlinear polarization* $\boldsymbol{P}^{NL}$.

The coefficient $\chi^{(n)}$ is the n^{th} order *susceptibility* and it is a $n+1$-rank tensor[3], representing both the polarization and frequency dependent nature of the interaction as well as the symmetries of the nonlinear material. The n^{th} order optical susceptibility has in general 3^n different components, but in a crystal this number is highly reduced depending on the symmetry group it belongs to. It is beyond the scope of this thesis to go into detail on symmetry properties of nonlinear susceptbilities in crystals and the interested reader can find more detailed overviews on this subject elsewhere [37, 39]. Nevertheless, a common property of the even order susceptibilities is its absence in centro-symmetric materials, as it will be shown in Chaper 3. In these materials, the sum in eq. 2.7 reduces only to odd powers in electric field.

2.1.1 Nonlinearities as a wave mixing process

The polarization vector defined in eq. 2.7 can be inserted in the Maxwell equations to describe the electromagnetic interactions in the nonlinear material. By doing so after some manipulations we can deduce the nonlinear wave equation, given by [37, 38]:

$$\nabla^2 \boldsymbol{E} - \frac{n^2}{c^2} \frac{\partial^2 \boldsymbol{E}}{\partial t^2} = \frac{1}{\epsilon_0 c^2} \frac{\partial^2 \boldsymbol{P}^{NL}}{\partial t^2} , \tag{2.11}$$

where c is the speed of light in vacuum and n is the refractive index of the material. This is an inhomogeneous differential equation where the inhomogeneous term

$$\frac{1}{\epsilon_0 c^2} \frac{\partial^2 \boldsymbol{P}^{NL}}{\partial t^2}$$

[2]The Einstein's summation convention is used and it will also be used in the remainder of this thesis to simplify the sum notations

[3]In this manuscript, we represent a $n+1$ rank tensor either by a bold letter with n bars over it or by its indices. For instance, $\chi^{(2)}$ in its tensorial form shall be represented as $\overline{\boldsymbol{\chi}}^{(2)}$, or simply by $\chi_{ijk}^{(2)}$

acts a driver or source of electromagnetic waves. One of the consequences of this is a nonlinear interaction that will result in frequencies being combined in a process called "wave mixing" [36].

Consider in particular the contribution of second order nonlinear polarization $\boldsymbol{P}^{NL} = \epsilon_0 \chi^{(2)} \boldsymbol{E}^2$. In that case, by considering two lightwaves with two different frequencies

$$\boldsymbol{E}(t) = \boldsymbol{E}_1 \cos(\omega_1 t) + \boldsymbol{E}_2 \cos(\omega_2 t) \ , \tag{2.12}$$

the final $\boldsymbol{P}^{NL}$ will contain frequency components at $2\omega_1$, $2\omega_2$,$\omega_1 + \omega_2$, $\omega_1 - \omega_2$, and 0. From eq. 2.11, this will generate new harmonics and thus produce propagating light waves with those new frequencies. These effects are respectively called *second harmonic generation*, or SHG, (corresponding to both $2\omega_1$ and $2\omega_2$), *sum frequency generation*, *difference frequency generation* and *optical rectification*.

The generation of new wavelengths from those existing initially is particularly relevant in photonics applications for wavelength conversion, particularly in silicon integrated circuits.

2.1.2 Nonlinearities as a refractive index variation process

Nonlinearities may also have a direct influence on the refractive index (n) of a material because it is intimately connected with its polarization. In fact, n is directly dependent on the *dieletric permittivity tensor* $\overline{\epsilon}$ of a material, which is defined as the tensor that satisfies the following relation [40]:

$$\boldsymbol{D} = \epsilon_0 \overline{\epsilon} \cdot \boldsymbol{E} \ . \tag{2.13}$$

From eq. 2.5 we see that the dielectric permittivity tensor can be written as a function of the polarization $\boldsymbol{P}$ of a material. In particular, consider the interaction between a static electric field $\boldsymbol{F}$ (with $\omega \sim 0$) and an optically oscillating electric field $\boldsymbol{E}$ with frequency ω. By putting together eqs. 2.5, 2.7 and 2.8, we can deduce the permittivity tensor as[4]

$$\overline{\epsilon}(\omega) = \overline{\boldsymbol{I}} + \overline{\boldsymbol{\chi}}^{(1)}(\omega) + 2\overline{\overline{\boldsymbol{\chi}}}^{(2)}(\omega) \cdot \boldsymbol{F} + 3\overline{\overline{\overline{\boldsymbol{\chi}}}}^{(3)}(\omega) : \boldsymbol{F}\boldsymbol{F} + \cdots \ . \tag{2.14}$$

[4]The tensorial products are represented by dot products. For instance, in terms of its components and using the Einstein summation notation, eq. 2.14 can be written as

$$\epsilon_{ij}(\omega) = \delta_{ij} + \chi^{(1)}_{ij}(\omega) + 2\chi^{(2)}_{ijk}(\omega) \cdot F_k + 3\chi^{(3)}_{ijkl}(\omega) F_k F_l \ .$$

The 2 and 3 multiplicative coefficients in $\chi^{(2)}$ and $\chi^{(3)}$ terms, respectively, arise from the Kleynman's symmetry condition that makes the sum over frequencies involve several components of the susceptibilities tensors [37].

The first two terms in the previous sum describe the linear dielectric permittivity

$$\overline{\epsilon}_L(\omega) = \overline{\boldsymbol{I}} + \overline{\boldsymbol{\chi}}^{(1)}(\omega) \,, \tag{2.15}$$

where $\overline{\boldsymbol{I}}$ is the identity matrix. In silicon and any other crystal with cubic symmetry, the linear susceptibility is isotropic and it is simply given by $\overline{\boldsymbol{\chi}}^{(1)} = \chi^{(1)}\overline{\boldsymbol{I}}$ [40]. Hence, we may attribute one single value to the linear permittivity and write it simply as

$$\epsilon_L(\omega) = 1 + \chi^{(1)}(\omega) \,. \tag{2.16}$$

Furthermore, it can be shown that the *principal refractive indices of a crystal* n_{ii} are given by [37]

$$n_{ii} = \sqrt{\epsilon_{ii}} \tag{2.17}$$

and thus in silicon and any other optically isotropic material $n = \sqrt{\epsilon_L} = \sqrt{1+\chi^{(1)}}$. This shows the direct relationship between the refractive index and the dielectric permittivity of a material.

The other two terms in eq. 2.14 are the nonlinear contributions to the total dielectric permittivity ϵ. The first one corresponds to the *Pockels effect* and it is given by

$$\overline{\epsilon}_P(\omega) = 2\overline{\overline{\boldsymbol{\chi}}}^{(2)}(\omega) \cdot \boldsymbol{F} \,. \tag{2.18}$$

It describes a linear electro-optic effect where the optical permittivity depends linearly on the applied field $\boldsymbol{F}$. As we can see, the intensity of Pockels effect depends deeply on the second order susceptibility ($\chi^{(2)}$) of the material. This phenomenon is very fast has an inherent temporal response down to the femtosecond range which enables ultrafast modulation beyond 1 THz.

The efficiency of this effect is usually quantified in terms of the *Pockels coefficients* r_{ijk}, related to the $\chi^{(2)}$ components through [41]:

$$r_{ijk}(\omega) = -\frac{\chi^{(2)}_{ijk}(\omega)}{n^2_{ii}(\omega) n^2_{jj}(\omega)} \,. \tag{2.19}$$

Typical Pockels media are $NH_4H_2PO_4$ (ADP), KH_2PO_4 (KDP) and $LiNbO_3$ whose Pockels coefficients values are in the range 1 pm/V to 10 pm/V [42]. Lithium niobate ($LiNbO_3$) is

the preferred material for electro-optics modulation and Pockels-based $LiNbO_3$ modulators have found widespread use in fiber-optic communication systems and have proven to be extremely reliable, becoming the traditional choice for high-speed optical interconnects [43, 27].

In centro-symmetric crystals, because $\chi^{(2)}$ vanishes identically, Pockels effect does not exist. Thus, in silicon this type of electro-optic effect is not present and the refractive index change is due to the second term in eq. 2.14, which corresponds to the *Kerr-effect*

$$\overline{\epsilon}_K(\omega) = 3\overline{\overline{\boldsymbol{\chi}}}^{(3)}(\omega) : \boldsymbol{F}\boldsymbol{F} \ . \tag{2.20}$$

This is a quadratic electro-optic effect, because ϵ varies with the square of applied field $\boldsymbol{F}$. This effect is determined by $\chi^{(3)}$ which is nonzero in every dielectric material. Kerr effect is present in silicon and a change of refractive index could in principle be achieved by the application of an electric field. However, Soref and Bennet [15] have estimated the Kerr effect in silicon to be very weak at room temperature in wavelengths ranging from $1\,\mu$m to $2\,\mu$m. Their calculation predicts a small refractive index change of $\Delta n = 1 \times 10^{-6}$ for an applied electric field $F = 1 \times 10^7\,\mathrm{V/m}$ [15] and stronger electric fields are above the breakdown limit in lightly doped silicon [42]. Consequently, optical modulation based on Kerr effect in Si is very inefficient and can only be driven at very intense electric fields, which is not compatible with the low power consumption requirement for modulation in silicon interconnects.

Pockels effect is the commonly used method for optical modulation in optical interconnects and strain can possibly induce it in silicon. For that reason, much attention has been put on this particular topic over the last years and in what follows we present the state of the art of strained silicon photonics and the context on which this thesis was developed.

2.2 Strain-induced $\chi^{(2)}$ for silicon photonics applications: the state of the art

Applying strain to silicon for technological applications is not new. The discovery that strain may enhance the mobility of electrons in silicon originated in the research of growing Si layers on SiGe buffers in the early 1980s, [44, 45] but the physical mechanism for the enhancement can be traced back to the critical work on deformation potentials by Bardeen and Shockley, in the early 1950s [46, 47]. The carrier velocity improvement in strained-Si channels [48, 49], resulting in higher current drive under fixed supply voltage and gate oxide thickness, has been recognized as a technology applicable to silicon based MOSFETs for

the development of more efficient electronic devices. Consequently, strained-Si near term technology nodes and have actually been included in 90nm logic CMOS technologies [50].

In photonics applications, strain has been widely known to be responsible of a variation of the refractive index in optical materials, known as *photo-elastic effect*. By controlling the direction of stress and strain in the waveguide, the dielectric permittivity tensor components can be modified to tailor the polarization of light in the silicon waveguide [51]. Since the photo-elastic effect was reported in crystalline bulk silicon in the 1970's[52], the use of stress to passively engineer the linear optical properties of materials, in particular the birefringence of the waveguide, has been reported by different authors [53–56]. This mechanism can be actively controlled by integrating it with a piezoelectric crystal that electrically changes the stress applied to the waveguide [57, 58].

Nonetheless, the most promising applications of strain in silicon devices for photonics applications are related with the enhancement of its nonlinearities. Breaking the crystal symmetry through the use of strain may induce nonlinear effects like Pockels and SHG, otherwise impossible in unstrained bulk silicon. Many demonstrations of these phenomena have been reported in strained silicon devices and the reported experimental results have been the target of continuous evolutions and re-interpretations over the past few years.

For that reason, we found it more useful to present the state of the art of second order nonlinear effects in strained silicon devices chronologically. By doing so, not only the evolution of this research field is clearer for the reader, but also it helps understanding the context during the development of the research work presented in this thesis.

2.2.1 The context before the beginning of the present research work

The first reported experimental work on second order nonlinear effects in strained silicon materials was performed by Govorkov and co-workers in 1989 [59]. The authors measured the SHG signal reflected from the silicon substrates and detected an enhancement of the anisotropic SHG reflected signal by a factor of ~ 20 in substrates strained by a stress overlayer made of SiO_2 (shown in Fig.2.1a) and by a factor of ~ 200 in those stress by Si_xNi_y. In addition to this experimental demonstration, the authors also performed the first reported theoretical analysis of the effects of strain on the $\chi^{(2)}$ tensor. By combining the formulation of *deformation potentials* in strained semiconductors with the sp3-orbital model of the covalent bonds of the silicon atoms, they calculated the strain contribution to $\chi^{(2)}$ in a silicon substrate strained uniaxially [59]. The results showed good qualitative agreement with the symmetry considerations of the $\chi^{(2)}$ tensor, but it was limited to the silicon substrates deformed under constant uniaxial stress.

The same theoretical approach was done by Huang *et al.* in 1994 [60] who combined it with Raman spectroscopy to investigate the effect of different levels of stress on the anisotropic SHG reflected from the strained Si surface. Their results showed that the SHG signal was dependent on the thickness of the SiO_2 stress overlayer (which directly affects the amount of strain in silicon), as shown in Fig. 2.1b), demonstrating a dependence of $\chi^{(2)}$ on the strain level.

However, it was not until 2006 that stress was applied to a waveguide towards strain-induced Pockels effect modulation in an operating silicon device. This achievement was reported by Jacobsen and co-workers in [28] and it represented one of the biggest breakthroughs in second order nonlinear effects in strained silicon devices and established a new route of research in silicon photonics.

In this work, the authors designed a strained photonic crystal waveguide (PCW) whose slow light characteristics increased the interaction with the medium, enhancing the $\chi^{(2)}$ effects. The strain was generated by the stack represented in Fig. 2.2a: a 1.2 μm-thick SiO_2 layer with an internal stress of 300 MPa was deposited directly on the PCW silicon structure and on top of it 750 nm of Si_3N_4 was deposited to generate a total stress of 1 GPa. This structure was then placed in a Mach-Zehnder Interferometer (MZI) (as shown in Fig. 2.2b) where an

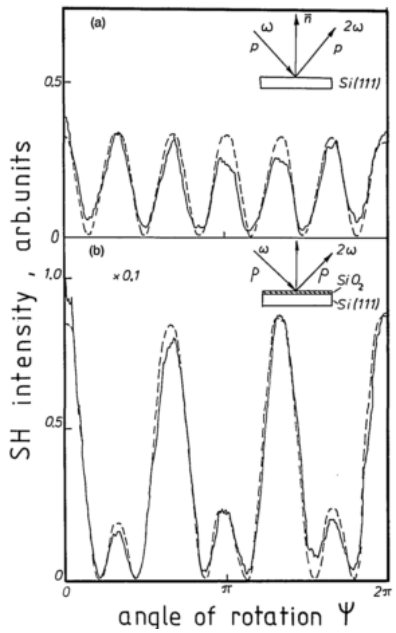

(a) Govorkov et al.

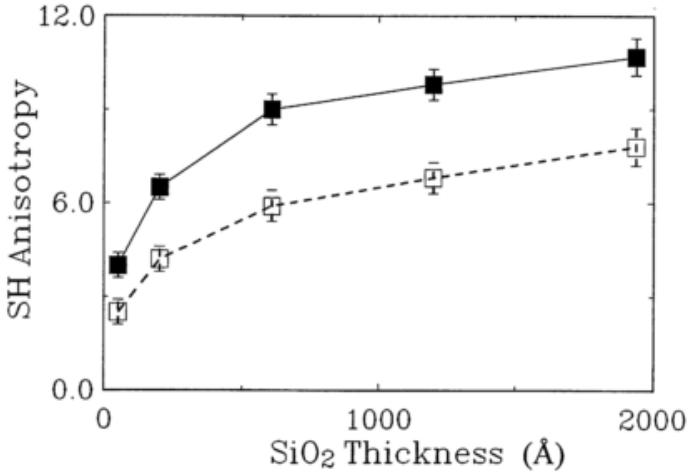

(b) Huang et al.

Fig. 2.1 (a)The comparison of the anisotropic SHG signal reflected from unstrained and strained silicon substrates as a function of the angle, reported by [59] (b)The dependence of the SHG reflected by strained substrates as a function of SiO_2 thickness [60].

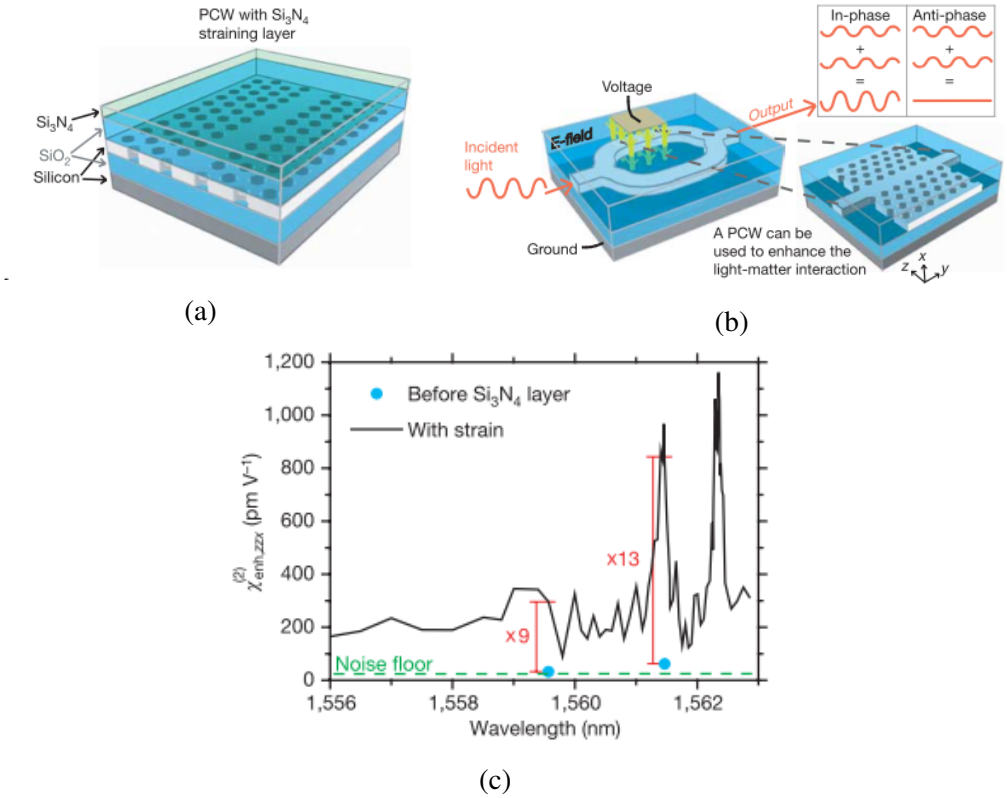

Fig. 2.2 The results reported by Jacobsen *et al.* in [28] (a) Diagram of the investigated PCW. (b) Diagram of a Mach–Zehnder modulator with the PCW strained structure. (c) Enhanced nonlinearity $\chi^{(2)}_{enh}$ measured before (blue points) and after (black line) applying the straining layer.

electric field was applied and optical modulation was detected, as represented in Fig. 2.2c. By comparing the phase shift with a $\chi^{(2)}$ driven $LiNbO_3$ modulator, they were able to measure $\chi^{(2)}_{enh} = 830\,\mathrm{pm/V}$ (enhanced by the PCW structure), corresponding to a strain-induced silicon $\chi^{(2)} \sim 15\,\mathrm{pm/V}$.

Several tests were performed by the authors to verify that the change in refractive index was due to a genuine strain induced Pockels effect and not by any other contribution. Firstly, the thick layer of SiO_2 directly above the silicon PCW ensured that "the guided light is confined well below the Si_3N_4 straining layer; that is, the optical field does not extend to this layer. This arrangement ensures that the only influence of the Si_3N_4 layer on the silicon waveguide is a physical strain, exerted through the SiO_2 layer". The authors also excluded the contributions from carriers, thermo-optic and photo-elastic effects by making separate specific measurements for all of them, some involving modulation at the kHz frequency range. These verification experiments are very important and for reasons that will be clear in section 2.2.3 this publication is still a reference in the field.

After the mentioned experimental breakthrough for Pockels effect in strained silicon devices, some further studies on SHG were reported. In 2009 Hon *et al.* [61] suggested a new kind of strained silicon devices, where the stress applied to the waveguide was periodically changed between compressive to tensile (named by the authors as *periodically poled silicon*) and represented in Fig. 2.3a. This configurations ensures a periodic change of the sign of $\chi^{(2)}$ in silicon and with the correct tuning could in principle enable quasi-phase matching conditions for SHG in strained silicon waveguides. However, this work relied only on simulations and on the assumption of a linear relation between $\chi^{(2)}$ and the strain distribution in the crystal, which lacked physical justifications. It is now widely recognized that this linear relation is not the best description of strain-induced $\chi^{(2)}$ in silicon.

Another important experimental result was reported by Schriever *et al.* in 2010 [62], who showed that the strain-induced $\chi^{(2)}$ has a linear dependence with the value of the internal stress (σ_0) of the stressing overlayer:

$$\chi^{(2)} \propto \sigma_0 \,. \tag{2.21}$$

This result, previously suggested by Govorkov *et al.* in [59], was obtained by measuring the reflection of the SHG signal from a silicon substrate. To generate stress, the silicon substrates were thermally oxidized in wet oxygen atmosphere and stress level was varied by changing the oxidation temperature between 700 °C and 1100 °C. The measurement of the anisotropic behaviour of the reflected SHG allowed the determination of a linear relation between the SHG enhancement (propotional do $\chi^{(2)}$) and σ_0 as shown in Fig. 2.3b.

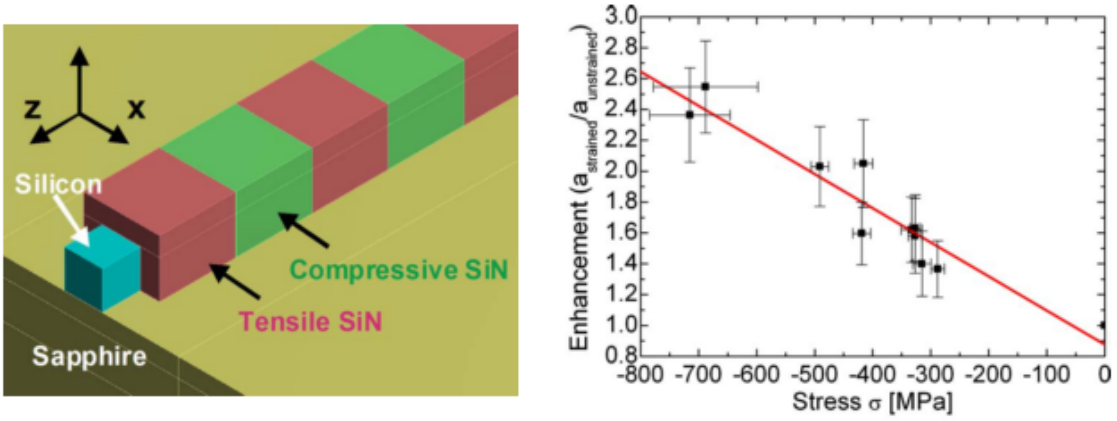

(a) (b)

Fig. 2.3 (a) An example of the *periodically poled silicon* waveguide formed by covering a silicon channel waveguide with two types of silicon nitride SiN stressed films periodically along the waveguide: one induces compressive stress, whereas the other one produces tensile stress. [61] (b) Enhancement of the second-order susceptibility a_{pp} polarization components as a function of the applied stress [62].

The approach of applying strain to silicon integrated devices initiated by Jacobsen *et al.* was followed by Chmielak an co-workers in 2011 [29]. Using RPCVD technique, the authors deposited a highly stressed SiN layer directly on SOI 400 nm×220 nm ridge waveguide, covered by a SiO_2 film and metallic electrodes, disposed as shown in Fig. 2.4a, the authors were able to detect a significant shift in MZI resonances under an applied voltage. The measured shift presented a linear relationship with the applied voltage, as shown in Fig. 2.4b, corresponding to a "Pockels-like" electro-optic effect. This linear response to an electric field corresponded to a maximum strain-induced $\chi^{(2)} = 122\,\mathrm{pm/V}$. This was a striking result as it was almost one order of magnitude higher than that reported by Jacobsen *et al.* in their first demonstration. This was justified by the enhancement of stress applied to the silicon waveguide by the direct deposition of SiN on it. The presented results opened the route for a new generation of high levels of strain-induced $\chi^{(2)}$ in silicon integrated devices.

Later in 2012, M. Cazzanelli, F. Bianco and co-workers in [30, 63] made another breakthrough in integrated silicon devices by reporting the first demonstration of SHG in a silicon integrated waveguide. In this work, silicon waveguides, with dimensions in the 2 μm range in order to accommodate the optical modes at pump wavelength $\lambda_P \sim 2.1\,\mu$m, were stressed by differently deposited SiN_x overlayers. A laser pulse centred at λ_P was sent through the waveguide and a peak in the transmission spectrum around $\lambda_{SHG} \sim 1.1\,\mu$m was detected as presented in Fig. 2.5a. To make a final verification that it was a SHG effect, the authors varied λ_P and showed that the detected generated peak satisfied $\lambda_{SHG} = \lambda_P/2$, shown in 2.5b,

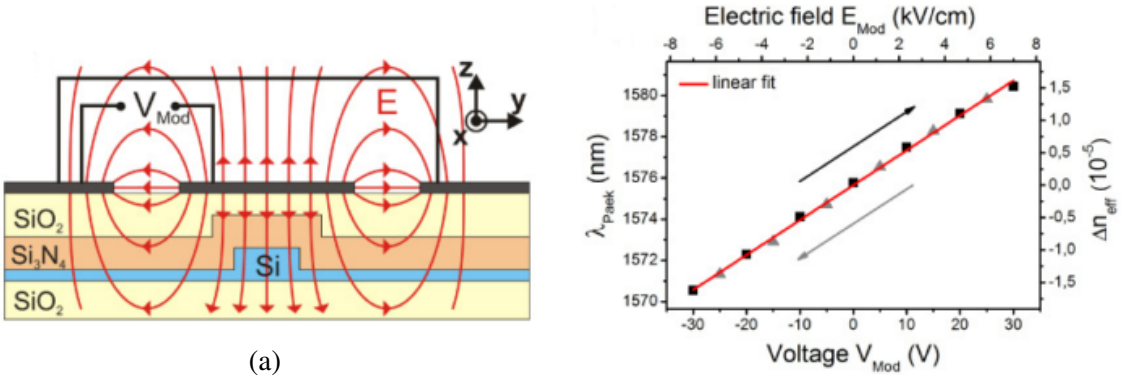

(a) (b)

Fig. 2.4 The results from Chmielak *et al.* in [29]. (a) Schematic cross section of one MZI arm with electrodes and electric field distribution. (b) Spectral shift of the of the MZI resonances versus V_{mod}, showing a linear behaviour.

confirming the SHG nature of the effect attributed to the strain-induced $\chi^{(2)}$ in the silicon waveguide.

In addition, the authors also presented micro-Raman measurements of the strain distribution in the facet of the waveguides and *ab-initio* simulations of the $\chi^{(2)}$ generation in silicon unit cells due to strained atoms, confirming the theoretical relationship between these two quantities. However, no formula was suggested clearly showing a practical relation between both strain and $\chi^{(2)}$ tensor components in silicon.

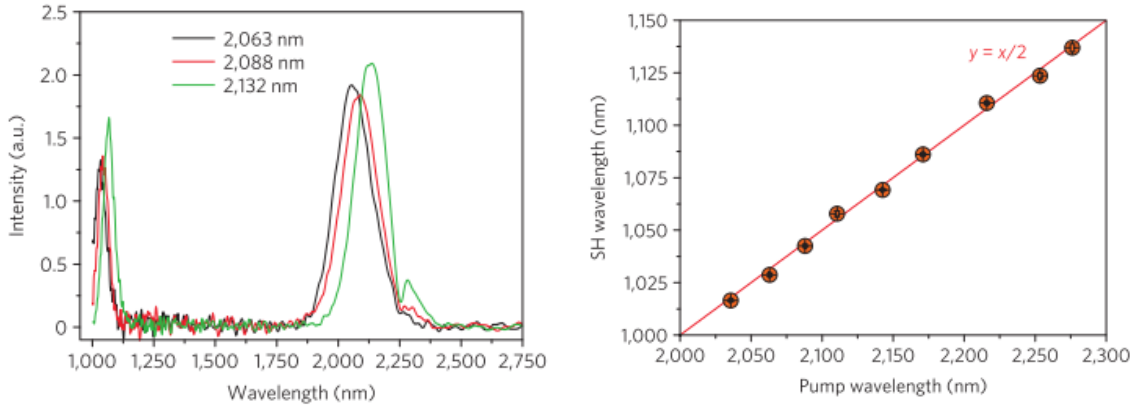

(a) (b)

Fig. 2.5 Results from Cazzanelli *et al.* in [30]. (a) The pump and detected SHG peaks located at respectively λ_P and λ_{SHG}. (b) Relation between λ_P and λ_{SHG} showing that the generated peak is located at $\lambda_{SHG} = \lambda_P/2$.

This was the context of the strained silicon devices for generation of nonlinear effects through symmetry breaking effects when we started our research work, in the end of 2012. At that moment, it was not clear how the strain-induced effects were generated and how one could engineer the strain distribution to excite a particular $\chi^{(2)}$ component.

2.2.2 The state of the art during the development of this thesis

The main focus of our research was the development and optimization of strain-induced Pockels effect in strained silicon waveguides. Therefore, when we started our work we concentrated on two main points: development of strained silicon devices for electro-optic modulation and investigation of the origins of strain-induced $\chi^{(2)}$ in centro-symmetric crystals. Because the highest value of $\chi^{(2)}$ at that moment was achieved by depositing a highly stressed layer of SiN on silicon MZI, reported by Chmielak *et al.* in [29], we chose to follow the same approach.

In the end of 2013, Chmielak and co-workers went a step further and studied the effect of the waveguide width (w_{WG}) on the effective $\chi^{(2)}$ value in strained silicon waveguides [31], using the same configuration presented in Fig. 2.4a. The results showed a clear increase of the effective $\chi^{(2)}$ for narrower waveguides as shown in Fig. 2.6a and a new record value of 190 pm/V was achieved for $w_{WG} = 300$ nm. Moreover, in this work, supported by simulations, they suggested a connection between the strain gradient distribution and the $\chi^{(2)}$ generation in the waveguide.

Approximately at the same time, we published our first preliminary studies on the origins of strain-induced $\chi^{(2)}$ in [64], suggesting the first general formula connecting $\chi^{(2)}$ components and strain gradient components[5]:

$$\chi^{(2)}_{ijk} = \Gamma_{ijk,lmn} \frac{\partial \varepsilon_{lm}}{\partial x_n} , \tag{2.22}$$

which will be developed in detail in Chapter 3 of this manuscript.

The number of publications started to increase as the results became more and more promising. In early 2014, Puckett and co-workers used a Fabry-Perot interferometer configuration to measure the refractive index change of a silicon waveguide strained by a 180 nm-thick layer of SiN_x (internal stress of 1.25 GPa). They measured the effective index of both TM and TE modes as a function of the applied voltage and measured a nonlinear behaviour in both curves, as shown in Fig. 2.6b. This nonlinearity was attributed to the contribution of silicon Kerr effect. By performing a numerical fit to both TM and TE curves

[5] In this equation $\overline{\boldsymbol{\varepsilon}}$ represents the strain tensor, which will be formally introduced in Chapter 3.

and extracting the linear contribution, they were able to measure two different components of the $\overline{\overline{\chi}}^{(2)}$ tensor: $\chi^{(2)}_{xxy} = -74\,\mathrm{pm/V}$ and $\chi^{(2)}_{yyy} = 188\,\mathrm{pm/V}$. In addition to this, the authors reported a structural study of the strain effects in a silicon unit cell and suggested the following relations between strain and $\chi^{(2)}$:

$$\chi^{(2)}_{xxy} = C_{xxy}\frac{\partial \varepsilon_{xx}}{\partial y} \quad , \quad \chi^{(2)}_{yyy} = C_{yyy}\frac{\partial \varepsilon_{xx}}{\partial y} \tag{2.23}$$

and determined $C_{xxy} = -5.89 \times 10^{-15}\,\mathrm{m^2/V}$ and $C_{yyy} = 3.06 \times 10^{-14}\,\mathrm{m^2/V}$. These formulas were supported by the claim that $\chi^{(2)}$ was generated by strain gradients in the silicon waveguide, but no further rigorous quantitative justification was suggested.

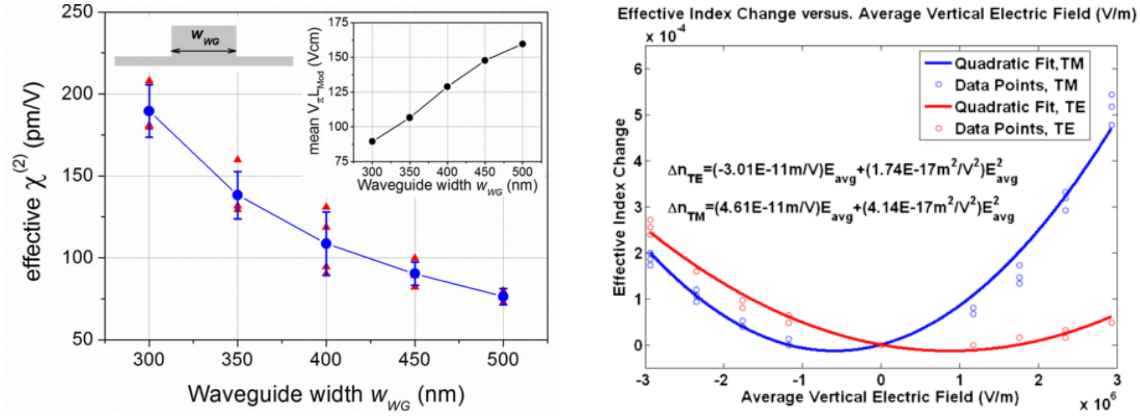

(a) Chmielak et al.

(b) Puckett et al.

Fig. 2.6 (a)Effective $\chi^{(2)}$ plotted versus waveguide width obtained by Chmielak *et al.* in [31]. (b) Observed index changes of the TE- and TM-like modes resonances in response to applied voltages, obtained by Puckett *et al.* in [33].

Later in 2014 we published our first experimental results, in Ref. [32]. We followed the same approach previously done by Chmielak *et al.* in [29, 31] and deposited a SiN layer by PECVD (internal stress of 1.2 GPa) on a silicon strip waveguide in a MZI configuration, whose schematic cross-section is shown in Fig. 2.7a. In order to get a higher level of strain into the waveguide, we used one single thin layer of SiN and avoided the use of SiO_2 which has a smaller level of internal stress. By applying a voltage to the silicon waveguides, we detected a linear relationship between the change in mode effective index and the voltage applied, as shown in Fig. 2.7b. This "Pockels-like" behaviour allowed the determination of the corresponding strain induced $\chi^{(2)}$ and by doing this to every MZI resonance in the wavelength range $1.3 - 1.63\ \mu$m and for 3 different waveguide widths, we were able to determine the wavelength dependence of $\chi^{(2)}$ in this range of the Near Infra-Red window. The results are shown in Fig. 2.7c and from them we were able to conclude that $\chi^{(2)}$ unequivocally increased

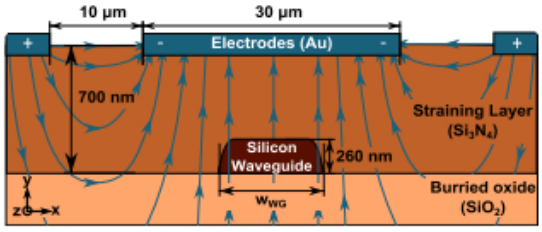

(a)

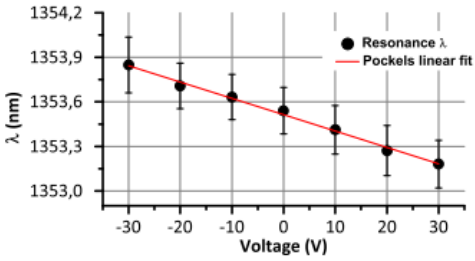

(b)

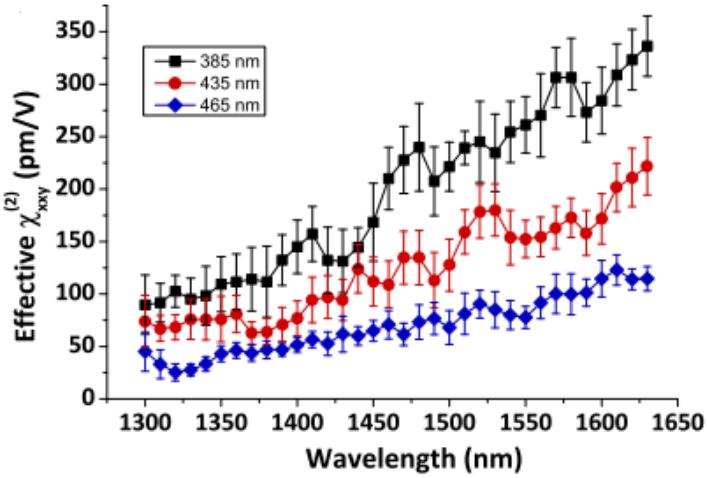

(c)

Fig. 2.7 Results from our publication in [64]. (a) The diagram of the cross section of the analysed structure. (b) The detected linearity between the resonance shift and the applied voltage. (c) The measured $\chi^{(2)}$ as a function of the light wavelength and for different waveguide widths.

for longer wavelengths. Furthermore, we confirmed the growing trend of $\chi^{(2)}$ for narrower waveguides, as previously reported in [31]. This work led to the highest reported value of $\chi^{(2)}$ in strained silicon waveguides, corresponding to 336 pm/V, achieved for $\lambda = 1.63\,\mu$m and $w_{WG} = 335$ nm.

After this publication, Jeremy Witzens in [65] presented a self-consisted method to calculate the deformation potentials of silicon under uniaxial and shear strain by solving for the electronic wavefunctions with a finite-difference method. The formulation consists on calculating the effects of the strain in the position of the atoms in the crystal unit cell and deduce the energy-band diagram from which the deformation potentials can be calculated. The results for the photo-elastic constants shown very good agreement and the author claims the same method can be useful to estimate the effects of strain on $\chi^{(2)}$ in silicon, that can be used to engineer the strain-induced $\chi^{(2)}$ in silicon waveguides.

2.2.3 Carriers effects in strained silicon waveguides: a game changer

In the end of 2014, researchers started to report a connection between second order nonlinear effects in strained silicon devices and free carrier effects. The first publication mentioning the effects of free carriers on strained silicon devices was done by Schriever *et al.* in [34]. The authors suggested that the SiN cladding, rich in positive charged centres (which will be discussed in higher detail in Chapter 5 of this thesis) could bring the silicon waveguide immediately into a strong inversion regime where a strong electric field was developed in the space charge region created at the interface, as represented in Fig. 2.8a. This strong electric field contributed to the observed SHG through a $\chi^{(3)}$ effect known as electric-field-induced-second harmonic generation (EFISH). This third order effect masked the real value of the strain induced $\chi^{(2)}$ and resulted in its over-estimation by around 50%.

In the same paper, the authors went a step further in the characterization of the SHG signal and compared the SHG effect in different waveguides and claddings, as shown in Figs. 2.8b and 2.8c. The results were compared with a Figure of Merit (FOM) for the generated $\chi^{(2)}$ based on the sum of the stress gradients averaged over the waveguide:

$$FOM = \int \left|\frac{\partial \sigma_{xx}}{\partial x}\right| + \left|\frac{\partial \sigma_{xx}}{\partial y}\right| + \left|\frac{\partial \sigma_{yy}}{\partial x}\right| + \left|\frac{\partial \sigma_{yy}}{\partial y}\right| + \left|\frac{\partial \sigma_{xy}}{\partial x}\right| + \left|\frac{\partial \sigma_{xy}}{\partial y}\right| \, dA \, . \tag{2.24}$$

The authors did not provide any physical justification for such formula and claimed that "a rigorous analysis would require the study of the influence of the local stress gradient on the local nonlinear optical properties", recognizing the need for the development of such analysis towards a consistent quantitative relation between $\chi^{(2)}$ and strain effects.

The definite proof of the strong contribution of free carriers on the measurement of Pockels effect in strained silicon devices was made by S. Azadeh and co-workers in early 2015 [66]. It was shown that the electro-optic measurements performed in the DC characterizations of strained silicon structures performed in previous publications were primarily due to free carrier effects. Furthermore, the measured linear relation between the applied voltage and the detected Δn_{eff} could be explained by the contribution of charged centres in the SiN cladding which bring the silicon device directly into inversion, in agreement with the claim made by Schriever *et al.* [34], mentioned above.

The authors of the referred work arrived at this conclusion after carefully studying the electro-optical response of a silicon waveguide covered by a PECVD-deposited SiN straining layer. They detected phenomena like hysteresis and a clear voltage soaking dependence of the response of the device (see Fig. 2.9a). These features could not be explained by Pockels effect alone, but could be easily explained considering the plasma dispersion effect together with the trapping and charging mechanism of the SiN cladding. Furthermore, the

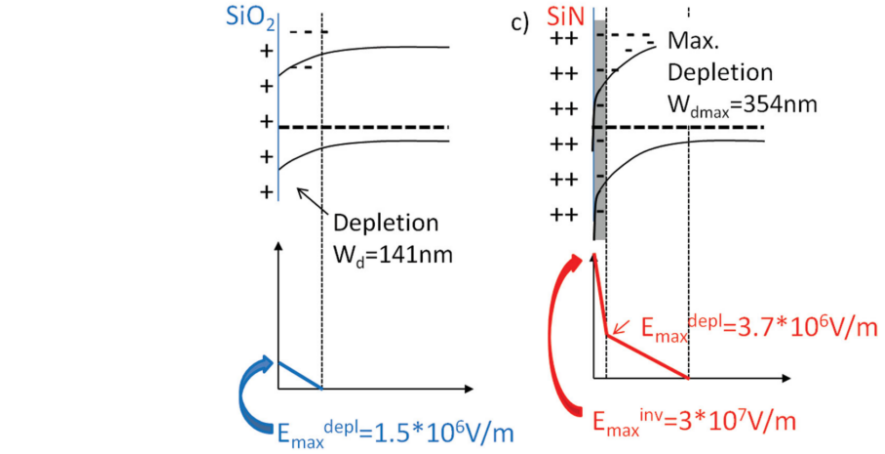

(a)

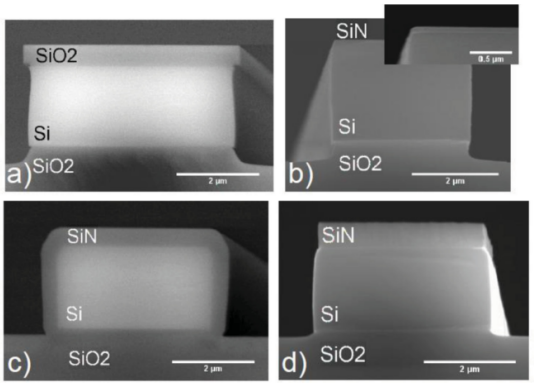

(b)

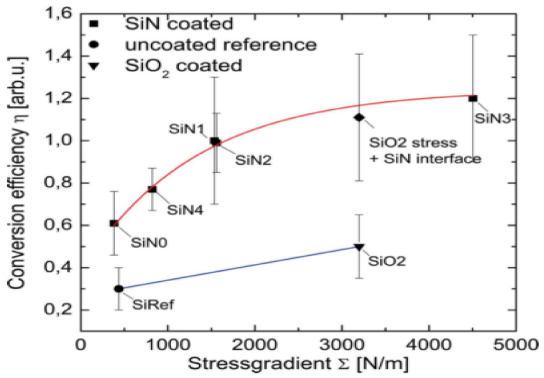

(c)

Fig. 2.8 The results reported by Schriever *et al.* in [34]. (a) The silicon band bending phenomena arising from the charges at the cladding interface, for both SiO_2 and SiN. The generated electric field is also represented. (b) The SEM images of the different measured samples. (c) Dependence of the experimentally determined nonlinear conversion efficiency η on the total stress gradient FOM for waveguides under different stressing conditions.

authors performed semiconducting simulation based on TCAD softwares of the free-carriers behaviour occurring in the waveguide and were able to justify the apparent "linear electro-optic effect" once confused with Pockels, by the presence of fixed charges at the Si/SiN interface which was responsible for moving the voltage dependent plasma-dispersion effect into a linear regime, as shown in Fig. 2.9b.

These results changed everything. Not only they proved that the measurement of Pockels effect in strained silicon devices in a DC regime were not being made under the right conditions, but more importantly it showed that the problem was not being addressed correctly and a change of approach was required. Until that moment, the description of a strained silicon waveguide did not take into account its semiconductor properties and assumed silicon as behaving like a regular dielectric where free carriers do not play a role. This assumption is wrong and the results from Azadeh *et al.* in [66] show why. Any serious analysis of strained silicon devices must include the effects of free carriers in the silicon waveguide and treat them together with the charge properties of the SiN cladding.

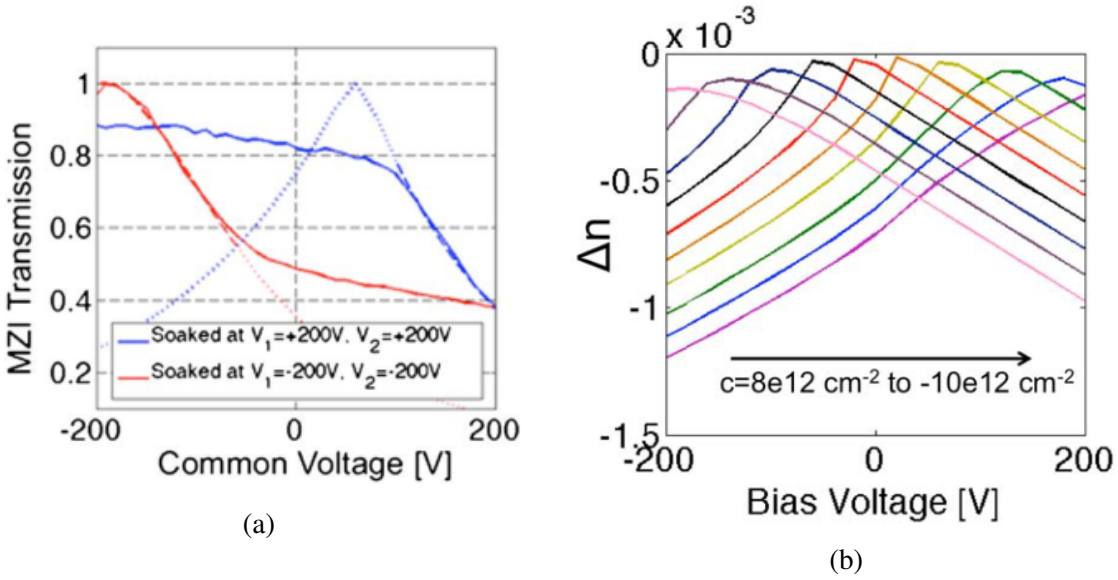

(a) (b)

Fig. 2.9 Results published by Azadeh *et al.* in [66]. (a) Transmission through the MZI as a function of the common voltage applied to the waveguides. The dashed and dotted curves show modeling results based on the free-carrier plasma effect. (b)Simulated waveguide effective index change as a function of voltage applied to the electrode for a single waveguide, for several assumed surface charge concentrations in the SiN film.

The immediate consequence of the referred results was compromising the validity of the $\chi^{(2)}$ values reported by DC measurements of "Pockels effect in strained silicon", particularly those reported in [29, 31–33]. The considerations made by Azadeh and co-workers show that the $\chi^{(2)}$ values were erroneously obtained and they provided a reasonable justification

for the surprisingly high $\chi^{(2)}$ values detected in the DC measurement of strained silicon structures. This affected our work strongly because it required a completely new approach to the problem and a re-frame of the research project. In fact, one of the few works on Pockels effect measurements in strained silicon devices that was not directly affected by these results was the first publication made by Jacobsen *et al.* in [28] because authors ruled out the contribution from both carriers and the SiN layer and the conditions described by Azadeh *et al.* do not apply to their structure. Nevertheless, it is not clear if the plasma dispersion effect was correctly considered in the results reported in Ref. [28], as the authors do not provide much detail on this particular contribution.

The contribution from free carriers reported by Azadeh *et al.* was later confirmed by R. Sharma, M. Puckett and co-workers, first by simulations in [67] and later experimentally in [68]. In these publications, the authors studied the influence of different cladding materials, SiN_x, SiO_2 and Al_2O_3 on the DC electro-optic response of a silicon ring resonator, whose crossection is represented in Fig. 2.10a. By using plasma dispersion effect in the silicon waveguide and the respective cladding charge properties, they found very good agreement between the TCAD simulation of Δn_{eff} as a function of the applied voltage and the experimental results (shown in Fig. 2.10b).

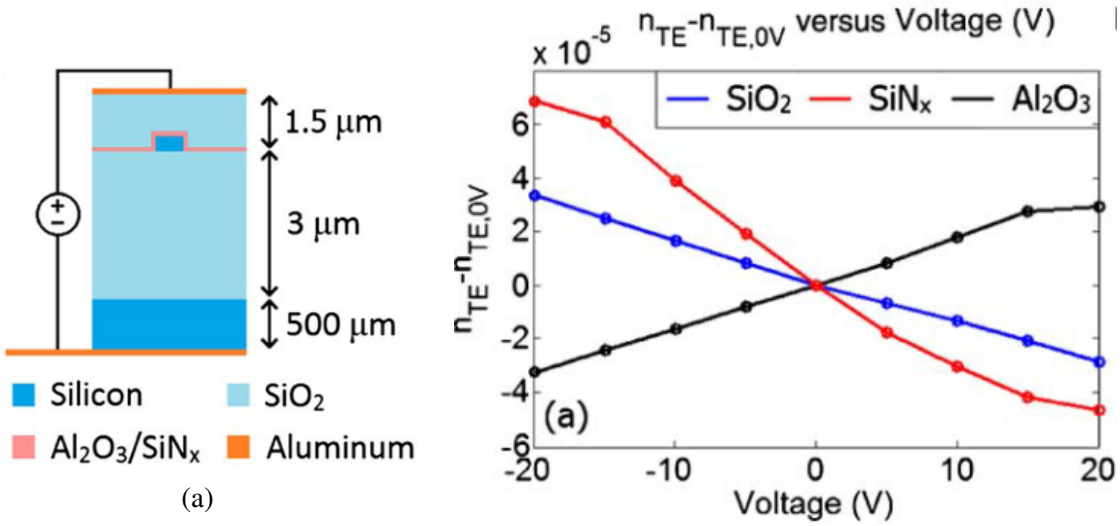

(a) (b)

Fig. 2.10 Results published by Sharma *et al.* in [68]. (a) Cross section of the voltage application method. (b) Electro-optic characteristics in terms of the effective index (n_{eff}) for waveguides clad with either SiO_2 (blue), SiN_x (red), or Al_2O_3 (black).

In the meantime, two theoretical/simulations works were reported. First, Manganelli *et al.* developed a theoretical description of the relation between $\chi^{(2)}$ and the strain distribution in silicon, reported in [69]. Using symmetry arguments, the authors published a theoretical

proof that justified the relation between $\chi^{(2)}$ and the strain gradients, confirming equation 2.22 previously suggested by us and claiming that there are only 15 independent components of the tensor $\Gamma_{ijk,lmn}$. In addition, the authors presented a way to quantitatively describe the strain-induced $\chi^{(2)}$ in silicon through the srain gradient distribution in the waveguide which allows the definition of the so-called *effective strain gradients*. However, the carriers contribution was not included in their model and they strongly affect the electric field inside the waveguideas we shall see in chapter 5.

In other theoretical work by E. Luppi and co-workers [70], detailed *ab-initio* calculations were done on the effects of strain on SHG in the silicon crystal structure. The authors analysed the effects of tensile and compressive strain in different directions and for different light polarizations and wavelengths. Even thought this work is very detailed, it can "just give a qualitative description and understating of the complex process in waveguides" and cannot go further and provide a clear quantitative description between the strain and $\chi^{(2)}$ tensors distribution.

The reported works on the free carriers contribution to $\chi^{(2)}$ also changed the priorities in this research field. Researchers started to focus on an unequivocal proof of the existence of Pockels effect in strained silicon. One property that distinguishes Pockels from plasma dispersion effects is the speed response: while Pockels effect is intrinsically high speed and limited in the THz scale, plasma-carrier effect is slower and it is typically limited in the GHz range. Consequently, as an attempt to detect Pockels effect in strained silicon waveguides, M. Borghi *et al.* [71] made high speed measurements of a silicon waveguide whose stress could be mechanically controlled, as represented in Fig. 2.11a. The detected electro-optic effect is shown in Fig. 2.11b and is limited above 3 GHz, agreeing with the fact that the modulation was primarily caused by the "slow" free carrier effects.

Furthermore, the authors claimed that no strain-induced Pockels effect was detected in their experiment because they did not detect any change in modulation due to a stress variation. This fact suggests that this effect should be weaker than the detection limit of their optical setup and thus should correspond to $\chi^{(2)}$ lower than 8 pm/V. This value is closer to the one detected by Jacobsen *et al.* in [28] and to those reported by SHG measurements in [30, 34]. Nonetheless, it is not clear how this value was estimated because, as we shall see in Chapter 6, for the correct determination of $\chi^{(2)}$, carrier effects must be included and the authors do not specify whether they were included in the calculation of the reported $\chi^{(2)}$ numerical values.

Very recently, we have published our own theoretical model making a connection between $\chi^{(2)}$ and the strain distribution in a waveguide, published in [72]. This model is presented in Chapter 3 of this manuscript and theoretically justifies, on the grounds of the quantum

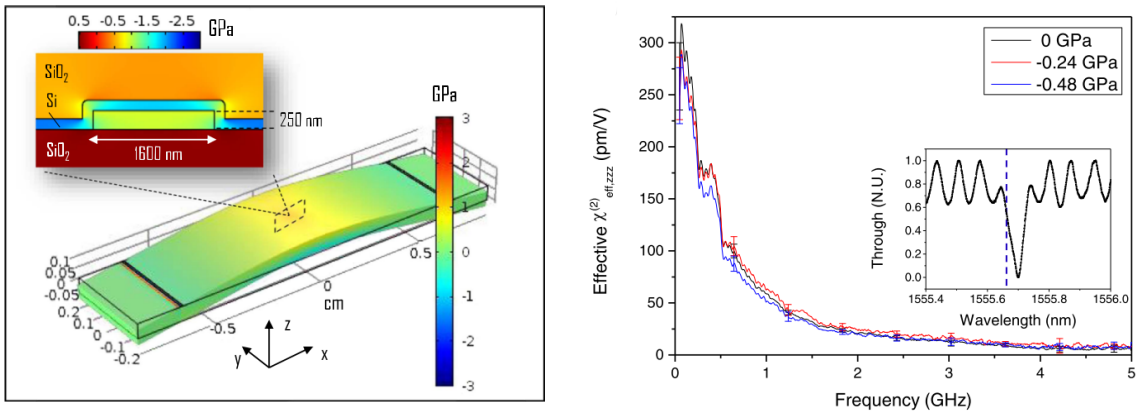

(a) (b)

Fig. 2.11 Results published by Borghi *et al.* in [71]. (a) Finite element simulation of the stress distribution on the sample subjected to a screw displacement. The inset shows the stress profile along the waveguide cross section. (b) Effective $\chi^{(2)}$ as a function of the electrical modulation frequency for three different stress levels in the waveguide. The inset shows the working point of the electro-optic measurement.

mechanics of electrons in the silicon bonds, why $\chi^{(2)}$ is connected to the strain gradients, providing a relation where only two parameters are unknown. This publication can highly contribute for the development of optimization techniques of the nonlinear effects in strained silicon waveguides.

2.3 The evolution and the trends of research

To sum up the description of the state of the art of the strained silicon photonics for nonlinear applications, in Fig. 2.12 we represent the timeline of the publications we described above, together with the most important milestones (on the bottom) and in the background is the evolution of the reported value of "$\chi^{(2)}$ ". It clearly shows an evolution of the framework during the period of development of this thesis, between 2012 and 2016. The most recent works since 2015, make it apparent that the field of strain-induced $\chi^{(2)}$ effects in silicon was the target of many developments, resulting in a fundamental re-frame of the phenomena where free carriers also have their role to play and the real strain-induced $\chi^{(2)}$ is approximately 2 orders of magnitude smaller than what was reported few years ago. This is clear by the big drop in "$\chi^{(2)}$ " represented in the background graph, between 2014 and late 2015.

This resulted in a big step back of the research performed by the community in general, which is apparent by the publications published by groups previously working on strained silicon for nonlinear applications. The need to understand the cladding effects on the silicon

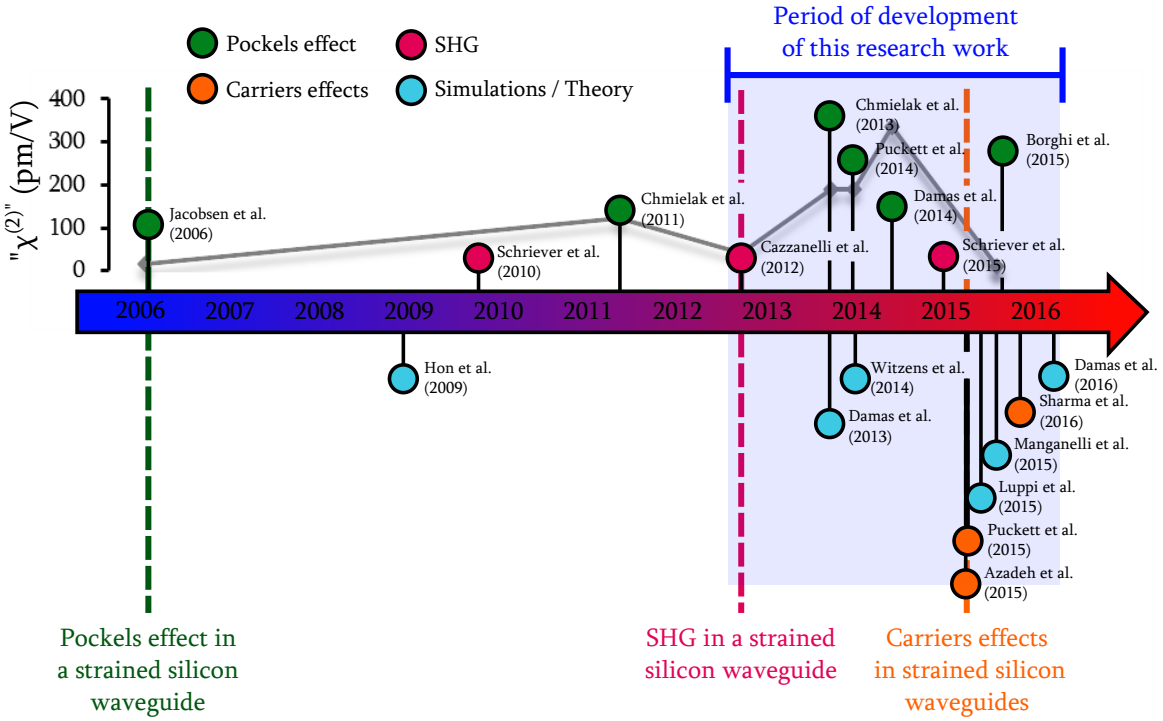

Fig. 2.12 The timeline of the evolution of the strained silicon devices since the demonstration of the first integrated strained silicon device, with the representation of the most relevant works and the most important milestones. On the background is represented the evolution of the reported "$\chi^{(2)}$ " throughout the years.

waveguide forced us to re-think the research priorities for a better understanding of the effects occurring when a silicon waveguide is subjected to a (rather intense) electrostatic field. The result of that research work is presented in this thesis.

Lastly, it is striking the growth of the number of publications on this particular subject of silicon photonics in the past years, clearly showing that this is indeed an exciting topic of research which is capturing the attention of more and more research groups.

Chapter 3

Strain and generation of $\chi^{(2)}$ in silicon

Despite de growing interest in the nonlinear properties of strained silicon, there is a lack of fundamental understanding on the processes through which the deformation of the crystal lattice generates non vanishing $\chi^{(2)}$ tensor components. In other words, there is no available general quantitative relationship between the spatial distribution of strain and $\chi^{(2)}$. Such type of model is fundamental in the field of strained silicon photonics because it permits a connection between the distribution of strain effects in the device, easy to simulate with the right computational tools, and the respective induced nonlinearities.

Many attempts have been made in the past, but no model proved to describe these effects fully and correctly. Nevertheless, there is a convergence on the claim that there is a direct relationship between the second order nonlinear susceptibility and the strain gradients inside the silicon crystal [30–34].

In this chapter we approach the problem of describing $\chi^{(2)}$ in silicon and relate it with the strain effects. For that, we introduce the most important concepts in finite elasticity theory and connect them with the crystal structure. It will help to describe and develop a better understanding on the strain-induced $\chi^{(2)}$. Finally, those concepts will be used together with the quantum mechanical properties of the bonds between the atoms in the silicon crystal, to develop a new and original theory on the generation of second order nonlinear effects. We will show that the developed model not only directly connects $\chi^{(2)}$ with the gradients of strain inside the crystal, as it is claimed in the literature, but it also increases the depth of understanding between these two quantities.

3.1 Nonlinear susceptibility and strain

For a particular nonlinear order effect to take place in a material, it must possess the corresponding nonlinear order optical susceptibility $\chi^{(n)}$. Although every existing material has

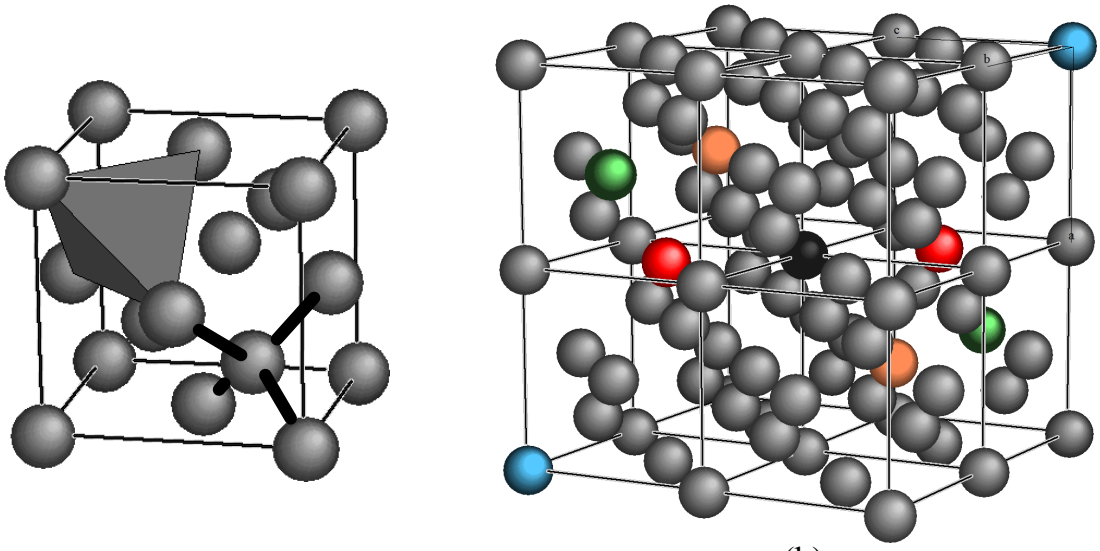

(a) (b)

Fig. 3.1 (a) Representation of the silicon crystal unit cell, with one tetrahedron structure. It is a FCC diamond structure belonging to the O_h symmetry group. Its centro-symmetry is represented by the pairs of coloured atoms in (b), which are symmetric to each other for an inversion operation in respect to the black atom in the center.

nonzero $\chi^{(1)}$ and $\chi^{(3)}$ [39, 37], the existence of $\chi^{(2)}$ depends strongly on the symmetry group of the crystal, vanishing for crystals possessing inversion symmetry,as already mentioned. To understand how strain impacts the generation of $\chi^{(2)}$ in a crystal, it is imperative to first understand how the symmetry of a crystal impacts on the optical susceptibilities and the reasons why some of them vanish for crystals possessing centro-symmetry. Once these concepts are understood, we are in a better position to face the problem on how strain can be applied to break the centro-symmetry of a crystal and how it can be used optimally generate $\chi^{(2)}$.

3.1.1 The silicon crystal and centro-symmetry

Atoms in crystalline silicon are arranged in the *Face-Centered diamond Cubic* structure. The unit cell of such structure is presented in Fig. 3.1. We can see that in each unit cell, each silicon atom is connected to 4 other atoms, forming tetrahedron structures where the connections between atoms, or *bonds*, point in the same four directions. For this reason, silicon is also called a *tetrahedral crystal*.

The diamond crystal structure belongs to the O_h symmetry group, which possesses the highest symmetry from all the groups of crystal lattices [73]. In particular it presents *inversion symmetry* or *centro-symmetry*, which means that any rotation by π around any

axis going through the inversion point followed by a reflection on a plane perpendicular to the rotation axis brings the lattice into coincidence with itself, leaving it invariant [39, 73]. The inversion symmetry of the silicon crystal is represented in Fig. 3.1, where the pairs of coloured atoms are in the inverse position from each other, in respect to the black central atom. We note the inversion operator by $\mathbb{I}$ and performing it twice, of course, brings the atoms back to their original positions, i.e. $\mathbb{I}^2 = \bar{\boldsymbol{I}}$, $\bar{\boldsymbol{I}}$ being the identity operation.

The relevance of the inversion operation $\mathbb{I}$ is that crystals invariant under this operation do not possess second-order nonlinear optical susceptibility, i.e. $\chi^2 = 0$. This can easily be shown by using symmetry arguments and the Neumann's principle, which states that *any property of a crystal that relates two physical quantities must include all of the symmetry operations contained in the point group of the crystal* [39].

We shall now apply this concept to $\overline{\overline{\boldsymbol{\chi}}}^{(2)}$. For that we recall its definition (eq. 2.9), which relates the polarization $\boldsymbol{P}$ and the electric field $\boldsymbol{E}$ as:

$$\boldsymbol{P} = \overline{\overline{\boldsymbol{\chi}}}^{(2)} : \boldsymbol{E}\boldsymbol{E} \tag{3.1}$$

From Neumann's principle, because silicon crystal has inversion symmetry, $\chi^{(2)}$ tensor must be invariant under the $\mathbb{I}$ operation. Thus $\mathbb{I}\overline{\overline{\boldsymbol{\chi}}}^{(2)} = \overline{\overline{\boldsymbol{\chi}}}^{(2)}$. On the other hand, the operation of inverting a vector results in its symmetric, i.e. $\mathbb{I}\boldsymbol{P} = -\boldsymbol{P}$ and $\mathbb{I}\boldsymbol{E} = -\boldsymbol{E}$. Therefore, performing the inversion operation to the quantities in eq. 3.1 yields:

$$\begin{aligned} \mathbb{I}\boldsymbol{P} &= (\mathbb{I}\overline{\overline{\boldsymbol{\chi}}}^{(2)}) : (\mathbb{I}\boldsymbol{E})(\mathbb{I}\boldsymbol{E}) \Leftrightarrow \\ \Leftrightarrow -\boldsymbol{P} &= \overline{\overline{\boldsymbol{\chi}}}^{(2)} : \boldsymbol{E}\boldsymbol{E} \Leftrightarrow \\ \Leftrightarrow -\boldsymbol{P} &= \boldsymbol{P} \Longrightarrow \boldsymbol{P} = 0\,. \end{aligned}$$

Because the previous argument is independent of the electric field $\boldsymbol{E}$, it leads us to the conclusion that $\overline{\overline{\boldsymbol{\chi}}}^{(2)} = 0$ for any crystal possessing centro-symmetry. The same approach can be used to generalize to any $\chi^{(n)} = 0$ for even n or any odd-rank tensor dependent on the crystal properties.

Although it is very efficient in showing that $\chi^{(2)}$ vanishes in centro-symmetric crystals, the previous argument gives us very little insight on the physical processes behind the cancellation of $\chi^{(2)}$, which are very important to understand how strain can be applied to the crystal to overcome it. In order to investigate this problem in a deeper level, next we cover the most relevant concepts in theory of elasticity that allow us to have a better understanding on the deformation state of a crystal.

3.2 Fundamentals of Elasticity Theory

The mechanics of solid bodies form the contents of the *Theory of elasticity*. Under the action of applied forces, solid bodies exhibit deformations, i.e. they change in shape and volume. The deformations are described mathematically in the following way. We define the position of any point in the body by the vector $\boldsymbol{r}$ (with components $x_1 = x$, $x_2 = y$ and $x_3 = z$). When this body is deformed, every point is in general displaced. The point located in position $\boldsymbol{r}$ before the deformation, is generally located in position $\boldsymbol{r'}$ (with components x_i') after the body is deformed. The change of position of this point due to the deformation is called the *displacement vector* and is denoted by $\boldsymbol{u}$ [74]:

$$\boldsymbol{u} = \boldsymbol{r'} - \boldsymbol{r}\,. \tag{3.2}$$

The coordinates x_i' of the displaced point are, of course, functions of the coordinates x_i of the point before displacement. The displacement vector $\boldsymbol{u}$ is therefore also a function of the coordinates x_i and once $\boldsymbol{u}(\boldsymbol{r})$ is known, it determines entirely the deformation of the body.

3.2.1 The deformation gradient and strain tensors

The deformation state of a crystal is completely defined by the displacements $\boldsymbol{u} = \boldsymbol{u}(\boldsymbol{r})$. *Finite strain theory* is the general theory of elasticity that deals with deformations in which displacements are arbitrarily large, opposed to *infinitesimal strain theory* where the displacements are assumed to be infinitesimally small. In the general approach, the local deformation at $\boldsymbol{r}$ is described by a rank-2 tensor, the so-called *deformation gradient tensor*[1] $\overline{\boldsymbol{F}}$, whose components are defined by [75, 76]:

$$F_{ij} \equiv \frac{\partial u_i}{\partial x_j} + \delta_{ij}\,, \tag{3.3}$$

where δ_{ij} is the *Kronecker delta function* which in matrix form corresponds to the *identity matrix* $\overline{\boldsymbol{I}}$. From this definition, the displacement of a point in $\boldsymbol{R}$ in respect to another point in $\boldsymbol{r}_0$ is directly given by:

$$\boldsymbol{u}(\boldsymbol{R}) = \boldsymbol{u}(\boldsymbol{r}_0) + \int_{\boldsymbol{r}_0}^{\boldsymbol{R}} \left(\overline{\boldsymbol{F}}(\boldsymbol{r}) - \overline{\boldsymbol{I}}\right) \cdot d\boldsymbol{r}\,. \tag{3.4}$$

[1] In this manuscript we use the notation of 1 bar over the corresponding letter for rank-2 tensors and two bars for rank-3 tensors.

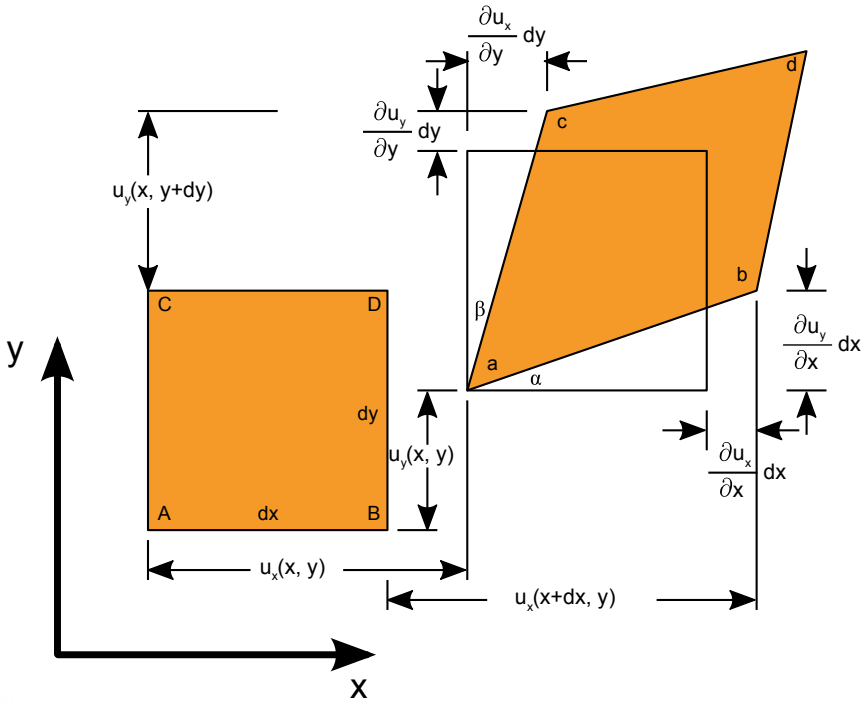

Fig. 3.2 Schematic representation of the infinitesimal displacements $\boldsymbol{u}$ and its derivatives, which constitute the components of the *strain tensor*, ε_{ij}.

The previous equation is extremely important because it allows us to relate the displacement of a point in a material in terms of its deformation state, fully described by $\overline{\boldsymbol{F}}$.

The strain state of a body is determined by the change in element length when the body is deformed. An example is shown in Fig. 3.2. By using that consideration, the *finite strain tensor* $\overline{\boldsymbol{E}}$ is generally defined by [75–77]

$$\overline{\boldsymbol{E}} \equiv \frac{1}{2}\left(\overline{\boldsymbol{F}}^T\overline{\boldsymbol{F}} - \overline{\boldsymbol{I}}\right) \tag{3.5}$$

which characterizes the deformation state of a body.

The *infinitesimal strain tensor* $\overline{\boldsymbol{\varepsilon}}$ is immediately deduced from $\overline{\boldsymbol{E}}$ by only considering very small displacements, i.e. neglecting all 2^{nd} order terms in $\frac{\partial u_i}{\partial x_j}$. Using this condition in eq. 3.5, the components of $\overline{\boldsymbol{\varepsilon}}$ are shown to be given by [74, 78]

$$\varepsilon_{ij} = \frac{1}{2}\left(\frac{\partial u_i}{\partial x_j} + \frac{\partial u_j}{\partial x_i}\right). \tag{3.6}$$

This is the form commonly known for the strain tensor usually found in the literature [74, 78]. In fact, in what follows we will consider the infinitesimal limit except when it is explicitly told otherwise because in strained crystals the deformations are very small

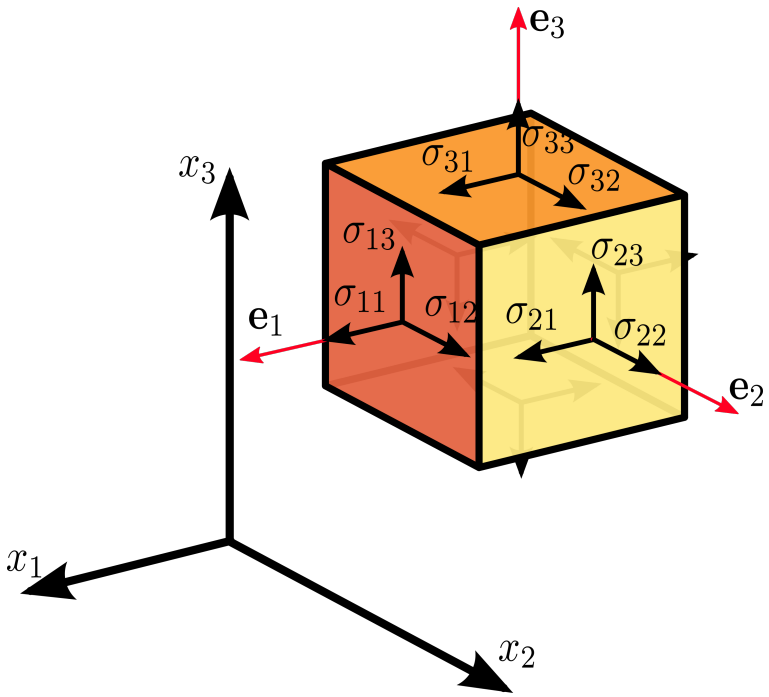

Fig. 3.3 Representation of the components σ_{ij} of the *stress tensor*.

and the infinitesimal description fits very well. However, for the correct application of the infinitesimal theory of the strain in solids (or crystals in particular), it is important to know where this definition comes from and how we can directly relate it to equation 3.4 in order to calculate the displacement of any point in terms of the strain tensor.

The state of translation or rotation of the points in a body is described by the antisymmetric *rotation tensor* $\overline{\boldsymbol{\omega}}$, whose components are given by [74, 78, 79]

$$\omega_{ij} = \frac{1}{2}\left(\frac{\partial u_i}{\partial x_j} - \frac{\partial u_j}{\partial x_i}\right). \tag{3.7}$$

Putting the previous two definitions together, we deduce that

$$\overline{\boldsymbol{F}} = \overline{\boldsymbol{\varepsilon}} + \overline{\boldsymbol{\omega}} + \overline{\boldsymbol{I}} \tag{3.8}$$

The previous equation shows that any displacement in a deformed body can be decomposed by a *pure deformation* $\varepsilon_{ij}dx_j$ and a *pure rotation* $\omega_{ij}dx_j$. While the former originates entirely from the deformation of the neighbourhood of the point in consideration, the latter comes from the rotation of the neighbourhood of that point as an absolutely rigid body about it. For that reason, a body is considered to undergo a *pure deformation* when $\overline{\boldsymbol{\omega}} = 0$ and a *rigid displacement* whenever $\overline{\boldsymbol{\varepsilon}} = 0$ [78, 79].

Replacing 3.8 into eq. 3.4 results in

$$\boldsymbol{u}(\boldsymbol{R}) = \boldsymbol{u}(\boldsymbol{r}_0) + \int_{\boldsymbol{r}_0}^{\boldsymbol{R}} (\overline{\boldsymbol{\varepsilon}} + \overline{\boldsymbol{\omega}}) \cdot d\boldsymbol{r} \,. \tag{3.9}$$

In the very particular case of pure deformations, eq. 3.8 becomes $\overline{\boldsymbol{F}} = \overline{\boldsymbol{\varepsilon}} + \overline{\boldsymbol{I}}$ and eq. 3.9, becomes

$$\boldsymbol{u}(\boldsymbol{R}) = \boldsymbol{u}(\boldsymbol{r}_0) + \int_{\boldsymbol{r}_0}^{\boldsymbol{R}} \overline{\boldsymbol{\varepsilon}} \cdot d\boldsymbol{r} \,. \tag{3.10}$$

The previous equation is valid in cases of pure deformations or when the shear components of strain vanish i.e. $\varepsilon_{ij} = 0$ for $i \neq j$.

The previous equations, are of extreme importance for the model we develop in section 3.4.5 and it can be strongly simplified in cases of homogeneous strain, where the deformation state of a body is the same everywhere.

The atomic description of strain in crystals

So far we have considered continuous bodies where the displacement function $u(\boldsymbol{r})$ can be defined everywhere and x is a continuous variable. However, in a crystal, the value of the displacement field is only known and defined at the discrete atomic positions $\boldsymbol{R}_i$, where the general atom i is located. Even though it does not change the definition of the concepts developed so far, it does poses problems when evaluating the integrals defined in the previous section, namely eq. 3.4, since the variables are not defined continuously, but only at discrete points of space.

This problem has been studied in the field of computational elasticity in crystals and the most common way of solving the problem is by tessellating the crystal space into tetrahedral discrete elements and considering that inside each element α, the deformation gradient $\overline{\boldsymbol{F}}(\boldsymbol{r}) = \overline{\boldsymbol{F}}_\alpha \ (\boldsymbol{r} \in \alpha)$ is homogeneous and determined exclusively by the displacement vectors of the four corner atoms, as represented in Fig. 3.4 [75–77]. In three-dimensional space, each tetrahedral element connects four atoms, and the nodal displacements are interpolated linearly inside each element [76].

Under this definition, the edge vectors $\boldsymbol{R}'_{mn} = \boldsymbol{R}'_n - \boldsymbol{R}'_m$ connecting two atoms m and n in the deformed crystal [2], can be computed from the deformation gradient $\overline{\boldsymbol{F}}_\alpha$ by using eq. 3.4, which results in [76]

$$\boldsymbol{R}'_{mn} = \overline{\boldsymbol{F}}_\alpha \boldsymbol{R}_{mn} \,. \tag{3.11}$$

[2] Later in this chapter we will see that this corresponds to the *bond vector* between two atoms in the silicon crystal.

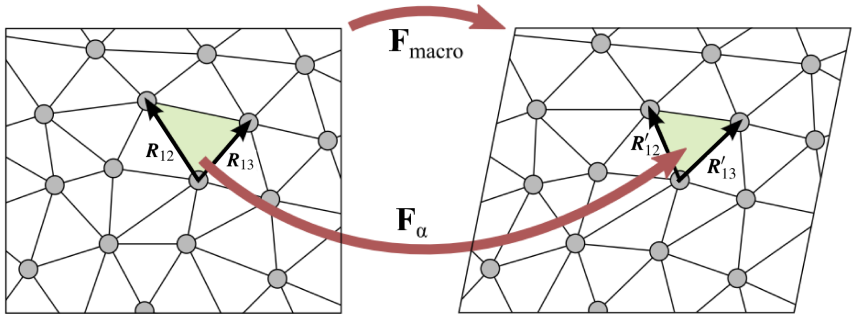

Fig. 3.4 Schematic illustration of the tessellation of space representing the continuous macroscopic deformation gradient field and the discrete $\overline{\boldsymbol{F}}_\alpha$ based on a space-filling elements of the atomistic system. Figure adapted from [76].

In the infinitesimal limit, the previous equation can be rewritten in terms of the strain vector as

$$\boldsymbol{R}'_{mn} = \left(\bar{\boldsymbol{I}} + \overline{\boldsymbol{\varepsilon}}_\alpha\right) \cdot \boldsymbol{R}_{mn} \,. \tag{3.12}$$

The previous equations take into account the discrete nature of the atomic distribution in crystals and it will be used later in the description of the strain effects in the bonds between silicon atoms.

3.2.2 The stress tensor and Hooke's law

In a body that is not deformed, its molecules are in thermal equilibrium and the internal forces in any small element of the body is zero. When a deformation occurs, the arrangement of molecules change and the body leaves its equilibrium state. As a result, internal forces arise which tend to bring it back to its original state, which we call *internal stresses*.

If we consider a small portion of the body with volume dV, like the one in Fig. 3.3 (b), the ith component of the total force component in that volume is given by $\int F_i dV$. Because within that portion of material the internal forces cancel out (Newton's Third Law of Mechanics), the resultant force comes from the forces external from that volume applied on its surface. With that in mind, we may define the *stress tensor* σ_{ij} such that the component F_i of the force satisfies

$$F_i = \sum_j \frac{\partial \sigma_{ij}}{\partial x_j} \,. \tag{3.13}$$

With this definition, the total force F_i over any volume can be written as [74]

$$\int F_i dV = \sum_j \oint \sigma_{ij} dS_j \tag{3.14}$$

and from eq. 3.14, it can be seen that the component σ_{ij} of the stress tensor is the ith component of the force on the unit area dS_j perpendicular to the x_j-axis. This is represented in Fig. 3.3.

The previous discussion makes clear that while the strain is related to the deformation state of a body, the stress provides information on the infinitesimal internal forces applied in the body. Therefore, the states of stress and strain are not independent from each other and must be related somehow. The linear law for the relation between the infinitesimal strain and stress is called generalized *Hooke's law*, which is written as follows [78]:

$$\sigma_{ij} = \sum_{kl} C_{ijkl}\varepsilon_{kl} \,. \tag{3.15}$$

The quantities C_{ijkl} form a tensor of rank-4 and are called the *elastic coefficients*. These coefficients depend on the material, but in very general lines they can be written in terms of the Young modulus Y and the Poisson coefficients ν of the material [74, 78]. In a crystal, they also depend strongly on its symmetry and a detailed treatment of the problem can be found elsewhere [39, 74, 78, 79]. The previous analysis gives us all the relevant tools on the Theory of Elasticity not only to have a better understanding of the quantities that will be discussed throughout this work, but also to follow all the calculations and simulations where these quantities are used.

3.2.3 Homogeneous strain and centro-symmetry

The concepts on elasticity theory discussed above can now be applied to analyse the impact of an homogeneous strain on the inversion symmetry of a crystal. By homogeneous we mean that the strain tensor $\overline{\boldsymbol{\varepsilon}}$ is the same everywhere, i.e. $\overline{\boldsymbol{\varepsilon}}(\boldsymbol{r}) = \overline{\boldsymbol{\varepsilon}}$. We shall now describe the effects of an homogeneous strain in the position of the atoms and then take conclusions about the nature of $\chi^{(2)}$.

In its original state, the atom n in the crystal lattice occupies the position $\boldsymbol{R}_n$. After the crystal undergoes a deformation, the same atom will occupy the new position $\boldsymbol{R}'_n$ related to $\boldsymbol{R}_n$ by eq. 3.2:

$$\boldsymbol{R}'_n = \boldsymbol{R}_n + \boldsymbol{u}_n \tag{3.16}$$

To relate $\boldsymbol{u}_n$ with the strain in the crystal, consider, without any loss of generality, that at the origin of the coordinate system there is no displacement of atoms, i.e. $\boldsymbol{u}_0 = \boldsymbol{0}$ [3]. In a homogeneous pure strain field, the strain tensor is the same in all elements α of the crystal.

[3] If this was not true, it would introduce a constant term $\boldsymbol{u}^0$ which corresponds to a new lattice just shifted in respect to the initial one, which does not change any results we are trying to prove.

Therefore, using eq. 3.12 for any vector $\boldsymbol{R}_n$ we immediately deduce the position of any atom in an homogeneous strain field as

$$\boldsymbol{R}'_n = (\bar{\boldsymbol{I}} + \bar{\boldsymbol{\varepsilon}}) \cdot \boldsymbol{R}_n \,. \tag{3.17}$$

This is a general result widely used in the literature for the atomic positions of a homogeneously strained crystal [73, 80, 81].

We shall now check the effect of an homogeneous strain in the centro-symmetry of a crystal. The definition of inversion symmetry implies that for any atom n in position $\boldsymbol{R}_n$, there is an equivalent atom m in position $\boldsymbol{R}_m = \mathbb{I}\boldsymbol{R}_n = -\boldsymbol{R}_n$. If that same crystal is deformed by a homogeneous strain, the new position of atom n is $\boldsymbol{R}'_n = (\bar{\boldsymbol{I}} + \bar{\boldsymbol{\varepsilon}}) \cdot \boldsymbol{R}_n$. If there is an equivalent atom in position $\mathbb{I}\boldsymbol{R}'_n$ it proves that the centro-symmetry is kept. This is indeed the case because:

$$\mathbb{I}\boldsymbol{R}'_n = -(\bar{\boldsymbol{I}} + \bar{\boldsymbol{\varepsilon}}) \cdot \boldsymbol{R}_n = (\bar{\boldsymbol{I}} + \bar{\boldsymbol{\varepsilon}}) \cdot \boldsymbol{R}_m = \boldsymbol{R}'_m \,. \tag{3.18}$$

Thus, if atom m was in the inversion position of atom n, then in an homogeneously strained crystal, it still is and the crystal preserves the centro-symmetry. With these simple arguments we reach an important conclusion:

Homogeneous strain fields do not break centro-symmetry.

This also leads to the conclusion that homogeneous strains do not induce $\chi^{(2)}$ effects in a centro-symmetric crystal. Therefore, we shall look into the effects of strain in the crystal to understand what strain effects contribute to $\chi^{(2)}$ generation.

3.3 Strain effects on nonlinear optical susceptibilities

We can apply the previous concepts to study how a deformation affects the nonlinear susceptibilities and what properties arise from these effects. The macroscopic polarization $\boldsymbol{P}$ can be written as (recall from eq. 2.7)

$$\boldsymbol{P} = \boldsymbol{P}^{(0)} + \boldsymbol{P}^{(1)} + \boldsymbol{P}^{(2)} + \cdots \tag{3.19}$$

where the term $\boldsymbol{P}^{(n)}$ is the n^{th} order of the nonlinear polarization and it is related with the n^{th} order susceptibiltiy (eq. 2.7).

In general, the optical susceptibilities in a inhomogeneously deformed material are not constant and they will be a function of the position $\boldsymbol{r}$ in the crystal. Therefore, we assume that all strain dependent quantities are locally dependent on the deformations occurring at

that same point $\boldsymbol{r}$ in space. Furthermore, because the strain in the material is not constant, we define a rank-3 *strain gradient tensor* $\overline{\boldsymbol{\eta}}$ whose components are related to the rate of change of the strain tensor itself and are defined by

$$\eta_{ijk} \equiv \frac{\partial \varepsilon_{ij}}{\partial x_k}. \tag{3.20}$$

We now study the effects of both strain and strain gradients on the different polarization orders assuming that in general $\boldsymbol{P}^{(n)}$ is a local function of both $\overline{\boldsymbol{\varepsilon}}$ and $\overline{\overline{\boldsymbol{\eta}}}$ and all quantities depend on the position $\boldsymbol{r}$. Therefore, we can generally write $\boldsymbol{P}^{(n)}(\boldsymbol{r};\overline{\boldsymbol{\varepsilon}},\overline{\overline{\boldsymbol{\eta}}})$ (and equivalently for the corresponding susceptibility $\chi^{(n)}$) and we shall analyse the cases with $n = 0, 1$ and 2.

3.3.1 Order 0: The effect of strain on the spontaneous polarization

The polarization $\boldsymbol{P}^{(0)}$, is the spontaneous polarization a crystal presents in the absence of any external electric field. The most common effect of strain on the spontaneous polarization is the *piezoelectric effect*, which is a linear response of the dielectric polarization to a mechanical strain $\overline{\boldsymbol{\varepsilon}}$ [82–85]. In addition to this, there is also a less known high-order electromechanical phenomenon known as *flexoelectricity* which is an electromechanical effect in which the dielectric polarization exhibits a linear response to a strain gradient $\overline{\overline{\boldsymbol{\eta}}}$ [84–87].

Putting these two effects together, the spontaneous polarization $\boldsymbol{P}^{(0)}(\boldsymbol{r},\overline{\boldsymbol{\varepsilon}},\overline{\overline{\boldsymbol{\eta}}})$ can generally be written as [84, 85]

$$P_i^{(0)} = e_{ijk}\varepsilon_{jk} + \mu_{ijkl}\eta_{jkl}\,. \tag{3.21}$$

The first term in the previous equation describes the piezoelectric effect and the rank-3 tensor e_{ijk} is called the *piezoelectric tensor*. The second term describes the flexoelectric effect and the μ_{ijkl} is called the *flexoelectric tensor*. In centrosymmetric crystals, because $\overline{\overline{\boldsymbol{e}}}$ is a rank-3 tensor, it vanishes identically [4] and there is no piezoelectric effect in silicon or any other crystal with inversion symmetry.

The particularity about the flexoelectricity is that, unlike the piezoelectric tensor, the flexoelectricity tensor is nonzero for all materials. This implies that all dielectric crystals, including the centro-symmetric ones, are in principle capable of producing a spontaneous polarization given that a highly inhomogeneous strain with high values of $\overline{\overline{\boldsymbol{\eta}}}$ is applied to it. This property has therefore been the target of much attention for novel effects based in multiferroics [88] and very recently it has been applied to silicon based structures [89].

[4] Exactly for the same reasons as $\chi^{(2)}$ does and described in section 3.1.1.

3.3.2 Order 1: Photo-elasticity, the effect of strain on $\chi^{(1)}$

The polarization $\boldsymbol{P}^{(1)}$ is generated by a linear response to an applied electric field through the linear susceptibility by (recall from eq. 2.8)

$$\boldsymbol{P}^{(1)} = \epsilon_0 \overline{\boldsymbol{\chi}}^{(1)} \cdot \boldsymbol{E} \, . \tag{3.22}$$

Under strain, the linear susceptibility $\overline{\boldsymbol{\chi}}^{(1)}$ changes. The photo-elastic effect corresponds to the linear dependence of the change of the permittivity tensor, defined by $\overline{\epsilon} = \overline{\boldsymbol{I}} + \overline{\boldsymbol{\chi}}^{(1)}$ (eq. 2.15), on the strain tensor $\overline{\boldsymbol{\varepsilon}}$. This effect is usually described in terms of the inverse of permittivity tensor ($\overline{\epsilon}^{-1}$) and the variation of this tensor due to strain $\delta\left(\overline{\epsilon}^{-1}\right)$ defines the photoelastic tensor p_{ijkl}, which is a rank-4 tensor: [51, 65, 90, 91]

$$\delta\left(\overline{\epsilon}^{-1}\right)_{ij} = p_{ijkl}\varepsilon_{kl} \tag{3.23}$$

The components p_{ijkl} can be written in terms of $\overline{\boldsymbol{\chi}}^{(1)}$ as

$$p_{ijkl} = -\frac{1}{\epsilon^2}\left(\frac{\partial \chi_{ij}^{(1)}}{\partial \varepsilon_{kl}}\right)\Bigg|_{\varepsilon_{kl}=0} \, . \tag{3.24}$$

We neglect the contribution from strain gradients η_{ijk} to $\overline{\boldsymbol{\chi}}^{(1)}$ because this relationship is done through a rank-5 tensor which vanishes in centro-symmetric tensors, unlike the photoelastic effect which exists in all dielectric materials. Furthermore, the strain contribution is usually much higher than that of the strain gradients, so the effects on $\overline{\boldsymbol{\eta}}$ are only relevant when the dependence on $\overline{\boldsymbol{\varepsilon}}$ does not exist.

The tensor p_{ijkl} is symmetric in both pairs of symmetric indices, so we can contract the notation by mapping the indices into a "six-vector" so we can refer to p_{ijkl} simply as $p_{\alpha\beta}$ with the correspondence [90].

$$11 \to 1 \, , \; 2 \to 2 \, , \; 33 \to 3 \, , \; 23,32 \to 4 \, , \; 13,31 \to 5 \, , \; 12,21 \to 6 \, . \tag{3.25}$$

In crystals with cubic symmetry, due to the symmetry of the crystal, the tensor $p_{\alpha\beta}$ has only 3 independent coefficients (p_{11}, p_{12} and p_{44}) and its "six vector" matrix takes the form

[90]

$$\begin{pmatrix} p_{11} & p_{12} & p_{12} & 0 & 0 & 0 \\ p_{12} & p_{11} & p_{12} & 0 & 0 & 0 \\ p_{12} & p_{12} & p_{11} & 0 & 0 & 0 \\ 0 & 0 & 0 & p_{44} & 0 & 0 \\ 0 & 0 & 0 & 0 & p_{44} & 0 \\ 0 & 0 & 0 & 0 & 0 & p_{44} \end{pmatrix} . \tag{3.26}$$

The photo-elastic effect can be generally used to engineer the birefringence of a silicon waveguide [51, 56, 91].

3.3.3 Order 2: The effect of strain on $\chi^{(2)}$

We shall concentrate now on the influence of strain on $\chi^{(2)}$. Again, we assume that $\chi^{(2)}_{ijk} = \chi^{(2)}_{ijk}(\boldsymbol{r}; \overline{\boldsymbol{\varepsilon}}, \overline{\overline{\boldsymbol{\eta}}})$ and by considering only the linear (or 1st order) contributions from the strain $\overline{\boldsymbol{\varepsilon}}$ and strain gradients $\overline{\overline{\boldsymbol{\eta}}}$, we obtain:

$$\chi^{(2)}_{ijk} = \chi^{(2)}_{ijk}\Big|_{\varepsilon=0} + \Upsilon_{ijk,mn}\varepsilon_{mn} + \Gamma_{ijk,lmn}\eta_{lmn}\,, \tag{3.27}$$

where

$$\Upsilon_{ijk,mn} = \left(\frac{\partial \chi^{(2)}_{ijk}}{\partial \varepsilon_{mn}}\right)\Bigg|_{\varepsilon=0} \tag{3.28}$$

is a rank-5 tensor and

$$\Gamma_{ijk,lmn} = \left(\frac{\partial \chi^{(2)}_{ijk}}{\partial \eta_{lmn}}\right)\Bigg|_{\varepsilon=0} \tag{3.29}$$

is a rank-6 tensor.

The previous equation, when applied to centro-symmetric crystals is largely simplified. From section 3.1.1, because crystalline silicon is centro-symmetric, the constant term $\chi^{(2)}_{ijk}\Big|_{\varepsilon=0}$ in eq. 3.27 vanishes. In addition, from the previously fact demonstrated in section 3.2.3 that homogeneous strain fields do not break centro-symmetry, $\chi^{(2)}$ must not depend directly on ε, so the tensor $\Upsilon_{ijk,mn}$ must also vanish.

These two conclusions can also be directly deduced from the fact that both $\chi^{(2)}_{ijk}$ and $\Upsilon_{ijk,mn}$ are odd-rank tensors and in centro-symmetric materials they must vanish. This was the technique used by Manganelli and co-workers in [69].

Finally, we arrive at the conclusion that the only linear dependence of $\overline{\overline{\boldsymbol{\chi}}}^{(2)}$ is on $\overline{\boldsymbol{\eta}}$ and it can be written as

$$\chi^{(2)}_{ijk}(\boldsymbol{r};\overline{\overline{\boldsymbol{\eta}}}) = \Gamma_{ijk,lmn}\eta_{lmn}\,. \tag{3.30}$$

The last results in eqs. 3.30 and 3.29 are of extreme relevance. Firstly, we conclude that the lowest order of strain effects contributing to $\chi^{(2)}$ is not the strain itself, but the strain gradients η_{mnl}, i.e. the rate of variation of strain. Secondly, we see that every component of $\chi^{(2)}$ is a linear combination of every strain gradient directions, weighted by the coefficients $\Gamma_{ijk,mnl}$. Lastly, $\Gamma_{ijk,mnl}$ is a 6-rank tensor whose components depend only on the nature of the original crystal and the coordinate system [5].

The previous simple but strong symmetry arguments allowed us to take these important conclusions. However, they do not provide us with any insight on the value of the coefficients $\Gamma_{ijk,mnl}$, which are indispensable if we look for a practical equation describing the spatial dependence between $\overline{\overline{\boldsymbol{\chi}}}^{(2)}(\boldsymbol{r})$ and $\overline{\overline{\boldsymbol{\eta}}}(\boldsymbol{r})$. This task cannot be achieved by relying exclusively on symmetry properties, but requires a deeper understanding of the electronic phenomena taking place when an inhomogeneous strain is applied to crystal, which we shall approach next.

3.4 The effect of strain on the nonlinear properties of covalent crystals

As referred in the introduction of this chapter, there have been different attempts to create a model which efficiently describes the generation of $\chi^{(2)}$ in strained silicon. The first proposed models connecting $\chi^{(2)}$ with the deformation of the crystal [59, 60] were based on the *deformation potentials in semiconductors*. The deformation potentials theory relies on the de-localisation of the Bloch wavefunction over the entire crystal and when applied to the description of nonlinear optical phenomena in inhomogeneously strained media, because it is not a local theory, its description of the effects is very limiting [59, 92].

Later, simpler models based on classical Coulomb interactions between atoms were also suggested [61, 92], but this oversimplifies the description of the effects and it does not result in a consistent model. To overcome this difficulty, *ab-initio* calculations were performed as an attempt to understand how the change in position of the atoms enables $\chi^{(2)}$ in the crystal [30, 70]. Even though they proved to be an accurate description of the problem, they are very computationally demanding and do not provide a practical, quantitative and spatial

[5] Similarly to what happens to the elastic coefficients C_{ijkl}.

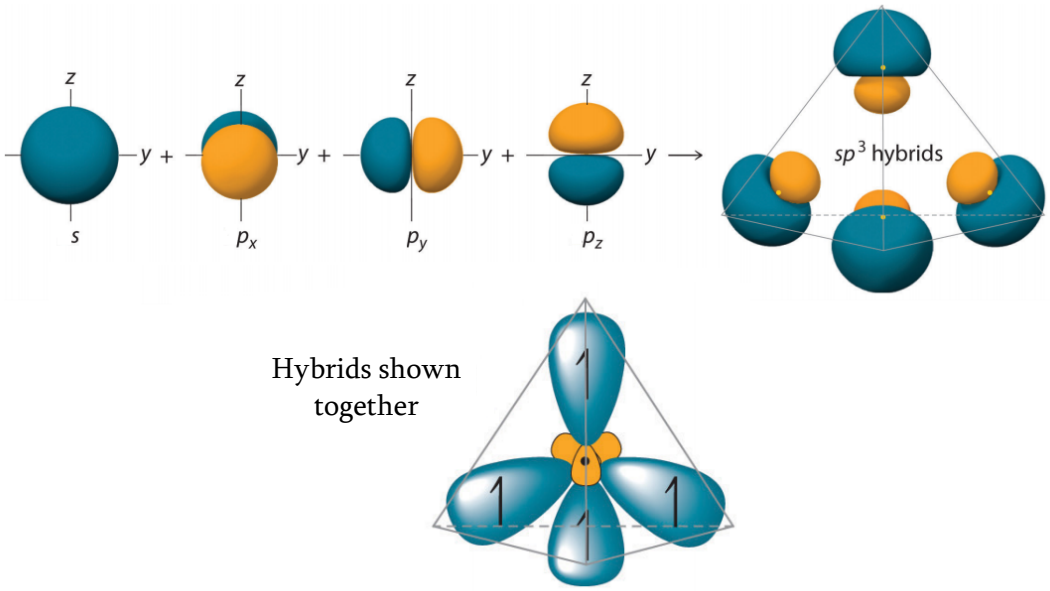

Fig. 3.5 The 3D representation of sp^3 hybridization process and the resulting distribution of hybrids in the tetraheadron unit cell, when the 4 hybrids are put together (figure adapted from Ref. [93]). In this picture, blue means positive and yellow means negative.

relationship between $\chi^{(2)}$ and the strain $\overline{\boldsymbol{\varepsilon}}$ in the crystal and thus do not allow for device design over the strain distribution.

In what follows, we use the concepts of the bonding properties in tetrahedral covalent crystals, like silicon, to develop an atomistic model that connects the nonlinear optical effects with the strain effects.

3.4.1 Fundamental concepts on Tetrahedral covalent crystals

The silicon atom has 4 valence electrons in its most energetic shell, two in s and in p orbitals, as it can be seen by its electronic configuration [Ne]$3s^2 3p^2$.

In its crystallographic configuration, however, as already shown in Fig. 3.1, silicon atoms tend to organize in a tetrahedral configuration. This is achieved through two fundamental processes. On the one hand, neighbour silicon atoms connect by sharing electrons to create a bond between them, the so called *covalent bond*, making silicon a covalent crystal. On the other hand, because of the tetrahedral configuration, it becomes energetically favourable to promote one of the s electrons into a p orbital, ending up with one $|s\rangle$ and three $|p\rangle$ ($|p_x\rangle$, $|p_y\rangle$ and $|p_z\rangle$) orbitals. This change in electronic distribution occurring in crystalline silicon is called sp^3 *hybridization* [93, 94] and the process is represented in Fig. 3.5.

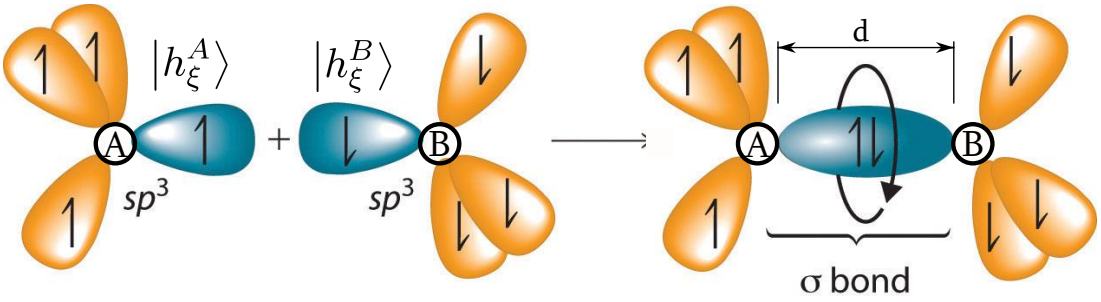

Fig. 3.6 The representation of the formation of a covalent bond (or σ bond) and the resulting tetrahedron orientation in the unit cell. The orbitals involved in the bond formation are in blue (figure adapted from Ref. [93]).

Because of the tetrahedral configuration, the four electrons tend to organize themselves in *hybrid orbitals* (or simply *hybrids*), each of them pointing to the nearest neighbour in the unit cell, as shown in Fig. 3.6. The hybrids are identified by the atom they belong to and their direction. Each one of them points towards one of the four nearest atoms in the tetrahedron structure (compare Fig. 3.5 with Fig. 3.6) and their direction is identified by the *bond vector*, the vector connecting the two atoms. Therefore, there are four bond vectors, $\boldsymbol{\xi}_i$ (i =1,2,3 or 4), given in the crystal coordinates $\{\hat{\mathbf{1}},\hat{\mathbf{2}},\hat{\mathbf{3}}\} = \{[100],[010],[001]\}$ by

$$\boldsymbol{\xi}_1 = \frac{d}{\sqrt{3}}(1,1,1)\ ,\ \boldsymbol{\xi}_2 = \frac{d}{\sqrt{3}}(1,-1,-1)\ ,\ \boldsymbol{\xi}_3 = \frac{d}{\sqrt{3}}(-1,1,-1)\ ,\ \boldsymbol{\xi}_4 = \frac{d}{\sqrt{3}}(-1,-1,1)\,, \tag{3.31}$$

where d is *bond length*, or the distance between the atoms.

For example, the hybrid orbital (or wavefunction) belonging to atom A and pointing in the ξ direction is denoted by h_ξ^A and is given by [95] (see Fig. 3.6):

$$\left|h_\xi^A\right\rangle = \frac{1}{2}\left(\left|s^A\right\rangle + \sqrt{3}\left|p_\xi^A\right\rangle\right)\,. \tag{3.32}$$

The normalized orbital $\left|p_\xi^A\right\rangle$ determines the direction of the hybrid. A *bond* ξ between two atoms A and B is then formed by the overlap of the two adjacent hybrids pointing in opposite directions in A and B (see Fig. 3.6). The explicit form of the four hybrids orbitals are identified by the corresponding bond vectors in eq. 3.31 and in the tetrahedral configuration

are given by: [94]

$$\begin{aligned}
\left|h_1^A\right\rangle &= \frac{1}{2}\left(\left|s^A\right\rangle + \left|p_x^A\right\rangle + \left|p_y^A\right\rangle + \left|p_z^A\right\rangle\right) \text{ , pointing in the } \boldsymbol{\xi}_1 \text{ direction;} \\
\left|h_2^A\right\rangle &= \frac{1}{2}\left(\left|s^A\right\rangle + \left|p_x^A\right\rangle - \left|p_y^A\right\rangle - \left|p_z^A\right\rangle\right) \text{ , pointing in the } \boldsymbol{\xi}_2 \text{ direction;} \\
\left|h_3^A\right\rangle &= \frac{1}{2}\left(\left|s^A\right\rangle - \left|p_x^A\right\rangle + \left|p_y^A\right\rangle - \left|p_z^A\right\rangle\right) \text{ , pointing in the } \boldsymbol{\xi}_3 \text{ direction;} \\
\left|h_4^A\right\rangle &= \frac{1}{2}\left(\left|s^A\right\rangle - \left|p_x^A\right\rangle - \left|p_y^A\right\rangle + \left|p_z^A\right\rangle\right) \text{ , pointing in the } \boldsymbol{\xi}_4 \text{ direction.}
\end{aligned}$$

The hybrid orbitals on any given atom are orthogonal to each other, i.e. $\left\langle h_\alpha^A \middle| h_\beta^A \right\rangle = \delta_{\alpha\beta}$, when the crystal is perfectly tetrahedral, because $\left|s^A\right\rangle$ and $\left|p^A\right\rangle$ are atomic orbitals and thus orthogonal between each other [95]. The overlap between two adjacent hybrids creates a bond orbital (or bond wavefunction) by the process shown in Fig. 3.6.

Because the valence electrons organize themselves in hybrids located around the bonds between atoms, understanding any local property of the crystal (like $\chi^{(2)}$) requires studying the quantum mechanical interactions of these electrons. This can be achieved by using a *bond model* that describes the electron mechanics in the crystal.

However, to make it clearer for the reader, before entering in any mathematical description, we start by discussing the process we propose in this thesis for the generation of $\chi^{(2)}$ in each strained bond.

3.4.2 The local bond theory and the generation of $\chi^{(2)}$

On the validity of a bonding theory for $\chi^{(2)}$ generation

There has been a strong discussion in the past years about the best way to describe the nonlinear susceptibilities in semiconductors, namely in covalent crystals [96]. It has been proposed that to describe nonlinear effects, electrons should not be considered as localized particles, but as waves propagating through the whole crystal, in a fully quantum mechanical energy-band picture [97, 98]. Other theories [99–102], however, suggest that a localized picture, where the electrons are considered to be very localized to the bonds, is the one that gives better experimental agreement than other calculations and a better capacity to deal with a wide range of complex crystal structures [101].

The modern theory of crystals, where density functional theory is used to describe the energy bands, relies on the fact that the material is a periodic structure, which occurs for any crystal or homogeneously deformed one. In that case, this formalism is capable of deduce very precise values of nonlinear coefficients [97, 98]. But from the discussion developed in

section 3.1, we already know the exact solution to the problem of calculating the second order nonlinear susceptibility ($\chi^{(2)}$) in silicon or any centro-symmetric crystal: *it is identically zero*. The atomic structure must be intrinsically non-periodic for $\chi^{(2)}$ effects to take place.

The nonvanishing value of $\chi^{(2)}$ arises from the local variation of strain in the crystal, which is a local function of space. If we assume the strain $\varepsilon(\boldsymbol{r})$ to be a small perturbation to the periodicity of the crystal, the final value of $\chi^{(2)}$ will be given by:

$$\chi^{(2)}(\boldsymbol{r}) = \chi_0^{(2)} + \chi_\varepsilon^{(2)}(\boldsymbol{r}) = \chi_\varepsilon^{(2)}(\boldsymbol{r}) \tag{3.33}$$

where $\chi_0^{(2)}$ is its unstrained value (zero in Si) and $\chi_\varepsilon^{(2)}(\boldsymbol{r})$ is the perturbation due to the strain and is related to a distribution of atoms which has no periodicity. Thus, $\chi^{(2)}$ will be a local function of space and in that case a localized theory of electrons should provide a better description of the process.

This problem is very similar to the analysis of $\chi^{(2)}$ on the surface of Silicon, where the periodicity of the crystal is abruptly lost and $\chi^{(2)}$ is generated at the surface. Just like in the strained crystal, this is also a local problem: $\chi^{(2)}$ is well localized at the surface. Powell *et al.* in [102] analysed this problem and they found very good phenomenological agreement between experimental data and a local-bond theory (the Bond Charge Model). Moreover, because in this kind of model the crystal structure is incorporated at the atomic level, tensor properties emerge automatically. This resulted in a very good phenomenological agreement with experimental data [102].

The arguments presented above show that a local bond theory has much to offer in the description of local effects. Thus, we based our description of the strain effects on the *Bond Orbital Model*, first developed by Walter Harrison in [95], because it is a local-theory of electrons, and it uses the well established concepts of quantum mechanics, namely the hybridization process in silicon atoms. This model was already used to separately characterize the strain effects [103] and the nonlinear optical properties [94] in covalent crystals, establishing a good starting point to develop our own model to put these two phenomena together.

Bond description of the generation of $\chi^{(2)}$

Before entering into the complex quantum mechanical mathematics of the theory we are going to develop, first we explain the physical mechanism it relies on for the generation of $\chi^{(2)}$ in strained covalent crystals, so that it becomes easier for the reader to follow.

In a covalent crystal, $\chi^{(2)}$ depends primarily on the polarity of the bonds connecting the atoms [101, 104, 105]. The polarity of a bond is the difference of energy between the two

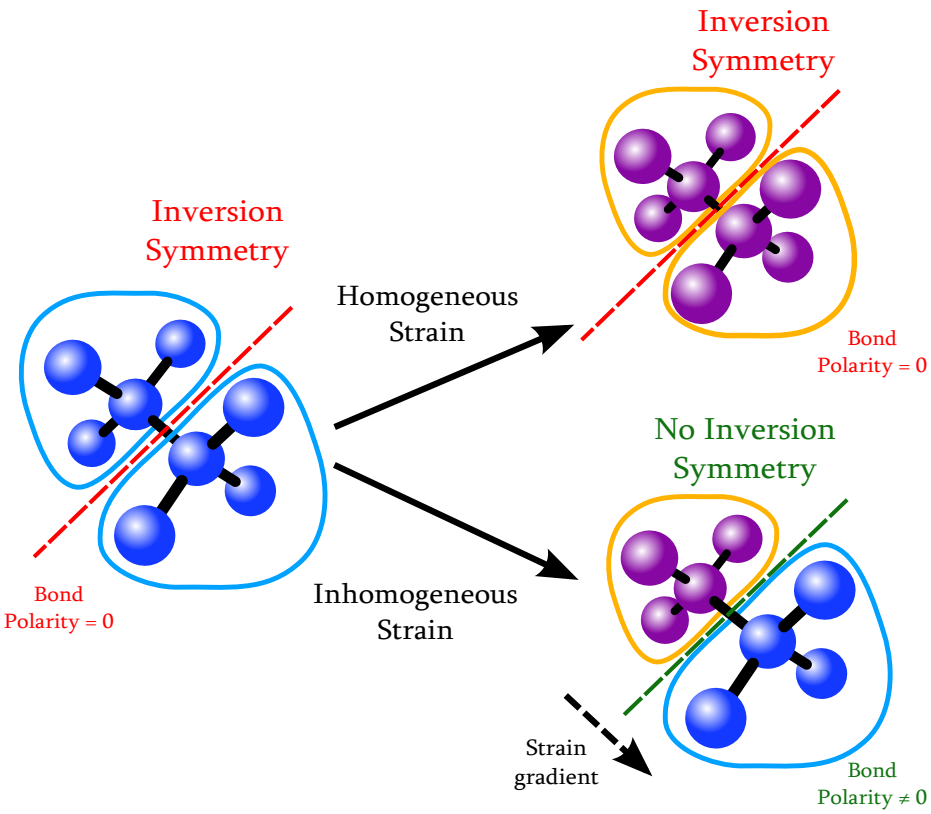

Fig. 3.7 The representation of the process of generation bond polarity, where different contour colours represent different electron energies. An homogeneous strain changes the energy of the bonding electrons, but it is still the same in both sides of the bond (yellow contours), keeping its inversion symmetry. However, a strain gradient, changes the energy in both sides of the bond (represented with the yellow and blue contours), creating a difference in energy polarity and destroying the inversion symmetry. The generated bond polarity is the origin of $\chi^{(2)}$ in that bond.

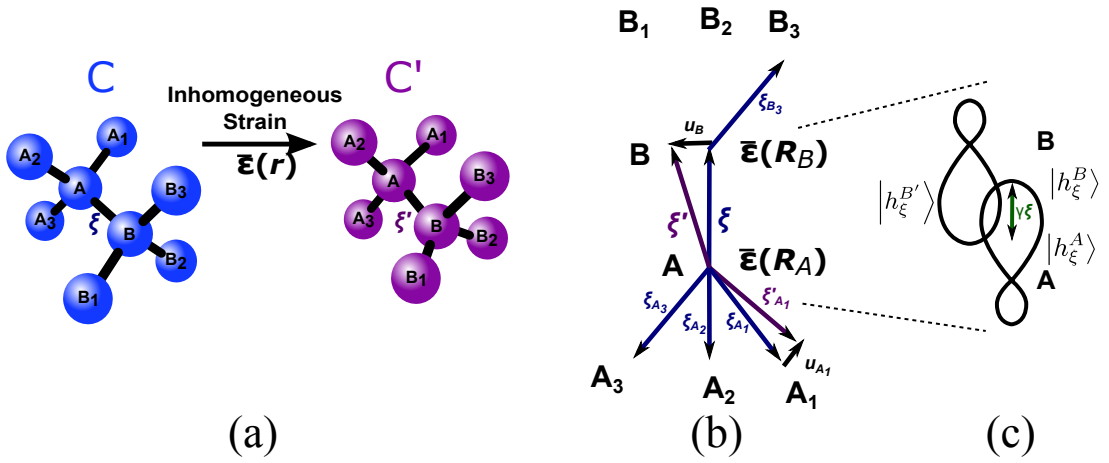

Fig. 3.8 a) 3D Representation of the bond ξ between the general atoms A and B in a unstrained silicon lattice $\mathfrak{C}$ unit cell, in blue. In purple is the corresponding structure when an inhomogeneous strain field is applied, generating the lattice $\mathfrak{C}'$. b) The 2D projection of the unit cells in a), with the representation of the relevant vectors used in the text. c) Schematic representation of the bond hybrids in the original and in the strained crystal.

adjacent hybrids that form the bond. In a centrosymmetric crystal, since the electrons feel the same energy in both directions through any inversion center, the bonds are unpolar, as schematically represented in Fig. 3.7. However, when strain is applied to a crystal, the atomic configuration changes and a bond becomes polar if and only if there is a strain gradient in the direction of the bond. This process is presented schematically in Fig. 3.7, where the blue and yellow contours represent different values of energy. This explains why inhomogeneous strain fields are required to induce bond polarity and thus $\chi^{(2)}$: because homogeneous strain changes the electronic energy, but in the same way in both electrons of the bond.

This is the idea behind the mathematical and quantum description of our model: first we calculate how the strain changes the polarity of a bond and from there we deduce how that strain induces second order nonlinear effects. Moreover, even though in this work we focus on silicon atoms, this procedure can be applied to any covalent diamond crystal structure.

3.4.3 Covalent bonding in a strained crystal

We know proceed on developing the Bond Orbital Model (BOM) onto the strained silicon crystal. For that, consider the original silicon crystal lattice, which you shall denote by $\mathfrak{C}$, represented in blue in the 3D scheme of Fig. 3.8a (compare with Fig 3.6) and the crystal lattice after deformation, denoted by $\mathfrak{C}'$ (represented in purple). Because of the strain effects, each atom n in $\mathfrak{C}'$ is slightly moved by a vector $\boldsymbol{u}_n$ in relation to its position in $\mathfrak{C}$. The new atomic organization in $\mathfrak{C}'$ will change a bond ξ into ξ' (see Fig. 3.8 b)).

To study this new bonding, it may sound appealing to construct four new hybrids out of the atomic orbitals, pointing in the direction of the 4 new deformed bonds ξ_i', instead of using the original hybrids shown in eq. 3.33. However, since the atoms are not arranged in a tetrahedral configuration anymore, such set of hybrids would not be orthogonal and the mathematical problem would require a special treatment afterwards [106]. To overcome this problem, we will construct the wavefunction of the electrons in any atom n as a combination of the original hybrids $\left|h_\xi^n\right\rangle$, placed in the new atomic positions. This is schematically represented in the Fig. 3.8 c), and makes it possible to deal with the quantum mechanical subtleties of our problem, as it will be apparent later on.

Consider now, without any loss of generality, atom A, taken as the atom which preserves the same position in $\mathfrak{C}'$ and $\mathfrak{C}$, as shown in Fig. 3.8 a) and b). This atom is connected to four other atoms. We focus on one of its four bonds, connecting atom A with a general atom B and call it bond ξ. The bond vector $\boldsymbol{\xi}$ (associated with bond ξ) is defined as the vector from atom A to atom B. (Fig. 3.8 b)).

To study the quantum mechanical properties of the electrons in the bond, we must start by building its Hamiltonian. The one-electron Hamiltonian of the strained crystal lattice $\mathfrak{C}'$ is given by [107]:

$$H' = T + \sum_n V_n' = T + V_A' + V_B' + \sum_{n\neq A,B} V_n' \tag{3.34}$$

where T is the kinetic energy of the electron and $V_n'(\boldsymbol{r}) = V(\boldsymbol{r} - \boldsymbol{R}_n')$ is the potential due to the atom in position $\boldsymbol{R}_n'$. This potential can be written as

$$V_n'(\boldsymbol{r}) = V_n(\boldsymbol{r}) + \Delta V_n(\boldsymbol{r}) \,, \tag{3.35}$$

with $V_n(\boldsymbol{r}) = V(\boldsymbol{r} - \boldsymbol{R}_n)$ and $\Delta V_n(\boldsymbol{r})$ being the contribution from the strain effects, vanishing for an unstrained crystal. We have explicitly separated V_A' and V_B' from the sum in eq. 3.34 because we are focusing on the bond between atoms A and B and its treatment is more clear this way.

The matrix element of H' in $\left|h_\xi^A\right\rangle$ is given by

$$\left\langle h_\xi^A \right| H' \left| h_\xi^A \right\rangle = \left\langle h_\xi^A \right| T + V_A' \left| h_\xi^A \right\rangle + \left\langle h_\xi^A \right| V_B' \left| h_\xi^A \right\rangle + \sum_{n\neq A,B} \left\langle h_\xi^A \right| V_n' \left| h_\xi^A \right\rangle \,. \tag{3.36}$$

The corresponding expression is true for $\left|h_\xi^{B'}\right\rangle$, which is the translation of the hybrid $\left|h_\xi^B\right\rangle$ to the new location of atom B in the strained crystal $\mathfrak{C}'$, but pointing in the original direction of B to A in $\mathfrak{C}$, as shown in Fig. 3.8 c). We should now relate these matrix elements with ones of the unstrained Hamiltonian $H = T + \sum_n V_n$ in the original hybrids basis. Since the

hybrid wavefunctions $\left|h_\xi^A\right\rangle$ and $\left|h_\xi^{B'}\right\rangle$ are respectively centred at the atoms A and B in $\mathfrak{C}'$, the interaction of the hybrid with the potentail of each atom itself is not changed by the strain

$$\left\langle h_\xi^A\right| T+V_A'\left|h_\xi^A\right\rangle = \left\langle h_\xi^A\right| T+V_A\left|h_\xi^A\right\rangle \tag{3.37}$$

$$\left\langle h_\xi^{B'}\right| T+V_B'\left|h_\xi^{B'}\right\rangle = \left\langle h_\xi^B\right| T+V_B\left|h_\xi^B\right\rangle \tag{3.38}$$

Moreover, because of the symmetry of the bond, the potential of A in $\left|h_\xi^{B'}\right\rangle$ is the same as the potential of B in $\left|h_\xi^A\right\rangle$. Thus,

$$\left\langle h_\xi^A\right| V_B'\left|h_\xi^A\right\rangle = \left\langle h_\xi^{B'}\right| V_A'\left|h_\xi^{B'}\right\rangle = E_{AB}+\Delta E_{AB} \tag{3.39}$$

where $\epsilon_{AB} = \left\langle h_\xi^A\right| V_B\left|h_\xi^A\right\rangle$ and $\Delta\epsilon_{AB}$ is the correction accounting for the new relative position of atoms A and B in $\mathfrak{C}'$.

For all the other atoms ($n \neq A,B$), we can separately write the strain effects from the original interactions by doing:

$$\left\langle h_\xi^A\right| V_n'\left|h_\xi^A\right\rangle = \left\langle h_\xi^A\right| V_n+\Delta V_n\left|h_\xi^A\right\rangle = \left\langle h_\xi^A\right| V_n\left|h_\xi^A\right\rangle + \left\langle h_\xi^A\right| \Delta V_n\left|h_\xi^A\right\rangle \tag{3.40}$$

$$\left\langle h_\xi^{B'}\right| V_n'\left|h_\xi^{B'}\right\rangle = \left\langle h_\xi^{B'}\right| V_n+\Delta V_n\left|h_\xi^{B'}\right\rangle = \left\langle h_\xi^B\right| V_n\left|h_\xi^B\right\rangle + \left\langle h_\xi^{B'}\right| \Delta V_n\left|h_\xi^{B'}\right\rangle \tag{3.41}$$

From the previous analysis and after eq. 3.36, we are in conditions of writing the matrix elements of H' as

$$\left\langle h_\xi^A\right| H'\left|h_\xi^A\right\rangle = E_A+\Delta E_{AB}+\sum_{n\neq A,B}\left\langle h_\xi^A\right| \Delta V_n\left|h_\xi^A\right\rangle \tag{3.42}$$

$$\left\langle h_\xi^{B'}\right| H'\left|h_\xi^{B'}\right\rangle = E_B+\Delta E_{AB}+\sum_{n\neq A,B}\left\langle h_\xi^{B'}\right| \Delta V_n\left|h_\xi^{B'}\right\rangle \tag{3.43}$$

$$\left\langle h_\xi^A\right| H'\left|h_\xi^{B'}\right\rangle = U_\xi' \tag{3.44}$$

The Hamiltonian crossterm U_ξ' is called the *colavent energy of the bond*. The other terms $\left\langle h_\xi^A\right| H\left|h_\xi^A\right\rangle = E_A$ and $\left\langle h_\xi^B\right| H\left|h_\xi^B\right\rangle = E_B$ are the average energy of $\left|h_\xi^A\right\rangle$ and $\left|h_\xi^B\right\rangle$ in $\mathfrak{C}$. Because of the centro-symmetry, they have both the same value $E_A = E_B$.

3.4.4 The optical dipole moment

The nonlinear optical properties of the bond are extracted from its dipole moment, which in turn is calculated from the bond wavefunction. To do that, we now approach the problem as

done by Harrison *et al.* in the original theory, reported in Ref. [104]. The bond wavefunction $\left|b_\xi\right\rangle$ of the bond ξ is considered to be a combination of the two adjacent hybrids of the atoms forming that bond, as shown in Fig. 3.6 (or in Fig. 3.8c) [95, 104, 106], so we can write:

$$\left|b_\xi\right\rangle = v_A \left|h_\xi^A\right\rangle + v_B \left|h_\xi^{B'}\right\rangle \tag{3.45}$$

and the coefficients v_A and v_B are obtained by minimizing the bond energy $E_b = \frac{\left\langle b_\xi \left| H' \right| b_\xi \right\rangle}{\left\langle b_\xi \middle| b_\xi \right\rangle}$. In doing so, we are implicitly neglecting all the other matrix elements of the Hamiltonian H' and all other hybrid overlaps are neglected (or absorbed in the parameters we have retained). It is important to bear in mind that $\left\langle h_\xi^A \middle| h_\xi^{B'} \right\rangle = S \neq 0$. Under these conditions, the explicit values for v_A and v_B can be found in the original work presented in Ref. [104].

The average position of the bond wavefunction $\left|b_\xi\right\rangle$ in a strained crystal, in respect to the center of the bond, can be shown to be given by [104, 108] (see Appendix A.2)

$$\langle \boldsymbol{r} \rangle = \left\langle b_\xi \middle| \boldsymbol{r} \middle| b_\xi \right\rangle = \left(v_B^2 - v_A^2\right) \left[\frac{\boldsymbol{\gamma}_\xi}{2}\right] \tag{3.46}$$

where $\boldsymbol{\gamma}_\xi = \boldsymbol{u}_B + \gamma \boldsymbol{\xi}$ and $\boldsymbol{u}_B$ is the displacement of atom B. In a non-strained crystal $\langle \boldsymbol{r} \rangle$ reduces to $\left(v_B^2 - v_A^2\right) \gamma \boldsymbol{\xi}/2$ which is the same result presented in Ref. [104]. In the original work, Harrison [104] introduces the parameter γ which accounts for the distance between the "center of gravity" of each hybrid as shown in Fig. 3.8 c) and it would be unity if they were centred at the nucleus.

The optical effects are introduced by considering an optical electric field $\boldsymbol{E}$ that interacts with the bond and induces a dipole moment in it. Because the bond is made out of 2 electrons, its dipole moment is given by $\boldsymbol{p}_\xi = \langle \boldsymbol{p} \rangle_\xi = -2e\langle \boldsymbol{r} \rangle_\xi = -2e \left\langle b_\xi \middle| \boldsymbol{r} \middle| b_\xi \right\rangle$, as represented in red in Fig. 3.9 a).

This optically-induced dipole moment changes the Hamiltonian by a term $\Delta H = \boldsymbol{p} \cdot \boldsymbol{E} = -2e\boldsymbol{r} \cdot \boldsymbol{E}$, which must be included in the calculation of the bond wavefunction $\left|b_\xi\right\rangle$, resulting in coefficients v_A and v_B with some dependence on $\boldsymbol{E}$. The optically induced dipole moment in the bond will not only depend on $\boldsymbol{E}$ but also on the displacement $\boldsymbol{u}_B$ and the resulting expression is

$$\boldsymbol{p}_\xi = -2e \frac{\sigma_\xi + \frac{e\boldsymbol{\gamma}_\xi \cdot \boldsymbol{E}}{2}}{\sqrt{U_\xi'^2 + (1 - S^2)\left(\sigma_\xi + \frac{e\boldsymbol{\gamma}_\xi \cdot \boldsymbol{E})}{2}\right)^2}} \,. \tag{3.47}$$

The quantity σ_ξ is the so-called polar energy (or polarity) of the bond ξ in the strained crystal and is defined by the difference of the average energy of both hybrids making part of the

bond [95, 104] :

$$\sigma_\xi = \frac{\left\langle h_\xi^A \middle| H' \middle| h_\xi^A \right\rangle - \left\langle h_\xi^{B'} \middle| H' \middle| h_\xi^{B'} \right\rangle}{2} . \tag{3.48}$$

This is a measure of the energy difference in both sides of the bond and in a non-strained centrosymmetric crystal it vanishes, i.e. $\sigma_\xi = 0$.

Expanding the dipole moment in a Taylor series in the local optical field $\boldsymbol{E}$, yields $\langle \boldsymbol{p}_\xi \rangle = \boldsymbol{p}_\xi^{(0)} + \boldsymbol{p}_\xi^{(1)} + \boldsymbol{p}_\xi^{(2)} + ...$ where the different order terms are given by:

$$\boldsymbol{p}_\xi^{(0)} = 2e \left[\frac{\sigma_\xi}{\left(U_\xi'^2 + (1-S^2)\sigma_\xi^2 \right)^{\frac{1}{2}}} \right] \frac{\boldsymbol{\gamma}_\xi}{2} \tag{3.49}$$

$$\boldsymbol{p}_\xi^{(1)} = 2e \left[\frac{U_\xi'^2}{\left(U_\xi'^2 + (1-S^2)\sigma_\xi^2 \right)^{\frac{3}{2}}} \right] \cdot \left(\frac{e\boldsymbol{\gamma}_\xi \cdot \boldsymbol{E}}{2} \right) \cdot \frac{\boldsymbol{\gamma}_\xi}{2} \tag{3.50}$$

$$\boldsymbol{p}_\xi^{(2)} = -2e \left[\frac{3}{2} \frac{(1-S^2)U_\xi'^2 \sigma_\xi}{\left(U_\xi'^2 + (1-S^2)\sigma_\xi^2 \right)^{\frac{5}{2}}} \right] \cdot \left(\frac{e\boldsymbol{\gamma}_\xi \cdot \boldsymbol{E}}{2} \right)^2 \cdot \frac{\boldsymbol{\gamma}_\xi}{2} \tag{3.51}$$

The n^{th} order of the macroscopic polarization can be calculated from the previous equations by summing the contributions of the 4 bonds in the unit cell (compare with eq. 2.8)

$$\boldsymbol{P}^{(n)} = \frac{1}{2v_c} \sum_{\xi=1}^{4} \boldsymbol{p}_\xi^{(n)} , \tag{3.52}$$

where $v_c = 2.01 \times 10^{-2}$ nm^3 is the volume of the unit cell and the factor 2 accounts for the consideration of two electrons in the dipole moment of one bond.

The previous equations allow us to determine the macroscopic polarization in terms of the bond properties, in particular the covalent energy $U_\xi^{'}$ and the bond polarity σ_ξ. In order to know how strain affects the macroscopic polarization, we must study the effects of strain on both $U_\xi^{'}$ and σ_ξ.

The covalent study, because it is dependent on the structural interaction between the hybrids, is a function of the strain $\overline{\boldsymbol{\varepsilon}}$ in the crystal [103, 109, 110]. A quantitatively estimation of U_ξ' is not a simple task and the best descriptions are achieved by considering multiple potential contributions in computational simulations [65].

In this model, our main attention is put on the second order effects and as we can see from eq. 3.51 it depends directly on the bond polarity. Under no strain $\sigma_\xi = 0$ and from eq. 3.51 we see that $\boldsymbol{P}^{(2)}$ vanishes. This explains why there is no $\chi^{(2)}$ effects in centrosymmetric covalent crystals like Si. For that reason, we will concentrate now on describing the strain effects on the bond polarity σ_ξ to understand how we can overcome this limitation and make $\boldsymbol{P}^{(2)} \neq 0$.

3.4.5 Strain-induced bond polarity

From the results in eqs. 3.42 and 3.43, the polar energy (or polarity) of a bond defined in eq. 3.48 becomes:

$$\sigma_\xi = \sum_{n \neq A,B} \frac{\left\langle h_\xi^A \middle| \Delta V_n \middle| h_\xi^A \right\rangle - \left\langle h_\xi^{B'} \middle| \Delta V_n \middle| h_\xi^{B'} \right\rangle}{2} \tag{3.53}$$

and it can be immediately seen that if $\Delta V_n = 0$, i.e. no strain is applied to the crystal, $\sigma = 0$ and the bonds are non-polar. This is the reason behind the vanishing $\chi^{(2)}$ in non-strained centrosymmetric crystals.

By reducing the sum in equation 3.48 only to the interaction between the first neighbours of atoms A and B individually, which we denote by A_i and B_i $i = 1,2,3$ respectively as shown in Fig. 3.8 a) and b), equation 3.48 reduces to

$$\sigma_\xi = \sum_{i=1}^{3} \frac{\left\langle h_\xi^A \middle| \Delta V_{A_i} \middle| h_\xi^A \right\rangle - \left\langle h_\xi^{B'} \middle| \Delta V_{B_i} \middle| h_\xi^{B'} \right\rangle}{2} \tag{3.54}$$

Despite we have not said anything about the form of the crystal potential $V(\boldsymbol{r})$ yet, we know it is a central potential ($V(\boldsymbol{r}) = V(r)$) and for r big enough, it should behave like a Coulomb potential. Therefore, for small displacements of the atoms, we may assume that the distances between the electron and the atom are much smaller than $\|\boldsymbol{r} - \boldsymbol{R}_n\|$ are in general much higher than $\|\boldsymbol{u}_n$. Thus, the form of $\Delta V_n(\boldsymbol{r})$ defined in equation 3.35 can be taken by performing a first order Taylor expansion of the potential $V_n'(\boldsymbol{r})$:

$$V_n'(\boldsymbol{r}) = V(\boldsymbol{r} - \boldsymbol{R}_n') = V(\boldsymbol{r} - (\boldsymbol{R}_n + \boldsymbol{u}_n)) \sim V(\boldsymbol{r} - \boldsymbol{R}_n) - \nabla V(\boldsymbol{r} - \boldsymbol{R}_n) \cdot \boldsymbol{u}_n$$

By defining $\nabla V_n \equiv \nabla V(\boldsymbol{r} - \boldsymbol{R}_n)$, it is clear that

$$\Delta V_n = -\nabla V_n \cdot \boldsymbol{u}_n \tag{3.55}$$

which can only be evaluated once we know the explicit form of $V(\boldsymbol{r})$.

Using this definition along with the symmetries of the bond, the central properties of the potential $V(\boldsymbol{r})$ and bearing in mind that the hybrid wavefunctions statisfy $h_\xi^{B'}(\boldsymbol{r}) = h_\xi^A(\boldsymbol{R}'_B - \boldsymbol{r})$, we show in Appendix A.1 that

$$\left\langle h_\xi^A \middle| \Delta V_{A_i} \middle| h_\xi^A \right\rangle = -\left\langle h_\xi^A \middle| \nabla V_{A_i} \middle| h_\xi^A \right\rangle \cdot \boldsymbol{u}_{A_i} \tag{3.56}$$

$$\left\langle h_\xi^{B'} \middle| \Delta V_{B_i} \middle| h_\xi^{B'} \right\rangle = \left\langle h_\xi^A \middle| \nabla V_{A_i} \middle| h_\xi^A \right\rangle \cdot (\boldsymbol{u}_{B_i} - \boldsymbol{u}_B) \tag{3.57}$$

leading to the simplification of equation 3.54 into

$$\sigma_\xi = \sum_{i=1}^{3} \frac{\left\langle h_\xi^A \middle| \nabla V_{A_i} \middle| h_\xi^A \right\rangle \cdot (\boldsymbol{u}_B - \boldsymbol{u}_{B_i} - \boldsymbol{u}_{A_i})}{2} \tag{3.58}$$

We define now $\boldsymbol{\xi}_{A_i}$ as the bond vector pointing from atom A to A_i and the corresponding for B (Fig. 3.8 b)) We can now use the concepts from elasticity theory shown in section 3.2.1. From the discussion made in section 3.2.1, $\overline{\boldsymbol{F}}$ is considered to be constant and equal to $\overline{\boldsymbol{F}}_A$ in the tetrahedron limited by the 3 vectors $\boldsymbol{\xi}_{A_i}$. The same is valid to $\overline{\boldsymbol{F}}_B$.

Therefore, from eq. 3.4 we can generally write that

$$\boldsymbol{u}_{A_i} = (\overline{\boldsymbol{F}}_A - \overline{\boldsymbol{I}}) \cdot \boldsymbol{\xi}_{A_i} \tag{3.59}$$

$$\boldsymbol{u}_{B_i} = \boldsymbol{u}_B + (\overline{\boldsymbol{F}}_B - \overline{\boldsymbol{I}}) \cdot \boldsymbol{\xi}_{B_i} \,. \tag{3.60}$$

The previous equation is the most general form but if we consider a material undergoing an infinitesimal pure deformation, then $\overline{\boldsymbol{\varepsilon}} = (\overline{\boldsymbol{F}} - \overline{\boldsymbol{I}})$ and eqs.3.59 and 3.60 become

$$\boldsymbol{u}_{A_i} = \overline{\boldsymbol{\varepsilon}}_A \cdot \boldsymbol{\xi}_{A_i} \tag{3.61}$$

$$\boldsymbol{u}_{B_i} = \boldsymbol{u}_B + \overline{\boldsymbol{\varepsilon}}_B \cdot \boldsymbol{\xi}_{B_i} \,. \tag{3.62}$$

The last two equations are also valid whenever the shear components of the strain tensor are much smaller than the principal components ε_{ii}, so we can neglect its contribution. In fact, this is usually the case in the bulk of strained nanostructures and in the remainder of the present model we will neglect the contribution of the shear components of strain.

Putting together equations 3.58, 3.61, 3.62 and bearing in mind that $\boldsymbol{\xi}_{B_i} = -\boldsymbol{\xi}_{A_i}$ (Fig. 3.8 b)), we deduce

$$\sigma_\xi = \frac{1}{2} \sum_{i=1}^{3} \left\langle h_\xi^A \middle| \nabla V_{A_i} \middle| h_\xi^A \right\rangle \cdot [\overline{\boldsymbol{\varepsilon}}_B - \overline{\boldsymbol{\varepsilon}}_A] \cdot \boldsymbol{\xi}_{A_i}$$

Since the strain changes slowly in distances of the bond length d, and because $\boldsymbol{R}_B = \boldsymbol{R}_A + \boldsymbol{\xi}$, we can relate the components of the strain tensor in atoms A and B by making a first

order Taylor expansion

$$\varepsilon_{kl_B} \sim \varepsilon_{kl_A} + \nabla\varepsilon_{kl}(\boldsymbol{R}_A)\cdot\boldsymbol{\xi}$$

Using the definition of the strain gradient tensor $\overline{\overline{\boldsymbol{\eta}}}$ and putting together the previous two equations, we finally arrive at the relation between the strain gradients $\overline{\overline{\boldsymbol{\eta}}}$ and the polarity of a bond ξ in atom A as

$$\sigma_\xi\left(\overline{\overline{\boldsymbol{\eta}}}\right) = \frac{1}{2}\sum_{i=1}^{3}\boldsymbol{\theta}_i^\xi\cdot\overline{\boldsymbol{\Xi}}_\xi\left(\overline{\overline{\boldsymbol{\eta}}}\right)\cdot\boldsymbol{\xi}_{A_i} \tag{3.63}$$

where we have defined the rank-2 tensor $\overline{\boldsymbol{\Xi}}_\xi(\overline{\overline{\boldsymbol{\eta}}};\boldsymbol{R})$, related to the bond ξ, in the atom located in position $\boldsymbol{R}$ and with explicit dependence on the strain gradients $\overline{\overline{\boldsymbol{\eta}}}$ in that position, given by

$$\overline{\boldsymbol{\Xi}}_\xi\left(\overline{\overline{\boldsymbol{\eta}}};\boldsymbol{R}\right) = \overline{\overline{\boldsymbol{\eta}}}(\boldsymbol{R})\cdot\boldsymbol{\xi}\ . \tag{3.64}$$

In addition, the vector $\boldsymbol{\theta}_i^\xi$ is defined by

$$\boldsymbol{\theta}_i^\xi = \left\langle h_\xi^A\middle|\nabla V_{A_i}\middle|h_\xi^A\right\rangle = \tag{3.65}$$

$$= \int_\infty |h_\xi^A(\boldsymbol{r})|^2\cdot\nabla V(\boldsymbol{r}-\boldsymbol{R}_{A_i})dV = \tag{3.66}$$

$$= \int_\infty |h_\xi^A(\boldsymbol{r})|^2\cdot\left.\frac{\partial V}{\partial r}\right|_{\boldsymbol{r}-\boldsymbol{R}_{A_i}}\cdot\frac{\boldsymbol{r}-\boldsymbol{R}_{A_i}}{\|\boldsymbol{r}-\boldsymbol{R}_{A_i}\|}dV\ . \tag{3.67}$$

Its evaluation can be done with the help of the scheme in Fig. 3.9 a). It does not depend on the atom A in particular, but only on the unstrained bonds $\boldsymbol{\xi}_i \equiv \boldsymbol{\xi}_{A_i}$, $i = 1,2,3$, which are the 3 bonds in the unit cell different than ξ, the one considered for the calculation of the polarity (compare Fig. 3.9 a) with Fig. 3.8 b)).

The closed form of $\boldsymbol{\theta}_i^\xi$ can only be found once the correct potential $V(\boldsymbol{r})$ is known. However, regardless of that, because $\boldsymbol{\xi}_i$ and $\boldsymbol{\xi}$ are not parallel, they span all space and we can define

$$\boldsymbol{\theta}_i^\xi = \alpha\boldsymbol{\xi} + \beta\boldsymbol{\xi}_i \tag{3.68}$$

where α and β are parameters whose values are related to the projections of $\boldsymbol{\theta}_i^\xi$ on $\boldsymbol{\xi}$ and $\boldsymbol{\xi}_i$ respectively and are characteristic of the crystal species in consideration. This definition together with equation 3.63, allows us to write

$$\sigma_\xi(\overline{\overline{\boldsymbol{\eta}}}) = \frac{1}{2}\sum_{i=1}^{3}[\alpha\boldsymbol{\xi} + \beta\boldsymbol{\xi}_i]\cdot\overline{\boldsymbol{\Xi}}_\xi\left(\overline{\overline{\boldsymbol{\eta}}}\right)\cdot\boldsymbol{\xi}_i\ . \tag{3.69}$$

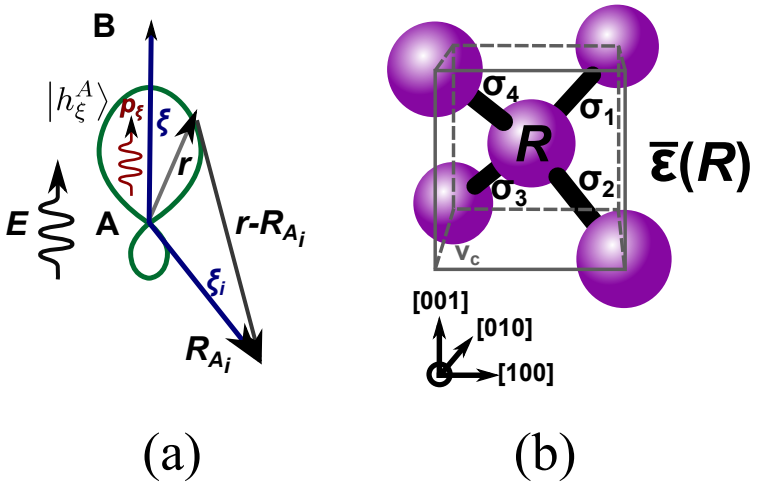

Fig. 3.9 a) Representation of the optical electric field $\boldsymbol{E}$ generating the bond dipole moment $\boldsymbol{p}_\xi$ and the vectors representation of the atomic position $\boldsymbol{R}_{A_i}$ of atom A_i and electron position $\boldsymbol{r}$, useful for the integral in eq. 3.67. b)Silicon unit cell (with volume v_c) centred at the position $\boldsymbol{R}$ where each bond has its own polarity σ_i induced by the strain tensor $\bar{\boldsymbol{\varepsilon}}(\boldsymbol{R})$ in the center of that unit cell.

Expression 3.69 is the final expression for the polar energy (or polarity) of any bond ξ in an atom centred in the unit cell located in $\boldsymbol{R}$ (see Fig. 3.9 b)). The subscript ξ identifies one of the four bonds, which defines the corresponding bond vector $\boldsymbol{\xi}$ and then the 3 other vectors $\boldsymbol{\xi}_i$, $i = 1,2,3$. We see that it depends explicitly on the strain gradients through $\bar{\bar{\Xi}}_\xi(\bar{\bar{\eta}};\boldsymbol{R})$, which is non-zero only if there is a strain gradient component in the direction of the bond ξ. This is relevant because it shows that in a centro-symmetric crystal not only a strain gradient is required to create a polar bond, but it also gives the preferred gradient direction to obtain maximum polarity in bond $\boldsymbol{\xi}$.

Moreover, once the strain distribution $\bar{\boldsymbol{\varepsilon}}(\boldsymbol{r})$ is known, the only parameters left to know are α and β. These two coefficients are the only unknowns of the model presented so far and their value (defined in equation 3.68) should be found experimentally, but this particular point requires further attention and it will be discussed later in section 3.5.3.

3.5 The strain dependent macroscopic polarization

From the previous analysis, we have concluded that $U'_\xi(\bar{\boldsymbol{\varepsilon}})$ is a function of strain itself and $\sigma_\xi(\bar{\boldsymbol{\eta}})$ is a function of the strain gradients. We can now use equations 3.49 to 3.51 to deduce the dependencies of the $\boldsymbol{P}^{(n)}$ on the strain effects for the different orders n.

3.5.1 Order 0: Strain effect on the spontaneous polarization

The spontaneous polarization can be deduced from equation 3.49. We see that the linear dependence on strain is made through $\sigma_\xi(\overline{\overline{\boldsymbol{\eta}}})$. Therefore, the spontaneous polarization is dependent on the strain gradients and not on the strain itself. This is compatible with the discussion made in section 3.3.1 where we have deduced that the piezoelectric effect vanishes in tetrahedral covalent crystals and the only electromechanical effect is the flexoelectricity.

The flexoelectric tensor components μ_{ijkl} could be in principle deduced from eq. 3.49 by

$$\mu_{ijkl} = \frac{1}{2v_c} \sum_{\xi=1}^{4} \left(\frac{\partial p_{\xi_i}^{(0)}}{\partial \eta_{jkl}} \right) \Bigg|_{\varepsilon=0} \tag{3.70}$$

but this calculation is beyond the scope of the present work.

3.5.2 Order 1: The photoelastic effect

For the linear polarization $\boldsymbol{P}^{(1)}$, equation 3.50 shows the linear dependence on $U'_\xi(\overline{\boldsymbol{\varepsilon}})$, once again consistent with the fact that the linear effect of strain in $\chi^{(1)}$ depends on strain itself and it corresponds to the photo-elastic effect.

To study this effect, we consider an homogeneous strain, as no gradients are required. In that case $\overline{\overline{\boldsymbol{\eta}}} = 0$, $\sigma_\xi = 0$ and $\boldsymbol{\gamma}_\xi = (\gamma\bar{\boldsymbol{I}} + \overline{\boldsymbol{\varepsilon}}) \cdot \boldsymbol{\xi}$. Consequently, putting together eqs. 3.50 and 3.52 for $n = 1$ yields

$$\boldsymbol{P}^{(1)} = \frac{e^2}{2v_c} \sum_{\xi=1}^{4} \frac{\boldsymbol{\xi} \cdot (\gamma\bar{\boldsymbol{I}} + \overline{\boldsymbol{\varepsilon}}) \cdot \boldsymbol{E}}{U_\xi(\overline{\boldsymbol{\varepsilon}})} \cdot \left[(\gamma\bar{\boldsymbol{I}} + \overline{\boldsymbol{\varepsilon}}) \cdot \boldsymbol{\xi} \right] . \tag{3.71}$$

The difficulty in evaluating the previous expression is in the explicit dependence of $U_\xi(\overline{\boldsymbol{\varepsilon}})$ on both the bond direction and strain effects. In general, the explicit form of $U_\xi(\overline{\boldsymbol{\varepsilon}})$ is not known but for some special cases, it can be estimated.

In this analysis we are mainly interested in checking the validity of the previous expression for $\boldsymbol{P}^{(1)}$ in a phenomological way i.e. check whether the photoelastic tensor properties deduced from eq. 3.71 match those of eq. 3.26. A quantitatively estimation of the photoelastic coefficients p_{11}, p_{12} and p_{44} deeply depends on the correct expression for $U_\xi(\overline{\boldsymbol{\varepsilon}})$, which is not a simple task and best results are achieved by considering multiple potential contributions in computational simulations [65]. To deal with this problem, we should select strain types where $U_\xi(\overline{\boldsymbol{\varepsilon}})$ is the same in every bond, so that we can remove the index ξ and simplify the sum for $\boldsymbol{P}^{(1)}$. This is the case, for instance, of the uniaxial strain.

	Parameters		Experimental			Calculated
	U (eV)	γ	p_{11}	p_{12}	$p_{11}-p_{12}$	$p_{11}-p_{12}$
C	6.94	1.13 [94]	-0.249	0.043	-0.292 [111, 112]	-0.251
Si	2.98	1.4 [94]	-0.094	0.017	-0.111 [51, 65, 112]	-0.108
Ge	2.76	1.6 [94]	-0.154	-0.126	-0.030 [113]	-0.070

Table 3.1 Comparison between the calculated and experimental values of the photoelastic constants for Si, C and Ge. The two strain types studied in this work are compared with the respective experimental values.

Therefore, consider an uniaxial strain in the [001] direction. This corresponds to the situation where the only nonzero component of the strain tensor is $\varepsilon_{zz} = \varepsilon$. In this case, the strain makes the bonds undergo the same type of deformation in respect to each other and the covalent energy changes evenly in all bonds. Therefore $U_\xi(\overline{\boldsymbol{\varepsilon}}) = U(\varepsilon)$ and from eq. 3.71, using the definitions described in section 3.3.2, the linear susceptibility $\overline{\boldsymbol{\chi}}^{(1)}$ can be calculated to give

$$\overline{\boldsymbol{\chi}}^{(1)}(\varepsilon) = \frac{d^2e^2}{3\epsilon_0 v_c U(\varepsilon)} \begin{pmatrix} \gamma^2 & 0 & 0 \\ 0 & \gamma^2 & 0 \\ 0 & 0 & (\gamma+\varepsilon)^2 \end{pmatrix} . \tag{3.72}$$

Expanding this expression in first order in ε and using eq. 3.24, it results in the following dielectric tensor change

$$\delta\left(\overline{\epsilon}^{-1}\right) = -\frac{d^2e^2}{3\epsilon_0 v_c n^4 U^2} \begin{pmatrix} \gamma^2\widehat{U} & 0 & 0 \\ 0 & \gamma^2\widehat{U} & 0 \\ 0 & 0 & \gamma(\gamma\widehat{U}-2U) \end{pmatrix} \varepsilon , \tag{3.73}$$

where $\widehat{U} = \left.\frac{\partial U}{\partial \varepsilon}\right|_{\varepsilon=0}$. The same tensor in terms of the photoelastic coefficients, for this type of strain, can be calculated from eq. 3.26 and is given by [90]

$$\delta\left(\overline{\epsilon}^{-1}\right) = \begin{pmatrix} p_{12} & 0 & 0 \\ 0 & p_{12} & 0 \\ 0 & 0 & p_{11} \end{pmatrix} \varepsilon . \tag{3.74}$$

Comparing eqs. 3.73 and 3.74 shows that $\delta\left(\overline{\epsilon}^{-1}\right)$ has the same shape and this shows that the strain dependent polarization deduced from our model has the symmetries expected for a

cubic crystal. The corresponding photoelastic coefficients are

$$p_{11} = \frac{d^2 e^2 \gamma (2U - \gamma \widehat{U})}{3\epsilon_0 v_c n^4 U^2} \tag{3.75}$$

$$p_{12} = -\frac{d^2 e^2 \gamma^2 \widehat{U}}{3\epsilon_0 v_c n^4 U^2}\,. \tag{3.76}$$

In spite of not knowing the value of $\widehat{U}$, we may check the validity of the previous equations by calculating

$$p_{11} - p_{12} = \frac{2d^2 e^2 \gamma}{3\epsilon_0 v_c n^4 U} \tag{3.77}$$

and then compare with the experimental values.

We did so for diamond (C), silicon (Si) and germanium (Ge) and the results are presented in Table 3.1. It is clear the very good agreement between experimental p_{11} and the corresponding calculated value for the uniaxial strain, particularly for Si, whose error is less than 3%.

The shape of $\delta\left(\overline{\epsilon}^{-1}\right)$ in eq. 3.73 together with the excellent numerical relation of $p_{11} - p_{12}$ for three different tetrahedral centrosymmetric crystals, suggest that strain effects are well described by our model for this type of materials.

3.5.3 Order 2: Strain-induced $\chi^{(2)}$

To analyse the effects of strain on $\chi^{(2)}$, we consider eq. 3.51. By considering only first order terms in $\overline{\boldsymbol{\varepsilon}}$ and $\overline{\overline{\boldsymbol{\eta}}}$ this expression can be drastically simplified. Because σ_ξ is linear with the strain gradients, for to keep only 1st order terms, we must remove all $\overline{\boldsymbol{\varepsilon}}$ terms from eq. 3.51. Moreover, in centro-symmetric covalent materials, $U'_\xi \ll \sigma$ and under this conditions, eq. 3.51 is simplified into

$$\boldsymbol{p}_\xi^{(2)} \simeq -3\left(\frac{e\gamma}{2U_\xi}\right)^3 \sigma_\xi (1 - S^2)\,(\boldsymbol{\xi}\cdot\boldsymbol{E})^2 \cdot \boldsymbol{\xi} \tag{3.78}$$

Putting this expression in eq. 3.52, the second order macroscopic polarization is given by

$$\boldsymbol{P}^{(2)} = K \sum_{\xi=1}^{4} \sigma_\xi \,(\boldsymbol{\xi}\cdot\boldsymbol{E})^2 \cdot \boldsymbol{\xi}\,, \tag{3.79}$$

where $K = -\frac{3}{2v_c}\left(\frac{e\gamma}{2U_\xi}\right)^3 (1 - S^2)$. Using the corresponding values for Si, taking $\gamma = 1.4$ [94] and $S = 0.5$ [104], we obtain $K = -7.26 \times 10^{-4}\,\text{Å}^{-3}\text{V}^{-3}$.

To identify the explicit form of the polarization in the crystal coordinates, we replace the bond vectors by their explicit forms in eq. 3.31. By doing so, we can write the final components of the 2nd order nonlinear polarization in the crystal coordinates as

$$P_x = \frac{Kd^3}{3\sqrt{3}}\left[\Omega_1 \cdot \left(E_x^2+E_y^2+E_z^2\right) + 2\Omega_2 \cdot E_xE_y + 2\Omega_3 \cdot E_xE_z + 2\Omega_4 \cdot E_yE_z\right] \tag{3.80}$$

$$P_y = \frac{Kd^3}{3\sqrt{3}}\left[\Omega_2 \cdot \left(E_x^2+E_y^2+E_z^2\right) + 2\Omega_1 \cdot E_xE_y + 2\Omega_3 \cdot E_yE_z + 2\Omega_4 \cdot E_xE_z\right] \tag{3.81}$$

$$P_z = \frac{Kd^3}{3\sqrt{3}}\left[\Omega_3 \cdot \left(E_x^2+E_y^2+E_z^2\right) + 2\Omega_1 \cdot E_xE_z + 2\Omega_2 \cdot E_yE_z + 2\Omega_4 \cdot E_xE_y\right] \tag{3.82}$$

where

$$\Omega_1 = (\sigma_1+\sigma_2-\sigma_3-\sigma_4) \tag{3.83}$$

$$\Omega_2 = (\sigma_1-\sigma_2+\sigma_3-\sigma_4) \tag{3.84}$$

$$\Omega_3 = (\sigma_1-\sigma_2-\sigma_3+\sigma_4) \tag{3.85}$$

$$\Omega_4 = (\sigma_1+\sigma_2+\sigma_3+\sigma_4)\ . \tag{3.86}$$

The previous set of equations, together with the definition of $\chi^{(2)}$ in eq. 3.1 determines every component of the $\chi^{(2)}$ tensor in the crystal coordinates in terms of the polarity of each bond σ_ξ in the unit cell, as represented in Fig. 3.9 b). This polarity, depends on the sum of the strain gradients projected on the direction of each bond, as shown by equation 3.64, leading to a different polarity of each bond in the unit cell. Therefore, in general, every component of $\chi^{(2)}$ will be non-zero, contrasting with the case of a zync-blend crystal where each bond has the same polarity σ. In that case, Ω_4 is the only nonvanishing factor and equations 3.80, 3.81 and 3.82 lead to the well known fact that $\chi^{(2)}_{xyz}$ is the only nonvanishing component.

The explicit calculation of the $\chi^{(2)}$ components in terms of the strain gradients, requires an explicit expansion of the sum defining σ_ξ in equation 3.69. That expansion allows for the deduction of the different $\Gamma_{ijk,mnl}$ which can then be used to calculate each component of $\overline{\overline{\boldsymbol{\chi}}}^{(2)}$ in terms of every strain gradient $\overline{\overline{\boldsymbol{\eta}}}$ component.

Evaluation of the proposed model

It is now important to comment on the potential and validity of the previous model and of eqs. 3.79-3.82. The previous theory, based on a well established quantum mechanical approach (the Bond Orbital Model), provides a direct relation between the spatial distribution of $\chi^{(2)}$ and the strain gradients, which can be used to estimate how a strain profile affects

and generates $\chi^{(2)}$ in a silicon structure. This is extremely relevant for the strained-silicon photonics field because with this approach simple stress/strain simulations, which are straightforward to do using computational tools, can directly provide the distribution of $\chi^{(2)}$ in any structure, which can then be used to optimize and engineer the best structure for a given outcome.

However, the previous theoretical calculations, based on first order effects of strain in a crystal, can only be relevant if they match, up to some degree, the experimental data for strain-induced $\chi^{(2)}$ in strained silicon. However, as already mentioned in the introduction, very recently it has been shown that the experimental data available in the literature on $\chi^{(2)}$ phenomena in strained silicon, has a strong contribution from free carriers effects [34, 66, 67]. This parasitic response masks the real value of strain-induced $\chi^{(2)}$ in silicon, descrediting most of the quantitative values of $\chi^{(2)}$ in strained silicon presented in the literature [29, 31–33]. Consequently, no reliable data is available to confidently compare the results from our model with.

In any case, we shall apply our model to a standard structure, take conclusions and confirm some known properties of $\chi^{(2)}$ in strained silicon structures[6]. To do that, we will use the general waveguide structure shown in Fig. 3.10 a), which has the dimensions usually used in strained silicon devices for Pockels effect modulation [29, 31, 32]. The straining layer placed on top of the waveguide has an initial stress σ_0, which will induce a strain field $\overline{\boldsymbol{\varepsilon}}(\boldsymbol{r})$ in the waveguide. In this analysis we are merely interested in the study of the strain-induced $\chi^{(2)}$ distribution in the waveguide to give an example how the model can be applied to a practical device. We are not including any electrical or optical property to the system and we will leave that to Chapter 6, where we will study the full electro-optic properties of strained silicon waveguides and show some of trends we can deduce from the theory presented above.

Because $\chi^{(2)}$ is a characteristic of the crystal structure, it is dependent on the crystal orientation, just any tensor dependent on the crystal structure. In other words, for the same stress source, strain-induced $\chi^{(2)}$ depends on the crystal orientation. This property comes directly from our model because we can choose different laboratory coordinates $\{\hat{\boldsymbol{x}},\hat{\boldsymbol{y}},\hat{\boldsymbol{z}}\}$ in respect to the crystal coordinates $\{\hat{\mathbf{1}},\hat{\mathbf{2}},\hat{\mathbf{3}}\}$, which leads to different expressions of $\chi^{(2)}$ in terms of the components of $\overline{\overline{\boldsymbol{\eta}}}$ in the lab coordinates.

To account for this effect, we fix σ_0 in the x direction, as shown in Fig. 3.10a and we "orient" the waveguide in different directions in respect to the crystal coordinates, by changing the angle φ, as shown in Fig. 3.10 b). This procedure establishes the following

[6]For now, we ask the reader to accept the simulations results and the design of the device as given. We will focus on both of these questions later on in the text, where it will be clearer how we got these results.

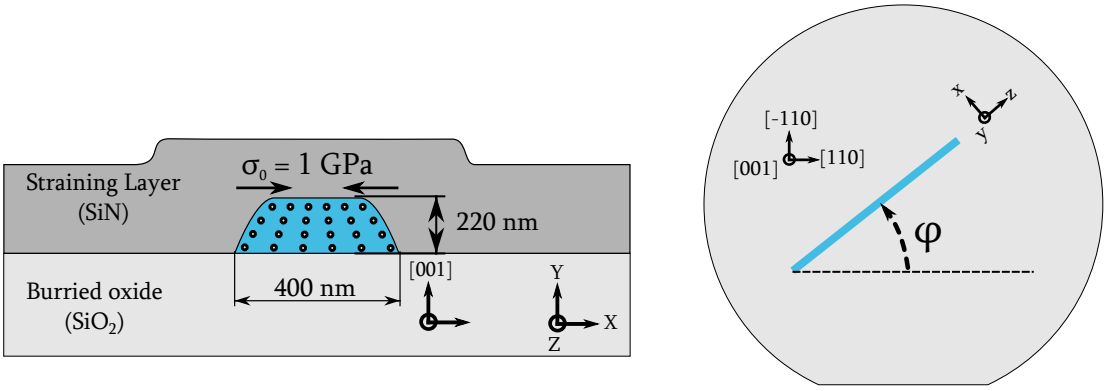

(a) Cross section (b) Top view

Fig. 3.10 (a) Cross section of the strained silicon device under consideration. (b) Orientation of the waveguide in the silicon wafer, relating both the lab and the crystal coordinate systems by φ.

relation between the two coordinate systems:

$$\hat{\boldsymbol{x}} = \sin\left(\varphi - \frac{\pi}{4}\right)\hat{\mathbf{1}} + \cos\left(\varphi - \frac{\pi}{4}\right)\hat{\mathbf{2}} \quad , \quad \hat{\boldsymbol{y}} = \hat{\mathbf{3}} \quad , \quad \hat{\boldsymbol{z}} = \cos\left(\varphi - \frac{\pi}{4}\right)\hat{\mathbf{1}} - \sin\left(\varphi - \frac{\pi}{4}\right)\hat{\mathbf{2}} \,. \tag{3.87}$$

Since the waveguide extends over the z direction, $\overline{\boldsymbol{\varepsilon}}$ and $\overline{\overline{\boldsymbol{\eta}}}$ components involving z can be neglected. In addition, for the reasons described above, we neglect the shear components of strain ε_{ij}, $i \neq j$, because their contribution is much smaller than the other components. Therefore, the only strain gradient components to be considered are η_{xxx}, η_{yyx}, η_{xxy} and η_{yyy}.

The strain-induced bond polarities (eq. 3.69) in the waveguide coordinates, are calculated after rewriting the bond vector coordinates (Eq. 3.31) in the lab coordinate system $\{\hat{\boldsymbol{x}}, \hat{\boldsymbol{y}}, \hat{\boldsymbol{z}}\}$. The $\chi^{(2)}$ components in the lab coordinates can be extracted after replacing the polarities σ_ξ into equation 3.79 for the macroscopic polarization.

These calculations were performed and the most relevant $\chi^{(2)}$ components for this kind of structure are given by:

$$\begin{aligned}
\chi^{(2)}_{xxx} &= \frac{d^6 K}{54\epsilon_0}\left([(\beta - 3\alpha)\cos(4\varphi) - 5\alpha + 7\beta]\cdot\eta_{xxx} + \right. \\
&\qquad \left. + [(3\beta - \alpha)(3 + \cos(4\varphi)]\cdot\eta_{yyx}\right) \qquad (3.88) \\
\chi^{(2)}_{yyx} &= \frac{d^6 K}{27\epsilon_0}\left([5\beta - 3\alpha - (\alpha + \beta)\cos(4\varphi)]\cdot\eta_{xxx} - 2[\alpha - 3\beta]\cdot\eta_{yyx}\right) \qquad (3.89) \\
\chi^{(2)}_{xxy} &= \frac{d^6 K}{27\epsilon_0}\left([5\beta - 3\alpha - (\alpha + \beta)\cos(4\varphi)]\cdot\eta_{xxy} - 2[\alpha - 3\beta)]\cdot\eta_{yyy}\right) \qquad (3.90) \\
\chi^{(2)}_{yyy} &= \frac{d^6 K}{27\epsilon_0}[3\beta - \alpha]\cdot(\eta_{xxy} + \eta_{yyy}) \qquad (3.91)
\end{aligned}$$

This set of equations provides us with all the required information about the $\chi^{(2)}_{ijk}$ components in any point of the device in terms of the η_{mnl} components in that same point. We can now compare this result with the main claims on strain-induced $\chi^{(2)}$ in silicon.

We start by noticing that the previous equations have the form of eq. 3.30 which is a linear combination of strain gradients. This result was first deduced in section 3.3.3 only by using symmetry arguments, it was also suggested in Refs. [64, 69] and is recovered here by using the previous detailed quantum mechanical approach. This is in line with the claims that $\chi^{(2)}$ should be proportional to strain gradients and not to strain itself, as it has been suggested in many publications in the past years [30–33, 69];

Furthermore, the equations above not only provide us with the coefficients $\Gamma_{ijk,lmn}$, but explicitly accounts for the angle dependence φ on the direction of the waveguide. For instance, from eq. 3.90 we extract

$$\Gamma_{xxy,xxy}(\varphi) = \frac{d^6K}{27\epsilon_0}\left[(5\beta - 3\alpha - (\alpha+\beta)\cos(4\varphi))\right] \tag{3.92}$$

$$\Gamma_{xxy,yyy}(\varphi) = -\frac{d^6K}{27\epsilon_0}\left[2(\alpha - 3\beta)\right] \ . \tag{3.93}$$

This procedure can be done to find any coefficient $\Gamma_{ijk,lmn}$, only in terms of only α and β to give the weight of each strain gradient direction for the desired $\chi^{(2)}$ component.

Another known property of strain-induced $\chi^{(2)}$ has a linear relationship with the initial stress σ_0 [60, 62, 114] and equations 3.88 to 3.91 predict that. In Fig. 3.11, we see the simulation of the average η_{xxy} and η_{yyy} in the waveguide, for different values of σ_0 and it is clearly a linear relationship between these quantities. This is true for any η_{ijk} component. Since $\chi^{(2)}$ is linear with η_{ijk}, it is straightforward to conclude that, regardless of the values of α and β, our model predicts

$$\chi^{(2)} \propto \sigma_0 \ , \tag{3.94}$$

which is coherent with the results presented in [62].

The previous analysis shows that our model is in line with the known phenomenological properties of the strain-induced $\chi^{(2)}$ in silicon. Moreover, it also provides a quantitative way of calculating $\chi^{(2)}$ in terms of the strain gradients effects, only depending on two parameters: α and β. These two quantities, even though have a clearly definition in our model (eq. 3.68), they should be determined experimentally as it is common practice in any semi-empirical model. The reason for that is because the model presented in the last pages has some approximations like the possible matrix elements between bond and antibonding orbitals in adjacent hybrids [104], the eventual distortion of charge distribution which can give local fields and thus change the Hamiltonian due to the optical field and other effects we may

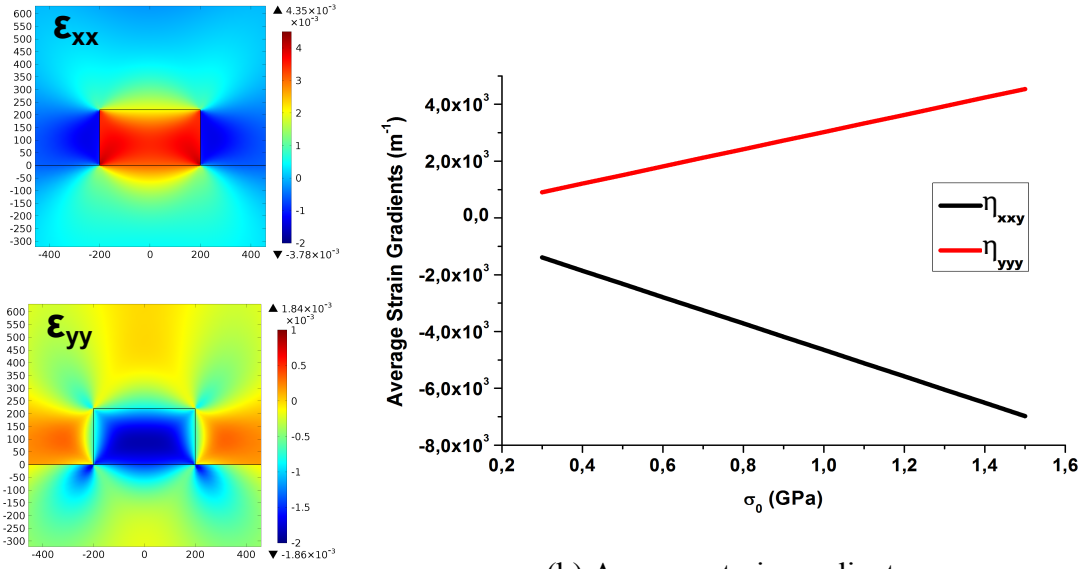

(a) Strain distribution

(b) Average strain gradient

Fig. 3.11 (a) Principal strain components $\varepsilon_{xx}(x,y)$ and $\varepsilon_{yy}(x,y)$ generated by the strain overlayer with $\sigma_0 = 1$ GPa. (b) Linear relation between the average strain gradients components $\eta_{xxy} = \partial\varepsilon_{xx}/\partial y$ and $\eta_{yyy} = \partial\varepsilon_{yy}/\partial y$ in the waveguide and the initial stress σ_0.

have not considered. Therefore, by fitting α and β to experimental data, we absorb all the numerical corrections in these two parameters.

Estimation of the order of magnitude of $\chi^{(2)}$

Fitting α and β to the experimental data available in the literature the moment is very complicated as referred in Chapter 3, because all the reported values of strain-induced $\chi^{(2)}$, in particular those in Refs. [29, 31, 33, 32], have strong parasitic contributions from carrier effects. The best we can do to numerically estimate α and β, is by approaching the integral in eq. 3.65. This is not a simple task, not only because it is a difficult integral to evaluate, but mainly because the real form of the silicon crystal potential $V(\boldsymbol{r})$ must be entirely known for the obtained value to be correct. The crystal potential results from the contribution of many different effects and it is recognized to be a complex problem [65, 115, 116]. Consequently, results deduced from $V(\boldsymbol{r})$ are likely to have errors. By using experimental data, we can absorb the effects we are not considering in the fitting parameters, establishing a viable way of determining α and β semi-empirically.

With the previous considerations born in mind, we will seek for an estimate of the order of magnitude of $\chi^{(2)}$ in eqs. 3.88-3.91. To evaluate the order of magnitude of $\boldsymbol{\theta}_i^{\xi}$, we start by simplifying the integral in eq. 3.65. For that we make the approximation

$\|\boldsymbol{r}-\boldsymbol{R}_{A_i}\| \sim \|\boldsymbol{R}_A-\boldsymbol{R}_{A_i}\| = d$, which basically means that the hybrid wavefunction $h^A_\xi(\boldsymbol{r})$ is considered to be strong only close to the original atom. Despite not being entirely true because the hybrid extends along its bond, this is the only simple way we have to estimate the integral of eq. 3.65 and get an estimate of the order of magnitude of the evaluated quantities. In that case, eq. 3.67 becomes

$$\boldsymbol{\theta}^\xi_i \sim \left.\frac{\partial V}{\partial r}\right|_d \frac{1}{d}\int |h^A_\xi(\boldsymbol{r})|^2 \cdot (\boldsymbol{r}-\boldsymbol{R}_{A_i})\, dV \tag{3.95}$$

$$\sim \frac{1-\gamma}{2d}\cdot \left.\frac{\partial V}{\partial r}\right|_d \boldsymbol{\xi} - \frac{1}{d}\left.\frac{\partial V}{\partial r}\right|_d \boldsymbol{\xi}_i \tag{3.96}$$

The previous equation leads to

$$\alpha \sim \frac{1-\gamma}{2d}\cdot \left.\frac{\partial V}{\partial r}\right|_d \quad , \quad \beta \sim -\frac{1}{d}\left.\frac{\partial V}{\partial r}\right|_d . \tag{3.97}$$

Because the determination of the real Si crystal potential $V(\boldsymbol{r})$ is a very complex problem, in this work we will only compare the numerical results for two different crystal potentials V. The first one is the simplest Coulomb potential generated by a Si^{4+} ion

$$V_C(\boldsymbol{r}) = -\kappa\frac{4}{r}\,, \tag{3.98}$$

with $\kappa = e^2/(4\pi\epsilon_0) = 2.3\times 10^{-28}$ kg m^3/s^2.

The second, is a local pseudopotential $V_{PS}(r)$ developed by Huang *et al.* in Ref. [117] using the modern tools of Density Functional Theory for the Si crystal. The explicit form of $V_{PS}(r)$ around $r = d = 0.235$ nm was obtained by fitting that region of the corresponding curve in Fig. 3 of Ref. [117] with an analytical function.

We apply this to eq. 3.97 for both of these potentials, taking $d = 0.235$ nm and focusing only on the $\chi^{(2)}_{xxy}$, we get:

$$\Gamma_{xxy,xxy} \sim 5\times 10^{-17}\,\mathrm{m}^2/\mathrm{V} \quad \text{and} \quad \Gamma_{xxy,yyy} \sim 8\times 10^{-17}\,\mathrm{m}^2/\mathrm{V} \tag{3.99}$$

for the Coulomb potential and

$$\Gamma_{xxy,xxy} \sim 1\times 10^{-16}\,\mathrm{m}^2/\mathrm{V} \quad \text{and} \quad \Gamma_{xxy,yyy} \sim 2\times 10^{-16}\,\mathrm{m}^2/\mathrm{V} \tag{3.100}$$

for the pseudopotential case.

These results define the value of the strain-induced $\chi^{(2)}$ once the distribution of the strain gradients $\overline{\overline{\boldsymbol{\eta}}}$ are known, as we discussed before. The comparison of this prediction of the

order of magnitude of the Γ components with the our measured experimental values will be done later in Chapter 8. From the previous numerical analysis, though, it is clear the dependence of $\chi^{(2)}$ on the choice of potential $V(\boldsymbol{r})$. It means that any difference between predicted and experimental results can be attributed to a limitation of a simple potential $V(\boldsymbol{r})$ to describe the electrons in the crystal. This problem can only be overcome by using a semi-empirical method and fit α and β to available experimental data. Any other way of obtaining these two parameters, will inevitably have errors associated because the used potential $V(\boldsymbol{r})$ will always be an approximation to the much more complex potential felt by the electrons in a real crystal.

3.6 Final remarks

Throughout the last pages, we have analysed from very basic grounds, why the inversion symmetry present in silicon affects the nonlinear polarization $\boldsymbol{P}^{(n)}$, from $n = 0$ to $n = 2$. Furthermore, we have seen how strain affects any of these polarization orders and in particular how strain can be used to overcome the limitations imposed by the inversion symmetry on $\chi^{(2)}$ and generate second order nonlinear effects in silicon.

The most important idea to bear in mind is that $\chi^{(2)}$ depends on the strain gradients inside silicon and not on the strain itself. We have shown this fact not only using symmetry arguments in section 3.3.3, but also by developing an original model, based on the application of the Bond Orbital Model to the strain in the silicon bonds. This last method, allowed us to show an explicit form for the relation between the $\chi^{(2)}_{ijk}$ and the strain gradients η_{mnl} components, only in terms of two material parameters, α and β. From this approach, the crystal orientation dependence of $\chi^{(2)}$ emerges automatically.

Furthermore, this model can be also used to describe any nonlinear order effect and we have used it in photo-elastic effect and the results show very good agreement to the experimental values for Si, Ge and Diamond. This suggests that strain effects are well described by our model for this type of materials.

In addition, we would like to point out that the main purpose of this work is to develop a phenomenological model to describe the dependence of the $\chi^{(2)}$ components on the different directions of strain.In fact, this kind of information brings us much closer to have a way of developing an optimization process for strained structures for nonlinear photonics. The strain distribution in the crystal can then be engineered to maximize the most relevant $\chi^{(2)}$ components for the desired device and it will be used in Chapter 6 for the design of different structures and give a trend on the performance of optical waveguides with different geometries.

Chapter 4

Stress in micro and nano structures

In the previous chapter we approached the problem of how stress and strain can break the inversion symmetry of the silicon crystal structure. Now, it becomes relevant to understand how the internal stresses can be produced and how we can strain silicon micro-structures and devices.

To deform micro and nano devices to an extent where atomic displacements are not neglectable, strong internal stresses are required. Such kind of mechanical stresses may be achieved by directly perturbing the equilibrium state of molecules in the device, using for example ion implantation, which by inserting ions in the crystal lattice of a material, generate strong and very localized internal stresses [118, 119]. However, the most commonly used process to achieve stress in micro and nano-structures, is an indirect one, where highly stressed thin films are deposited on the structure intended to be strained. The growth of thin films is a process that occurs by no means in thermodynamical equilibrium [120] and usually lead to the development of strong internal stresses within the film. These stresses may then be transferred to the desired micro-structure, deforming the whole system.

In this chapter we focus on two main points. Firstly, we will study the different ways of generating stress in micro-structures, analysing the most relevant concepts to understand how stress is developed in thin films and how that stress can be properly used to strain the crystal underneath. Because in our work the method we used to generate strain in the silicon structures was by depositing highly stressed SiN_x thin films, we will study its mechanical properties and how its internal stress is developed during the deposition. Then, we present different methods for measuring the stress state of a film or device and finally, we will put all these concepts together to show how we can simulate stress in strained silicon waveguides.

4.1 Stress generation in thin films

As referred in Section 3.2.2 of the previous Chapter, internal stresses occur as an attempt of the molecules in the material to restore their equilibrium state. In thin films, this happens during its formation and depends on the nature of the film, its deposition conditions and on the substrate it is deposited on.

Stresses in thin films can either be *compressive* (defined as negative) or *tensile* (defined as positive). Films under compression will try to expand, and if the substrate is thin, the film will bow the substrate with the film being on the convex side. Films with tensile stress try to contract bowing the substrate so the film is on the concave side [121–123]. These effects are illustrated in Fig. 4.1 for both kinds of stress. Additionally, while tensile stress will relieve itself by microcracking of the film, compressive stress will relieve itself by buckling.

Generally we can identify three very different types of contributions for the final internal stress (σ_0) of a film: the external stress (σ_{ext}) caused by external mechanical forces, occurring for example by manually bending the sample mechanically like that reported in [71] and in general it is not present ($\sigma_{ext} = 0$); the *thermal stress* (σ_{th}), and the so-called *intrinsic stress*

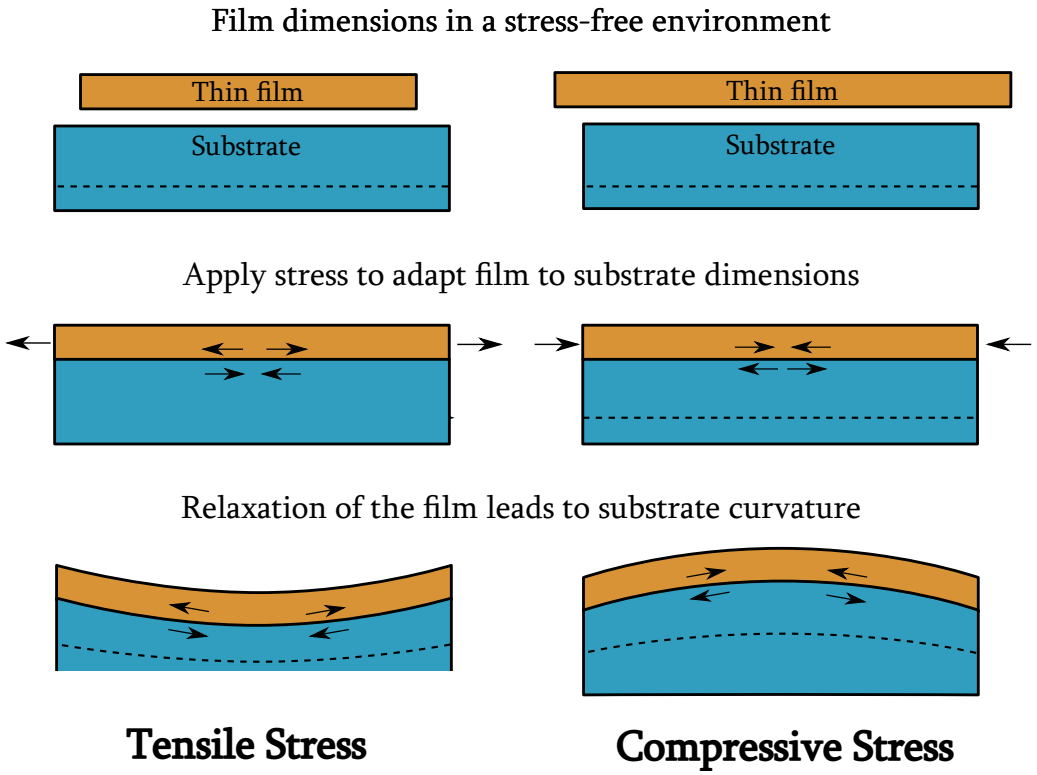

Fig. 4.1 Representation of compressive (a) and tensile (b) stresses in thin films.

(σ_i) [124]:

$$\sigma_0 = \sigma_{ext} + \sigma_{th} + \sigma_i \, . \tag{4.1}$$

4.1.1 Thermal Stress

The thermal stress σ_{th} is an extrinsic stress in the sense that it is not the result of the growth process but usually arises when the external parameter "temperature" (T) is changed after the film deposition [120]. Thermal stress originates from the mismatch between the substrate and thin film thermal expansion coefficients, α_s and α_f respectively. It develops during cooling down from deposition temperature T_D to room temperature T_R and it is given by [120, 125, 126]

$$\sigma_{th} = \frac{Y_f}{1-\nu_f} \int_{T_D}^{T_R} (\alpha_s - \alpha_f)\, dT \, , \tag{4.2}$$

where Y_f and ν_f are the Young's Modulus and the Poisson coefficient of the film, respectively. Typically, this stress source is very small unless the deposition is made at $T \gg 800\,^{\circ}\mathrm{C}$ and in the cases where the difference in α_s and α_f is not negligible, i.e. $\Delta\alpha \gg 10^{-6}\,\mathrm{K}^{-1}$ [124].

In materials like SiN and SiO_2 typically deposited at $T < 700\,^{\circ}\mathrm{C}$ on Si substrate, the thermal expansion difference is typically $\Delta\alpha \sim 1 \times 10^{-6}\,\mathrm{K}^{-1}$ (see Table 4.1). Using eq. 4.2, this corresponds to maximal thermal stresses on the order of 100 MPa. In fact, the thermal stress measurements in this kind of structures are reported to range from 10 MPa [127] and can only reach values as high as 300 MPa [128, 129].

Table 4.1 Coefficients of thermal expansion (α_{th}) for selected materials.

Material	α_{th} $\left(10^{-6}\,\mathrm{K}^{-1}\right)$
Si	2.6
SiN	~ 3 [130]
SiO_2	~ 1 [129]

4.1.2 Intrinsic stress

The third component in equation 4.1 is called intrinsic stress and it is usually the relevant contribution to the internal stress σ_0 of a thin film, having typical values ranging from 100 MPa to a few GPa. It arises from all the processes taking place during the deposition of the film which bring it into a stressed state. Because every material is different and every deposition unique, the mechanisms which generate intrinsic stresses are not well characterized quantitatively. It is indeed a very complex topic of research and many processes

for different materials and deposition conditions have been studied over the last decades [120, 121, 124, 127, 131–133]. Nevertheless, it is the major source of stress in thin films and thus it justifies its deeper study.

Despite the complexity of the processes involved, one can separate the sources of intrinsic stress in two general groups: the stress caused by the growth process of the film and located in the bulk of the film, which is called volume stress (σ_{vol}) and the stresses arising at the surface between the film and the substrate, the surface stress (σ_s). Therefore, generally, we can write [124]

$$\sigma_i = \sigma_{vol} + \sigma_s \, . \tag{4.3}$$

Sources of volume stress

Despite the specific processes occurring in crystalline, polycrystalline and amorphous thin films have different specifications, next we identify the most general mechanisms for stress generation in the film during its growth.

- **Coalescence of grain boundaries:** In the early stage of the film growth, coalescence of the small grains generates a tensile stress. The closing of the gaps between crystallites causes their elastic deformation. The driving force of this phenomenon is cohesion (Fig. 4.2 (a)) [120, 131, 134, 135].

- **Domain walls:** The boundaries between different islands can be regarded also as domain walls, because they separate epitaxial film domains. Their merge results in compressive stress at domain walls, in contrast to the tensile stress of grain boundaries (Fig. 4.2 (b)) [120, 134].

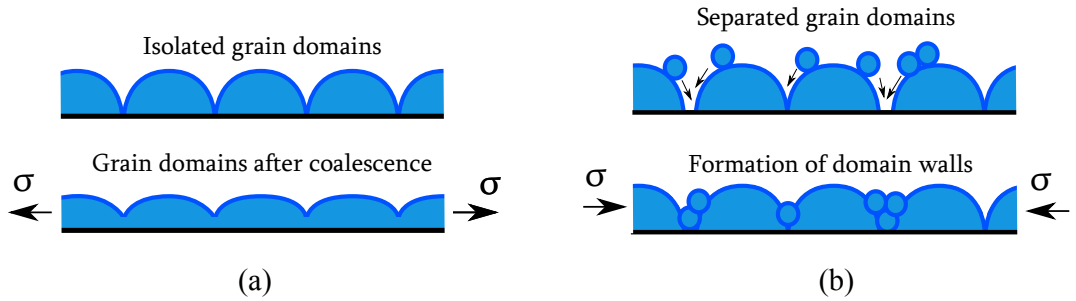

Fig. 4.2 (a) Coalescence of grain boundaries generate tensile stress. (b) The merging of domain walls with other material volumes generate compressive stress.

- **Vacancies:** During deposition, the vacancy concentration in the films can be much larger/smaller than at equilibrium. Therefore, when the vacancies are subsequently

annihilated/created, the film volume changes, resulting in a compressive/tensile stress generation (Fig. 4.3 (a)) [131, 136]. This occurs very often in amorphous thin films.

- **Impurities:** This process is very important in the case of amorphous thin films. During the deposition, molecules can be incorporated into the films at interstitial sites or at grain boundaries, contributing for the compressive stress in the film. This includes effects like ion bombardment in CVD depositions (Fig. 4.3 (b)) [120, 132, 127].

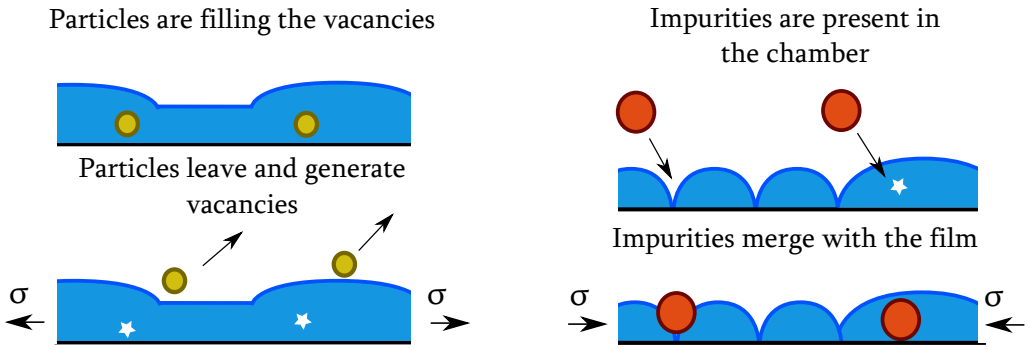

Fig. 4.3 (a) Generation of Tensile stress through vacancies annihilation in the film. (b) Generation of Compressive stress through the implantation of impurities in the film.

Sources of surface stress

Surface stresses occur at the initial stages of the deposition and it is localized at the surface between the film and the substrate. It is more common between crystalline structures, but it may also occur in polycrystalline and amorphous films. Next we present the most common mechanisms that contribute to σ_s.

- **Solid state reactions and phase transitions:** When two solid phases are brought together, they may undergo a chemical reaction by means of which a new compound is formed at the interface. Frequently, these solid state reactions are accompanied by considerable stress generation and may occur in the deposition of amorphous films [120, 137].

- **Epitaxial stress:** In the case of epitaxial film growth, the lattices of film and substrate are not usually identical but differ at least with respect to the magnitude of the lattice constants in certain crystallographic directions. This is illustrated in Fig. 4.4. Epitaxial Stresses arise in the attempt of the film to match the lattice of the substrate and the

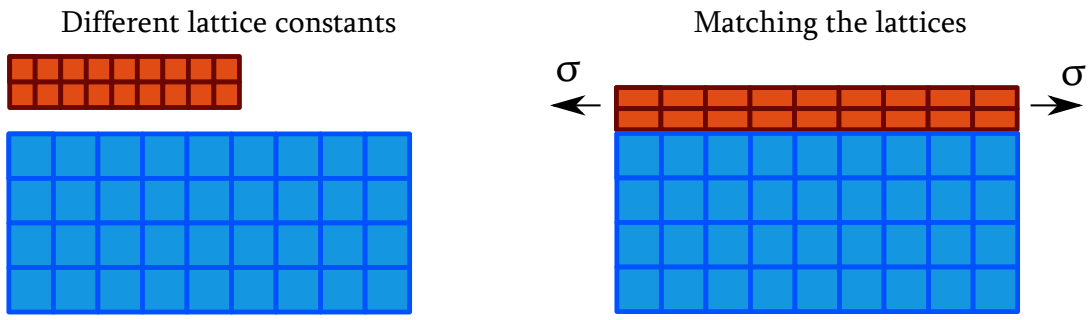

Fig. 4.4 The mismatch between lattice constants between film and substrate, leads to the stretch of the film to adapt to the substrate. In this case tensile stress is generated.

lattice misfit f (along a certain crystallographic direction) is conveniently defined as [120, 121]

$$f = \frac{a_s^0 - a_f^0}{a_s^0}\,, \tag{4.4}$$

with a_f^0 and a_s^0 being the stress free lattice constants of film and substrate, respectively. For coherent growth, the surface misfit surface strain ε_s is equal to f. It is noteworthy that the misfit stress, depending on the value of f, can reach values of 1 GPa to 10 GPa, which are considerably bigger than the contributions of other stress mechanisms [120].

However, if the lattice mismatch between the two materials is very high, defects can be generated. As the film thickness increases, the elastic energy stored within the film due to the lattice mismatch increases. At some thickness, it becomes energetically favourable to relieve this misfit strain by breaking atomic bonds at the strained interface and the plastic deformation of the crystal will induce relaxation towards its bulk lattice constant, as represented in Fig. 4.5 [138]. This results in the formation of dislocations at or near the substrate/film interface, the so-called *misfit dislocations*. These dislocations destroy the coherency of the interface and form discontinuities in the lattice structure and break the commensurate nature of the misfit interface. This relaxation reduces the actual strain in both the film and the substrate, strongly limiting the actual maximal strain that can be practically induced by epitaxial growth [139].

Furthermore, these deformations may propagate along lines which form discontinuities in the lattice structure. Such type of defects, for instance, may arise in Silicon-Germanium (SiGe) multilayers, because of the $f = 4.17\%$ lattice mismatch between these two materials [139].

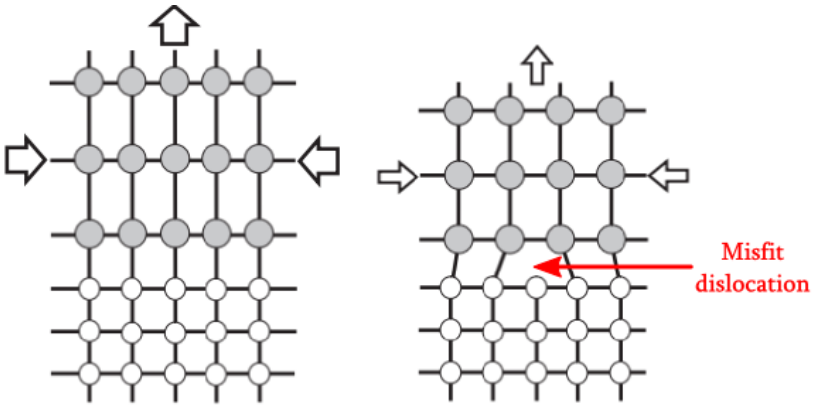

Fig. 4.5 Representation of the formation of misfit dislocations during the epitaxial growth of thin films (picture adapted from [139]).

The analysis described above presents the different techniques we can use to generate strain in a silicon micro-structure like a waveguide. Even though the epitaxial growth is a very promising method to achieve the highest levels of strain in silicon, further developments are required to achieve a compatible epitaxial growth in silicon that fulfils the high stress generation while not damaging the waveguide and also presenting low optical losses. It is also important to bear in mind that silicon has a mechanical fracture stress limit σ_{frac} of around 5 GPa to 6 GPa [140, 141], which corresponds to the highest level of stress it can be applied to the crystal before it starts to compromise its structure and develop microfractures. This sets an upper bond to the maximum level of stress we can apply and any stressing levels higher than 5 GPa may be expected to compromise the integrity of the crystalline structure.

In our work, the stress of the silicon structured device was induced by the deposition of a highly stressed layer of SiN. This choice was based on the compatibility of the deposition of this film with our fabrication facilities, but also because it can deliver considerably high levels of stress and it is also commonly used in other strained silicon devices for Pockels effect [28, 29, 31–33]. This film plays a very important role in our devices and thus it is fundamental to understand the origin of stress in SiN, so we can know its distribution inside the film and then be able to properly simulate the stress in the silicon structure underneath.

4.2 Silicon Nitride thin film

Stoichiometric Silicon Nitride has the chemical composition Si_3N_4 and it can occur in two crystalline forms, α and β, containing respectively 14 and 28 atoms per unit cell [142]. Si_3N_4 consists of a network of Si-N covalent bonds between tetrahedrally coordinated Si sites and

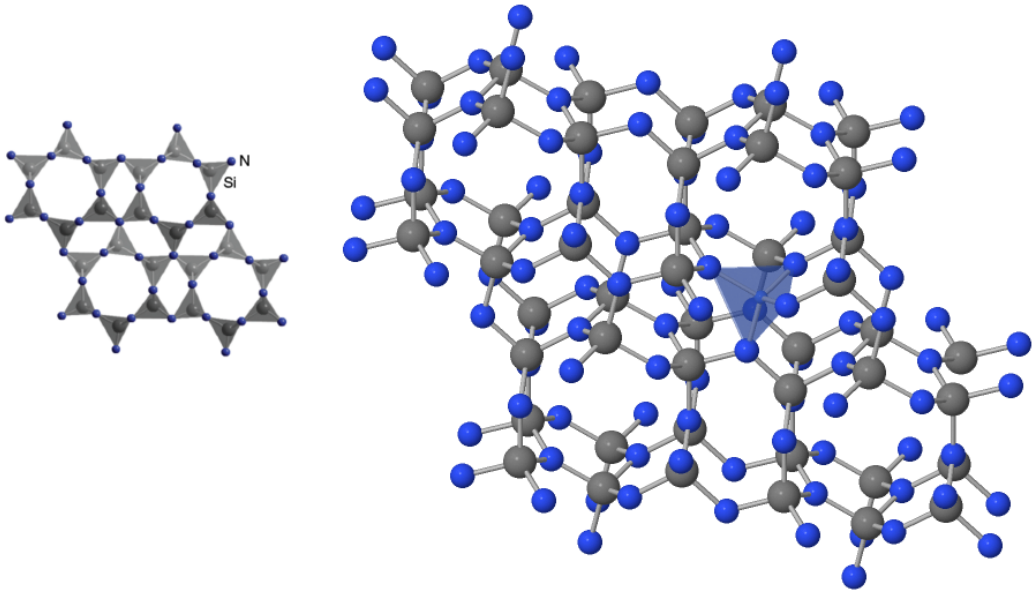

Fig. 4.6 The crystal structure of stoichiometric Silicon Nitride Si_3N_4.

planar threefold-coordinated N sites, in a planar or near-planar configuration [142, 143]. Its crystal structure can be seen in Fig. 4.6.

Usually, silicon nitride is prepared by some kind of Chemical Vapour Deposition (CVD), being the most common methods the Plasma-Enhanced CVD (PECVD) and the Low-Pressure CVD (LPCVD). Both deposition methods result in an amorphous material, denoted $a-SiN_x$, consisting of a random network of Si−N and Si-Si bonds. N-N bonds are uncommon in the alloys because of their low energy and this limits the stoichiometry x to a maximum value of $x = \frac{4}{3}$, the Si_3N_4 case [142]. The deposition conditions of the material will determine not only its chemical composition, the distribution of the chemical network, but also the stress state of film.

Even though LPCVD and PECVD are two kinds of CVD deposition techniques, they present some differences. In the former technique, the chemical reactions are thermally driven, requiring high temperatures (600 °C to 800 °C), but the low pressure involved in the deposition (20 Pa to 70 Pa) results in slow rates of reaction, higher control, higher film purity and very high levels of internal stress (200 MPa to 2000 MPa) [144]. In PECVD the deposition is aided by a plasma, resulting in high energetic reactions at low temperatures (as low as 300 °C), leading to higher deposition rates, but high level of impurities and lower levels of stress (300 MPA to 1600 MPA). In our facilities, the available deposition technique by the time this work was developed was PECVD. Because this technique is characterized by

many complex processes, which have direct influence on the distribution and level of stress, in the next section we analyse the details of such type of deposition method.

4.2.1 PECVD a-SiN

The PECVD method is one of the preferred techniques for deposition of amorphous materials in electronic devices. This method is CMOS compatible and it is regularly used to deposit silicon based thin film materials, namely SiN, SiO_2 [145, 146] and a−Si [127].

In PECVD reactors, all processing gases are excited by an electromagnetic field and the samples are located within the plasma. The electromagnetic field has a frequency of either 13.56 MHz (the "high-frequency" method) or in the 10−500 kHz range (the "low-frequency" regime) (see Fig. 4.7 for schematic representation). The plasma excitation frequency has a strong impact on the electronic properties of the resulting Si-SiN interfaces. The reason is that below the so-called plasma frequency (∼4 MHz) ions are able to follow the plasma excitation frequency and therefore produce a strong surface bombardment [147]. This is a advantage compared to regular CVD depositions, where high temperatures on the range 800 °C to 1000 °C [148] are required, whereas in PECVD, because the plasma enhances the reactivity of the chemical species, temperatures are typically lower, in the range 300 °C to 400 °C.

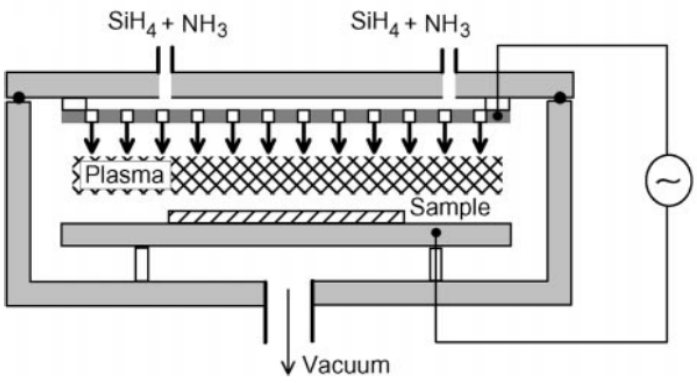

Fig. 4.7 Schematic representation of the deposition of SiN in direct-PECVD deposition process (Figure taken from Ref. [147]).

For the deposition of SiN_x thin films, in the reaction chamber, a mixture of silane (SiH_4), ammonia (NH_3) and an inert carrier like N_2 constitutes the plasma. The interaction between flow rate (measured in sscm units), pressure, temperature, RF power and frequency of the plasma generator, is very complex, but in general the SiN films are created from the chemical

reaction [149][1]

$$SiH_4 + NH_3 + N_2 \longrightarrow Si_xN_yH_z\,. \tag{4.5}$$

During the chain reaction occurring inside the chamber, Si−H and Si−N bonds are created during the deposition process . The hydrogen content in the SiN layers is determined by ion bombardment at low temperatures, while at high temperatures it is determined by thermal desorption and can be over 35% [150]. This is the reason why the SiN deposited by PECVD is usually referred as *Hydrogenated amorphous silicon nitride* and denoted by a−SiN_x:H. The hydrogen content, however, plays a major role in the stress and electronic properties of the deposited film.

4.2.2 Intrinsic stress generation in SiN thin films

Intrinsic stresses in Si-based amorphous thin films arise from systematic modifications of atomic positions after a slip-free adhesion layer forms with the substrate [127]. We can attribute these stresses to be a balance between two but competitive processes: the collapse of hydrogenated nanovoids after being formed in the deposition layer, generating tensile stresses; and lattice expansion effects through the implantation of ions (after the ion bombardment) into the previously deposited layers (often referred to as ion peening), which are responsible for the creation of compressive stresses in the film [127, 150–152]. These two competing mechanisms are illustrated in Fig. 4.8.

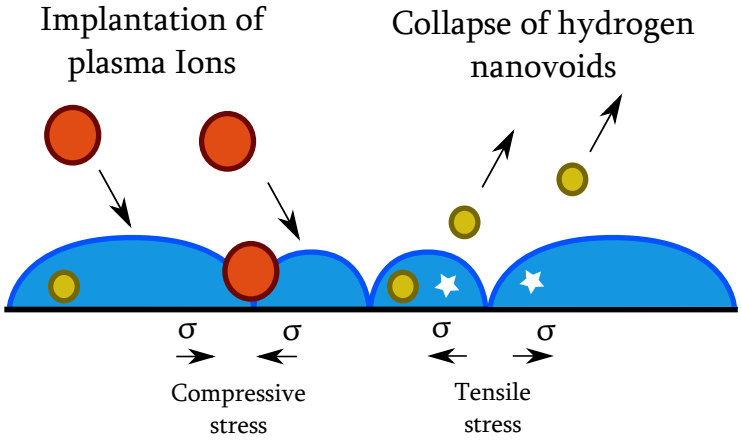

Fig. 4.8 Two competing processes for the development of stress in SiN thin films. While the implantation of plasma ions generates compressive stress, the collapse of hydrogenated voids contributes to the tensile stress.

[1] A more detailed study on the reaction chain occurring inside the chamber is given in Ref. [150].

While plasma ion momentum dictates both of these forces, it is their relative strength at any given moment that determines the net intrinsic stress state of the films. Every PECVD input variable has influence in the plasma ion momentum and thus influence the internal stress of the film. The influence of these parameters have been studied by different groups in the past years and the main conclusions are: low values of pressure, RF Power and frequency favours compressive stresses, whereas high values of pressure, RF power and frenquecy favours tensile stresses [127, 150, 151, 153]. The influence of the temperature is not that linear [150]. Some of these results can be seen in Fig. 4.9. It is also notable that it is easier to achieve higher values of stress in a compressive state rather than in a tensile one.

We now focus at the particular case of a$-SiN_x$:H films and look a little deeper on how the different parameters influence the stress in the film.

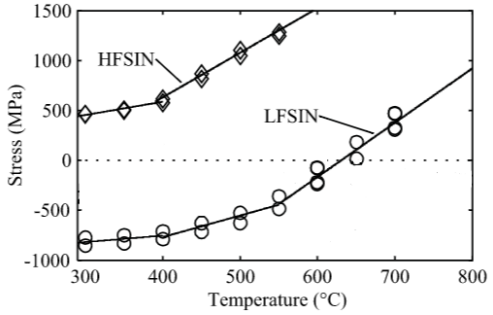

(a) Influence of temperature on SiN stress for HF and LF modes. Data taken from [154] and acquired in our facilities.

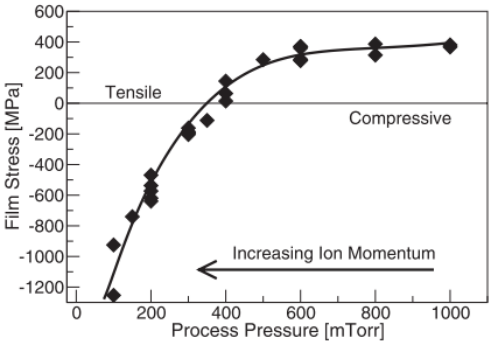

(b) Influence of pressure on a$-$Si stress [127]. Similar tendencies can be found for SiN [150].

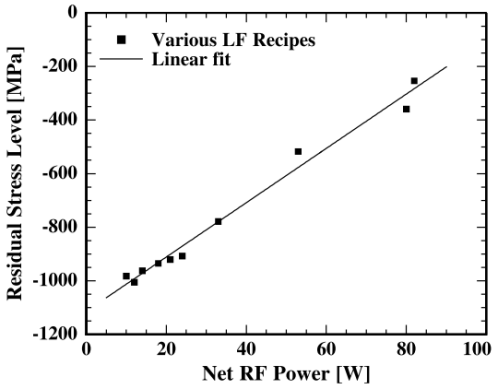

(c) Influence of RF power on SiN stress [153].

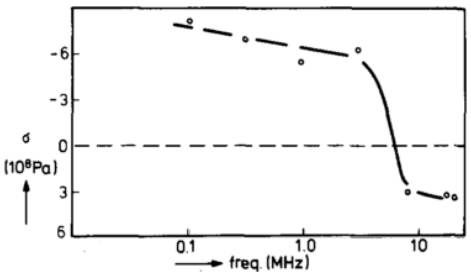

(d) Influence of operating frequency on SiN stress.[150]

Fig. 4.9 Influence of different parameters on the internal stress of amorphous thin films deposited by PECVD. These results show that low pressure, low frequency and low RF power contribute for stronger compressive stress within the films.

Compressive stresses SiN layers deposited at low temperatures and at low RF frequencies are compressive. The lower the excitation frequency the more the ions in the plasma are able to oscillate according to the alternating electric field and hence increase their momentum [150, 155]. This is also achieved by decreasing the pressure in the chamber [127]. In turn, higher ion momentum increases ion bombardment, inducing the expansion of the layer due to implanted atoms and broken Si−N bonds, resulting in a rupture of the short-range order in the Si−N structure. If the temperature is too low to anneal out the implantation damage, this process outweights the tensile stress from the collapse of nanovoids, the nitride layer expands, leading to a net compressive stress [150].

Tensile stresses At high pressures and consequent low average ion momentum levels, the contribution of hydrogen nanovoid collapse (through ion injection collapsing more deeply buried voids) easily outweighs the relatively rare deep ion implantations [127]. Also at low temperatures and high RF frequencies, the hydrogen desorption rate is thermally controlled and the implantation damage is prevented or annealed out. The net tensile stress can then be explained by a hydrogen desorption rate which easily outweighs the compressive effects of bulk expansion from the ions inserted into Si−N bonds, leading to a nitride layer which tends to shrink. Regardless, if the temperature is high enough, the resulting film is tensile regardless of the RF frequency or power [150].

It is also important to point out that the voids available to collapse are inherently finite, whereas the limit to compressive stress from implantation does not contain such an abrupt limitation [127]. This explains why compressive stresses in amorphous thin films are in general stronger than those in the tensile regime.

The selected PECVD recipe

The previous discussion provides us with the information to understand the choice of parameters of our SiN deposition. After several deposition tests, we selected a PECVD recipe with the parameters listed below in Table 4.2.

This configuration ensured the best trade off between the highest stress and mechanical and electronically stability of the SiN layer. Before every deposition the PECVD chamber was prepared by a etching procedure, followed by a 1 μm-thick layer of SiO_2. The resulting internal stress of the a−SiN_x:H film was measured to be $\sigma_0 \sim 1.2\,\text{GPa}$. The details of the stress measurement procedure will be discussed in section 4.3.

No further measurements were performed to evaluate specifics of the quality of the film, namely measurements of the hydrogen content or homogeneity of the film. Nonetheless,

Parameter	Value
SiH_4 flow rate	40 sccm
NH_3 flow rate	30 sccm
N_2 flow rate	2000 sccm
Pressure	650 mTorr
Temperature	300 °C
RF Power	20 W
RF Frequency	380 kHz

Table 4.2 Parameters of the selected SiN recipe for stress generation.

the low optical losses measured in the Si waveguides covered by this SiN film suggest a reasonable quality of the material.

4.2.3 The stress distribution in the film

The analysis of the desorption/ion implantation processes described above, occurring during the deposition of SiN_x, are relevant because it shows that the internal stress in the film is mainly a volume stress σ_{vol}, i.e. a stress located in the bulk of the film and independent of the interface with the substrate. In fact, it has been reported that in the early stages of deposition, some surface effects take place that interfere with the deposition processes and originate a surface stress contribution σ_s to the final internal stress of the SiN_x film, $\sigma_0 = \sigma_{vol} + \sigma_s$ [124, 152]. However, this contribution is very small compared with the σ_{vol} and we may assume that $\sigma_0 \sim \sigma_{vol}$ and that the internal stress is homogeneously distributed in the SiN bulk.

To illustrate that, in Fig. 4.10 is represented the distribution of the SiN_x internal stress within the SiN film reported by Sherman *et al.* in [149] for a micro-structure. We see that it is very homogeneous and parallel to the substrate within the SiN film. Therefore, we can conclude that *in the a−SiN_x:H film deposited by PECVD, the overall internal stress is compressive, with value* $\sigma_0 \simeq -1.2$ GPa *and homogeneously distributed inside the film*. This concept will be used to simulate the stress in the micro-structures strained by SiN_x films.

4.3 Measurement of stress in micro-structures

So far we have analysed the sources of stress and how a device can be strained. The stress state of the structure can then be measured. There are mainly two ways of measuring the strain state: either by directly measuring the strains in the micro-structure itself or by

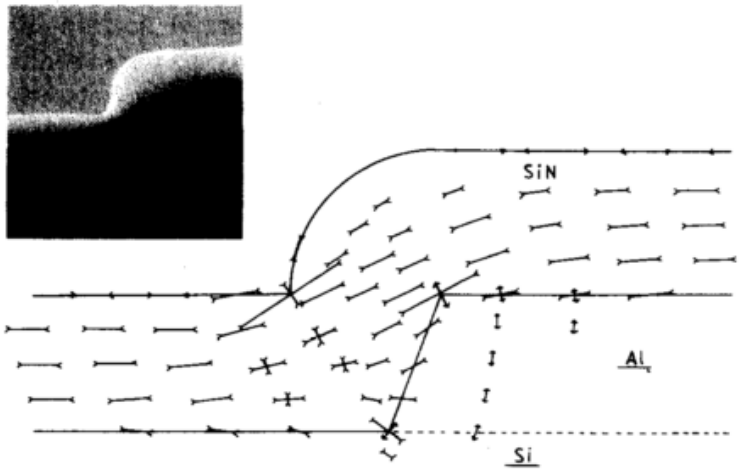

Fig. 4.10 Schematic distribution of the stress inside a SiN thin film deposited on an Al microstructure [149]

measuring the internal stress of the thin film that causes the device to strain. The former is commonly achieved by Raman spectroscopy or by X-Ray diffraction, whereas the latter is usually done by measuring the curvature radius of a substrate strained by the thin film.

4.3.1 Measuring strain by Raman Spectroscopy

Micro-Raman spectroscopy is a stress-measurement method which combines high accessibility and accuracy of the measurement of stress in a material. This technique uses an optical microscope coupled with a high resolution optical spectrometer to detect the local photon remitted after *Raman scattering* in the material [156, 157]. The laser light interacts with the atomic vibrations (or *phonons*) or other excitations in the system, resulting in the energy of the laser photons being shifted up or down, as represented in Fig. 4.11a. The shift in energy gives information about the vibrational modes in the system, in particular of the stress in the system.

Silicon is a Raman active material i.e. its phonons can be optically excited in Raman scattering and each peak of its spectrum acts like a fingerprint of a particular feature of the crystal structure. Therefore, the energy of the scattered photon contains information on the crystalline structure of the medium and thus and it can be used to probe structural deformations.

In the presence of strain, the phonon energies are changed which changes the Raman spectrum. The frequency shift $\Delta\omega = \omega_0 - \omega$ of the resonances in the Raman spectrum between the deformed and undeformed crystals provides information about the stress state. Such shift is illustrated in Fig. 4.11b, reported by B. Chmielak and co-workers in [29]. It can

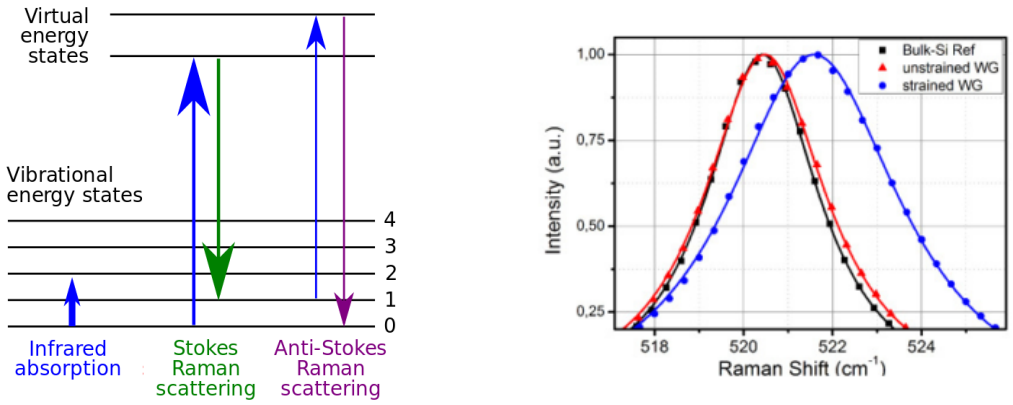

(a) (b)

Fig. 4.11 (a) Transition of energetic levels occurring during Raman scattering. (b) The Raman shift due to strain in the silicon crystal, as reported by Chmielak *et al.* in [29].

be shown that under weak strain, the phonon frequencies are given by the solutions of the following secular equation [156, 157]

$$\det\left(K_{ijkl}\varepsilon_{kl} - (\omega^2 - \omega_0^2)\delta_{ij}\right) = 0\,, \tag{4.6}$$

where $\overline{\boldsymbol{\varepsilon}}$ is the strain tensor and K_{ijkl} are the components of the so called *force constant tensor*. By calculating the eigenvalues of this equation ($\lambda_n = \omega_n^2 - \omega_0^2$, with $n = 1,2,3$), the Raman frequency shift $\Delta\omega_n$ can be obtained, which describes the n^{th} component of the polarization vector of the phonon in the presence of strain.

Therefore, the experiment for determination of the strain in a crystal can be simply evaluated by performing a Raman scattering experiment to measure the Raman frequency and by solving the secular equation that relates the measured Raman frequency with the strain [156]. This method is non-destructive, it is relatively fast and unlike other techniques, it can be done directly on the structured sample, not requiring any particular preparation. This is a major advantage of this technique because it provides directly the real value of the strain in the silicon device itself.

Furthermore, Raman spectroscopy can be implemented in a way that the laser beam moves in respect to the sample. This allows the spatial 2D-mapping of the local strain distribution with micrometer spatial resolution in the device [158]. This technique was recently adopted by M. Cazzanelli and co-workers in [30] to measure the stress distribution of silicon waveguides stressed by a SiN overlayer. The 2D-map of the cross-section of $2-3\,\mu$m wide waveguides under different stressing conditions are shown in Fig. 4.12.These results clearly show the enormous potential of Raman spectroscopy for spatial mapping of

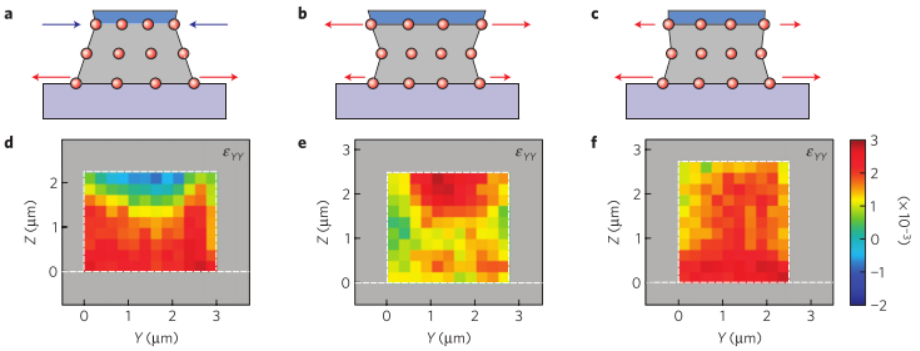

Fig. 4.12 The 2D-mapping of the strain distribution in the cross-section of silicon waveguides strained by a SiN stress overlayer, under different stressing conditions. These results were achieved by Raman spectroscopy measurements and reported by M. Cazzanelli *et al.* in [30].

the strain in silicon micro-structures, even though the highest resolution is typically in the hundred nanometers scale, set by the spotsize of the laser beam.

Although Raman spectroscopy presents the preferred characteristics for an accurate measurement of strain in silicon microstructures, this technique was not available during the period of development of this thesis and other measurement methods were used instead.

4.3.2 Measuring strain by X-Ray diffraction

X-ray diffraction can be used to determine the stress state of single crystal substrates and it relies on the fundamental interference occurring upon the diffraction of an X-ray beam on a crystal lattice. The resulting diffraction pattern depends strongly on the crystal lattice given by Bragg's law [159] and the resonances act like a fingerprint of the atomic disposition in the crystal. When a material is strained, elongations and contractions are produced within the crystal lattice, which change the inter-planar spacing of the lattice planes. This change in atomic arrangement will cause a shift and broadening in the diffraction pattern. By precise measurement of this shift, the change in the inter-planar spacing can be evaluated and thus the strain within the material deduced [159, 160]. This, however, requires precise measurement of an unstrained sample of the material but for most substrates, like silicon, the unstrained lattice parameters are known and thus can be directly compared with the measured pattern [121].

To perform strain measurements, the sample is placed in the X-ray diffractometer, and it is exposed to an X-ray beam that interacts with the crystal lattice to cause diffraction patterns. By scanning through an arc of radius about the substrate, the diffraction peaks can be located and the necessary calculations made to determine the strain [160].

4.3.3 Measuring the internal stress in thin films by the curvature method

On a planar substrate, the stress in a thin film is biaxial, i.e. the stresses act along the two principal axes in the plane of the film, as represented in Fig. 4.13. This is because the film along the y direction, normal to the substrate[2], can move freely, and thus $\sigma_y = 0$. Because there is usually a radial symmetry in the substrate, it is convenient to use cylindrical coordinates. In amorphous thin-films, the internal stress is radial $\sigma_0 = \sigma_r$[3], as shown in Fig. 4.13 and because the material is isotropic, it can be shown, using the Hooke's Law (eq. 3.15) that:

$$\varepsilon_r = \frac{1-\nu_s}{Y_s}\sigma_r \quad \text{and} \quad \varepsilon_y = \frac{\nu_s}{Y_s}\sigma_r\,, \tag{4.7}$$

where Y_s and ν_s are the Young modulus and Poisson cofficient of the substrate, respectively.

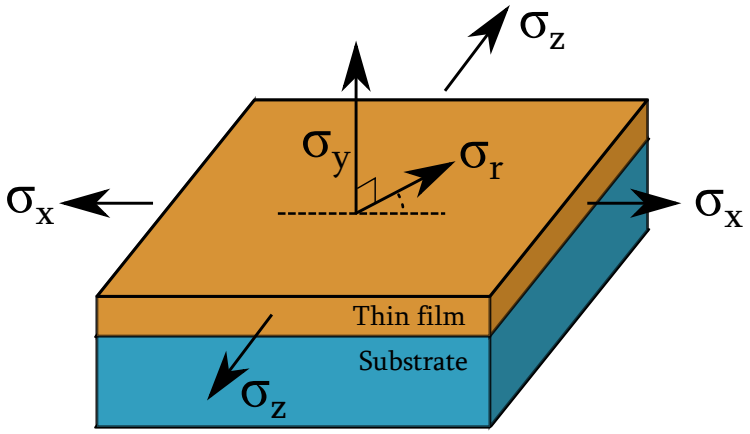

Fig. 4.13 Representation of biaxial stress in a thin film. σ_r is the radial stress in the film plane resulting from the biaxial stress from σ_x and σ_z.

The edge forces exerted on the substrate by the biaxial (or radial) stress in the film causes the substrate to deform elastically in a radial bending, as anticipated in Fig. 4.1. The amount of bending, i.e. the change in radius R of the curvature undergone by the substrate, depends on the nature of the substrate, namely on its thickness (t_s) and elastic properties (Y_s, ν_s), but generally it is proportional to the internal stress σ_0.

Under the assumptions that the substrate is elastically isotropic in the plane of the film, the substrate and film thicknesses are small compared to the lateral dimensions and the film thickness t_f is much lower than the substrate thickness t_s and that the stress σ_0 is constant in the film, the internal stress is given in function of the change in radius of curvature R by the

[2] In this manuscript we always consider y to be the direction normal to the substrate.
[3] In amorphous thin films, there is no curl in the stress field and thus $\sigma_\theta = 0$ [161].

so-called Stoney's equation [121, 161–163]:

$$\sigma_0 = \frac{Y_s}{1-\nu_s}\frac{t_s^2}{6\cdot R\cdot t_f}\ . \tag{4.8}$$

This equation is limited to the case where there is only one homogeneous layer of thin film. Generalizations of this formula for the case of multi-layered films and some relaxation on the assumptions can be found elsewhere [162–164]. After Stoney's formula, the stress in a film is found my measuring the curvature of the substrate both before and after the film is deposited. This measurement can be achieved by different methods, namely *X-ray diffraction* (described above) or *laser scanning*.

The laser scanning technique is one of the simplest and most popular methods for measuring curvature changes associated with thin film stresses. The measurement consists in a laser beam that reflects off the surface of a curved substrate at an angle θ that depends on the orientation of the surface. Upon moving (or scanning) the laser beam to a new position, the light reflects at a different angle if the substrate is curved. A position-sensitive photodetector is used to detect the change in angle of the reflected laser beam and thus find the change in curvature of the substrate [121]. This is a comparative technique, as the change in curvature radius of the substrate is obtained by comparing the measurements before and after the film is deposited. This was the measurement technique available in our facilities and the one used for stress measurements in the present work.

The measurement procedure we used to determine the internal stress of the SiN_x film described in section 4.2.2, consisted in depositing a 350 nm-thick SiN layer on highly flat silicon substrates with low Total Thickness Variation (TTV). The stress measurements were done by comparing the radius of curvature of the substrate before and after the SiN overlayer was deposited, using the FSM-500 TC stress measurement machine. This allowed us to deduce the initial stress of the film through the Stoney's formula (eq. 4.8). The results are presented below, in Table 4.3.

	Film thickness (nm)	Curvature Radius (m)	Stress (GPa)
No film	0	150	–
SiN film	345	-7.2	-1190

Table 4.3 Measurement of the radius of curvature for the stress calculation of SiN from the curvature method.

The previous Table shows that the internal stress of the films deposited by our PECVD recipe has the already mentioned value of $\sigma_0 \simeq -1.2\,\text{GPa}$. These measurements and results

were reproduced every time a new layer was deposited in a different device, to ensure consistency between the depositions of different devices.

4.4 Stress/strain simulation of micro and nano-structures

So far, we have analysed how the strain is generated in the SiN stress layer and how that stress can be characterized. The purpose of this material is to stress the silicon device it is deposited on. In order to know how the silicon micro-structure is strained, stress/strain simulations must be performed. These simulations consist in solving the equations for the displacement vector $\boldsymbol{u}$ and the stress σ in every point of the material. This is usually achieved by using numerical tools, particularly the Finite-Elements Method (FEM), which solves the corresponding differential equations by breaking the simulation space in small elements (called mesh) and solving each one individually [165, 166]. In all the FEM simulations performed in this work, we used COMSOL-Multiphysics FEM computational tool to get the distribution of strain/stress in the simulated structure.

In section 4.2.3, we concluded that the stress can be simulated by defining an initial homogeneous biaxial stress σ_0 in the whole SiN film. Therefore, the simulation of the distribution of strain in a device is done by defining the following features:

1. The constant initial stress in the whole SiN film with value $\sigma_0 = -1.2\,\text{GPa}$ which will act as the source of stress in the problem.

2. The fixed points in the structure, which act as boundary conditions for the simulation.

3. The mechanical properties of the materials involved in the simulation, namely the Young modulus and the Poisson ratio.

The differential equations describing such mechanical problem are linear and thus the system has always a definite solution and the FEM method always converge to that solution. Therefore, the refinement of the MESH required to solve the problem is only dependent on the required accuracy of the simulation and thus not play a role in its convergence.

4.4.1 Simulation of the stress state of a strip silicon waveguide

We now apply the concepts presented so far to the simulation of a strip silicon waveguide, with standard dimensions $400\,\text{nm}\times250\,\text{nm}$, strained by a 700 nm SiN thin film, like that in Fig. 4.14a. The SiN initial stress $\sigma_0 = -1.2\,\text{GPa}$ is considered to be oriented in the *xx*, we considered the lateral and bottom borders of the simulation region to be fixed (boundary condition) and the size of the MESH elements inside the waveguide was around 25 nm.

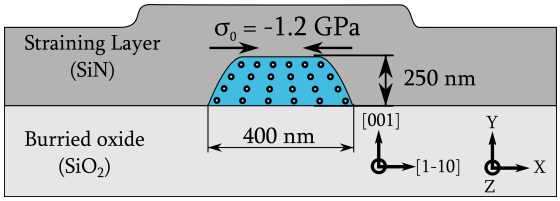

(a) Strip waveguide structure

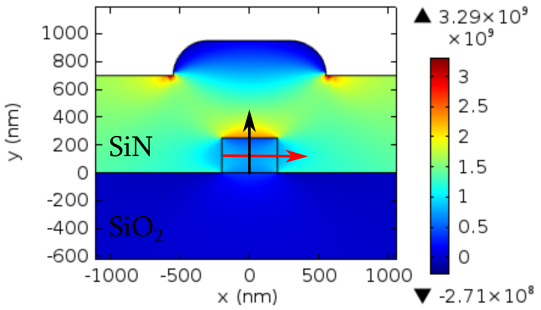

(b) 2D distribution of σ_{xx}.

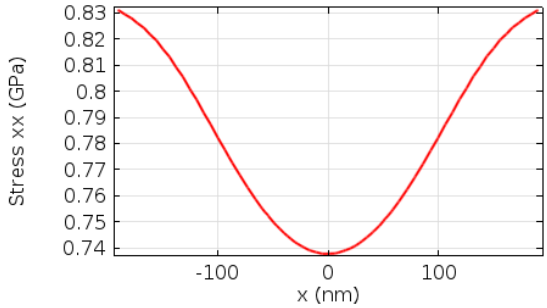

(c) σ_{xx} along the x directed red arrow.

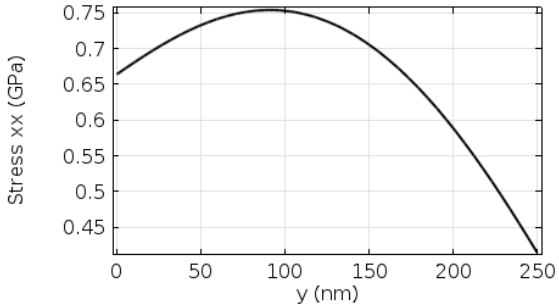

(d) σ_{xx} along the y directed black arrow.

Fig. 4.14 Distribution of the *xx* component of stress in the waveguide structure strained by a SiN thin film.

Since silicon is a crystal with cubic symmetry, its elastic properties depend on the crystal orientation [167]. This will be taken into account later when an explicit dependence on the crystal orientation is required, but for regular simulations of waveguides oriented in the [101] direction we used the values shown in Table 4.4 below.

Material	Young's Modulus	Poisson coefficient
Silicon	130 GPa	0.27
SiN	250 GPa	0.24

Table 4.4 Mechanical properties of the materials used in our simulations.

The resulting *xx* stress distribution of such structure is shown in Fig. 4.14. The stress components are related with the strain components by the generalized Hooke's law (eq. 3.15) and the corresponding strain tensor components distribution in the waveguide are shown in Fig. 4.15.

These simulations show that the strain and stress is very inhomogeneous inside the waveguide, as it can be confirmed by the 1D graphs showing the distribution of the strain and stress along the corresponding paths along the waveguide. Moreover, from the same graphs,

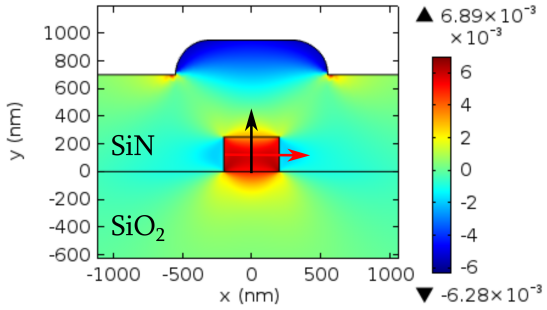

(a) 2D distribution of ε_{xx}.

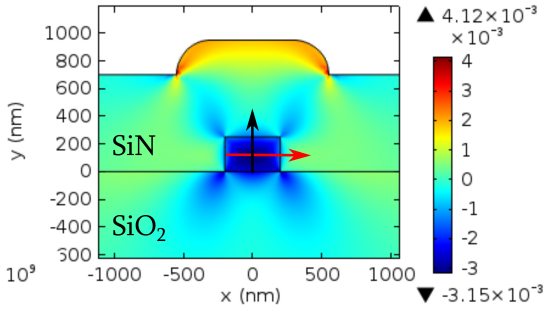

(b) 2D distribution of ε_{yy}.

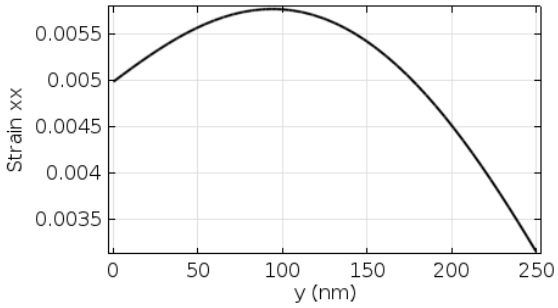

(c) ε_{xx} along the y directed black arrow.

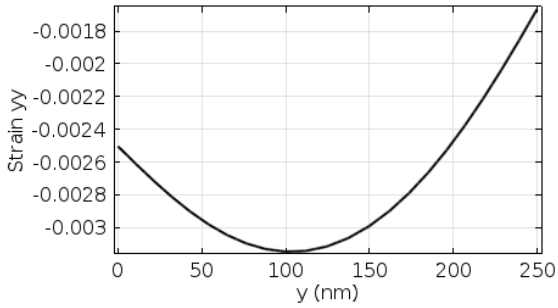

(d) ε_{yy} along the y directed black arrow.

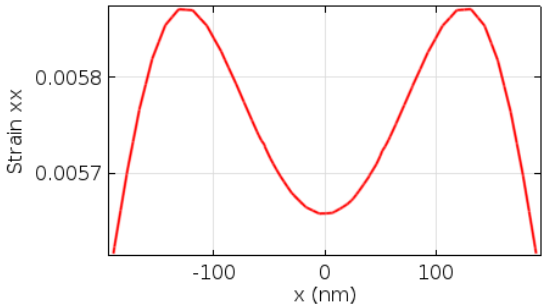

(e) ε_{xx} along the x directed red arrow.

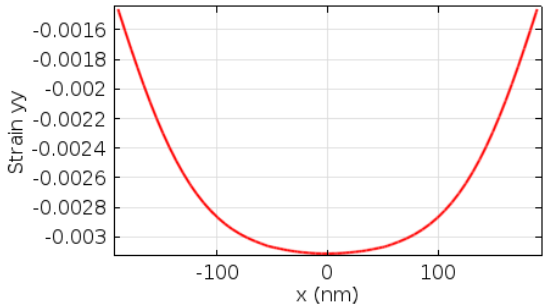

(f) ε_{yy} along the x directed red arrow.

Fig. 4.15 Distribution of *xx* and *yy* components of strain in the waveguide structure strained by a SiN thin film.

it is also clear that the stress and strain components are symmetric in the x direction (see red graphs), which is expected from the symmetry of the problem. This is not the case in the y direction (black graphs), because the structure is not symmetric in this direction. These facts will be exploited in Chapter 6 when we merge strain effects with optical effects.

Finally, it is relevant to point out that, although the internal stress of the SiN film is in the x direction, it strongly affects the ε_{yy} component of the strain, as shown in Fig. 4.15b, d and f. This explains why we need to consider all components of strain to unequivocally define the deformation state of the device.

4.5 Final Remarks

In this chapter we have described the generation, propagation and measurement of stress/strain in micro-structures and devices. We have focused in the SiN thin films because this is the material we have used to produce stress in our structure. The deep overview on the deposition of SiN thin films by PECVD had the main goal of showing that the stress can be considered to be homogeneously distributed in the SiN film so that we can use this concept to properly simulate the stressed silicon structures. This will be fundamental in chapter 6 when strain interactions with the optical mode will are considered and simulated.

However, the a$-SiN_x$:H thin film deposited by PECVD is also characterized by very particular electronic and charge properties. The same phenomena that contribute for a high level of stress in the film (the ion implantation and the hydrogen desorption competition) introduce electronic traps and charges which play a big role on the electro-optic properties of the silicon waveguide. In fact, silicon is a semiconductor whose free carriers distribution is affected by the electronic properties of the cladding and also by the electric field applied to the material. These effects play a major role in the performance of strained silicon devices and thus the next chapter is dedicated to the phenomena concerning the interaction of carriers in the silicon waveguide with the SiN cladding.

Chapter 5

Carriers effects in strained silicon waveguides

The main purpose of the present thesis is to investigate the non-linearities arising from the break of inversion symmetry in silicon, towards electro-optic modulation using Pockels effect. In this effect, an electric field is applied to the device which linearly changes its refractive index allowing light modulation.

However, there is a catch. Silicon is a semiconductor and applying an electric field, high enough to induce a reasonable refractive index changed based on Pockels effect, strongly changes the distribution and density of free carriers in Si. Consequently, as we shall see in detail, this modification of carriers concentration will not only change the refractive index of silicon by itself, but also influence the spatial distribution of electric field inside the crystal, which will immediately have an influence on Pockels effect. Therefore, by applying a modulating electric field to the silicon device with the goal of generating a strain-induced Pockels effect, we will inevitably induce free carrier effects in the structure which will strongly modify the results. This led to many overestimated results published in the literature for the strain-induced $\chi^{(2)}$ in strained silicon over the past years, including our first results, published in Ref. [32].

This type of semiconductor properties in silicon were neglected in the field of Pockels effect in strained silicon for many years and when it was detected in April 2015 [66], it was a complete game changer. It was clear then that to properly study and understand Pockels effect in strained silicon, one needed to have a clearer understanding of how the free-carriers distribution changes when a strong electric field is applied to a strained silicon device.

In this chapter we start by reviewing the most relevant concepts of the physics of semiconductors. Then we apply these concepts to simulate and explain how a voltage bias affects free-carriers in general semiconductor devices. Finally, we apply these concepts to the

particular case of silicon waveguides strained by a SiN overlayer, focusing not only on the refractive index change, but also on their influence on the distribution of electric field inside the silicon structure.

5.1 Physics of Semiconductors

In this section we are going to approach the physics of a semiconductor bearing in mind its relevance for what is fundamental to our application. The generalities and other details on the physics of semiconductors can be found in an endless number of other textbooks (namely Refs. [168, 169]) and it is not on the scope of the present work.

5.1.1 Semiconductors in thermal equilibrium

Semiconductors are materials which present a forbidden *energy bandgap* E_g in the $E(\boldsymbol{k})$ diagram of electronic states, between the *valence and conduction bands*. In this energy region no electronic states are allowed, which gives birth to a whole range of particular phenomena. In Fig. 5.1 is presented the silicon band diagram, with its respective indirect bandgap $E_g = 1.1\,\text{eV}$ at $T = 300\,\text{K}$ [168, 170].

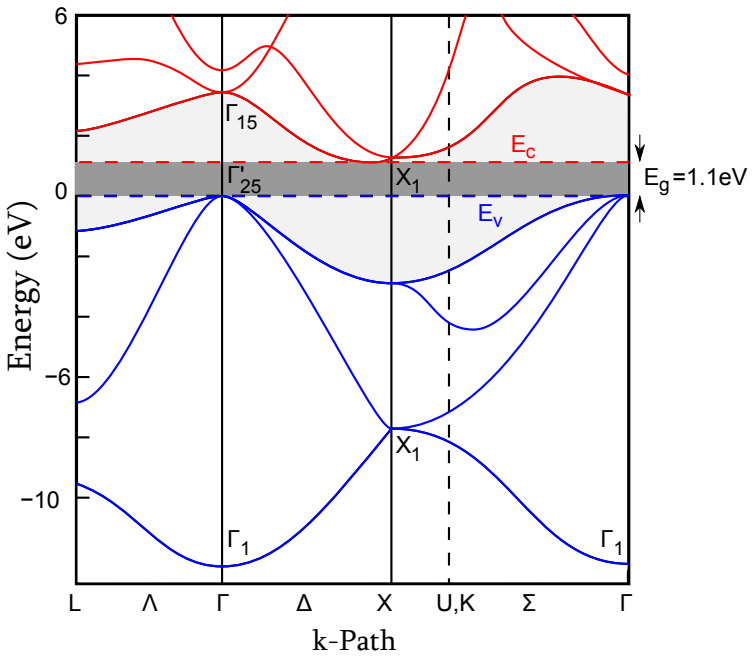

Fig. 5.1 Silicon energy band diagram with the representation of the valence bands (blue), conduction bands (red) and the corresponding energy band gap $E_g = 1.1\,\text{eV}$. The conduction and valence levels E_c and E_v are represented in dashed lines.

A very important property of crystals is that *electronic states in a filled band do not contribute for the current* [170]. In an undoped semiconductor, the *Fermi level* (E_F), which determines the probability of a given energy level to be occupied, is located in the middle of the bandgap and thus, at 0 K ($T = 0$), the valence band is completely filled and the conduction band is completely empty. Consequently, there are no *free carriers*, i.e. carriers which can move in the crystal lattice to contribute for the current.

At $T \neq 0$, the Fermi-Dirac distribution changes and T can be high enough (depending on E_g) to promote some electrons from the valence band to the conduction band. In that case, states are emptied in the valence band, creating free *holes* (with charge $+e$) and states are filled in the conduction band, creating free *electrons* (with charge $-e$). These *free carriers* are responsible for the current in a semiconductor.

The amount of free carriers can be drastically increased by *doping* the crystal with acceptors/donors (N_a/N_d) which lowers/raises the Fermi level, resulting in a higher number of holes/electrons. This process results in a p/n semiconductor (p for holes and n for electrons). The density of holes p and electrons n in a nondegenerate semiconductor in thermal equilibrium, depends mainly on the temperature and on E_F (which is mainly controlled by the doping level) and are in general given by [168]:

$$p = N_P \exp\left(-\frac{E_F - E_V}{k_B T}\right) \quad \text{and} \quad n = N_C \exp\left(-\frac{E_C - E_F}{k_B T}\right), \tag{5.1}$$

where E_V and E_C (as represented in Fig. 5.1) are the valence and conduction band energy levels and N_V and N_C are called effective density of state of these bands and depend mainly on the band structure of the crystal [168]. From the previous equation, the most important feature to point out is that the closer the Fermi level E_F is to the valence and conduction band, the higher are p and n, respectively.

5.1.2 Semiconductors out of equilibrium

The previous equations are only valid when the system is in thermodynamic equilibrium. In that case, the Fermi level is a well-defined quantity coming directly from the definition of chemical potential of the system [170]. When the system is brought out of equilibrium, which occurs by simply applying a voltage to the system, the concept of Fermi level ceases to be clear in a thermodynamical sense and the problem must be reinterpreted. For that reason, one considers two different Fermi levels, for holes E_{F_p} and electrons E_{F_n}, the so-called *quasi-Fermi levels*, which are defined by n and p out of equilibrium in the following way

[168]:

$$p \equiv N_P \exp\left(-\frac{E_{F_p} - E_V}{k_B T}\right) \quad \text{and} \quad n \equiv N_C \exp\left(-\frac{E_C - E_{F_n}}{k_B T}\right). \tag{5.2}$$

Of course, these energy levels take the same value in thermal equilibrium $E_{F_p} = E_{F_n} = E_F$. However, in out of equilibrium are usually calculated after simulations by explicitly calculating n and p.

In addition, to induce a change in carrier concentration, in a system out of equilibrium, dynamic changes may take place which produce currents inside the semiconductor, created by both holes ($\boldsymbol{J}_p$) and electrons ($\boldsymbol{J}_n$). The description of the dynamics of a semiconductor is extremely complex and the details can be found elsewhere [168]. Here we will just introduce the 3 sets of equations that define the dynamics of the system:

Poisson equation Relates the electrostatic field $\boldsymbol{F}$ with the density of charge in the semiconductor with permittivity ϵ_s:

$$\nabla \cdot \boldsymbol{F} = \frac{e(n - p + N_A - N_D)}{\epsilon_s}. \tag{5.3}$$

Drift-Diffusion equations Determines the total conduction current $\boldsymbol{J}_{cond}$ due to drift and diffusion effects of the free carriers:

$$\boldsymbol{J}_p = q\mu_p \left(p\boldsymbol{E} - \frac{k_B T}{e}\nabla p\right) = \mu_p p \nabla E_{F_p} \tag{5.4}$$

$$\boldsymbol{J}_n = q\mu_n \left(n\boldsymbol{E} + \frac{k_B T}{e}\nabla n\right) = \mu_n n \nabla E_{F_n} \tag{5.5}$$

$$\boldsymbol{J}_{cond} = \boldsymbol{J}_p + \boldsymbol{J}_n, \tag{5.6}$$

where μ_p and μ_n are the hole and electron *mobilities* respectively.

Continuity equations These equations introduce the time-dependence of the effects and ensures carrier conservation:

$$\frac{\partial p}{\partial t} = G_p - U_p - \frac{1}{e}\nabla \cdot \boldsymbol{J}_p \tag{5.7}$$

$$\frac{\partial n}{\partial t} = G_n - U_n + \frac{1}{e}\nabla \cdot \boldsymbol{J}_n, \tag{5.8}$$

where G and U are the generation and recombination rates, respectively, for both holes and electrons.

The previous sets of equations must be solved together with the right border conditions to find a solution for the carrier concentration at any point ($\boldsymbol{r}$) in space and time (t) in the semiconductor. This (usually hard) task is normally done using the right computational tools. Once $p(\boldsymbol{r},t)$ and $n(\boldsymbol{r},t)$ are known, the performance of the device can be investigated and from there the relevant quantities for the specific study can be taken.

5.1.3 Simulation of semiconductor effects

As just mentioned, the determination of $n(\boldsymbol{r},t)$ and $p(\boldsymbol{r},t)$ requires the resolution of the Drift-Diffusion equations together with the Poisson and Continuity equations. These coupled sets of equations are highly nonlinear and thus very hard to solve numerically. For that reason, computational tools based on finite-elements method and specifically designed for this task are required.

However, the choice of software must take into account the final integration with the physics of our specific problem. Because eventually we will want to merge the carriers (semiconductor) effects together with the strain/stress and optical effects, we opted to use COMSOL-Multiphysics as our simulation platform for the carrier effects in the semiconductor. By doing this, we ensure that all the physics we need in our device are simulated in the same platform, avoiding the need to integrate the results between different softwares, which are usually processes not only time consuming, but also susceptible of introducing errors (like adapting meshes between different simulations).

Even with the right simulation tools, finding a definite solution of the semiconductor nonlinear equations is far from being an easy task and for that reason it is worth describing very briefly what considerations were made in simulating these phenomena.

Just like in linear problems, the numerical method to solve nonlinear equations consists of iterating a solution until a minimum error is achieved. This is commonly known as the Newton-Raphson method [171]. However, unlike linear problems, nonlinear ones do not always have a solution or the algorithm converges to the right one and some measures must taken to ensure convergence of the simulation to the correct physical solution. Below we list the most important ones we used in our methodology [171]:

- **Correct initial solution** The correct initial solution, at thermal equilibrium (or zero voltage) is critical to ensure correct solutions when voltage is increased. For that reason, we force the initial distribution of n and p to be that of thermal equilibrium in the whole system.

- **Slowly increasing the voltage load** After the initial solution is calculated we slowly increase the voltage in very small steps, building up a solution from the one calculated

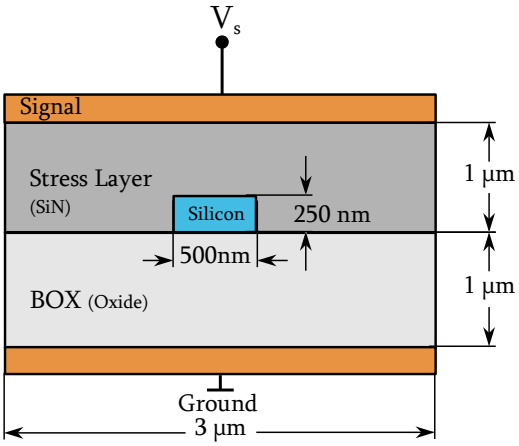

Fig. 5.2 The structure of the semiconductor waveguide capacitor.

before. Making small voltage steps ensures stability in solutions where stronger nonlinearities may arise.

- **Finer mesh** A fine mesh of the finite elements is required in regions where nonlinearities are stronger, typically close to the surface of the semiconductor. This ensures a more detailed calculation of the solutions in these areas leading to more consistent results.

In addition to these measures, the integrity of the obtained solution was confirmed by comparing the results with other simulation tool: DEVICE by Lumerical. The agreement between the results from both softwares and some publications gave us enough confidence on our results. Nevertheless, the solutions for very small structures (small silicon waveguides) are very unstable because of the strong border effects and before accepting a simulation outcome, a comparison between different solutions was performed to confirm the consistency of the results.

Consider now the silicon waveguide strained by an SiN layer as shown in Fig. 4.14a. In order to exploit the strain-induced Pockels effect, an electric field must be induced in the waveguide. The simplest way to do this is by adding two parallel electrodes to generate a vertical electric field in the waveguide. The resulting structure is the one presented in Fig. 5.2 which we will call the *waveguide capacitor*, because it is basically a regular capacitor with a silicon waveguide surrounded by SiO_2 and SiN.

By applying a voltage V_s to the *signal electrode* (located on top), we induce carrier concentration variations in the silicon waveguide. The most relevant effects arise close to the interface with the insulator cladding resulting in regimes like accumulation, depletion and

inversion which contribute for a strong change in refractive index inside the waveguide due to the plasma dispersion effect, even though no currents are associated. However, the tiny dimensions of the waveguide together with the fact that silicon is surrounded by insulators make it challenging to understand the carrier phenomena occurring in the device.

Nevertheless, the physical phenomena taking place in the waveguide capacitor has many similarities with those of the typical Metal-Insulator-Semiconductor (MIS) capacitor, shown in Fig. 5.3. For that reason, in order to make it easier to understand the more complex effects in the waveguide capacitor, we will first describe the physics of a regular MIS structure, when a potential difference is applied to the electrodes. This approach will be very helpful in understanding the structure in Fig. 5.2 and all the other strained silicon devices under and applied electrostatic field.

5.2 Metal-Insulator-Semiconductor Device

The Metal-Insulator-Semiconductor (MIS) configuration is one the most important basic structures in general electronics where an insulator (in general an oxide material, making it a MOS device) is put between a metallic contact (the Signal electrode, with $V = V_s$) and a semiconductor material, which is connected to the Ground electrode (with $V = 0$). This device, as shown in Fig. 5.3a for a p-semiconductor [1]. We shall now study the properties of this structure under different voltage conditions and how the insulator affects its performance.

The vacuum level E_{vac} is the energy of a free stationary electron that is outside of any material and it is related to the electrostatic potential V_s by

$$E_{vac} = -eV \ .$$

Therefore, E_{vac} must be continuous throughout the structure and in an ideal MIS it is the same everywhere and the rest of the energy levels adapt to this condition [168]. In thermal equilibrium ($V = 0$) the Fermi-level is constant and for an ideal MIS-structure this results in the energy-band diagram plotted in Fig. 5.3b.

When an ideal MIS (or MOS) structure is biased, i.e. $V_s \neq 0$, the structure ceases to be in thermal equilibrium and the Fermi level is not required to be the same in the whole structure. The energy levels of the metal (E_{vac} and E_F) will undergo an energy change $\Delta E = -eV$ which will act as a new boundary condition. Consequently, the energy-bands of the semiconductor will bend close to the I-S interface to account for the ΔE energy shift in

[1] We will focus only on p semiconductors.

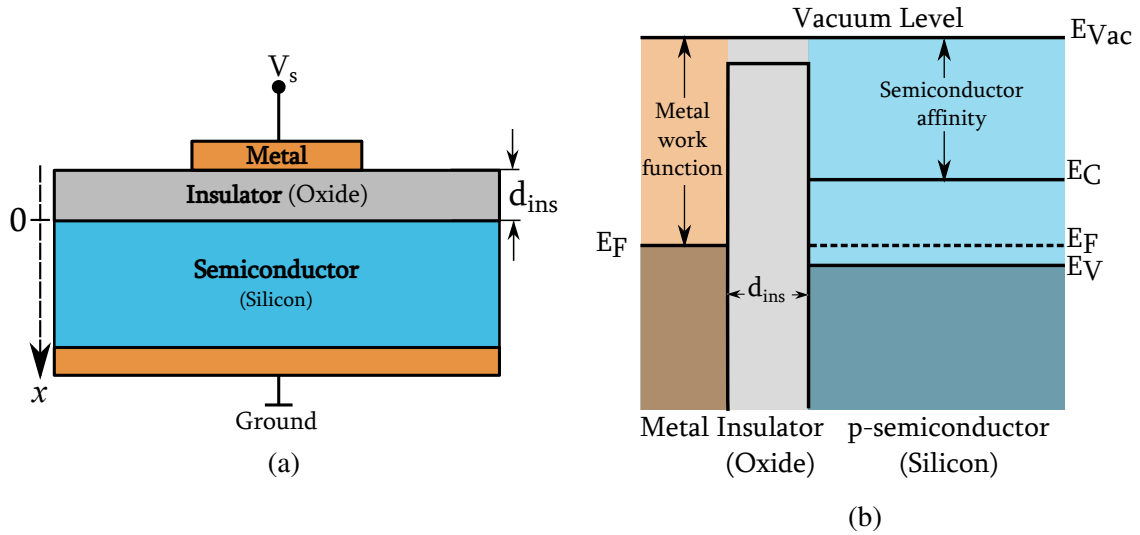

Fig. 5.3 (a) The Metal-Oxide-Semiconductor capacitor configuration. (b) The energy-band diagram of an ideal MOS capacitor in thermal equilibrium.

the metal. This *band bending* effect is schematically represented in Fig. 5.4 and has a strong impact on the distribution of carriers in the semi-conductor.

On the other hand, because of the insulator layer, regardless of the voltage applied, there are no currents flowing in this structure, and thus $\boldsymbol{J} = 0$. From eqs. 5.4 and 5.5 this immediately implies that the quasi-Fermi levels must be constant throughout the semiconductor:

$$E_{F_n} = E_{F_p} = E_F \ .^{2} \tag{5.9}$$

Since the semiconductor is considered to be very long (and this is a key point) and the other extreme grounded, the semiconductor remains unperturbed by the voltage far from the interface where the band-bending effects are relevant, fixing the Fermi level E_F. Therefore, while the conduction and valence bands of the semiconductor change because of the voltage, the quasi-Fermi level is not altered by V_s, as represented in Fig. 5.4 [168]. Consequently, this will drastically change the carrier distribution in the semiconductor, because the free-carrier density depends exponentially on the energy difference between E_F and the band energies (see eq. 5.2).

Three regimes may exist at the semiconductor surface depending on V_s, as represented in Fig. 5.4: accumulation, depletion and inversion. In accumulation, the majority carriers (holes, in this case) accumulate at the interface; in depletion, the voltage state repels the majority carriers away from the surface, resulting in very few carriers close to the surface, creating

[2]This is the reason why only one Fermi level is represented in the figures.

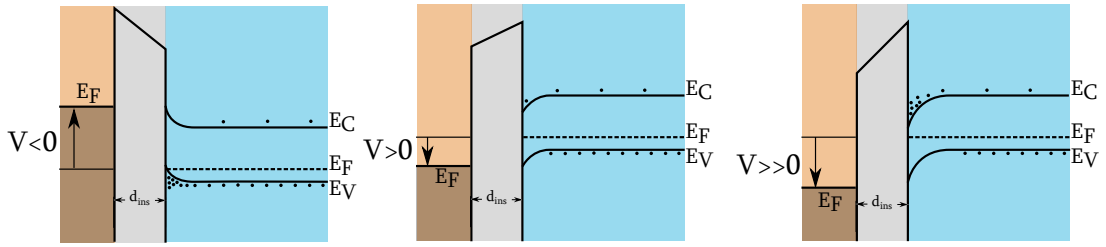

(a) Accumulation (b) Depletion (c) Inversion

Fig. 5.4 The band bending effects in a MIS structure with a *p*-type semiconductor for three different voltages and the corresponding three regimes it can work at.

a *depletion region*; in inversion the voltage is high enough to produce an accumulation of minority carriers (electrons) at the interface, inverting the type of carriers in this region.

5.2.1 Electronic simulations of a MIS-structure

To give a better insight on the influence of the voltage at the carrier distribution in the semiconductor, next we present the results of the COMSOL simulations for a regular ideal MIS-structure. The semiconductor is *p*-type silicon with $N_A = 1 \times 10^{15}\,\mathrm{cm}^{-3}$ and the oxide is SiO_2, with $d_{ins} = 1\,\mu\mathrm{m}$.

In Fig. 5.5 is represented the energy-band diagram (left side) and the corresponding carrier distribution in the semiconductor (right side) for different applied voltages V_s. For the case of $V_s = -3\,\mathrm{V}$ the potential difference between the electrode ($x = -1\,\mu\mathrm{m}$) and the semiconductor ($x = 0$) is 3 V. This makes the bands bend upwards and the valence band (in blue) gets closer to the Fermi level, leading to an *accumulation* regime where holes are accumulated at the interface. By increasing the voltage to $V_s = 1.2\,\mathrm{V}$, the bands are bent downwards and both E_C and E_V get farther from the Fermi level at the interface I-S, resulting in the *depletion* of carriers at the border of the semiconductor. Finally, by further increasing of the voltage, at $V_s = 3.5\,\mathrm{V}$ the conduction band (in red) gets closer to E_F and the concentration of electrons increase, corresponding to an *inversion* of carriers, where electrons are concentrated at the interface.

The graph in Fig. 5.5g shows the number of carriers close to the interface (the integration of *n* or *p* from $x = 0$ to $x = 500\,\mathrm{nm}$ in the semiconductor) as a function of V_s. From this graph it is clear the change in carrier concentration and the transition between the 3 main regimes of performance of the MOS structure described above.

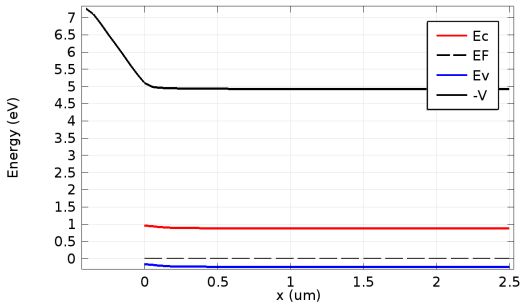

(a) Energy: accumulation ($V_s = -3\,\mathrm{V}$)

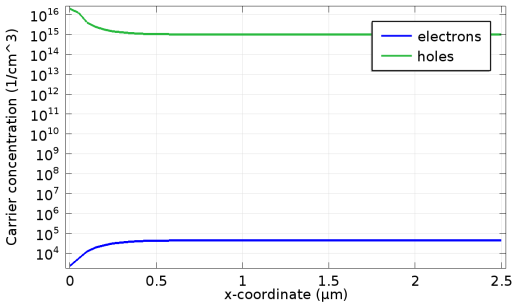

(b) Free-carriers: accumulation ($V_s = -3\,\mathrm{V}$)

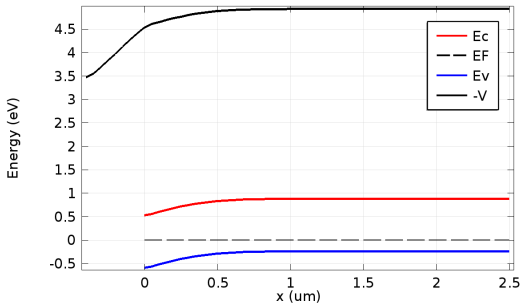

(c) Energy: depletion ($V_s = 1.2\,\mathrm{V}$)

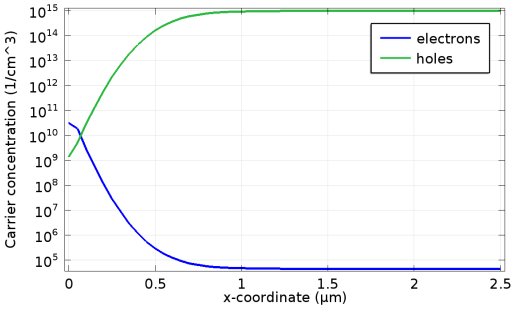

(d) Free-carriers: depletion ($V_s = 1.2\,\mathrm{V}$)

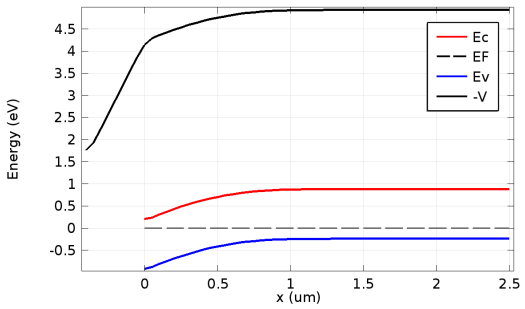

(e) Energy: inversion ($V_s = 3\,\mathrm{V}$)

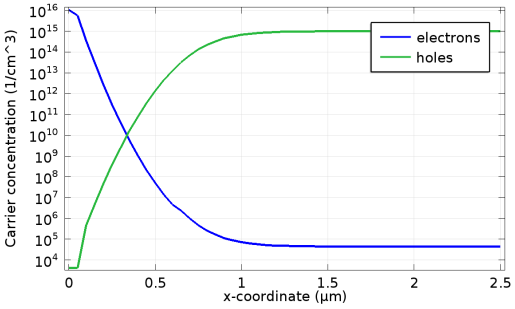

(f) Free-carriers: inversion ($V_s = 3\,\mathrm{V}$)

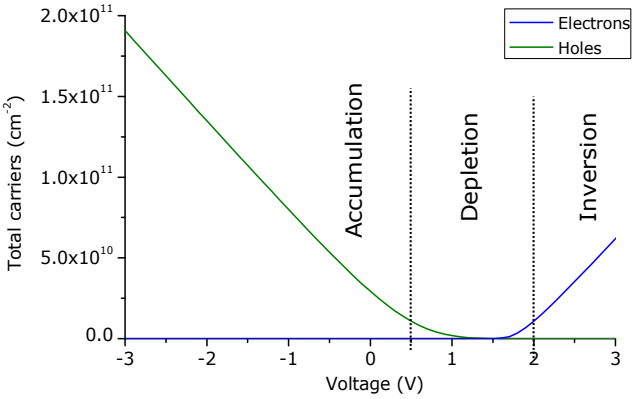

(g) The total number of free carriers present in 500 nm from the oxide interface into the semiconductor.

Fig. 5.5 Simulation of the MOS capacitor performance for different voltages, corresponding to different regimes. On the left is the band diagram along a line in the x direction; on the right is the carrier distribution. Graph (g) shows the total number of both types of free-carriers in terms of the voltage applied to the top metal.

5.2.2 The non-ideal MOS capacitor

The previous discussion was made with the assumption that the insulator/oxide layer was ideal. For a practical MOS capacitor, interface traps and charges exist that will, in a way or another, affect the ideal MOS characteristics. In general, these traps and charges can be classified in 3 different types [168]:

1. **Interface traps** (density D_{it}): Traps located at the Semiconductor-Insulator interface with energy states within the silicon forbidden bandgap and which can exchange charges with silicon.

2. **Fixed charges** (density Q_f): Charges localized in the insulator that are immobile under and applied electric field and can be either located at the interface with the semiconductor (fixed surface charges Q_{f_s}) or distributed inside the insulator layer (fixed volume charges Q_{f_v}).

3. **Mobile ionic charges** (density Q_m): Mobile ionic charges which are mobile within the insulator under bias or temperature conditions.

For our discussion, the most relevant are the interface traps D_{it} and fixed charges Q_f and we will see their effect on the ideal behaviour of the MOS-structure.

Fixed charges

It is the result of a fixed charge density ρ (which includes both Q_{f_s} and Q_{f_v}) per unit volume in the insulator. The fixed charge density is independent of the applied bias and behaves like a constant source of electric field in the insulator [172]. This charge density creates a voltage shift ΔV in the bias direction given by [168]

$$\Delta V = -\frac{1}{C_i}\left[\frac{1}{d_{ins}}\int_0^{d_{ins}} x\rho(x)dx\right] , \tag{5.10}$$

where C_i is the insulator capacitance and d_{ins} is the thickness of the insulator. The constant electric field created by the charges will affect the band-bending accordingly. Obviously, the effect on the voltage shift is weighted according to the location of the charge, i.e. the closer to the semiconductor interface, the higher shift it will cause. In case ρ is constant, the last expression takes the form $\Delta V = -Q_f/C_i$, where Q_f is the total fixed charge value.

To show the effect of fixed charges in the performance of devices, we simulated the effect of a constant Q_f (in cm^{-2} units) located at the interface Oxide-Silicon of the structure in Fig. 5.3. The electric field generated by the fixed charges located at the interface acts as if

there was an initial applied bias ΔV which induces a voltage shift of the curves shown in 5.5g. The results of the simulation are shown in Fig. 5.6 where we plot the total number of carriers in the top 500 nm of silicon for different Q_f in the Silicon-Oxide interface. We can see that different values of Q_f results in different shifts ΔV, changing the general shape of the curve.

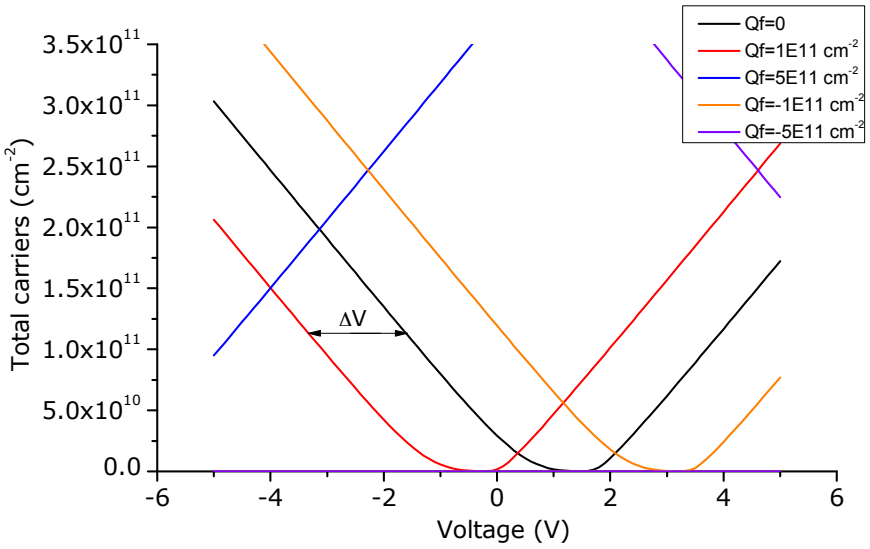

Fig. 5.6 The effect of different Q_f (in cm^{-2} units) on the total number of carriers in the top 500 nm of semiconductor. It is clear the variable shift ΔV created by the fixed charges.

Interface Traps

Interface trap states exist within the forbidden gap due to defects and change their charge state if they are filled or empty [168]. In general there are donor/acceptor trap states, which are neutral when empty and become positive/negative if full. Because the total interface trap energy density D_{it} arises from the sum of both types of traps (usually both present at the interface), it is convenient to define an energy level called the neutral level (E_0). Every trap state above E_0 are of acceptor type and below they are of donor type and its occupancy is determined by the Fermi level [168], so that the total charge Q_{it} due to the interface traps is given by

$$Q_{it} = -e \int_{E_0}^{E_F} D_{it} dE \quad , \text{if } E_F > E_0 \tag{5.11}$$

$$= +e \int_{E_0}^{E_F} D_{it} dE \quad , \text{if } E_F < E_0 \, . \tag{5.12}$$

Since a voltage bias alters the energy-band diagram of the semiconducor in respect to E_F, Q_{it} will strongly depend on the applied voltage. Furthermore, filling and emptying the

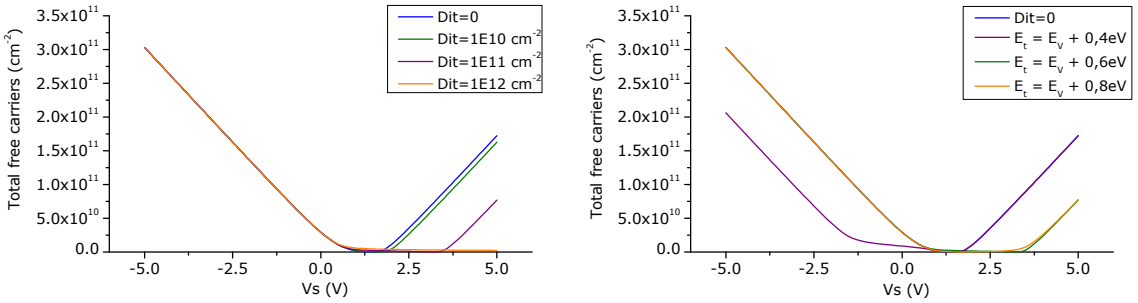

(a) (b)

Fig. 5.7 The traps effects on the MOS free carriers concentration $n+p$ in the 500 nm from the oxide interface into the semiconductor. (a) The traps energy level is fixed in the middle of the bandgap $E_t = E_i$ and we change the density of traps D_{it}. (b) The density is fixed $D_{it} = 1 \times 10^{11}\,\mathrm{cm}^{-2}$ and we change the position of the trap level.

traps is a dynamical process and may introduce a time dependence in the performance of the whole system [146, 173]. This fact, together with the possible difference in the efficiency of the processes of emptying and filling the traps [173], may result in strong hysteretic effects in the voltage dependent curves [173–176].

However, every trap, depending on its particular species, behaves differently and thus, the trapping behaviour of a semiconductor is the result of the interplay of numerous complex processes [168, 173, 177, 178]. Therefore, while the fixed charges make only a shift in voltage, the interface traps can completely change the shape of any curve that depends on the voltage.

To illustrate this, we consider a single trap energy level E_t in the forbidden bandgap and show its effect on the curve of Fig. 5.5g for different concentration D_{it} and energy level E_t. These results are shown in Fig. 5.7, where we considered the total free carrier concentration $n+p$.

In Fig. 5.7a we fix the energy of the single trap level at the middle of the bandgap ($E_t = E_V + 0.55\,\mathrm{eV}$) and change its density. We see that by increasing the concentration of traps, a higher V_s is required to reach the inversion regime, because more traps must be filled in the middle of the bandgap. It creates a longer depletion region as a function V_s, as shown in Fig. 5.7a in comparison with the no traps case.

In Fig. 5.7b we fix the trap density $D_{it} = 1 \times 10^{11}\,\mathrm{cm}^{-2}$ and consider different E_t in respect to E_V. Traps with energy close to the valence band move the Fermi level upwards and the depletion regime is reached for negative voltages ($V_s \sim -2.5\,\mathrm{V}$). On the other hand, it can be seen that higher E_t increases the voltage at which the inversion regime is reached.

The previous graphs show that a single discrete energy level trap may affect drastically the behaviour of a system, changing considerably the V_s dependent curves. Consequently, in order to understand the behaviour of a system where Si is surrounded by a Silicon Nitride layer (the stress layer), we must study the electronic properties of SiN, to know what are the trapping and charging characteristics of such type of cladding.

5.3 Electronic properties of Silicon Nitride

Silicon Nitride is a dielectric that has been widely studied because of its application on different electronic devices. As already mentioned in section 4.2, a−SiN:H alloys consist of a random network of Si−N and Si−Si bonds [143]. This random arrangement of atoms will change the electronic properties of the material in comparison to that of crystalline Si_3N_4, which consists of a network of Si−N covalent bonds between tetrahedrally coordinated Si sites and planar threefold-coordinated N sites. We have already seen in section 4.2.1 the important role H atoms play in PECVD deposited a−SiN:H, particularly its contribution to the thin film stress. The generation of stress is associated with implantation and vacancy of atoms in the SiN film. We may expect that the same mechanisms that contribute for stress generation may introduce defects in the SiN network. In fact, it is now known that the defect densities in a−SiN:H depend on the mobility of atomic H, as it is the hydrogen atom that mediates the reconstruction of defects into Si−Si bonds [143, 179]. These defects in SiN films can be so important that they play a major role in different type of applications, from charge storage in MNOS memory devices [172, 180–182] to passivation in solar cells [147, 183–187].

The defects arising in a−SiN_x:H can be of various types and have distinct origins. An extensive analysis of the defects, traps and charges in SiN thin films is beyond the scope of this thesis. This is indeed a very complex topic which has been the target of much research for many years and it is not our intention to develop a research work on this particular field. However, because the SiN cladding interacts directly with the silicon waveguide and it is the source of stress in our device, next we present an overview on the electronic properties of the a−SiN_x:H so that we have a clearer idea of what kind of phenomena we may expect in our devices.

5.3.1 Bulk electronic properties

As discussed in Chapter 3, silicon is a group IV element whose atoms are sp3 hybridized and form four covalent bonds with adjacent Si atoms. N is a Group V element with a s^2p^3

configuration. Si_3N_4 bonds by forming three $sp2$ hybrids which form the Si−N bonds and a p_z state which forms a lone-pair oriented normal to the Si−N bonding plane [142, 143, 188] (compare with Fig. 4.6).

In SiN_x alloys ($x = 0$ corresponds to crystalline silicon, while $x = 4/3$ is crystalline SiN), there is a replacement of Si−Si bonds by stronger Si−N bonds. Therefore, the bandgap increases with increasing x, resulting in the insulator characteristics known of SiN. This tendency is shown in Fig. 5.8a (after Refs. [143, 189]). The a−SiN:H alloys behave similarly, except that E_v is about 0.8 eV lower, owing to the replacement of upper Si−Si states by deeper Si−H states. [142, 143, 188]. A much deeper and detailed study of the electronic features of SiN thin films can be found elsewhere [142, 143, 188].

5.3.2 Defects in silicon nitride thin films

Defects in a chemically ordered network such as Si_3N_4 can basically be defined as the bonds that do not belong to the structure. These include Si−Si, N−N like-atom bonds and the Si and N dangling bonds (DB), i.e. broken bonds not connected to anything.

In Fig. 5.8b are represented the energy levels and occupancies of the main defects (from left to right): the Si−Si bond, the neutral Si DB (Si_0^3 or commonly called K-center), the N_4^+ centre (a shallow donor state bound by its Coulombic potential), the neutral N DB (N^0 or commonly called N-center) and the $=N-N^-$ group (a N-DB site at a N−N bond) [143, 189]. We clearly see that in SiN_x defects can be found in different energies within the bandgap. However, it has been reported that from all the defects, those present in higher concentration are the N and Si dangling bonds, or K and N centres respectively, represented in Fig. 5.9 [181, 183, 189, 190].

The K center consists of a silicon atom with a dangling bond, while three other bonds are satisfied with three N atoms, as represented in Fig. 5.9. The charge state is neutral (K^0) when a single electron is attached to the dandling bond, negative (K^-) when two electrons are attached to the dangling bond and positive (K^+) in the absence of electron bonding [181, 183, 189, 190]. The N centers are only observed in N-rich a−SiN_x:H (see Fig. 5.8b for $x > 1.3$) and like the K centers can have 3 charge states: N^-, N^0 and N^+ [189].

If both K and N centers are present, then *charge transfer* between defects may create K^+ and N^- centers,

$$K^0 + N^0 \longrightarrow K^+ + N^- \ ,$$

leaving some K^0 and N^0 centres, depending on which are present in excess. These charges may be present anywhere in the bulk of the SiN film [143, 179, 189, 190, 192, 193]. Normally,

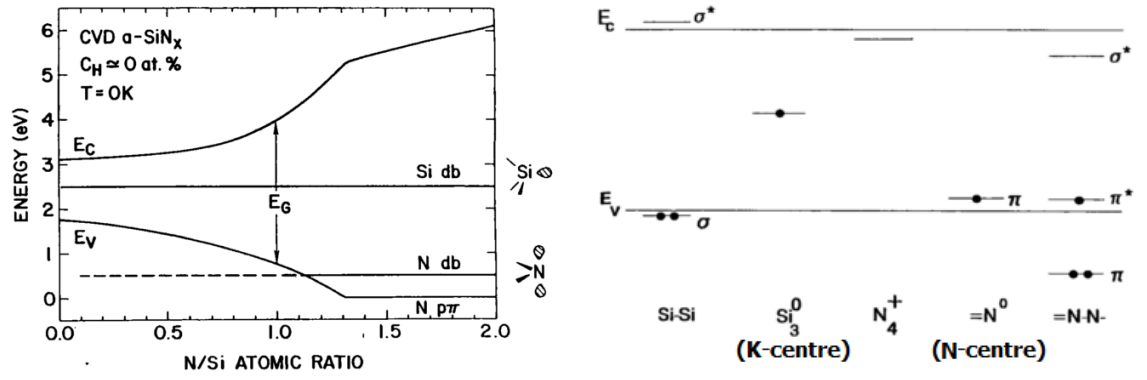

(a) (b)

Fig. 5.8 (a) The band-edges of SiN_x as function of the N/Si concentration x ($x = 0$ corresponds to crystalline Si while $x = 4/3$ corresponds to crystalline SiN). (b) The energy levels and occupancies of the main defects in the SiN_x network: Si−Si bond, neutral Si dangling bond, neutral N dangling bond, the $=N-N^-$ group and the N_4^+ centre [143].

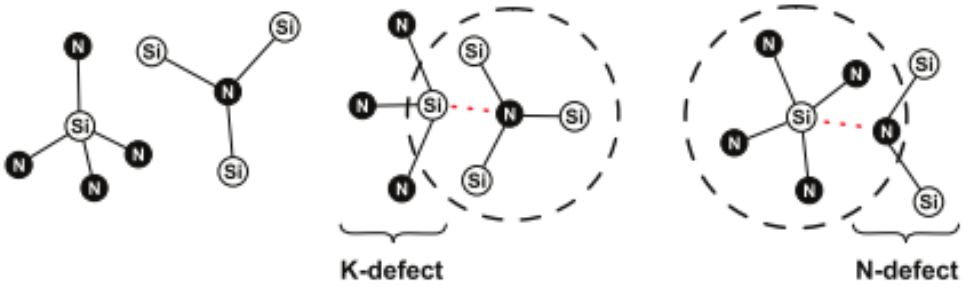

Fig. 5.9 Representation of the dangling bonds corresponding to the *K* and *N* centers, compared with the regular bonds between N and Si atoms [191].

the K centers are the dominant defect [185, 189, 190, 193] and they will play the most important role in the electronic dynamics of SiN films.

5.3.3 Electronic properties of the K-centers

The relationship between the high density of traps and charges in SiN_x films and the presence of K-centers was first introduced by Robertson and Powell [194]. Then it was experimentally confirmed [195, 196] and it was shown that the K center acts as amphoteric hole and electron traps, i.e. it can change their charge state between its -, 0 and + configurations according to the following equations [174, 183, 185]

$$K^0 + e^- \longrightarrow K^- \quad , \quad K^0 - e^- \longrightarrow K^+ \, . \tag{5.13}$$

Additionally, it was found that the K centers are thermodynamically more stable in their charged states K^- and K^+ (diamagnetic states with no unpaired electrons), rather than in the neutral state K^0 (the paramagnetic state) and among the charged states, K^+ is thermodynamically favourable [193, 195, 196]. In fact, during the deposition of a$-SiN_x$:H films, hydrogen intervenes to create K^0 centers through a series of reactions which then relax to its more stable K^+ state [193]. Thus, in thermodinamically equilibrium, a$-SiN_x$:H may present a net positive charge.

In fact, a characteristic feature of Si$-SiN_x$ interfaces is a very large positive insulator charge density $Q_f \sim 1 \times 10^{12}\,\mathrm{cm}^2$ built up in the first 20 nm of film [147, 179, 193, 197, 198]. This positive high value of Q_f at the interface can be explained by both the high number of K^+ centers and also by the presence of charges in the small oxynitride layer formed between Si and SiN [147, 179]. This is shown in the band diagram of the Si$-SiN_x$ interface presented in Fig. 5.10, as reported by Aberle *et al.* in [147].

In addition to the K-centres, the contribution of the N centres must also be considered because they are also present at the interface. The total Q_f value is thus determined by the variation of volume fractions of K and N centres at the a$-SiN_x$:H/Si interface region: when the concentration of (charged) K and/or N centres increases, Q_f increases correspondingly [179, 184]. This interplay between N and K centres at the interface of the Si layer was studied by Hintzsche *et al.* in [198] and they confirmed that a surplus of K^+ defects arise at the interface and that the number of K defects and the amount of positive charge at the interface are interrelated quantities [198], confirming the statement made in the previous paragraph.

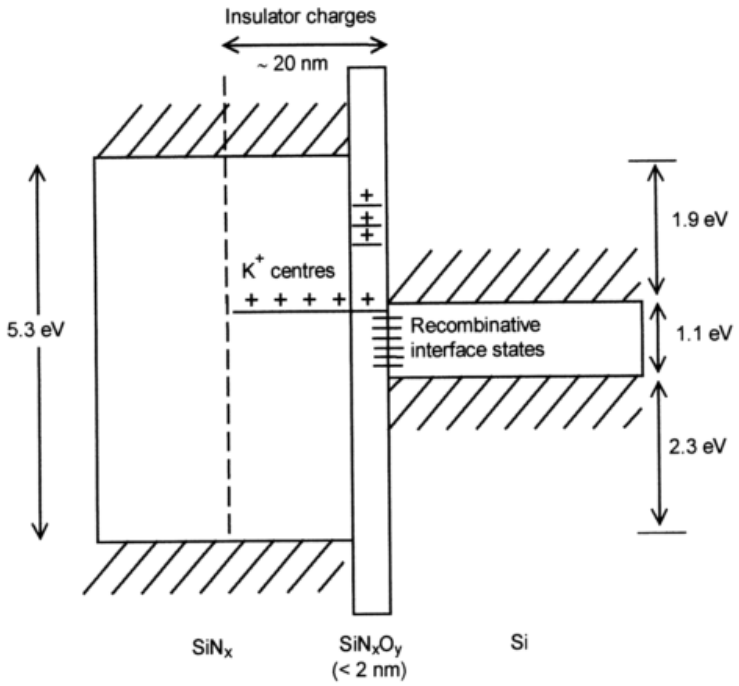

Fig. 5.10 The representation of the band-energy diagram of the interface a$-$SiN$_x$:H/Si, with the *K* centers energy levels, as proposed in [147].

5.3.4 Conclusion on the SiN electronic properties

The previous discussion had the purpose of showing that multiple effects may occur mainly due to the presence of *K*-centres in SiN. In fact, these defects can behave like charges which may change its charging state (amphoteric behaviour) by interacting with electrons and holes or even with other *N*-centres. Furthermore, they also act like traps, because holes and electrons can be captured during the charging of the film and with the interaction with the semiconductor. Therefore, it is not possible to predict with high degree of certainty which will be the final effect resulting from all these interactions.

Nevertheless, below we list the main features that can be attributed to the *K*-centres in SiN films:

- **High Q_f at the interface:** SiN films possess a high value of Q_f at its interface, presenting typical values of 1×10^{12} cm^{-2} to 3×10^{12} cm^{-2} [67, 147, 184, 199]. This high value is related to the number of K^+ centers present at the interface with Silicon [184, 198].

- **High density of traps:** Because the *K* centers behave like trapping mechanisms, the high number of *K* centers of the SiN films impact on the number of deep and interface

traps D_{it}. These traps are present both at the surface and in the bulk of SiN film and can be used for charge storage in devices like MNOS, where their filling state is controlled by a voltage variation [172, 180]. Because K centres are in the origin of both Q_f and D_{it}, there is a positive correlation between these two quantities [184].

- **Variable value of Q_f and hysteresis:** The amphoteric behaviour of the K-centers make its charging state variable. By applying a high voltage we can make the K^+ center change into its other stable K^- state, changing the value (and sign) of Q_f. This was reported in references [66, 174, 196]. The new charging state will remain the same until an opposite voltage is applied to bring the system back to its previous state. This process is the origin of the known hysteresis in voltage dependent experiments involving SiN films [66, 174, 196]. The hysteresis occurs because the charge state of the K centres (and the SiN film in general) does not change instantly when the applied voltage is modified and results from a charge build up. This creates a delayed response of the film on the applied voltage which will ultimately lead to hysteresis in V_s. This phenomenon will be discussed in higher detail in Chapter 8, when we consider time dependent phenomena.

These are the main characteristics expected from the electronic interaction between Si and SiN films. Consequently, the K-centers are associated with high values of both fixed charges and traps, they are expected to introduce big changes in the performances of the devices and are responsible for the appearance of undesired effects such as hysteresis on voltage sweeps.

5.4 The silicon waveguide capacitor

We now put our attention back on the strained silicon device in Fig. 5.2: the silicon waveguide capacitor. Although the physical mechanisms acting on this structure are basically the same as discussed in the MIS configuration, there are two differences that introduce big changes in its performance:

1. **Semiconductor dimensions:** In the MIS device (Fig. 5.5), we saw that the region where carrier concentrations change considerably are typically within $\sim$500 nm away from the interface with the insulator. Because of its dimensions, in the waveguide these effects are not "surface effects" but are effects that fill the whole semiconductor. Furthermore, there are 4 interfaces with insulator where this can happen, instead of a single one. Therefore, the carrier concentration is expected to be extremely sensitive to voltage changes.

2. **Floating Fermi level:** In this device, just like in the MIS device, there are no currents involved, so $\boldsymbol{J} = 0$ meaning that one single Fermi level E_F exists. However, unlike the MIS device, in this case the semiconductor is small and it is not connected to any electrode. This means that there is no boundary condition that fixes the Fermi level inside the semiconductor. In fact, the border conditions will be mainly determined by the voltage at the interface of the semicondutor. Therefore, the Fermi level in the semiconductor may vary under a voltage V_s, according to equations 5.2.

These two differences will have a big impact not only on the performance of the device, but mainly on the complexity of the computational resolution of this problem. Because of the strong interface effects, the problem is extremely nonlinear on the border of the waveguide and an extremely fine mesh in these regions ($\sim$1 nm) is required to solve the problem. Next, we present the simulations of the device to a signal voltage V_s sweep.

5.4.1 Carriers concentration in the waveguide capacitor

The physics of the device can be described as follows: a voltage is applied to the signal electrode and the conduction and valence band will bend to match the energy levels at the interface, just like in the MIS structure. At the same time, the Fermi level will also slightly change (as mentioned above) and the final carrier concentration will be the result of the interplay between the band bending and the E_F variation. The three regimes discussed in the MIS capacitor will also occur i.e. there is a regime where there is higher density of holes, other with depletion of carriers in the waveguide and finally another with higher density of electrons.

The simulations, as already referred, are highly nonlinear and the V_s dependent curves may present some features which are the result of the high nonlinearity involved in the simulations and do not represent any physical effect. We varied V_s from $-10\,\mathrm{V}$ to $10\,\mathrm{V}$ with the following considerations:

- The semiconductor is p-type silicon with constant doping $N_A = 1 \times 10^{15}\,\mathrm{cm}^{-3}$.
- The workfunction of the electrodes was assumed to be 5.5 eV, the value for Au metal.
- We used Maxwell-Boltzman statistics, with $T = 300\,\mathrm{K}$. At this temperature and for this doping level this is a good approximation which ensures easier convergence of the simulation.
- The mesh maximum element size is of 1 nm at the interface between the waveguide and the cladding and 4 nm inside the waveguide. This extremely fine mesh is required for

the simulation to converge, as this device is strongly dependent on the highly nonlinear phenomena occurring at the border of the waveguides.

- The initial solution was obtained by solving the Poisson equation for equilibrium carrier concentration at $V_s = 0\,\mathrm{V}$.
- The voltage was ramped from $V_s = 0\,\mathrm{V}$ progressively in steps of $\Delta V_s = 0.1\,\mathrm{V}$. Because the system is very unstable, the voltage must be changed slowly to ensure convergence of the solutions.

In Fig. 5.11 on the left side is represented, for 3 different voltages, the band energy diagram along a vertical line through the center of the waveguide $x = 0$; on the right side is represented the distribution of the logarithm of the holes concentration in cm^{-3} for the corresponding voltage. We can identify the same behaviour as described before for the MIS case, where a change in voltage makes the energy bands to change, which is reflected in the change of carriers distribution. As we increase the voltage, at $V_s \sim 1.5\,\mathrm{V}$ the conduction band starts to get closer to E_F and an inversion of majority carriers starts to take place. The corresponding carrier distribution (on the right side) shows that the free carriers accumulate mainly at the borders of the waveguide.

In Fig. 5.12 we present the calculated average concentration of carriers in the waveguide for both types of free carriers in the waveguide as a function of V_s. It is also represented the three different regimes where the majority carriers change. This clearly shows that the concentration of carriers inside the waveguide depends drastically on the applied voltage, corresponding to high density of holes, high density of electrons or low density of any free carriers.

Effects of fixed charges at the interface

From the discussion in section 5.3, we expect SiN to have a strong level of interface and volume fixed charges, corresponding to $Q_f \simeq 1 \times 10^{12}\,\mathrm{cm}^{-2}$ at the interface Si/SiN. Therefore, fixed charges must be included to properly simulate the carrier concentration in the Silicon waveguide. To illustrate this fact, we consider three different types of fixed charges at the interface and show its effects on the curve of Fig. 5.12. The results are shown in Fig. 5.13, where the ripples in the lines are due to computational instabilities and not to physical effects. As expected, the introduction of Q_f shifts the curve by ΔV depending on its density and sign: at $V = 0$, the presence of $Q_f > 0$ or $Q_f < 0$ brings the system to immediate inversion or higher accumulation, respectively.

It is important to point out that in general, with the presence of fixed charges, the system has an "apparent" linear relation between the total density of free carriers and the voltage, as

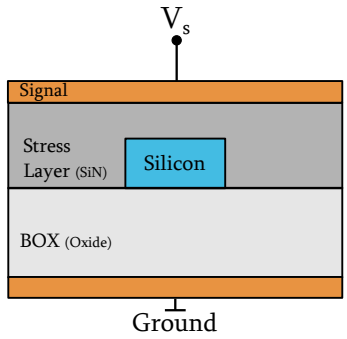

(a) Schematic view of the simulated waveguide capacitor

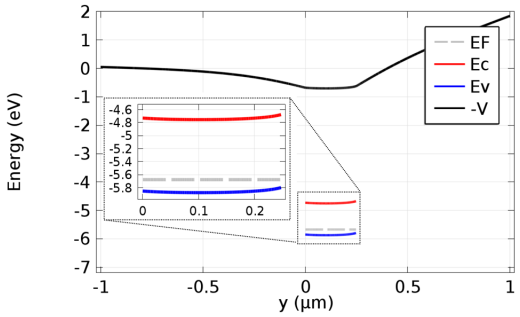

(b) Energy-band: accumulation ($V = -2\,\mathrm{V}$)

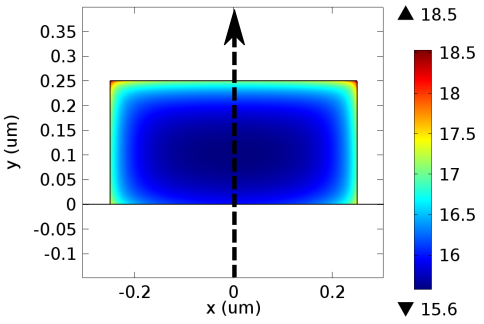

(c) $\log(p)$ ($V = -2\,\mathrm{V}$)

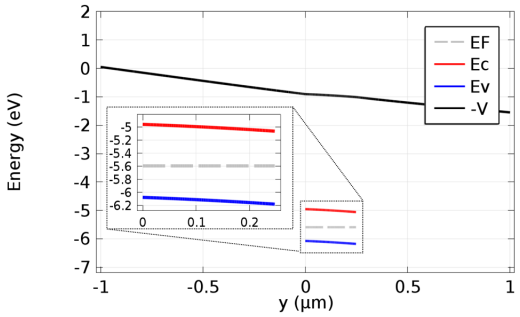

(d) Energy-band: depletion ($V = 1.5\,\mathrm{V}$)

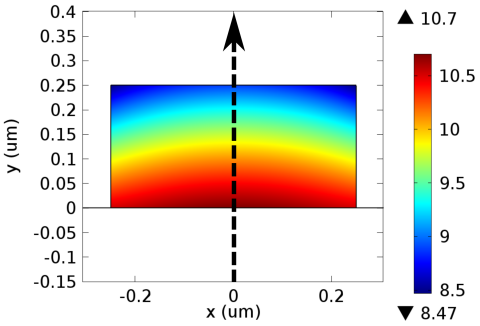

(e) $\log(p)$ ($V = 1.5\,\mathrm{V}$)

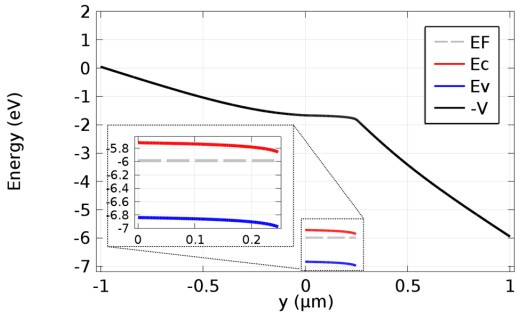

(f) Energy-band: inversion ($V = 6\,\mathrm{V}$)

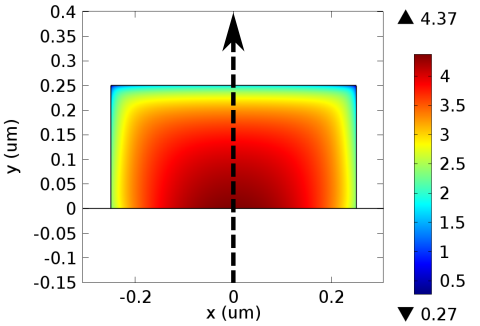

(g) $\log(n)$ ($V = 6\,\mathrm{V}$)

Fig. 5.11 Simulations of the silicon waveguide capacitor for different voltages, corresponding to different regimes. On the left is the band diagram along the line at $x = 0$ (represented as the dashed arrow on the right). On the right is represented the distribution of logarithm of holes concentration in cm^{-3}.

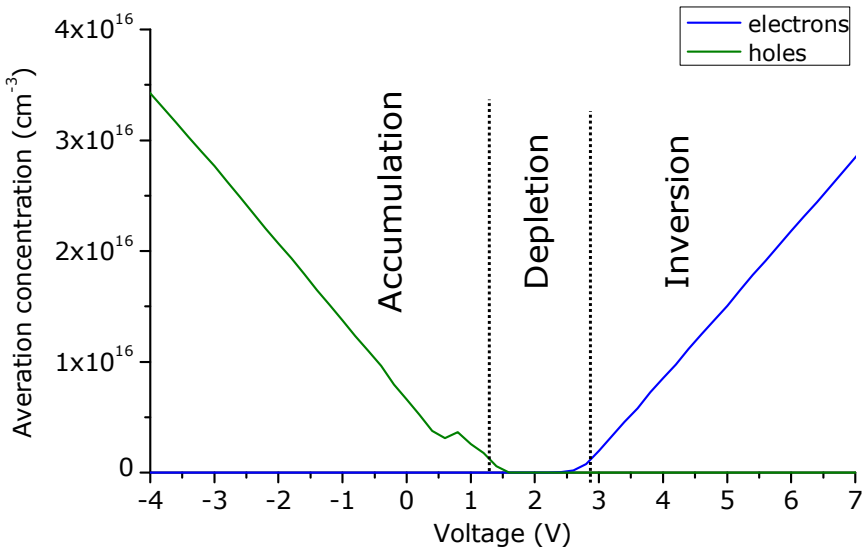

Fig. 5.12 The average number of free carriers in the waveguide. Just like in the MIS device, three regimes can be identified. The small bump in the holes concentration at $V_s = 0.5\,\mathrm{V}$ is a non-physical phenomenon and it is a simulation feature arising from the high nonlinearity of the computational problem.

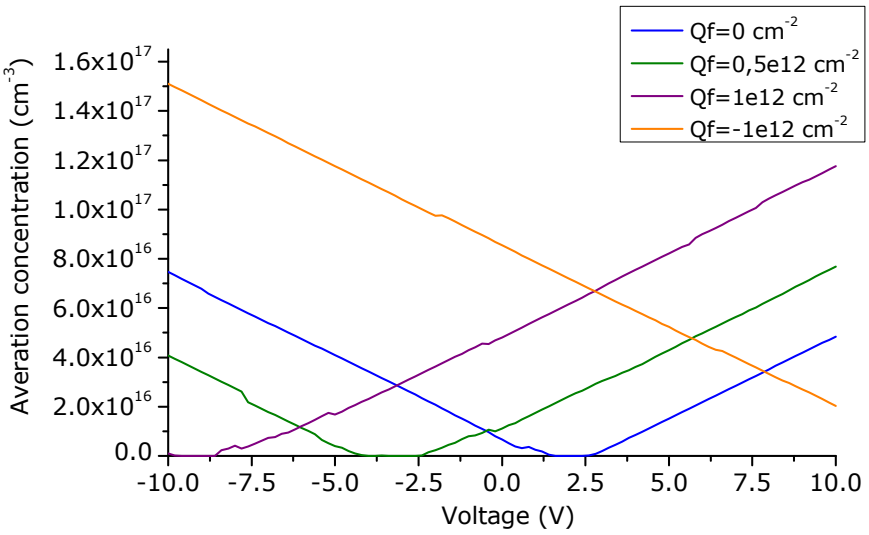

Fig. 5.13 Comparison of the average number of total carriers $(n+p)$ inside the waveguide for different values of Q_f at the interface Si$-$SiN.

shown by the curves for $Q_f = \pm 10^{12}\mathrm{cm}^{-2}$. This will be a key point later in Cfhapter 6 when we calculate the change of refractive index due to free carriers.

5.4.2 Electric field inside the waveguide

In Pockels effect, it is the interaction between $\chi^{(2)}$ and the electric field inside the waveguide that produces a change in refractive index. As we have just seen, applying a voltage to the system will also change the distribution of carriers which, in turn, will drastically change the electric field distribution. This is the key reason behind studying carrier phenomena when dealing with Pockels effect in strained silicon: even though we may not be interested in carrier effects in itself, carriers will *inevitably* play a role in Pockels effect because they have a strong impact on the electric field distribution inside the waveguide. Consequently, the simulation of semiconductor effects is crucial to understand Pockels effect in strained silicon waveguides.

However, in the most part of the results published on Pockels effect in strained silicon, in an electrostatics point of view, Si is considered to be an ideal dielectric where the electric field is nearly homogeneous in the waveguide [29, 31–33, 71], leading to fundamentally wrong results and misleading estimations of $\chi^{(2)}$. In this section we analyse the distribution of electric field in the structure after the carriers contribution is taken into account, for the cases with and without fixed charges.

Fig. 5.14 corresponds to the case without fixed charges. At the top is shown the distribution of the electric potential $V(\boldsymbol{r})$ in the structure together with the corresponding electrostatic field $\boldsymbol{F}$ for $V_s = -10\,\mathrm{V}$, $0\,\mathrm{V}$ and $10\,\mathrm{V}$. At the bottom, the waveguide is zoomed in and it shows the intensity of the F_y component of the electrostatic field. These plots can be compared with those with fixed charges $Q_f = 10^{12}\mathrm{cm}^{-2}$, shown in Fig. 5.15. These figures show the clear inhomogeneity of the electric field inside the waveguide, the effect of the fixed charges and also the importance of the borders on its distribution.

Finally, we take a closer look at the y component of $\boldsymbol{F}$, whose distribution is represented in the lower row of Figs. 5.15 and 5.14. It is clear that the accumulation of carriers at the borders of the waveguide acts as a screening mechanism of the elestrostatic field inside the waveguide, because it is much smaller inside the waveguide than outside.

If we assume that $\chi^{(2)}$ inside the waveguide is nonzero and constant everywhere [3], then the Pockels change in refractice index is proportional to the average F_y inside the waveguide. For that reason in Fig. 5.16a is presented the distribution of $F_y(y)$ along a vertical line along the center of the waveguide and in Fig. 5.16c is the average F_y in the waveguide as a function of the voltage, both for $Q_f = 0$ and $Q_f = 1 \times 10^{12}\,\mathrm{cm}^{-2}$. Fig. 5.16a and 5.16b shows that a change in V_s changes the distribution of carriers mainly at the top interface and that change is strongly decreased in the presence of fixed charges.

[3] We know it is not the case, but it helps for the discussion we are going to do and it does not change the reasoning behind it.

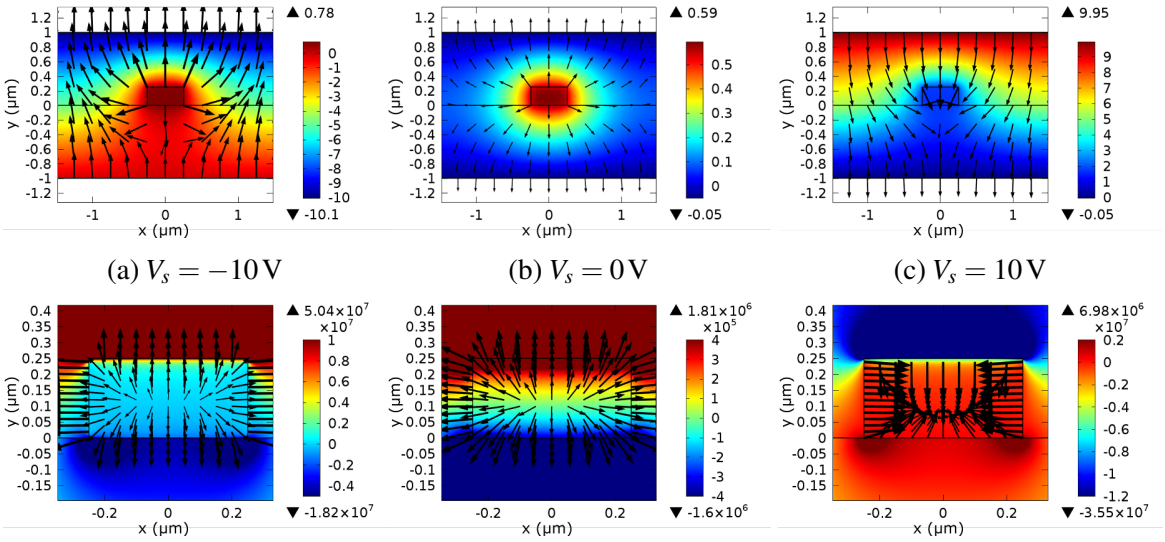

(a) $V_s = -10\,\mathrm{V}$ (b) $V_s = 0\,\mathrm{V}$ (c) $V_s = 10\,\mathrm{V}$

(d) $V_s = -10\,\mathrm{V}$ (e) $V_s = 0\,\mathrm{V}$ (f) $V_s = 10\,\mathrm{V}$

Fig. 5.14 Results without fixed charges at the interface Si−SiN ($Q_f = 0$). Top: representation of the electric potential V (coloured graph) together with the vectorial representation of the electrostatic field $\boldsymbol{F}$ in the device for different applied signals V_s. Bottom: zoomed view of the F_y component (coloured graph) and the vector field $\boldsymbol{F}$ in the waveguide.

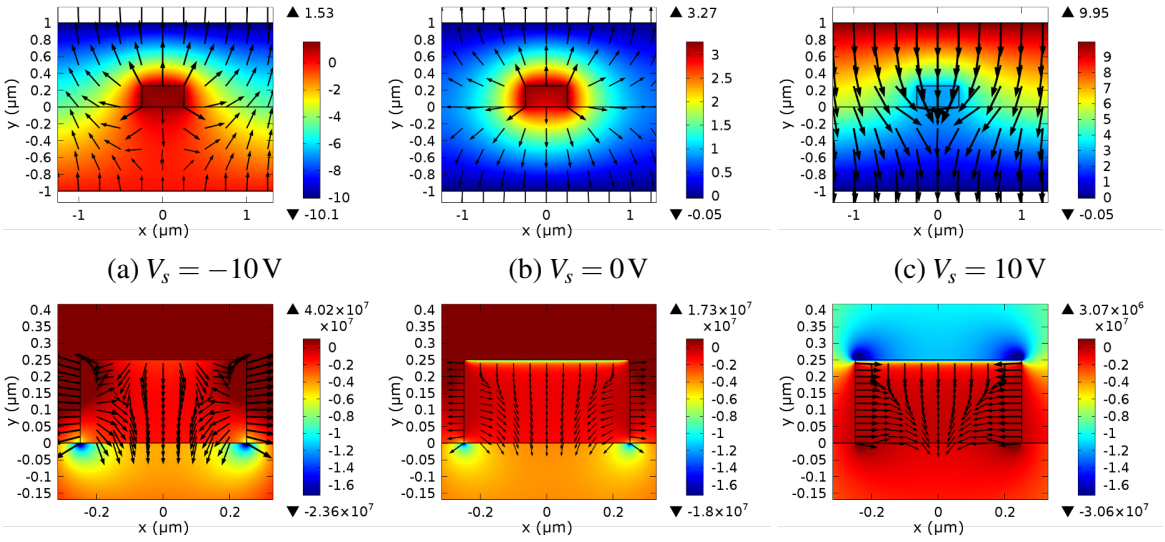

(a) $V_s = -10\,\mathrm{V}$ (b) $V_s = 0\,\mathrm{V}$ (c) $V_s = 10\,\mathrm{V}$

(d) $V_s = -10\,\mathrm{V}$ (e) $V_s = 0\,\mathrm{V}$ (f) $V_s = 10\,\mathrm{V}$

Fig. 5.15 Results with fixed charges at the interface Si−SiN ($Q_f = 1 \times 10^{12}\,\mathrm{cm}^{-2}$). Top: representation of the electric potential V (coloured graph) together with the vectorial representation of the electrostatic field $\boldsymbol{F}$ in the device for different applied signals V_s. Bottom: zoomed view of the F_y component (coloured graph) and the vector field $\boldsymbol{F}$ in the waveguide.

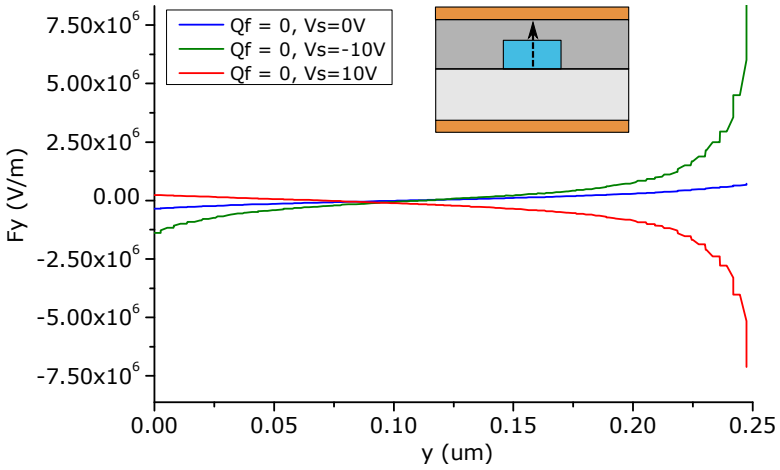

(a) F_y component of the electrostatic field, with $Q_f = 0$

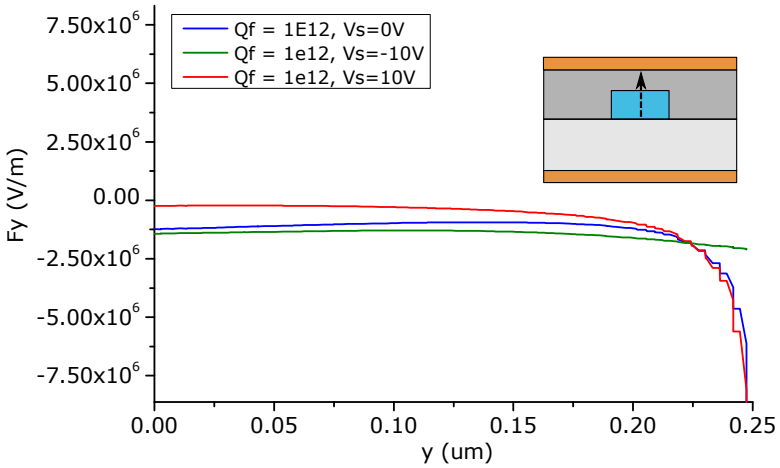

(b) F_y component of the electrostatic field, with $Q_f = 1 \times 10^{12}\,\mathrm{cm}^{-2}$.

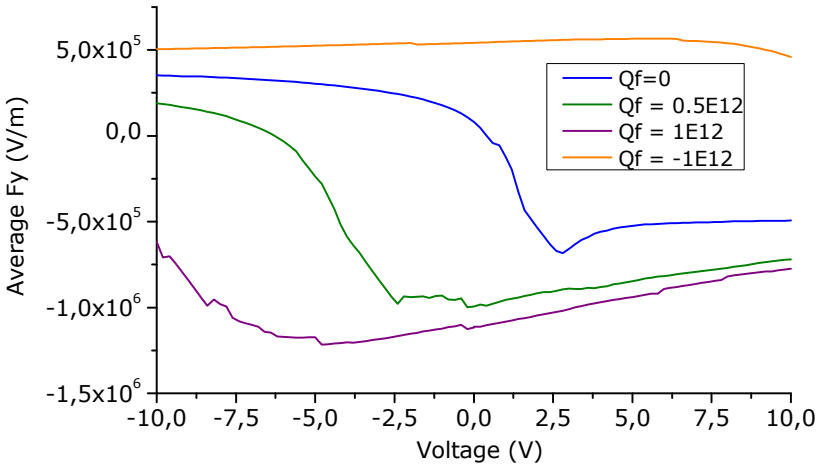

(c) Average F_y in the waveguide.

Fig. 5.16 (a) Representation of the y component of the electrostatic field $\boldsymbol{F}$ along a vertical line passing through the center of the waveguide. (b) The dependence of average electrostatic field F_y in the waveguide on V_s.

The shape of the curves shown in Fig. 5.16c are extremely important because they give us an hint of the curve for the Pockels effect voltage dependence.[4] Because Pockels is a linear effect, we are usually led to think that Δn is a linear function of V_s. In fact, Δn is proportional to $F_y(V_s)$ and we can see from Fig. 5.16c that, since F_y is not a linear function of V_s, then Δn is also a nonlinear function of the applied voltage.

Once again we see that Q_f makes a change of the position and shape of the curves, but more importantly we conclude that *in general there is a nonlinear relation between the Pockels shift Δn and the applied voltage to the electrodes V_s*. This is a key point that was not taken into account in previous publications on this topic [29, 31–33].

5.5 Final Remarks

The purpose of this chapter was understanding the result of applying an electric field to a silicon waveguide and we concluded that the change in optical response is twofold. On one hand, there are a variation and a redistribution of carriers concentration in the waveguide which, by the plasma dispersion effect, will lead to a change in the refractive index of the waveguide. On the other hand, the carrier concentration will drastically change the distribution of electric field in the waveguide, which in turn, will change the strain-induced Pockels effect.

Additionally, while silicon nitride is a very good material for strain generation, the same processes that introduce stress generate defects which gives it very special characteristics, namely a high density of fixed charges and traps. We have shown that these properties have high impact on the device performance, that cannot be easily avoided and must be integrated as well as possible in the design of the structure.

The effects presented in this chapter must now be put together with the optical physics and the strain effects, previously discussed in Chapter 4, to evaluate the total optical electro-optic response of such kind of device.

[4] n here is the refractive index, not to confuse with the electron density.

Chapter 6

Electro-optic design of strained silicon waveguides

Up to this point we have analysed how $\chi^{(2)}$ in silicon can be generated by strain, how that strain can be induced by a SiN overlayer and also how carriers affect the refractive index and electric field of a silicon waveguide under an electrostatic field. From that discussion it is clear that under a voltage, two different effects contribute to the change of refractive index of a strained silicon waveguide: the strain-induced Pockels effect and the carrier concentration dependent plasma-dispersion effect. These two effects are linked together, even though they have completely different origins, because the electrostatic field which activates the Pockels effect depends on the carrier distribution inside the waveguide.

In this chapter, we merge these effects with the optical phenomena for the design of a nano device which merges all the electro-optic effects together. The design procedure starts with the description of the different contributions to the final refractive index change, it goes through the waveguide, cladding and electrodes architecture and concludes with the final electro-optic simulations of the whole structure, pointing out some strategies to separately evaluate Pockels effect experimentally.

6.1 The general change of refractive index

Light is a wave characterized by a temporal and spatial variable electric and magnetic fields, $\boldsymbol{E}(\boldsymbol{r},t)$ and $\boldsymbol{H}(\boldsymbol{r},t)$ respectively. In a photonic device like an optical waveguide, these fields propagate under the form of *optical modes*, which are stationary solutions of the wave equation for that particular structure and are characterized by their polarization and *effective index* (n_{eff}). The change in *effective index* of an optical mode is responsible for a phase shift

in the optical wave and if the change Δn_{eff} is the result of the application of an electrostatic field $\boldsymbol{F}$, we say that an *electro-optic effect* took place. For a given voltage change ΔV, the higher Δn_{eff}, the more efficient is the electro-optic effect and high efficiency is usually desired for optical modulation.

From the discussion done in the previous chapters, we have seen that there are two types of electro-optic effects taking place in a strained silicon waveguide: the strain-induced Pockels effect, associated with an effective index change Δn_{eff_P}; and the carriers dependent plasma-dispersion effect, associated with Δn_{eff_c}. Therefore, we may say that the total effective index change will be given by

$$\Delta n_{eff} = \Delta n_{eff_P} + \Delta n_{eff_c} \,. \tag{6.1}$$

In order to analyse the final electro-optic effect, we must first understand the contribution of each of these effects individually.

6.1.1 Effectice index in Pockels effect

Pockels effect occurs due to the interaction between an electrostatic electric field $\boldsymbol{F}$ and the second order nonlinear susceptibility tensor $\overline{\overline{\boldsymbol{\chi}}}^{(2)}$.

The spatial change of dielectric permittivity $\overline{\epsilon}(\boldsymbol{r})$ (which is related to the change of refractive index $n(\boldsymbol{r})$) of a material undergoing Pockels effect is given by (recall from eq. 2.18):

$$\Delta\overline{\epsilon} = 2\overline{\overline{\boldsymbol{\chi}}}^{(2)} \cdot \boldsymbol{F} \tag{6.2}$$

This spatial dependent variation in the optical permittivity is responsible for a mode effective index change Δn_{eff_P}. This is calculated in Appendix B.1 for a mode with electric field profile $\boldsymbol{E}(x,y)$ and propagating in the z direction, where it is shown that for Pockels effect, eq. 6.2 leads to

$$\Delta n_{eff_P} = \frac{1}{N}\int_{wg} 2\chi^{(2)}_{ijk} E_i E_j F_k \, dS \tag{6.3}$$

where the integration is done over the entire waveguide. The normalization constant N corresponds to the active power of the optical mode that propagates in the waveguide, given by

$$N = \frac{2}{c\epsilon_0}\int_{\infty} \mathrm{Re}\,(\boldsymbol{E}\times\boldsymbol{H}^*)\cdot\hat{\boldsymbol{z}}\, dS \,. \tag{6.4}$$

Equation 6.3 may be put together with equation 3.30, which relates $\chi^{(2)}$ with strain gradients by

$$\chi^{(2)}_{ijk}(\boldsymbol{r};\overline{\overline{\boldsymbol{\eta}}}) = \Gamma_{ijk,lmn}\eta_{lmn} \,, \tag{6.5}$$

leading to the following relation:

$$\Delta n_{eff} = \Gamma_{ijk,mnl} \widehat{\eta_{mnl}^{ijk}} \, . \tag{6.6}$$

The *effective strain gradients* $\widehat{\eta_{mnl}^{ijk}}$ are thus defined by

$$\widehat{\eta_{mnl}^{ijk}} = \frac{2}{N} \int_{wg} \eta_{mnl} E_i E_j F_k \, dS \, . \tag{6.7}$$

The effective strain gradient corresponds to the overlap integral between the optical mode, strain gradient and electrostatic field spatial distributions inside the waveguide. We have already seen in Chapters 3 and 4 that the strain gradients and the electrostatic field are mainly concentrated at the border of the waveguides, so this region will play a major role in the value of Δn_{eff_P}.

The previous equations tell us that Pockels effect depends very deeply on the interaction between the strain effects, optical mode and electrostatic field applied. Moreover, we see that, in principle, all the components of the η and $\chi^{(2)}$ tensors contribute to the Pockels effective index change. The contribution of each term is weighted by the $\Gamma_{ijk,mnl}$ coefficients (which depend entirely on the crystal, recalling from section 3.3.3) and thus, in general, the sum in eq. 6.6 has $3^6 = 729$ terms. Of course, as we will show later in this chapter, because of the geometry of the waveguide, its symmetries and properties of the optical mode, most of the terms vanish and the sum is highly simplified.

6.2 Effective index in Plasma dispersion effect

The plasma dispersion effect was introduced in the Introduction chapter and it is the process by which the refractive index of a semiconductor changes due to a variation of free-carrier concentration (Δn_c). The relation between these quantities is established by the Soref-Bennet equations which, at $\lambda = 1.55\,\mu$m are given by (recall from eq. 1.3):

$$\Delta n_c = -\left(8.8 \times 10^{-22} \Delta n + 8.5 \times 10^{-18} \Delta p^{0.8}\right) \, . \tag{6.8}$$

In cases where the refractive index change Δn_{Si} is small compared to n_{Si}, as shown in Appendix B.2, the change in effective index Δn_{eff_c} is given by [1]

$$\Delta n_{eff_c} = \frac{2 n_{\mathrm{Si}}}{N} \int_{wg} \boldsymbol{E}^2 \cdot \Delta n_c \, dS \tag{6.9}$$

[1] In this manuscript we use the vector notation $\boldsymbol{E}^2 = \boldsymbol{E} \cdot \boldsymbol{E} = E_x^2 + E_y^2 + E_z^2$.

where the integral is evaluated over the waveguide.

From eq. 6.9 we can see that Δn_{eff_c} depends only on the free carrier concentration and its overlap integral with the waveguide mode profile. In section 5.4 we concluded that the carriers are mainly concentrated at the surface of the waveguide, which means that this region will contribute the most to Δn_{eff_c}.

6.3 Total electro-optic effect

The final Δn_{eff} of the optical mode propagating in a waveguide will be the sum of both Δn_{eff_P} and Δn_{eff_c}, as shown in eq. 6.1. The biggest challenge on the characterization of strained silicon waveguides is the clear distinction of this two contributions and isolate Pockels effect. On the one hand, because the strain-induced $\chi^{(2)}$ is very small, a high electrostatic field $\boldsymbol{F}$ must be applied to produce any considerable Δn_{eff_P}. On the other hand, these strong effects will induce high plasma-dispersion effect, to a point where Δn_{eff_c} is at least comparable to Δn_{eff_P}. For that reason, in order to extract Δn_{eff_P}, one must be able to know in advance a very precise knowledge of Δn_{eff_c}.

However, there are many variables that make this a very hard task. In fact, we have seen in chapter 5 that we must know exactly the trapping and charging states of the material surrounding the waveguide in order to simulate with high precision the plasma dispersion effect. In the case of a$-SiN_x$:H, from section 5.3, we have a clearer understanding of what to expect, but a high precision measurement of Q_f and D_{it} must be performed to properly simulate it, which was not done. Furthermore, as we shall see later, the characterization of waveguides surrounded by SiN involves many parasitic features which make it even more difficult to isolate both effects. Therefore, estimating the Pockels contribution from $\Delta n_{eff_P} = \Delta n_{eff} - \Delta n_{eff_c}$ is very challenging because that would require a very precise simulation of Δn_{eff_c}, which is very difficult to achieve due to the lack of precise knowledge about the real trapping and charging conditions of the cladding in the structure.

Nevertheless, there are intrinsic physical differences between Δn_{eff_P} and Δn_{eff_c} which can help us detecting Pockels modulation in strained silicon waveguides.

Modulation Speed

One of the most important motivations for the development of Pockels effect-based modulators is its intrinsic high speed. In fact, Pockels does not involve physical displacement of charged carriers and thus has an inherent temporal response down to the femtosecond range which enables ultrafast modulation beyond 1 THz [27]. Therefore, the main source of speed

limitation is the capacitance of the system used to propagate the RF signal that modulates light, namely the electrodes.

However, as already mentioned in the Introduction chapter, the speed of the plasma-dispersion effect is highly limited by the carrier mobility and recombination [11]. In fact, devices based on carrier accumulation are limited to bandwidths typically in the $1-5\,\mathrm{GHz}$ range [11, 71], which is much smaller than one may expect for Pockels effect.

Therefore, one way to detect Pockels effect is by increasing the modulation speed of the signal voltage V_s applied to the device to frequencies where carriers effects are not expected to be detected i.e. $\gg 1$ GHz. For that reason, our devices will be designed taking into account a high speed propagation of RF signal towards high speed modulation for detection of strain-induced Pockes effect.

Crystal orientation dependence

Another crucial difference between plasma-dispersion effect and strain-induced Pockels effect is its dependence on the crystal orientation. As discussed in section 3.5.3, coefficients $\Gamma_{ijk,lmn}$ depend on the orientation of the crystal. This is expected because for the same strain direction, different crystal orientations mean different relative displacement of the atoms, resulting in different strain-induced $\chi^{(2)}$.

This property is not shared by plasma dispersion effect. It is known that strain affects the bandgap of semiconductors [73, 81] and after the discussion made in section 5.1.2 it is clear that this may indeed have an influence on the distribution of carriers in the waveguide. However, even though strain affects the bandgap, no result has shown any dependence on strain direction and thus plasma-dispersion effect is not expected to be dependent on the direction of light propagation in the crystal.

Therefore, by placing waveguides in different orientations on a Si wafer, as shown in Fig. 3.10, the detection of any dependence of Δn_{eff} on the angle φ, should be due to a Pockels contribution, as given by

$$\Delta n_{eff}(\varphi) = \Delta n_{eff_P}(\varphi) + \Delta n_{eff_c} \,. \tag{6.10}$$

This strategy will also be adopted in our devices with the purpose of detecting and estimate the Pockels contribution to the final Δn_{eff}.

6.4 Design of the device structure

In the previous section we presented how the optical mode interacts with the refractive index variation mechanisms to create a change in n_{eff}. With that knowledge, we shall now design the photonic structures that enhance the strain-induced Pockels effect.

The real devices are made onto the Silicon On Insulator (SOI) platform. This technology refers to a stack of a thin single crystalline silicon on top of an insulator (the Buried Oxide, BOX), both deposited on a silicon substrate. In our particular case, the top silicon and the BOX thicknesses are 260 nm and 2 μm, respectively. The silicon of both the top layer and the substrate is Boron doped p-type with $N_a = 1 \times 10^{15}\,\mathrm{cm}^{-3}$ corresponding to a resistivity $15\,\Omega/\mathrm{cm}$.

The design of our structure will be based on these characteristics of the SOI wafer. Furthermore, we chose to work on the telecommunication wavelength $\lambda = 1.55\,\mu$m and this wavelength value is assumed by default. The choice of everything else in the device will be justified in the analysis presented below.

6.4.1 Design of the waveguide

For the design of the waveguide we could consider two types of configurations: strip and ridge waveguides. The *mode confinement* (τ), defined by

$$\tau = \frac{1}{N}\int_{wg} \boldsymbol{E}^2 dS \tag{6.11}$$

is very similar in both ridge and strip waveguides ($\tau \sim 0.5$). Therefore, the decision between these layouts is mainly justified by the fabrication feasibility of the structure. We decided to work with the strip waveguide because it is easier to fabricate because it does not involve as much control in the etching process as the ridge waveguide. Furthermore, we decided to work with TE-polarized mode because in shallow waveguides this is more confined than the TM mode.

Dimensions of the waveguide

Now we shall discuss the thickness (t_{WG}) and width (w_{WG}) of the waveguide. Its dimensions will affect the TE mode profile and the distribution of the electric field inside the waveguide. The waveguide thickness is fixed by the SOI platform, which for the substrates available for our study was set as $t_{WG} = 260\,$nm. However, because we do a thermal oxidation to grow 30 nm of SiO_2 around the waveguide (to be discussed in Chapter 7), the final Si thickness

will be lower, corresponding to $t_{WG} \simeq 250\,\text{nm}$. The waveguide width, on the other hand, can be freely optimized for our application.

As we have seen in Chapters 4 and 5, the strain gradients $\overline{\boldsymbol{\eta}}$ and the electrostatic field $\boldsymbol{F}$ are mainly concentrated near the borders of the waveguide. Therefore, on the one hand, to achieve higher Δn_{eff} we should look for higher overlap between the strain gradients, optical mode and electrostatic fields. This means a higher density of optical energy close to the borders, which is achieved for narrower waveguides. On the other hand, the narrower the waveguide, the lower is the mode confinement and the amount of optical energy in the active material: silicon. Therefore, there is a crucial trade-off, for the selection of w_{WG}: while smaller w_{WG} enhance the interaction between $\boldsymbol{E}$, $\boldsymbol{F}$ and $\overline{\boldsymbol{\eta}}$, it also decreases the confinement of the optical energy in the silicon core.

This situation is easily illustrated by considering the waveguide capacitor structure discussed in the previous chapter (structure in Fig. 5.2) and explicitly simulate the influence of w_{WG} on the absolute value of the effective strain gradients (eq. 6.7) when a TE mode propagates in the waveguide. We simulate this structure assuming stress effects from a 750 nm-thick SiN overlayer ($\sigma_0 = 1\,\text{GPa}$) and a signal voltage $V_s = -5\,\text{V}$ [2]. The results are shown in Fig. 6.1 where it can be seen a maximum on the curves corresponding to the optimal $w_{WG} \sim 350\,\text{nm}$ where absolute values of both $\widehat{\eta^{xxy}_{xxy}}$ and $\widehat{\eta^{xxy}_{yyy}}$ are stronger.

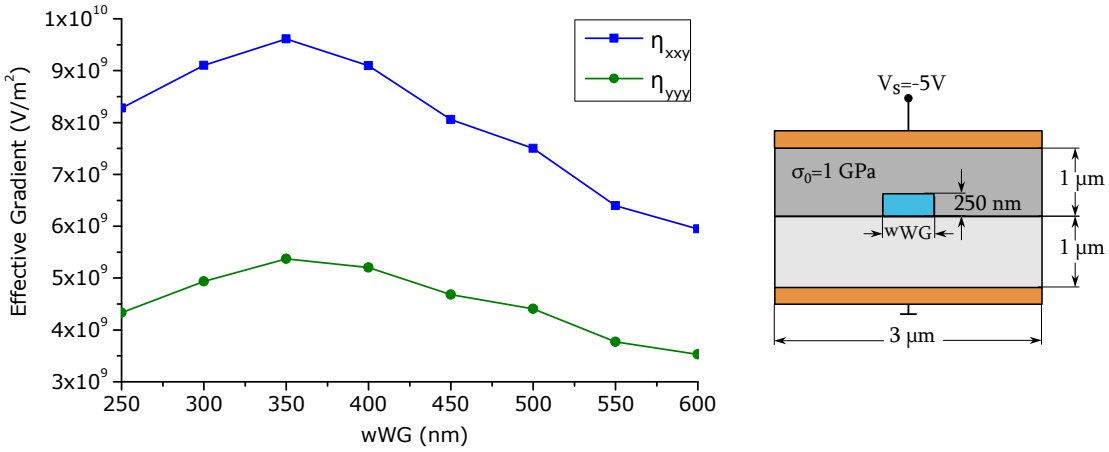

Fig. 6.1 Simulation of the absolute value of the effective strain gradient components $\widehat{\eta^{xxy}_{xxy}}$ and $\widehat{\eta^{xxy}_{yyy}}$ as a function of the w_{WG} (waveguide width) for the semiconductor capacitor structure represented on the right.

From this analysis, we decided to use $w_{WG} \simeq 400\,\text{nm}$. This value is very close to the maximum of the effective gradients curves in Fig. 6.1, while having a higher mode

[2] At this point we are not interested in understand very precisely the details of this simulation, but it is merely an example to show the efects of w_{WG} on the performance of the performance

confinement than $w_{WG} = 350\,\text{nm}$, which prevents eventual leakage of optical energy into the lossy metallic electrodes on top. Moreover, we ensure a safe single mode condition of the waveguide.

6.4.2 Design of the cladding

Now that we have analysed the nature of the waveguide, we can discuss the cladding. The cladding plays a fundamental role in our device because it will be responsible for the stress induced into the waveguide. As already mentioned in chapter 4, we chose to use SiN as our source of strain.

Thickness of the SiN layer

The electrodes to generate the electrostatic field are placed on top of the SiN layer and the separation between the waveguide and the electrodes is controlled by the thickness of the SiN layer. This distance affects the performance of the waveguide in two different ways. On the one hand, the closer the electrodes are to the waveguide, the higher is the electrostatic field $\boldsymbol{F}$ in the waveguide for the same potential V_s, which increases Δn_{eff_P} for fixed V_s. This is shown in Fig. 6.2a, where we present the effective index change as a function of t_{SiN}. These results were obtained by using the same simulation conditions of the previous section, but fixing $w_{WG} = 400\,\text{nm}$ and varying t_{SiN}.

On the other hand, the closer the metallic electrode is to the waveguide, the higher optical energy of the TE-mode interacts with the metal of the electrode. Metals like gold are very lossy materials at $\lambda = 1550\,\text{nm}$ and if the mode interacts with it, optical losses take place. Therefore, the lower is t_{SiN}, the higher will be the losses, as shown in Fig. 6.2b.Once again, we find a trade-off for the thickness of SiN cladding layer, clearly shown in Fig. 6.2, because while lower t_{SiN} increase the effective gradients, it also increases the losses.

We want the optical mode to propagate with nearly no losses, so, from Fig. 6.2b, we must have $t_{\text{SiN}} > 700\,\text{nm}$. Therefore, under this constraint, the higher effective gradients is obtained for $t_{\text{SiN}} \sim 700\,\text{nm}$ and this is our selection for the thickness of SiN layer.

The SiO_2 layer

We have seen in Chapter 5, that the a−SiN:H layer deposited by PECVD has specific electronic properties, such as charges and traps, which change the performance of the device. Therefore, a layer of SiO_2 below SiN may be considered as an attempt to minimize and control the charge effects of the SiN layer.

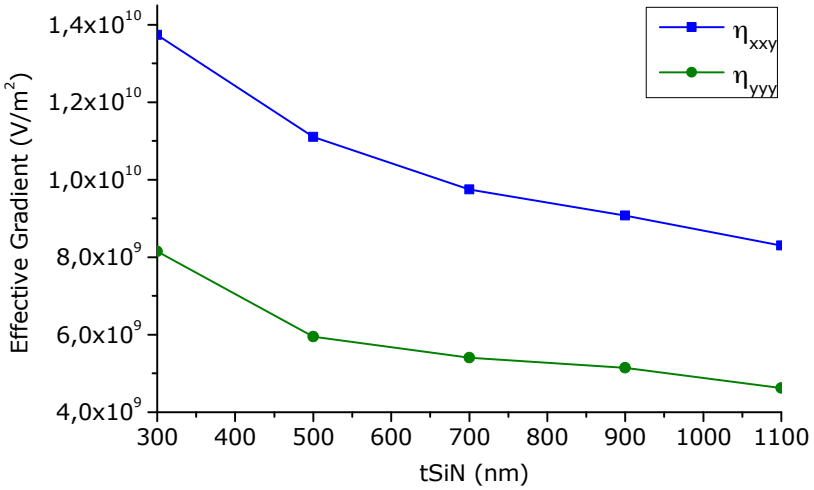

(a) Absolute value of the effective strain gradient components $\widehat{\eta_{xxy}^{xxy}}$ and $\widehat{\eta_{yyy}^{xxy}}$.

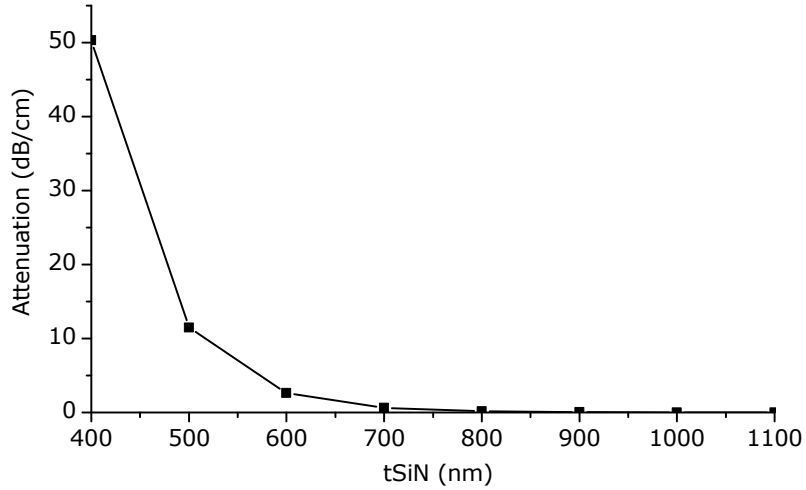

(b) The optical losses due to the interaction of the mode with the metallic electrode.

Fig. 6.2 The effects of the SiN layer on the performance of the device, as a function of t_{SiN}.

Electronic properties of the SiO_2 layer The reasons for the possible introduction of a SiO_2 layer between the silicon waveguide and the SiN stress layer are twofold. Firstly, it creates an insulating barrier between the silicon semiconductor waveguide and the SiN film which prevents the free carriers from flowing freely into the traps inside the SiN film, particularly into the *K*-centers. This concept used to be explored in SONOS (Silicon-Oxide-Nitride-Oxide-Silicon) devices to control the flow of free carriers in and out of the SiN traps and make it act like a charge storage device [181, 200]. Secondly, it also may serve to control the effect of the fixed charges Q_f on the waveguide, because it changes the interface and volume charging conditions of the cladding as a whole.

As we have seen in Section 5.3, the a−SiN:H layer may present some amount of volume fixed charges Q_{f_v}, independent of the interface. The *centroid of charge distribution* is the effective surface charges Q_{f_s} which results in the same effect created by the actual bulk distribution of Q_f [182, 201, 202]. This effective Q_f is the value actually measured in experiments involving MIS stacks (like the one in Fig. 5.3a) and for SiN these measurements report $Q_f = \sim 3 \times 10^{12}\,\mathrm{cm}^{-2}$ for a−SiN:H film as the insulator [67].

However, in a structure where the silicon waveguide is separated from the SiN layer by a SiO_2 thin film, it is not clear what Q_f to consider in the different interfaces, for different reasons. Firstly, the PECVD deposited SiO_2 layer usually contributes with Q_f itself, typically with values $Q_f \sim 1 \times 10^{12}\,\mathrm{cm}^{-2}$ [67], which is a smaller contribution than that of the SiN layer. Secondly, when one separates the SiN layer from the silicon waveguide, only the volume charges in SiN will play a role. Therefore, we expect the farther the SiN layer is from the waveguide, the smaller is the intensity of the electric field created by this volume effect inside the SiN film. As a result, the overall Q_f effect "felt" by the waveguide will be dependent and can be controlled by the thickness of the SiO_2 layer.

Because no specific measurements were made for the determination of the Q_{f_v} and Q_{f_s} contributions of the SiN layer, we have no way of knowing exactly what Q_f to consider in the stack and we will consider those reported in the literature for similar experiments [67].

Thickness of the SiO_2 layer We chose to maintain the thickness of the SiN layer constant in order to ensure that the stress coming from the SiN layer is the same. Therefore, inserting a SiO_2 layer in the stack will increase the total thickness of the cladding. As we have already discussed, this will decrease the electric field inside the waveguide for a fixed V_s.

Moreover, the SiO_2 layer is lightly stressed in comparison to SiN. In our facilities, the SiO_2 deposited by PECVD was measured to have an internal stress $\sigma_{0_{SiO_2}} \sim -500\,\mathrm{MPa}$. Therefore, the higher the separation between the SiN layer and the waveguide, the lower will be the average stress inside the silicon core because the contribution from SiN will be less "felt" in

the waveguide. Fig. 6.3 shows the average σ_{xx} component of stress inside the waveguide as a function of the SiO_2 thickness placed below the SiN layer, with $\sigma_{0_{SiN}} \sim -1.2\,GPa$. From this graph we see that this layer affects the strain in the waveguide and can also be used as a way to control the deformation state of Si.

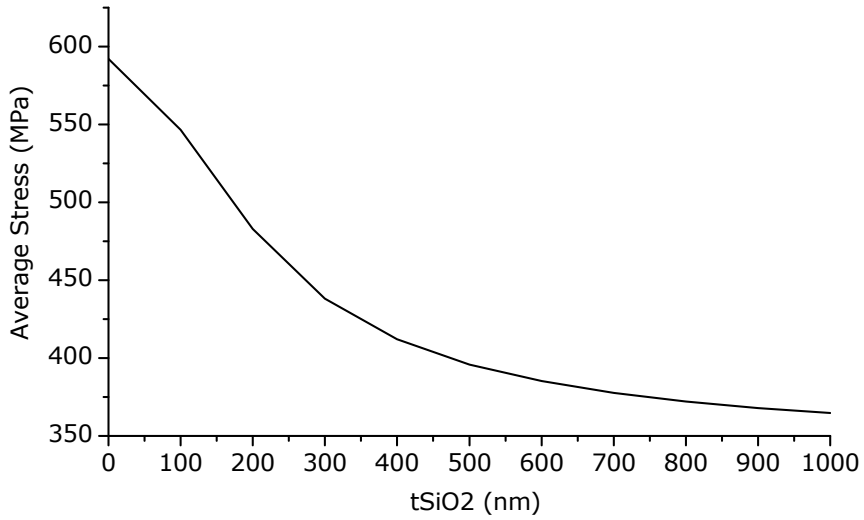

Fig. 6.3 The average $|\sigma_{xx}|$ component of stress inside the waveguide as a function of the SiO_2 placed below the SiN layer.

Final composition of the cladding

From the previous discussion, we decided to use different SiO_2 layers between the waveguide and the 700 nm-thick SiN stress layer. For all samples, we consider a thin layer with 30 nm of SiO_2 around the waveguide, grown by thermal oxidization. Then, we consider a second layer with three different thicknesses: $t_{SiO_2} = 0\,nm$, 250 nm and 500 nm. With this selection we can measure the influence of different levels of stress and charge effects into the waveguide in the electro-optic effect.

The choice of the 30 nm oxide layer between the waveguide and the stress layer is merely to introduce a physical barrier between the Si semiconductor and the SiN traps, which will prevent the free carriers to flow freely between this two materials. The stress will barely be affected by this layer, so this configuration will have the highest level of stress assumed to be the same as the total $t_{SiO_2} = 0$.

For the $t_{SiO_2} = 250\,nm$ and 500 nm cases, we are able to totally prevent the trapping effects from the SiN layer. Furthermore, we generate two different levels of stress into the waveguide, as shown in Fig. 6.3, and two different charging effects from the cladding, which can be insightful for the interpretation of the experimental data.

6.4.3 Design of the electrodes

The elements of the device still to be discussed are the electrodes. The electrodes will be responsible for the generation of the electrostatic field $\boldsymbol{F}$ that will activate the Pockels effect. Basically, the electrodes are made of a *Ground electrode* ($V = 0\,\mathrm{V}$) and a *Signal electrode* ($V = V_s$). We made the choice to study only the effect of a vertical electric field applied to the waveguide and we fix that as a constraint of the problem. The electrodes, thus, should be designed so that they satisfy this verticality condition.

Layout

Ideally, we are interested in the electrode configuration which delivers the highest electric field in the waveguide for some given V_s potential applied to the signal electrode. However, there are some other considerations to take into account, such as the constraints set by the SOI wafer and the fabrication feasibility of the structure.

The interest in having a vertical electrostatic field $\boldsymbol{F}$ sets some constraints in the design of the electrodes. For the generation of $\boldsymbol{F}$ mainly in the y direction, the best layout is that of the waveguide capacitor discussed in Chapter 4 and used so far, where the signal electrode is placed on top of the cladding and the ground is located between the BOX and the silicon substrate. However, this is not feasible with our standard SOI stack because there is no metallic layer between the BOX and the substrate. Therefore, another layout must be considered to achieve the verticality of the electrostatic field in the waveguide.

The alternative configuration is shown in Fig. 6.4, where the signal electrode is placed on top of the cladding, centered with the waveguide and between two ground electrodes set side by side. The symmetry of this configuration ensures $F_x = 0$ in the center of the waveguide and the field $\boldsymbol{F}$ can be considered mostly vertical inside the waveguide, as it can be seen by the electric field direction in the same figure.

One of the main differences between this configuration and the capacitor discussed in section 5.4 is that in this case the silicon substrate actively intervenes in the overall electric field distribution. In fact, the electrostatic field acts on the substrate and because it is made of a p-semiconductor the free carriers will move and act as shielding mechanism which prevents the electric field to penetrate the substrate. This is the reason why in Fig. 6.4, the substrate has the nearly constant potential, corresponding to $\boldsymbol{F} \sim 0$.

Dimensions

The electrodes in this configuration must be engineered so that they are capable of transmitting with the highest efficiency possible the high frequency RF signal used to modulate the device

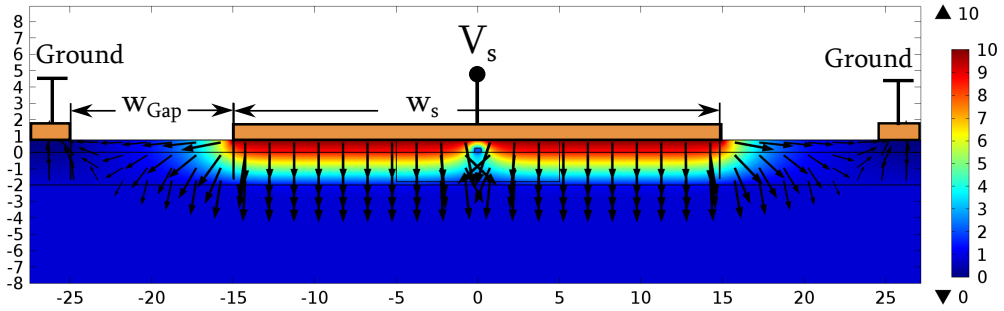

Fig. 6.4 The layout of the electrodes to achieve verticality of the electric field while being compatible with the standard SOI platform. The color graph represents the electrical potential V distribution for $V_s = 10\,\mathrm{V}$, while the arrows represent the $\boldsymbol{F}$ electrostatic field.

at high speed, which is essential to discriminate Pockels and Plasma-dispersion effects, as discussed above. An important criterion to take into account in the design for the electrodes is its well adaptation to a $50\,\Omega$ transmission line. This means that the impedance of the electrodes (Z_e), determined by the dimensions and the surrounding media, should satisfy $Z_e = 50\,\Omega$, otherwise the electrodes generate reflections which deteriorate the performance of the device. A detailed analysis of these processes and on the physics of a general transmission line can be found elsewhere [203] and it is beyond the scope of this manuscript.

The two dimensions to consider in the design of the electrodes is the gap (w_{gap}) and the width of the signal electrode (w_s). Different combinations of w_{gap} and w_s result in different Z_e. To calculate the impedance of the electrodes with the configuration shown in Fig. 6.4, we used the software AppCad from Avago Technologies. This software directly provides the value of Z_e by inputting w_{gap}, w_s and the permittivity of the substrate ϵ_s. The challenge here is what value of ϵ_s to consider because the "substrate" is the SOI stack which is made of both Si ($\epsilon_{\mathrm{Si}} = 11.8$) and SiO_2 ($\epsilon_{\mathrm{SiO_2}} = 3.9$). Therefore, to have a better estimate, we calculated an weighted average of ϵ_s, determined by the distribution of electric field $\boldsymbol{F}$:

$$\epsilon_s = \frac{\int |\boldsymbol{F}(\boldsymbol{r})|\,\epsilon(\boldsymbol{r})dS}{\int |\boldsymbol{F}(\boldsymbol{r})|\,dS}\,. \tag{6.12}$$

By calculating ϵ_s in this way for each combination of w_{gap} and w_s from $10\,\mu$m to $30\,\mu$m, we concluded that, in order to achieve the correct adaptation conditions and ensure $Z_e = 50\,\Omega$ the following ratio should kept:

$$\frac{w_s}{w_{gap}} \sim 3\,. \tag{6.13}$$

Obviously, the dimensions of the electrodes affect the intensity of the electrostatic field in the waveguide. In Fig. 6.5 is represented the effective strain gradients, simulated for the

structure in Fig. 6.4 for $V_s = -15\,\mathrm{V}$, for different values of w_s and keeping $w_s/w_{gap} \sim 3$. It is clear that the lower is w_s, the higher is $\widehat{\eta}$ because the stronger is F_y in the waveguide for the same applied V_s. Therefore, ideally we should look for the narrowest w_s compatible with the fabrication conditions discussed above.

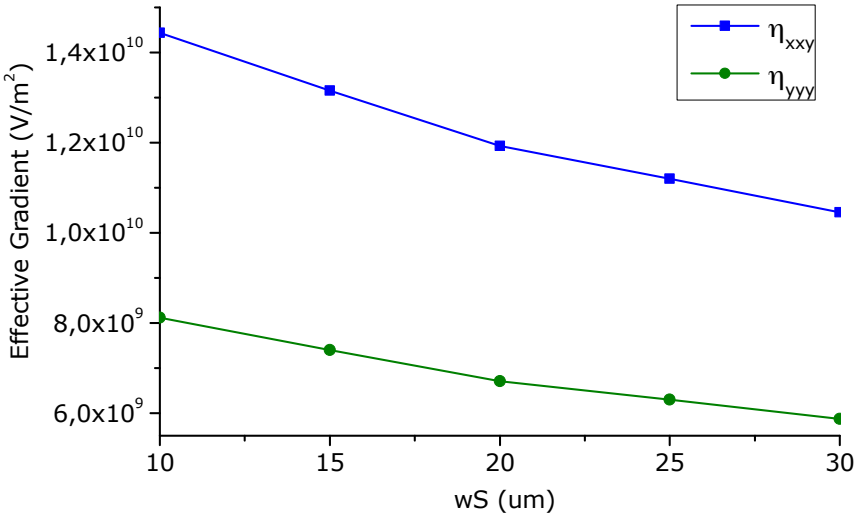

Fig. 6.5 The value of the effective strain gradients for the configuration of Fig. 6.4 as a function of w_s and keeping $w_{gap} = w_s/3$ for $V_s = -15\,\mathrm{V}$.

However, in order to be well within the fabrication tolerances of our fabrication procedure (to be described in Chapter 7), we decided to keep $w_{gap} = 10\,\mu\mathrm{m}$, which requires $w_s = 30\,\mu\mathrm{m}$, to satisfy the $Z_e = 50\,\Omega$ condition. The electrodes designed and fabricated under these conditions, in fact, presented a very good adaptation to the RF transmission line and were not the cause of any reasonable underperformance during the high speed characterization, as it will be discussed later in Chapter 8.

6.4.4 The final structure of the device

After all the discussions made above about the substrate, waveguide, cladding and electrodes, the final layout of our device is represented in Fig. 6.6. This configuration corresponds to a single TE mode waveguide, stressed by a SiN overlayer and with vertical electrostatic field $\boldsymbol{F}$ in the waveguide. Moreover, it optimizes all parameters for higher effective strain gradients $\widehat{\eta}$ while ensuring compatibility with our fabrication facilities and the variable t_{SiO_2} ensures a control of stress and charging effects. Three devices will be created and analysed, corresponding to 3 different SiO_2 thicknesses, $t_{SiO_2} = 0\,\mathrm{nm}$, 250 nm and 500 nm and named as Device 0, 250 and 500 respectively.

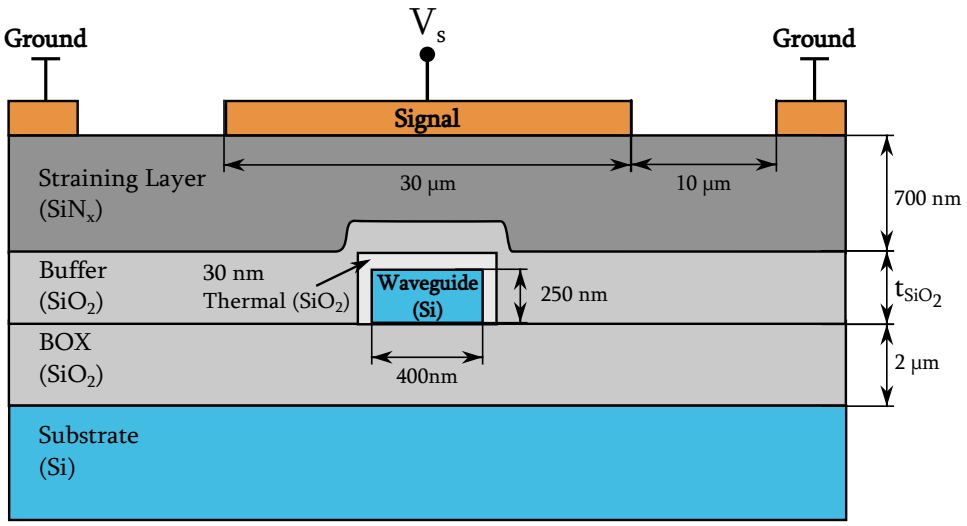

Fig. 6.6 Final layout of the device, where $t_{SiO_2} = 0$ nm, 250 nm and 500 nm.

The final electro-optic effect in the waveguide will be a combination of the plasma dispersion effect and the strain-induced Pockels effect. In order to understand what we may expect from the final Δn_{eff}, electro-optic simulations must be performed, where the optics, stress and semiconductor effects are put together. This is the subject of the next sections.

6.5 Simulation of the electro-optic effects

The plasma-dispersion effect and the strain-induced Pockels effect are both dependent on the voltage V_s applied to the electrodes. Therefore, in order to understand the physics of the real device, we must simulate the performance of the waveguide as a function of the voltage for both Δn_{eff_P} and Δn_{eff_c}. This analysis will be performed for the 3 different devices: Device 0, 250 and 500.

We start by focusing on the plasma dispersion effect and then move on to the analysis of the strain-induced Pockels effect.

6.5.1 The plasma-dispersion effect in the final device

As already referred in section 6.2, the plasma-dispersion effect corresponds to a change of refractive index due to the change of concentration of free carriers in the waveguide. The physics of the free carriers in a waveguide under an electric field was deeply discussed in Chapter 5 and here we shall present its effect on the optical Δn_{eff_c}.

Because the fixed charges Q_f in the cladding play such an important role, we shall show the effect of these on the device. We consider a TE-mode and explicitly calculate Δn_{eff_c}

from eq. 6.9 as a function of V_s applied to the central electrode. Fig. 6.7a presents the results of $\Delta n_{eff_c}(V_s)$ for different levels of interface fixed charges for Device 0. These results are comparable to those of Fig. 5.6 and are very similar to those published by Azadeh et al. in [66], showing that our results are in line with the most recent publications on the subject. It is also relevant to point out that this effect may be responsible for n_{eff} changes in the order of $\Delta n_{eff} \sim 1 \times 10^{-4}$.

Fig. 6.7a shows that for high levels of Q_f, in the vicinity of $V_s = 0\,\mathrm{V}$ there is a linear behaviour of $\Delta n_{eff_c}(V_s)$. This "linear" effect was the main reason for the early misinterpreation of the strain-induced Pockels effect in silicon waveguides [29, 31–33]. Since it is an apparent linear electro-optic effect, it was thought to be a Pockels-like effect, which is not the case because this linearity is entirely due to the fixed charges of the interface.

The comparison of the simulated plasma-dispersion effect of Devices 0, 250 and 500 is shown in Fig. 6.7b, where we have assumed $Q_f = 3 \times 10^{12}\,\mathrm{cm}^{-2}$ for Device 0 and $Q_f = 1 \times 10^{12}\,\mathrm{cm}^{-2}$ for the others. There is a clear difference in the response because of the cladding causes different shifts in the curve due to the variable Q_f at the interface. Another difference worth mentioning is the slope of the "tails" of the curve, which is smaller with increasing $t_{\mathrm{SiO_2}}$, because the same V_s, induces lower E_y in the waveguide due to the thicker SiO_2 layer.

6.5.2 The strain-induced Pockels electro-optic effect

Understanding and simulating the strain-induced Pockels effect is one of the major objectives of this work. The physics behind this effect is described in equation 6.6: the change in effective index of the mode is due to the sum of the contributions of the effective strain gradients in the waveguide. Therefore, the analysis of this effect is done mainly by studying the effective strain gradients and which components are the most relevant. Furthermore, because the sum in eq. 6.6 is weighted by the coefficients Γ, we understand why they are so important and why the theory developed in Chapter 3 is so relevant to properly understand Pockels effect in strained silicon, mainly because it provides us with a way to determine Γ so that they are not completely unknown.

Effective strain gradients and $\chi^{(2)}$ components

The explicit sum in eq. 6.6 extends to $3^6 = 729$ terms but the number of terms can be drastically lower by considering the symmetries of the problem. In the fundamental TE-mode, the most important component of the electric field is E_x. In addition to this, the electrostatic field $\boldsymbol{F}$ is vertically oriented and the only important component is F_y. Therefore,

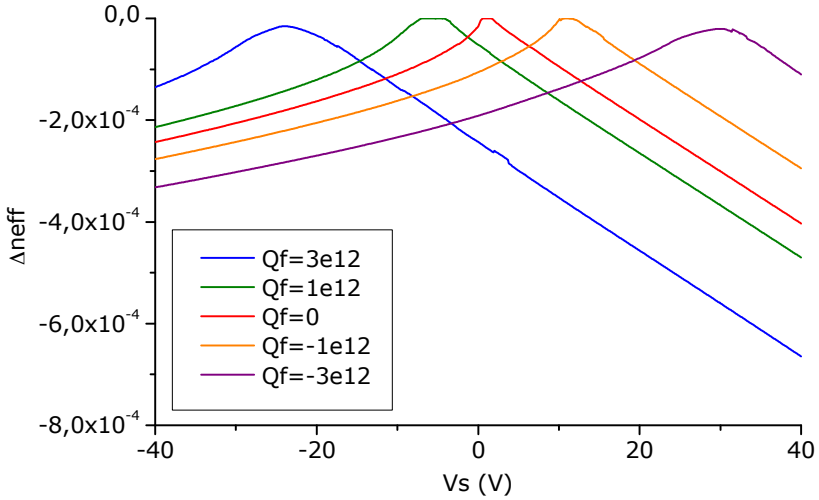

(a)

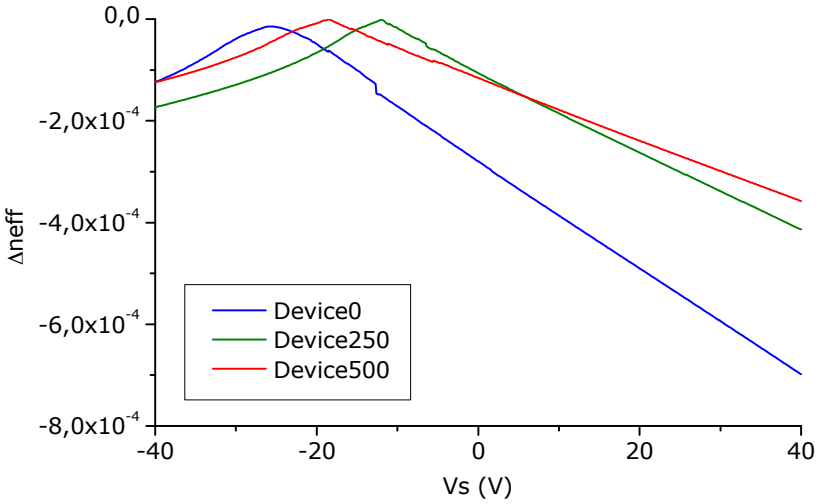

(b)

Fig. 6.7 The simulation of the Δn_{eff_c} due to the Plasma-dispersion effect as a function of the applied V_s voltage. (a) Effect of considering different values of Q_f on Device 0. (b) The response of Devices 0 (assuming $Q_f = 3 \times 10^{12}\,\mathrm{cm}^{-2}$), 250 and 500 (assuming $Q_f = 1 \times 10^{12}\,\mathrm{cm}^{-2}$).

the relevant component of the $\overline{\overline{\chi}}^{(2)}$ tensor for this problem is $\chi^{(2)}_{xxy}$ and we may concentrate only on the $\widehat{\eta^{xxy}_{ijk}}$ components of the effective gradients. This is in fact confirmed in Fig. 6.8 where we show the calculation of some selected effective strain gradients components as a function of V_s. It is clear that the components that do not contribute to $\chi^{(2)}_{xxy}$ are nearly zero.

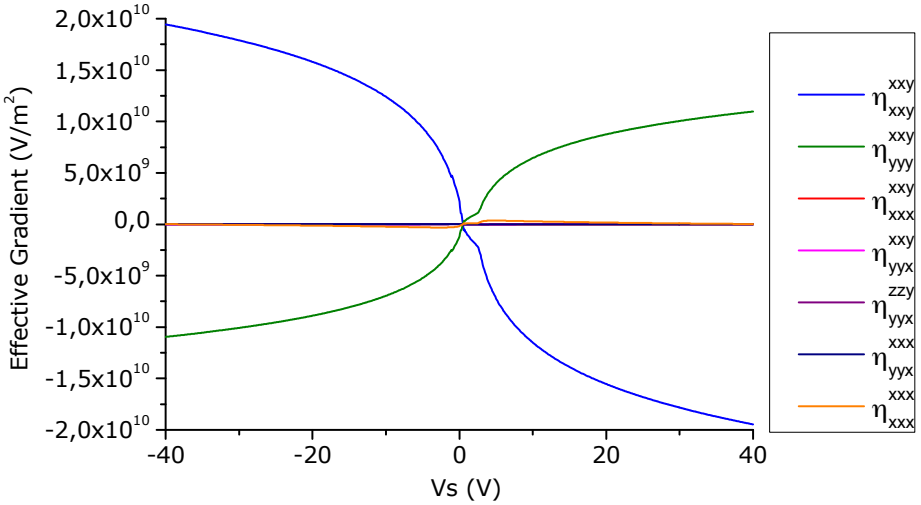

Fig. 6.8 Selected effective strain gradients components in Device 0 as a function of V_s.

The symmetries of the mode and the strain gradients can be used to restrict the number of coefficients even more. In Fig. 6.9 is represented the distribution of the principal strain gradients inside the waveguide. The shear strains (strain components ε_{ij} with $i \neq j$) are not considered because they are at least 2 orders of magnitude smaller than the principal strain components. As we can see, the η_{xxy} and η_{yyy} components are symmetric while the η_{xxx} and η_{yyx} are antisymmetric in the x direction in respect to the centre of the waveguide.

Because the E_x^2 components of the TE_0 mode are symmetric in the waveguide, the overlap integral defined in eq. 6.7 will identically vanish for the components $\widehat{\eta^{xxy}_{ijk}}$. This is also shown in Fig. 6.8, where these components are identically 0. This is not the case of the component $\widehat{\eta^{xxx}_{xxx}}$ (relating the F_x with the E_x and the η_{xxx} components) which is not zero due to the nonzero x component of the electrostatic field at the lateral borders of the waveguide (see Fig. 5.14). This effective gradient component, however, is very small compared with $\widehat{\eta^{xxy}_{xxy}}$ and $\widehat{\eta^{yyy}_{xxy}}$ and can be neglected.

From the previous analysis, we conclude that the main contributions for Δn_{eff_P} comes from $\widehat{\eta^{xxy}_{xxy}}$ and $\widehat{\eta^{xxy}_{yyy}}$ components, which have opposite signs. This is because the strain gradients have opposite signs in these two components, as we can see from the distributions in Fig. 6.9 [3]. Consequently, the Pockels effective index change can be considered to be given

[3] This agrees with the analysis made by Manganelli et al. in [69]

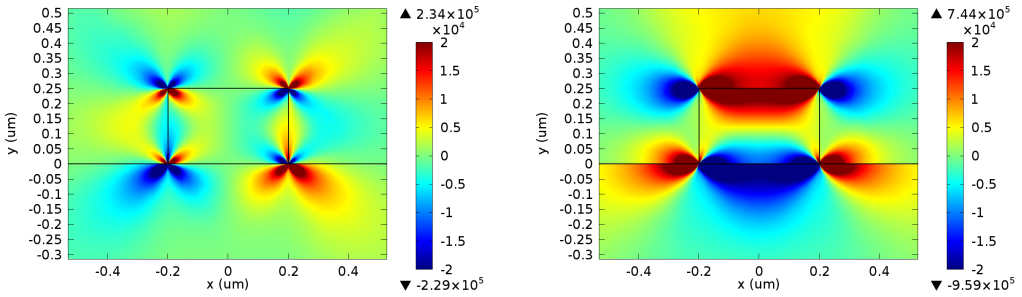

(a) η_{xxx}

(b) η_{xxy}

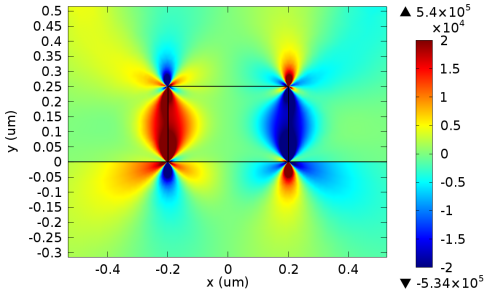

(c) η_{yyx}

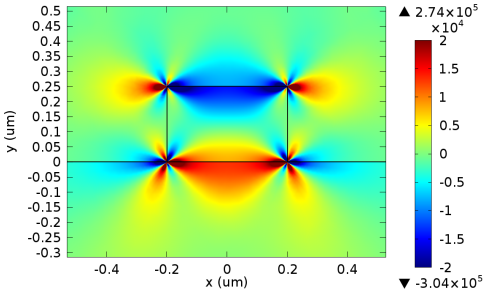

(d) η_{yyy}

Fig. 6.9 The distribution of the most relevant strain gradients components in the device in the waveguide, represented by the rectangle in the center.

by

$$\Delta n_{eff_P} \simeq \Gamma_{xxy,xxy}\widehat{\eta_{xxy}^{xxy}} + \Gamma_{xxy,yyy}\widehat{\eta_{yyy}^{xxy}} \ . \tag{6.14}$$

We now define

$$\zeta \equiv \frac{\Gamma_{xxy,xxy}}{\Gamma_{xxy,yyy}} \tag{6.15}$$

and rewrite eq. 6.14 as

$$\Delta n_{eff_P} \simeq \Gamma_{xxy,xxy}\left(\widehat{\eta_{xxy}^{xxy}} + \zeta\widehat{\eta_{yyy}^{xxy}}\right) \ . \tag{6.16}$$

The previous equation shows that, while the $\Gamma_{xxy,xxy}$ is a constant that affects the numerical value of Δn_{eff_P}, the parameter ζ will define the shape of all curves concerning Δn_{eff_P} and thus it plays a fundamental role in studying Pockels effect in strained silicon.

The effect of the ζ parameter

The parameter ζ, being a ratio between both Γ coefficients, depends only on the crystal structure. It is now that the theory developed in chapter 2 gets extremely important because

with that we can describe ζ in terms of α and β. From eq. 3.92 we see that

$$\zeta = \frac{\Gamma_{xxy,xxy}}{\Gamma_{xxy,yyy}} = \frac{5\beta - 3\alpha - (\alpha+\beta)\cos(4\varphi)}{2(\alpha - 3\beta)} \tag{6.17}$$

which means that once α and β are known, ζ is also known. However, this information is not available at the moment and the best we can do is making estimations.

In order to see how ζ affects the shape of $\Delta n_{eff_P}(V_s)$, we calculate $\widehat{\eta^{xxy}_{xxy}} + \zeta\widehat{\eta^{xxy}_{yyy}}$ for different values of ζ. We do this by also considering two different fixed charge values, $Q_f = 0$ and $Q_f = 3\times10^{12}\,\mathrm{cm}^{-2}$, which will change the free carriers distribution and thus affect the electric field $\boldsymbol{F}$ that intervenes in the effective gradients. The results are shown in Fig. 6.10, for Device 0. As we can see, different values of ζ change completely the shape of the curve $\Delta n_{eff_P}(V_s)$. This means that without knowing the real value of ζ (or equivalently α and β) we are not able to predict which is the shape of $\Delta n_{eff_P}(V_s)$.

Moreover, Fig. 6.10 provides us with important information, regardless of the ζ value. It is clear that the relation between Δn_{eff_P} and V_s is highly nonlinear and the linearity depends strongly on ζ and Q_f. Also, we see that the sign of Δn_{eff_P} changes at a specific $V_s = V_0$, corresponding to the inversion of carriers inside the waveguide, where there is a shift on the direction of F_y in the waveguide. As expected, V_0 depends strongly on Q_f. Finally, we see that the $\Delta n_{eff_P}/\Delta V_s$ ratio (or more correctly given by the derivative $\frac{\partial n_{eff_P}}{\partial V_s}$), which determines how much the effective index changes by a voltage variation, is higher around V_0. Therefore, ideally, in order to achieve higher Pockels modulation, the operating voltage of the device should be close to V_0, where the n_{eff} change is more efficient. Away from this point the curve is very flat and $\Delta n_{eff_P}/\Delta V_s$ ratio is very small.

Effect of the cladding

The effect of the cladding on both $\widehat{\eta^{xxy}_{xxy}}$ and $\widehat{\eta^{xxy}_{yyy}}$ is shown in Fig. 6.11. Once again, there is a shifting voltage V_0 where the effective strain gradients undergo a sign change. More importantly, we clearly see the difference caused by the cladding, due to reduction of both the F_y and stress in the waveguide which not only changes the intensity of the effect but also the shape of the curves. For this reason we may expect a stronger effect in Device 0 rather than in Devices 250 and 500.

The order of magnitude

In the previous discussion we have not discussed yet on how much Δn_{eff} we might expect to be due to Pockels effect. From equation 6.16, we know that the numerical value of Δn_{eff_P}

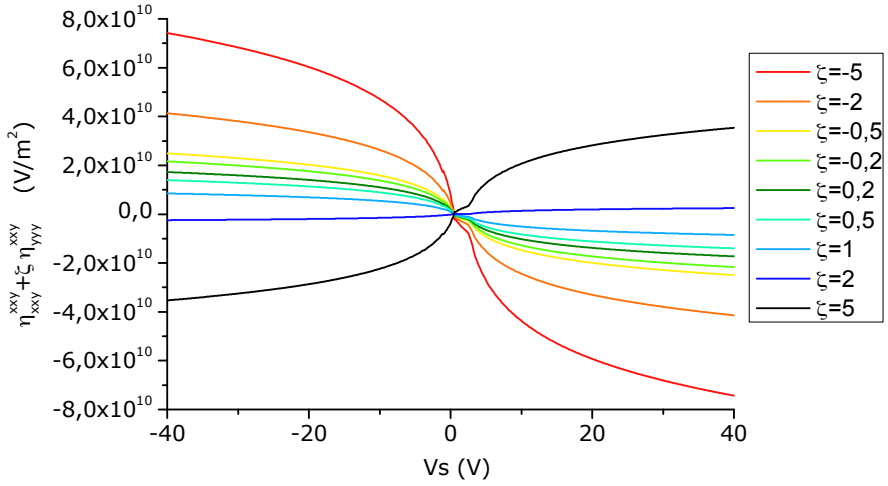

(a) $Q_f = 0$.

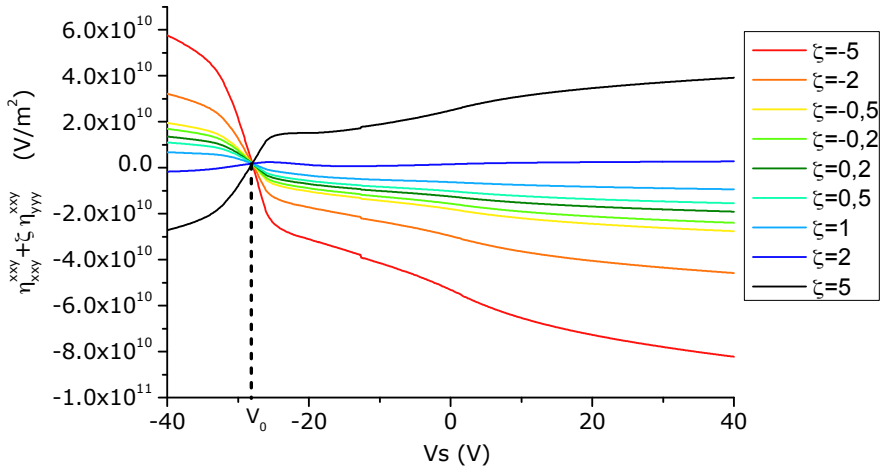

(b) $Q_f = 3 \times 10^{12}\,\mathrm{cm}^{-2}$.

Fig. 6.10 The curve $\widehat{\eta^{xxy}_{xxy}} + \zeta\,\widehat{\eta^{xxy}_{yyy}}$ for different values of ζ in Device 0.

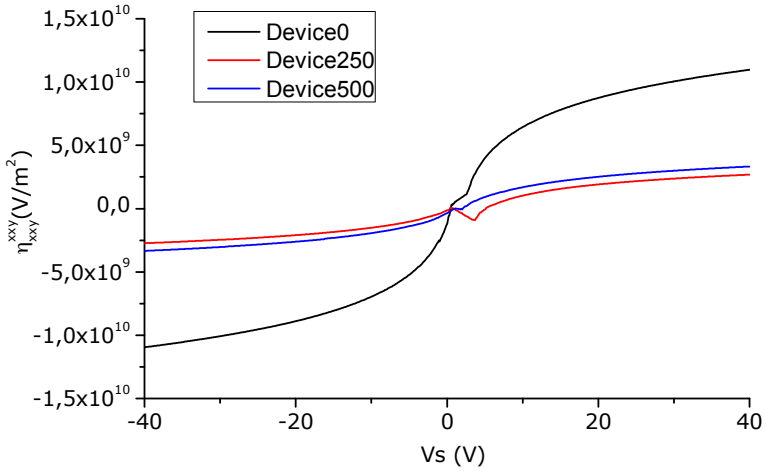

(a) $Q_f = 0$.

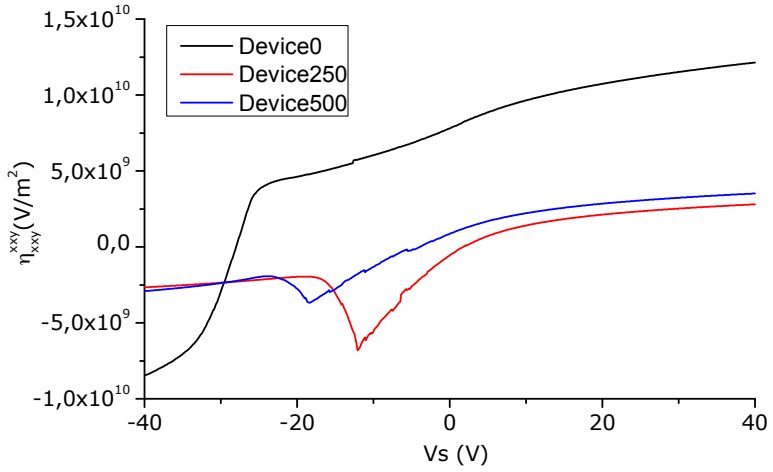

(b) $Q_f = 3 \times 10^{12}\,\mathrm{cm}^{-2}$.

Fig. 6.11 The curves $\widehat{\eta^{xxy}_{xxy}}$ as a function of the voltage for the three Devices 0, 250 and 500.

depends on the value of $\Gamma_{xxy,xxy}$ which in eq. 3.100 we have estimated to be on the order of magnitude $\Gamma_{xxy,xxy} \sim 1 \times 10^{-16}\,\mathrm{m}^2/\mathrm{V}$.

With this estimation, eq. 6.16 reads:

$$\Delta n_{eff_P} \sim 1 \times 10^{-16}\,\mathrm{m}^2/\mathrm{V}\left(\widehat{\eta_{xxy}^{xxy}} + \zeta\widehat{\eta_{yyy}^{xxy}}\right) \tag{6.18}$$

From the graphs in Fig. 6.10b we see that, depending on the value of ζ, under a voltage change $\Delta V_s = 10\,\mathrm{V}$, the corresponding variation in $\widehat{\eta_{xxy}^{xxy}} + \zeta\widehat{\eta_{yyy}^{xxy}}$ is between $1 \times 10^9\,\mathrm{V/m}^2$ and $1 \times 10^{10}\,\mathrm{V/m}^2$. Therefore, we may estimate the strain-induced Pockels to be

$$\Delta n_{eff_P} \sim 1 \times 10^{-7} \text{ to } 1 \times 10^{-6}\,, \quad \text{under } 10\,\mathrm{V}\,. \tag{6.19}$$

This is merely an estimation, which depend strongly on the very rough numerical analysis made in section 3.5.3, however it is the only estimative we have thus far. Nevertheless, any prediction results in a Pockels effect clearly smaller than what one can expect from the plasma-dispersion effect shown in Fig. 6.7. For this reason, we expect Pockels effect to act as a perturbation to $\Delta n_{eff_c}(V_s)$ and to be "hidden" in the overall $\Delta n_{eff}(V_s)$ curve.

6.5.3 The contribution from the angles

As referred in Section 6.3 one of the characteristics that distinguishes the plasma-dispersion and Pockels effects is the intrinsic dependence in crystal orientation of the latter. This is shown in eq. 6.14 because of the direct dependence of $\Gamma_{xxy,xxy}$ on the crystallographic angle φ, given by (see eq. 3.92)

$$\Gamma_{xxy,xxy}(\varphi) = \frac{d^6 K}{27\epsilon_0}\left[(5\beta - 3\alpha - (\alpha+\beta)\cos(4\varphi))\right]\,. \tag{6.20}$$

The dependence of $\widehat{\eta_{xxy}^{xxy}}$ on the crystallograhic orientation φ is plotted in Fig. 6.12. From this figure and equation 6.20 we have:

$$\Gamma_{xxy,xxy}(0) = \frac{d^6 K}{27\epsilon_0}(6\beta - 2\alpha)\,, \quad \text{in the [010] direction} \tag{6.21}$$

$$\Gamma_{xxy,xxy}\left(\frac{\pi}{4}\right) = \frac{d^6 K}{27\epsilon_0} 4(\beta - \alpha)\,, \quad \text{in the [110] direction}\,, \tag{6.22}$$

corresponding to a variation

$$\Delta\Gamma_{xxy,xxy} = \frac{d^6 K}{27\epsilon_0} 2(\beta + \alpha)\,. \tag{6.23}$$

Of course, this analysis only has numerical meaning if we know both α and β, but we may expect $\widehat{\eta}^{xxy}_{xxy}$ to change considerably when we change the angle orientation of the waveguide.

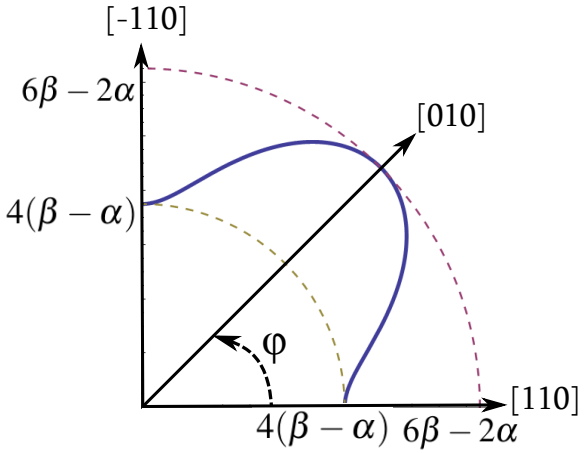

Fig. 6.12 The dependence of $\Gamma_{xxy,xxy}$ on the angle orientation in the silicon wafer. The angle φ is represented and the values are in units of $\frac{d^6k}{27\epsilon_0}$.

In equation eq. 6.14 we have assumed that the effective gradients $\widehat{\eta}$ do not depend on φ. In a detailed analysis, there is a slight dependence of n_{eff} on the angle orientation through the photoelastic effect. In this effect, n_{Si} is changed due to the stress applied to the crystal. Since the photoelastic coefficients depend on the crystal orientation [91], it means that the optical mode and n_{eff} depends on φ. Therefore, $\widehat{\eta}$ will depend on φ because the mode is slightly changed by the photoelastic effect.

However, this change is very small, as reported by Huang et al. in [91] who detected variations of only around 20% from $\varphi = 0^o$ to $\varphi = 45^o$ of the total photoelastic effect and we calculated this to correspond to $\Delta n_{eff} \sim 0.01$. This corresponds to a very small change of the propagation mode which should not influence the detected electro-optic effect. On the other hand, the coefficients Γ should have a high dependence on the crystal orientation, because the tensor components dependence on referential rotations typically change on the order of tens percent [204].

Finally, we shall attempt an illustration on how φ may affect the $\Delta n_{eff_P}(V_s)$ curve. However, this is only possible by making some assumptions for α and β and we shall do so for the sake of exemplifying the situation. For that reason, we recover the results from in eq. 3.97 where we have estimated that

$$\alpha \sim -\frac{1-\gamma}{2}\beta = 0.22\beta \, . \tag{6.24}$$

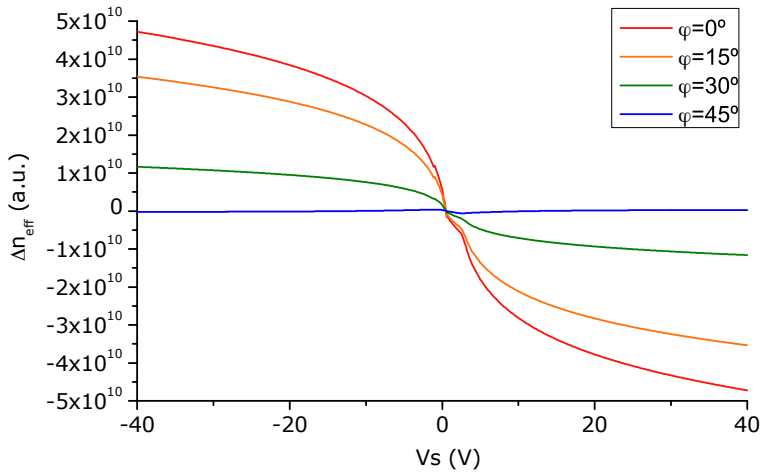

(a) $Q_f = 0$

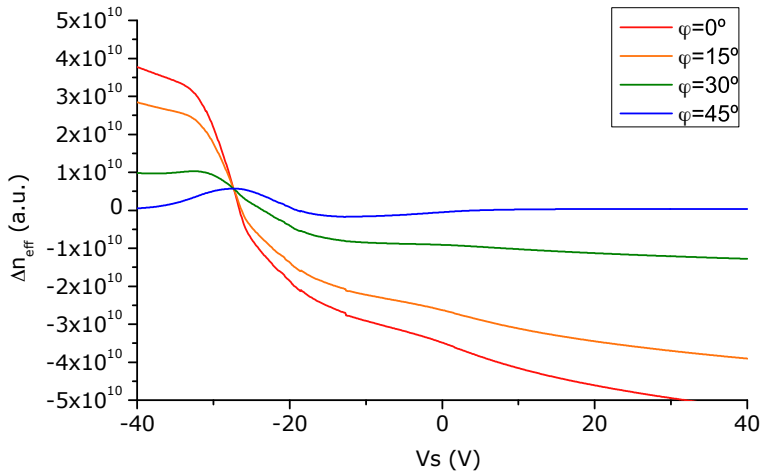

(b) $Q_f = 3 \times 10^{12}\,\mathrm{cm}^{-2}$

Fig. 6.13 The effect of the angle orientation on Δn_{eff_P} when assuming $\alpha = 0.22\beta$.

In this very particular case, Δn_{eff_P} becomes

$$\Delta n_{eff_P} = \frac{d^6 k}{27\epsilon_0}\beta\left(\left[4.34 - 1.22\cos(4\varphi)\right]\widehat{\eta_{xxy}^{xxy}} + 5.56\widehat{\eta_{yyy}^{xxy}}\right) \tag{6.25}$$

which allows us to plot the curves presented in Fig. 6.13, which show $\Delta n_{eff_P}(V_s)$ for different φ in Device 0, for the cases with and without fixed charges. By using this estimation for α and β (and we must stress the fact that this is merely an estimation, made only for the sake of allow the evaluation of the previous expressions), Fig. 6.13 shows that Δn_{eff_P} may change enormously if light propagates in different crystallographic directions of the silicon

wafer. This is the reason why we may expect to detect a change in modulation efficiency by considering different angle orientations of the waveguide.

6.6 Final Remarks

In this chapter we have put the photonics together with the semiconductor and stress effects inside the waveguide to describe and study the different electro-optic effects occurring when an electrostatic field is applied to a strained silicon waveguide.

The study of both plasma-dispersion and Pockels effects was done by simulating Δn_{eff} as a function of the applied voltage. From the several results presented we concluded that the final Pockels effect will mainly depend on the combination of two effective strain gradients: $\widehat{\eta_{xxy}^{xxy}}$ and $\widehat{\eta_{yyy}^{xxy}}$. However, the contribution of each of these depends entirely on the parameters α and β which are not entirely known and we can only make estimations of the possible outcomes. This limits our possible understanding of the problem because different combinations of α and β change completely both the $\Delta n_{eff_P} V_s$ and the angle dependence of the Pockels effect. In Chapter 8 we will compare the analysis made in this chapter with the experimental results to find an estimation of $\chi^{(2)}$ in strained silicon waveguides.

Finally, it is important to stress that the final Δn_{eff} will be the sum of the contributions from both Pockels and plasma-dispersion effects. Because the latter is expected to be stronger than the former, we also expect that the Pockels effect to be somehow "hidden" inside the Δn_{eff_c} curve which may make it very difficult to identify, as we will shall see in Chapter 8. For this reason, the crystal orientation and high speed characteristics of Pockels effect will be crucial for a better identification of this effect.

Chapter 7

Chip-design and fabrication

The discussion made so far was concentrated on the physical phenomena taking place in strain-induced Pockels effect in silicon. We have presented not only the physics of the processes, but also the design of the device for optimal Pockels effect and the simulations of the possible electro-optic outcomes of that device.

Now we focus on bringing all this into a real device to be characterized. In this chapter we concentrate on designing the real optoelectronic devices to measure strain induced Pockels effect in silicon waveguides. We start by presenting the possible ways of making the electro-optic characterization of such effect. Then we present the design of the chip that will allow us to measure $\Delta n_{eff}(V_s)$.

Finally we describe the fabrication process flow we adopted for the implementation of all the devices, focusing on the different approaches and techniques we used.

7.1 The Mach-Zehnder Interferometer

As we referred in the introduction of this thesis, an interferometer or resonator is required to convert a phase shift into an intensity output variation. There are numerous possibilities to achieve this in photonics, but the most commonly used for this purpose in silicon integrated circuits are Ring Resonators [205, 206] and Mach-Zehnder Interferometers (MZI). The decision to use one instead of the other was carefully examined and finally we opted to use the Mach-Zehnder Interferometers for mainly two reasons:

- **Fabrication reproducibility:** Because the Ring Resonators have so sharp resonances and the transmission spectrum depends so strongly on the coupling conditions, the fabrication reproducibility is harder than in a MZI. Any small difference occurring during the fabrication may have strong effects on the transmission spectrum, which

can be a problem when we want to reproduce, replicate and compare results between different chips fabricated in different times. This problem is not as important in the case of MZI's not only because the resonances are wider, but also because the device is not as sensitive to fabrication conditions.

- **Measurement of the crystal orientation:** Because in the MZI the light propagates in a straight line, we can orientate the MZI arms in the crystallographic direction of our choice and thus measure and compare the effects of the crystal orientation on Δn_{eff}. In the Ring Resonators, however, because there is no preferable crystal orientation in the circular ring, it is not easy to measure the $\chi^{(2)}$ dependence on the crystallographic direction.

Since the MZI play such a fundamental role in our structure, next we analyse its working principle and the most important metrics.

The Mach-Zehnder Interferometer

The Mach-Zehnder Interferometer (MZI) is one of the most commonly use interferometers for light modulation in silicon photonics. Its working principle is very simple to understand: light is guided into two different waveguides (or arms), with lengths L_1 and L_2, which are then merged together to create interference. The light travelling in arms 1 and 2 undergo phase shifts ϕ_1 and ϕ_2, respectively, after travelling through the corresponding paths. If the total phase difference between the light in both arms is given by $\Delta\phi = \phi_1 - \phi_2$, then it can be shown that the output intensity (I_{out}) of a MZI as a function of the input intensity (I_{in}) is given by:

$$I_{out} = I_{in} \cos\left(\frac{\Delta\phi}{2}\right)^2 . \tag{7.1}$$

The previous equation shows that a phase shift induced by an electro-refraction (or any other refraction effect), will make a variation in the intensity of the light output.

When the two arms have different lengths, i.e. $L_1 = L_2 + \Delta L$, as the one shown in Fig. 7.1a, the device is called an *asymmetric* MZI. In that case, in a passive regime $\phi_1 \neq \phi_2$ and interference takes place. This leads to the typical transmission spectrum shown in Fig. 7.1b. In this thesis concentrated in this kind of MZI because the resonances facilitate the characterization process, even though they are not commonly used for light modulation purposes.

The distance between two neighbour resonances is called *Free Spectral Range* (FSR) and it depends on ΔL through:

$$\mathrm{FSR} = \frac{\lambda_r^2}{\Delta L \cdot n_g} , \tag{7.2}$$

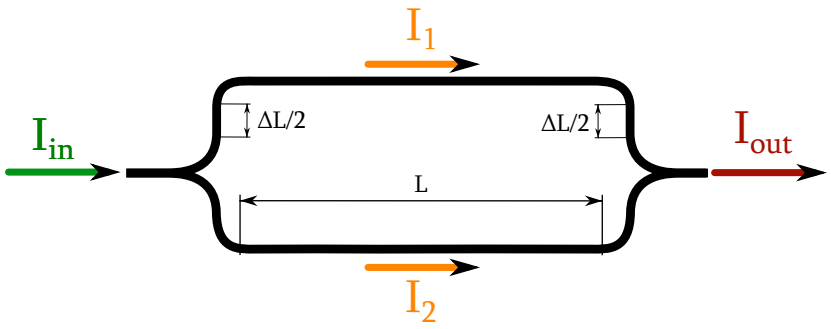

(a) MZI structure.

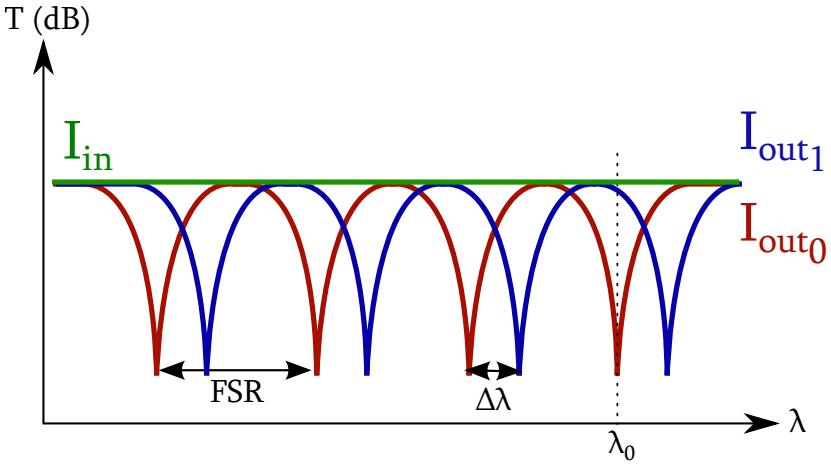

(b) MZI transmission spectra.

Fig. 7.1 (a) Typical structure of a Mach-Zehnder Interferometer with the corresponding lengths. (b) Typical transmission spectrum of an asymmetric MZI. An electro-refraction effect induces a shift in the spectra, changing the intensity output. I_{out_0} and I_{out_1} corresponds no transmission and full transmission respectively.

where n_g is the group index of the waveguide defined by

$$n_g = n_{eff} - \lambda \frac{dn_{eff}}{d\lambda} \tag{7.3}$$

and it describes the group velocity $v_g = \frac{c}{n_g}$ of the light in the waveguide [205].

By applying an electro-refraction effect to one of the arms, the induced Δn_{eff} changes the phase shift $\Delta\phi$, modifying the interference conditions, leading to a shift $\Delta\lambda$ in the transmission spectrum, as shown in Fig. 7.1b. This is schematically shown in Fig. 7.1b and this is the way to modulate light by using a MZI at fixed λ. The bigger $\Delta\lambda$, the higher intensity output change is detected. It can be shown that the spectral shift $\Delta\lambda$, at a given resonance wavelength λ_r, is related to Δn_{eff} by

$$\Delta n_{eff}(\lambda_r) = \frac{\lambda_r \cdot \Delta\lambda_r}{\mathrm{FSR} \cdot L}\,, \tag{7.4}$$

where $\Delta\lambda_r$ and L is the length of the arm where the electro-refraction effect is applied.

The previous equation shows that in order to obtain higher $\Delta\lambda$, for fixed Δn_{eff}, we may increase L. This property is very useful because when the electro-refraction effect is very weak, i.e. Δn_{eff} very small, we can increase the length of the MZI in order to create a bigger $\Delta\lambda_r$ and detect the spectral change more easily. Of course this has other disadvantages, such as increasing the footprint of the device or the losses of the RF signal propagating in the electrodes. Nevertheless, this is a crucial feature if we are concerned about studying a small effect like the strain-induced Pockels effect.

7.2 Design of the chip

The design of the devices has to be made taking into account the characterization method. Consequently, we must take into consideration different details: the coupling of light from an external source into the device, the application of the modulating electrostatic field, the measurement of the crystal orientation and the propagation of light inside the whole device. The complete device from the light input until the light output is shown in Fig.7.2.

We decided to couple the light into or off a chip directly to its edge, as represented in Fig. 7.3a, because we can couple any wavelength and any polarization, which is not the case with other methods like grating couplers [11]. In this coupling mechanism, the mode in the waveguide is expanded to have a better match with the mode in the lensed optical fibre. The easiest approach to accomplish this is adiabatic tapering. By slowly expanding the size of the waveguide core, light will stay in the guided fundamental mode and the size can

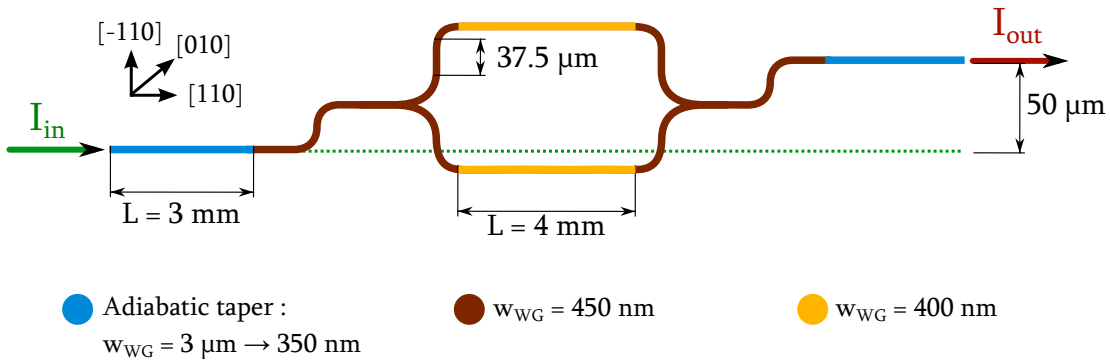

Fig. 7.2 Layout of the complete optical device which includes a MZI for characterization.

be expanded until it matches that of the lensed fibre. In our device we adopt the *in-plane adabatic taper*, where the silicon core is slowly widen in the plane of the chip, which can be easily lithography defined. This is schematically shown in Fig. 7.3b and as a rule of thumb, for good adaptation and low coupling losses from a wide to a narrow waveguide, the taper angle θ should satisfy [207]

$$\theta < \frac{\lambda}{2w_{WG_{max}}n_{eff}} \sim 2^\circ \,. \tag{7.5}$$

The input and output tapers are represented in blue in Fig. 7.2 and we used $w_{WG_{max}} = 3\,\mu$m.

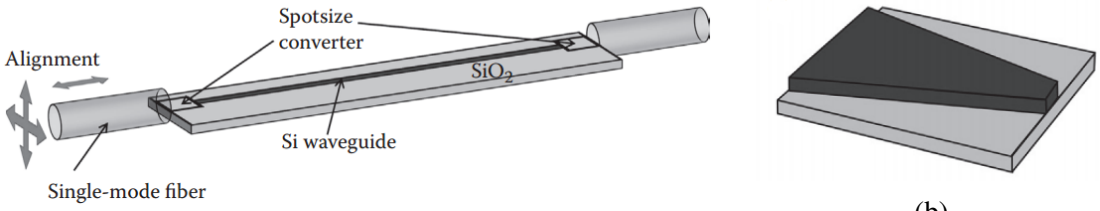

Fig. 7.3 (a) Schematic representation of the edge coupling from a chip to an optical fiber. (b) Example of an adiabatic in-plane taper. Figures taken from [11].

The light from the optical fibre may excite many optical modes in the initial 3 μm-wide taper because this dimension is compatible with multiple order modes. The final width of the taper is 350 nm, which is a single-mode waveguide and it ensures that the only propagating mode after this point of the line is the TE fundamental mode.

After this mode filtering, a small taper (100 μm long) increases the waveguide width until 450 nm because it has a higher confinement of light inside the core, for lower bending losses. The function of the "S-Curve" shown in brown in Fig. 7.2 after the blue taper, is to misalign the output with the input and ensure that the light coming from the input fibre is not

collected by the photodetector at the output. We placed two of these, resulting in a 50 μm distance between the input and the output, as shown in the same figure.

The "S-Curve" leads to the Mach-Zehnder Interferometer, which starts with a light splitter. There are different options for splitting light into two different channels and the most general beam splitters are the *Star Coupler* and Multimode Interference (MMI) splitters [208, 209]. The most important condition for the splitter is that it is equilibrated, i.e. it separates light equally into the two MZI arms and ensure that $I_1 = I_2 = I_{in}/2$, which is required for eq. 7.1 to be valid. Even though MMI splitters are more stable and consistent for this job, which may reduce the losses and improve the quality of light splitting, in this work we worked entirely with star coupler splitters, as shown in the MZI represented in Fig. 7.2 (see Fig. 7.14b for a closer view of the actual fabricated splitter).

The splitter is connected to two 90º waveguide bends with curvature radius of 100 μm, which is enough for low losses in a single-mode silicon waveguide. The difference between the top and bottom arms is the short waveguide with length $\Delta L/2 = 37.5\,\mu$m. This results in a $\Delta L = 75\,\mu$m, which defines the FSR through eq. 7.2.

After the second 90º bend, there is another small taper to the waveguide with $w_{WG} =$ 400 nm, the characteristics discussed in section 6.4.1. This is the waveguide which will be studied, to which we will apply the electrostatic field and its length is chosen to be $L = 4$ mm, which is long enough to see small shifts.

This waveguide is then connected to the output of the MZI which has the same properties as the input, making it a symmetric line.

In order to study the effect of the crystal orientation on the modulation, we designed the layout shown in Fig. 7.4. This type of layout ensures that only the MZI arms are changed by the angle orientation φ and *everything else* is kept constant which allows a direct comparison of the results between samples.

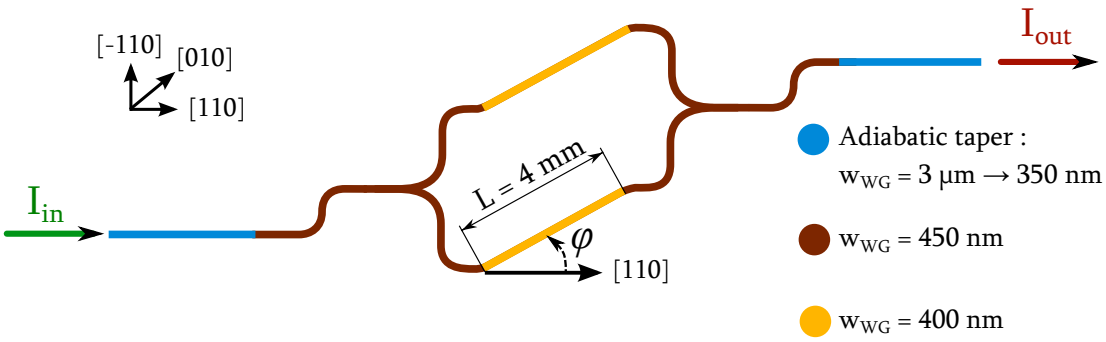

Fig. 7.4 Layout of the complete optical line when an angle rotation is included.

7.2.1 Final chip

The optical lines described above and represented in Figs. 7.2 and 7.4 involve a MZI that not only is more lossy than a straight waveguide, but the transmission of light depends on the wavelength. To facilitate the coupling and alignment, besides each MZI optical line and just 250 μm away from line input, we placed an waveguide similar to those described above, with the same $w_{WG} = 400$ nm as the arms of the MZI (see Fig. 7.5). This waveguide has higher output intensity than the MZI because there is no splitting of light, which is always associated with some losses, and the transmission spectrum is flat, which makes it easier to detect light. Once the light is coupled into this reference waveguide, it is easier to couple the light to the nearest MZI by moving the entire chip.

We decided to study 3 different angles: 0°, 15° and 30°, which ensures 3 different crystallographic directions. In addition, we chose to use two identical devices for the angles 0° and 30°, to decrease the possible degree of uncertainty in the results upon measurement. As referred before, Pockels effect is a very weak effect and by replicating two devices in the same chip, we are able to decrease the uncertainty from some defects for both 0º and 30º and thus increase the precision for detecting a precise difference between the measurements of these 2 devices.

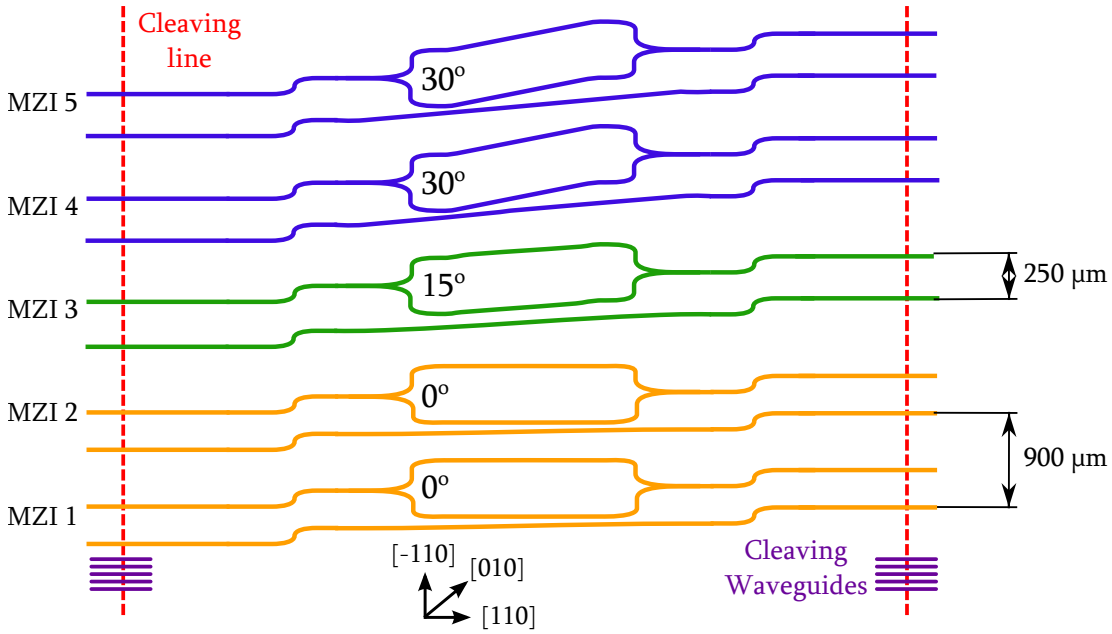

Fig. 7.5 The schematic representation of the Top-view of the chip with the corresponding angle φ in each MZI.

The final chip will consist of five devices as shown in Fig. 7.5. As stated in the previous chapter, we are interested in studying 3 different t_{SiO_2} and therefore, we fabricated different

chips like that of Fig. 7.5, with different SiO_2 cladding thicknesses: 0 nm, 250 nm and 500 nm.

7.3 The Fabrication of the samples

The fabrication of every structure described in this chapter (and manuscript in general) was performed in the Centrale Technologique Universitaire (CTU), which is the *Clean Room* facility attached to the IEF institute. This clean room has a wide range of different equipments and technologies for different platforms and materials. All the fabrication steps and procedures were performed under the supervision of Xavier Le Roux, the engineer responsible for the fabrication of devices in our team.

In this section we will describe in detail the fabrication process flow of the devices. The processes used in each stage were either developed specifically for this work (in which case we shall specifically describe) or were based on previously developed processes, which were already well established by the time this research project started. For simplicity, we will separate the fabrication description in two parts: the development of the waveguide and the deposition of the cladding and electrodes on top.

7.3.1 Fabrication of the waveguide

The fabrication process flow of the waveguides is shown in Fig. 7.6 and below we make a detailed description.

Resist spinning and e-beam lithography of waveguide

The process flow in Fig. 7.6 starts with the unprocessed, original SOI stack, with 2 µm-thick BOX and 260 nm-thick top silicon. The waveguides are defined using *e-beam lithography* which is a nanofabrication technique where a focused beam of electrons is used to draw custom shapes on a surface covered with an electron-sensitive film called *electronic resist* [210]. This resist consists of chains of polymers sensitive to electrons, enabling the selective removal of either the exposed (in a *positive resist*) or non-exposed (in a *negative resist*) regions of the resist by immersing it in a solvent, the *developer*.

In the established procedure for fabricating waveguides in SOI used in our facilities, the used resist is ZEP-520, which is a high performance positive e-beam resist which shows high resolution, high sensitivity, high fluidity and high dry etch resistance [211]. The deposition of the resist on the SOI structure is done by *spin coating* at rotation speed of 6000 rpm, leading

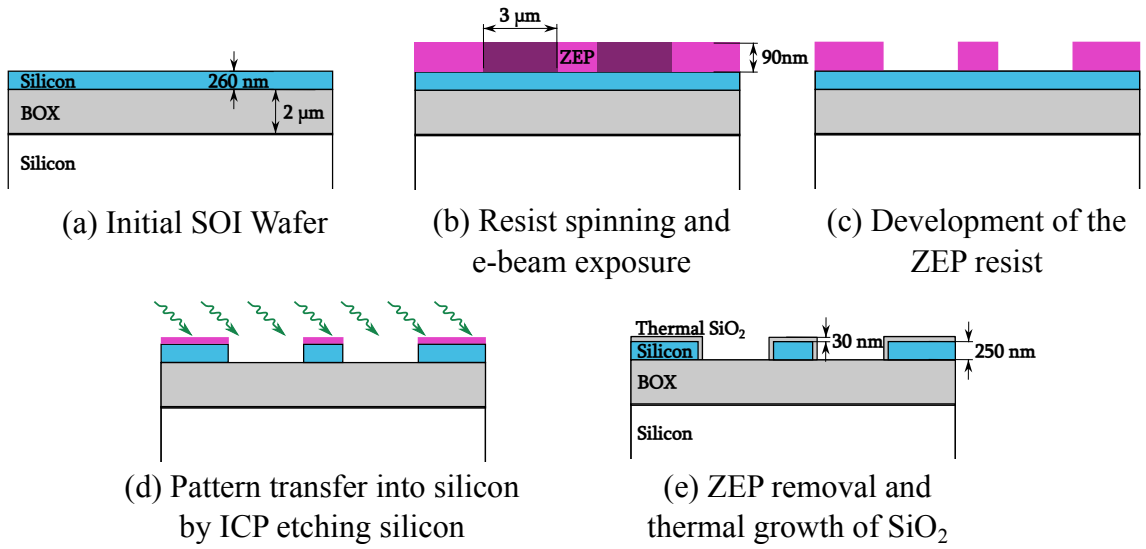

(a) Initial SOI Wafer

(b) Resist spinning and e-beam exposure

(c) Development of the ZEP resist

(d) Pattern transfer into silicon by ICP etching silicon

(e) ZEP removal and thermal growth of SiO_2

Fig. 7.6 The process flow for creating the silicon waveguide, surrounded by the oxidation layer.

to a ZEP thickness of 90 nm (see Fig. 7.6b). The resist is then baked at 170 °C for 2 min for hardening purposes.

The electronic-lithography is a very complex process which depends on many parameters and here we only focus on the most relevant. The e-beam lithography system we used was the "Nanobeam Ltd. NB4" available in the CTU. This system has an accelerating voltage of 80 kV and a maximal resolution of 2 nm. The current of the electron beam is set to 1.8 nA, value at which the system is calibrated for higher precision. The dose, i.e. the charge per unit area in the resist, is a critical parameter which has high influence on the definition of structures. We used a dose of 2.9 because previous studies in CTU concluded that this was the optimal dose for such type of nanostructures [212].

The pattern to be drawn in the e-beam lithography is defined in a GDS file, which is read by the NB4 system software. The exposure region is divided into writing fields, the *main-fields*, which are then divided into *sub-fields*. In a main field region, the substrate is fixed and the e-beam is deflected by a magnetic coil to write the patterns defined in it [210], before moving into another main-field. The dimension of the main-fields can be adjusted and we used $300 \times 300\ \mu m^2$, which was optimal for high definition while avoiding any stitching errors. When defining the GDS file for the structure in Fig. 7.5, we ensured that the MZI splitter, the most critical feature of our design, was centred in a main field region to prevent additional movements of the substrate during the writing of the splitter. In addition, all the MZI were separated by 900 μm in the vertical direction so that there was a main field periodicity in the chip among the MZI. To go from on sub-field to the other, the electron beam

is deflected using a second coil and it was chosen to be $10 \times 10\ \mu m^2$, which allows us to fit the lateral dimension of the waveguides in a single subfield and improve the homogeneity of the lithography.

Since ZEP is a positive resist, we define the waveguide by exposing the region besides it, wide enough for the optical mode to be isolated. This pad region is chosen to be $3\ \mu m$ wide, which is enough to isolate the mode in the waveguide, as shown in Fig. 7.6b.

Finally, after exposure, the resist is developed using the developer ZED-N50 for 40 s and then a mixture of MIBK and IPA (Isopropyl Acid) for 30 s. The final result is schematically shown in Fig. 7.6c.

Waveguide ICP etching and thermal oxidation

The waveguides are defined by etching the silicon thin film in the pad region. This is a critical step in the fabrication because for high performance and low loss waveguides, very high verticality and low roughness of the waveguide side walls are required. The established etching procedure in our group for high quality waveguides, developed in previous research works [212], uses the Inductively Coupled Plasma (ICP) ion etching, with the system ICP-STS available in CTU.

This is a dry-etching process, where a plasma is generated using the SF_6 and C_4F_8 gases which react with the silicon surface. While the former gas etches the silicon material, the latter reacts with the surface contributing for a passivation of the walls, improving their aspect ratio and verticality [212, 213]. In this method the silicon etching speed is very high and 19 s is enough to etch the corresponding 260 nm Si film. The process is also very selective and it stops naturally once all Si is consumed, not attacking the BOX layer (Fig. 7.6d). The remaining ZEP resist is removed by a H_2SO_4 + H_2O_2 (3:1) solution. The result is a strip waveguide and the Scanning Electron Microscopy (SEM) picture of its cross-section is shown in Fig. 7.7.

As referred in Chapter 5, we intend to create an oxide layer around the silicon waveguide to prevent the free carriers to move freely into the cladding. This is achieved by thermal oxidation of the silicon surface, which is a way to produce a thin layer of crystalline SiO_2 on the surface of silicon. In addition, it reduces the waveguide wall roughness and results in lower propagation losses. This technique forces an oxidizing agent to diffuse into the wafer at high temperature and react with it [11].

In order to grow $\sim$30 nm of thermal SiO_2, the patternized SOI substrate was put in a O_2 environment at 1000 °C for 1 hour. The final thickness of thermal SiO_2 was measured by optical ellipsometry and the result was 25 nm. For every 10 nm of SiO_2 thickness grown,

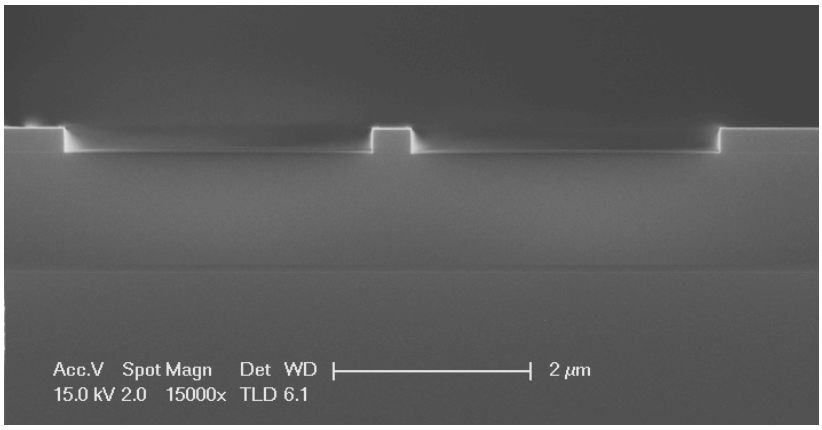

Fig. 7.7 The SEM picture of the waveguide cross-section after the ICP etching.

around 5 nm of Si crystal is consumed, therefore this results in a final $t_{WG} \simeq 250\,\text{nm}$, as represented in Fig. 7.6e.

7.3.2 Deposition of cladding and structuring of the electrodes

Once the waveguide is defined, corresponding to step (e) of Fig. 7.6, the cladding can be deposited, followed by the definition of the electrodes. The process flow for these fabrication processes is shown in Fig. 7.8 and below we describe the details of each step.

PECVD deposition of the cladding

The PECVD deposition process was performed in CTU by using the system PECVD-STS and its working principles were deeply described in section 4.2.1 and all the details on the PECVD deposition process, can be found in that section.

In devices Device 250 and 500, before the SiN stress layer, a SiO_2 thin film with the corresponding t_{SiO_2} must be deposited. This is also done by PECVD with the interaction of the N_2O and SiH_4. We used a standard recipe developed in CTU in previous research projects using a low frequency regime, whose deposition parameters are presented in Table 7.1. The SiO_2 deposition rate associated with this recipe is 67.7 nm/min. This process was done on Devices 250 and 500, for 3 min:20 s and 7 min respectively. The result is an amorphous SiO_2 thin film characterized with $n_{SiO_2} = 1.467$ and an internal stress $\sigma_0 = -500\,\text{MPa}$, measured in the same way described in Section 4.3.3 for the SiN thin film. The cross-section of the resulting structure is represented in Fig. 7.8a.

The SiN deposition was already described in section 4.2.1 and the deposition parameters of the recipe developed by us for high stress effects are rewritten in Table 7.1. The a−SiN:H film deposited in this way has a typical deposition rate of $\sim$15 nm/min and is characterized

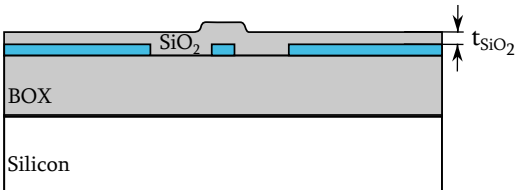

(a) PECVD deposition of SiO_2

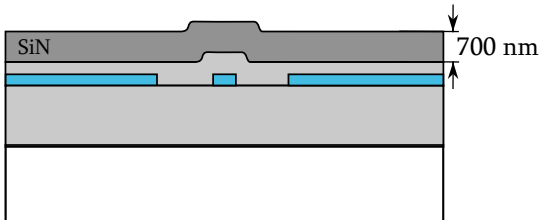

(b) PECVD deposition of SiN

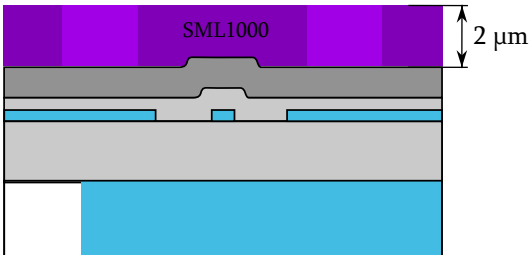

(c) Resist spinning and e-beam insulation

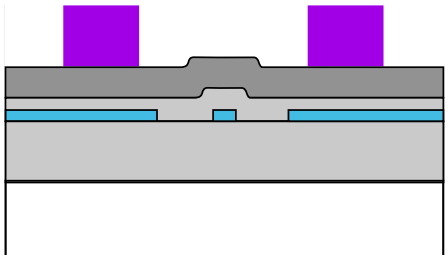

(d) Devolpment of the SML-1000 resist

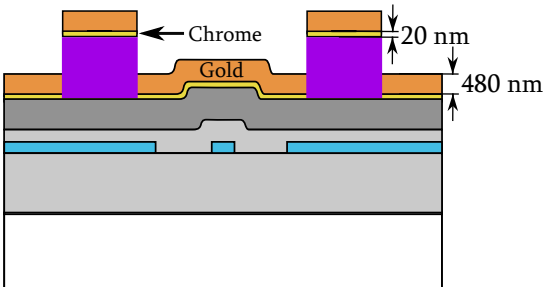

(e) Deposition of Chrome and Gold by e-beam evaporation

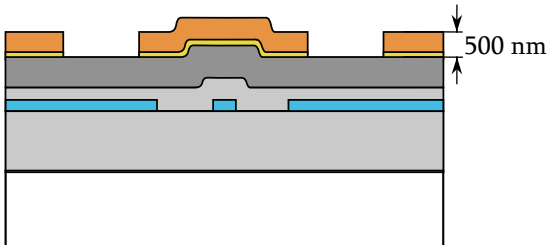

(f) Pattern transfer into the metal by lift-off

Fig. 7.8 single Figure

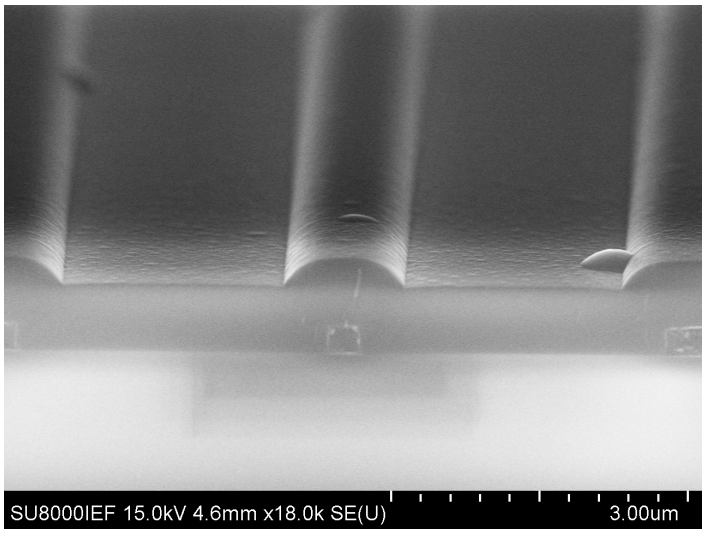

Fig. 7.9 Cross-section of the device after the SiN layer is deposited.

by $n_{\mathrm{SiN}} = 1.975$ (measured at $\lambda = 632\,\mathrm{nm}$) and an internal stress $\sigma_0 = -1.2\,\mathrm{GPa}$. Therefore, we performed this deposition method for 50 min in all the Devices, to achieve the same 700 nm-thick SiN layer with the same stressing conditions in every waveguide. This step is schematically shown in Fig. 7.8b and the SEM picture of the result for Device 0 is presented in Fig. 7.9.

Ideally, all the samples should have undergone the same fabrication procedure, except for the SiO_2 deposition, in order to achieve higher consistency of the results. However, the chip containing the Device 0 and the chips containing the Devices 250 and 500 were not made at the same time due to fabrication issues. Therefore, because the PECVD system available in our facilities is very sensitive to chamber conditions, which inevitably changes over time, there is a possibility that the film deposition was not *exactly* the same between Devices 0 and Devices 250 and 500.

Parameter	SiO_2	SiN
SiH_4 flow rate	400 sccm	40 sccm
NH_3 flow rate	-	30 sccm
N_2O flow rate	1420 sccm	-
N_2 flow rate	2000 sccm	2000 sccm
Pressure	550 mTorr	650 mTorr
Temperature	300 °C	300 °C
RF Power	60 W	20 W
RF Frequency	380 kHz	380 kHz

Table 7.1 Parameters of the selected SiN recipe for stress generation.

Resist spinning and e-beam lithography of the electrodes

Once the cladding is deposited in all samples, it is the time for the fabrication of the electrodes. We have different possibilities for the creation of the electrodes mainly because these are big structures whose features are typically on the μm scale. Even though these dimensions can be compatible with other types of lithography, such as Optical or Deep-UV lithography, we decided to use e-beam lithography because our process is more adapted to this technique and no further developments and optimizations of processes were required.

In the beginning of our research project, we started by defining the electrodes using e-beam lithography on PMMA resist which is a positive electronic resist which allows for extremely high resolution patterns [210]. The spin coated PMMA film was $\sim$250 nm-thick which was successfully compatible with the lift-off of 150 nm-thick electrodes, which was the thickness we used in the beginning.

However, we noted that thicker electrodes were required for different reasons. Firstly, in the characterization of the devices, the generation of the electrostatic field is achieved by putting in contact the external electric probes with the metallic thin films of the electrodes. When we used 150 nm thick metallic layers, we noticed that the electrodes of the chip were scratched away very easily, risking the performance of the device and therefore, thicker electrodes are needed. Secondly, for RF signal propagation, because the resistance of a line decreases with its cross section area, thicker electrodes have less resistance and thus present better performances in the transmission of the signal. Finally, the bump in the cladding created by the waveguide (see Fig. 7.8b), can generate electrode discontinuities if the metal layer is shallower than the bump height, because unlike the PECVD deposition, the metallic evaporation is not conformal to the surface. A situation where this effect occurred is shown in Fig. 7.10. In this case the metallic layer (brighter layer on top) is discontinuous in the region above the waveguide (highlighted in the figure) and this critically compromises the performance of the device. In order to avoid this risk, thicker electrodes are required.

To achieve thicker electrodes, however, new resist solutions must be found. In order to accomplish that, we selected the SML1000 which is a positive electronic resist which is able to be simultaneously patterned into high resolution and high aspect ratio patterns, even at low acceleration voltages and without proximity effect correction [214].

The SML1000 was spin coated at 1000 rpm and then baked for 3 min at 180 °C, resulting in a resist thickness of 2 μm [214], as represented in Fig. 7.8c. The drawback of the high sensitivity of the SML1000 resist is that it charges very easily, which is a problem during the alignment for the e-beam lithography. In order to solve that, we spin coated the resist "ESPACER 300Z" at 1000 rpm (no baking required) on top of the SML1000 layer which is

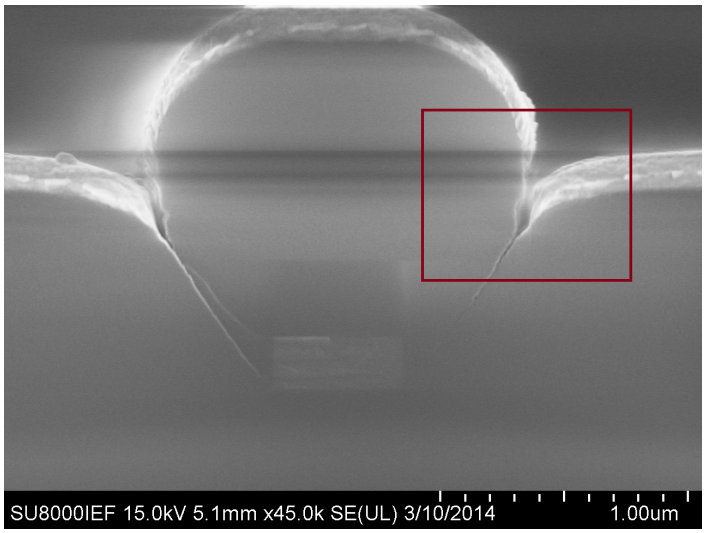

Fig. 7.10 The effect of a metallic layer shallower than the bump created by the waveguide, inside the red rectangle. This is an extreme case where the waveguide is thicker than usual, but it clearly shows that if the metal layer is not thick enough, we can get a discontinuity in the electrodes like the one seen in the corner of the bump above the waveguide, inside the red rectangle.

an anticharging resist that is able to avoid the over-accumulation of electrons in the resist during the visualization of the sample for alignment prior to the e-beam lithography.

The e-beam lithography of the SML1000 is also done in the NB4 e-beam lithography system, but in this case it requires a much higher current and dose, set to 12 nA and dose 13 C/cm^2 respectively.

We developed our own development procedure of this resist, consisting of 2 min in a IPA:H_2O (7:3) solution in very weak ultrasounds to facilitate the interaction of the resist with the solution. In order to finish the development, the sample was immersed for 1 s in a pure MIBK solution. This last step is extremely violent and longer immersions in MIBK risk the over development of the smaller features. The result is schematically presented in Fig. 7.8d. This process is well compatible for the lift-off of very thick metallic layers.

Metal evaporation and lift-off

The deposition of the metallic layer was done by e-beam evaporation. This is a physical vapor deposition in which a target anode, made of the metal to be deposited, is bombarded with an electron beam given off by a charged filament under high vacuum. The electron beam causes atoms from the target to transform into the gaseous phase, which then precipitate into solid form, coating everything in the vacuum chamber (within line of sight) with a thin layer of the anode material. The system available in CTU is the "Plassys MEB 550S".

The metal of our choice was Gold, because its deposition is very well established in our group and the film quality is very high. However, gold does not stick easily to the SiN surface and to ensure high adhesion, a 20 nm-thick thin film of Chrome is deposited before the gold evaporation, which promotes the adhesion to gold and sticks very well to the SiN layer. The gold layer is then evaporated at a very slow rate ($0.1\,\mathrm{nm/s}$) to ensure high quality film, until the final gold thickness of 480 nm is reached. Because, the evaporation of metal is a physical method, the deposition has a defined direction and the metallic layer is deposited only on top of the resist and not on the walls, unlike the CVD methods. This is shown schematically in Fig. 7.8e.

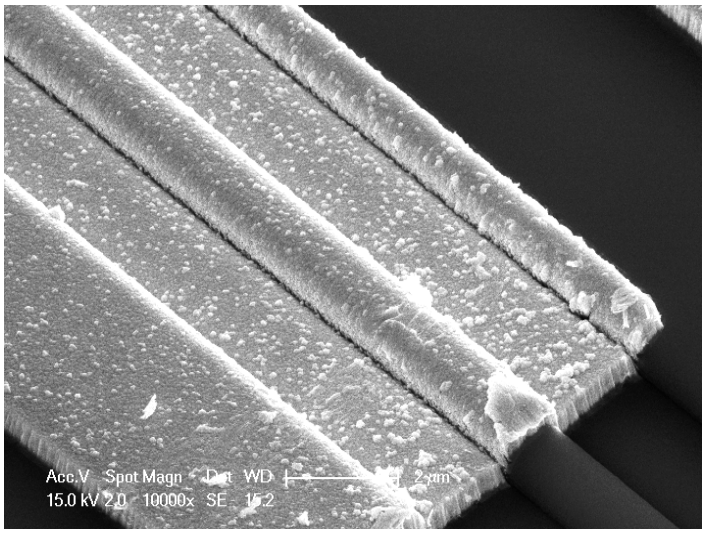

Fig. 7.11 SEM picture of the metallic layer of the electrodes over the cladding above the waveguide.

The metallic layer deposited on top of the resist is then removed by *lift-off* where a solvent dissolves the resist, removing the metal over it. This is done by immersing the samples in acetone overnight. The result of the metallic electrode on the waveguide is shown in Fig. 7.11.

7.3.3 Evaluation of the resulting devices

The visualization of cross-section of the devices is very important to know the final result of the fabrication. The way to observe the cross-section is to cleave the sample. The cleaving is done at the edges of the tapering, as shown in Fig. 7.5 and then we are able to visualize the cross section of everything on that facet. However, along that facet we are only able to visualize the cross-section of the tapers, which are $3\,\mu$m wide. In order to see the waveguide cross-section, we manually add small 400 nm-wide waveguides in the cleaving

region, as shown in purple in Fig. 7.5 for the sole purpose of analysing the cross-section of the waveguides in SEM.

The cross-section of Device 0, is shown in Fig. 7.12 and we clearly see the similarities with the expected result depicted in Fig. 7.8f. The silicon waveguide is in the center of the picture and it is covered by the conformal a−SiN:H layer. On top, lies the metallic layer. The visible crack in the metal is due to the cleaving process and it is not a fabrication defect.

In Fig. 7.12b is shown a closer view of the region around the waveguide with the dimensions of the different layers of the device. Firstly, we notice that the waveguide width is slightly lower than the desired 400 nm due to the etching and thermal oxidation processes. In any case, this is not a striking difference and it should not change the performance of the device. The thickness, however, is as expected: $t_{WG} = 250\,\text{nm}$. Additionally, the thermally grown SiO_2 layer may be identified by the bright line around the waveguide.

Secondly, we notice that the SiN layer is a little thicker than our goal, being closer to 750 nm rather than 700 nm. This was probably due to some disturbance on the PECVD deposition rate, which was very sensitive to the deposition conditions. This change, however, corresponds to only 6% in t_{SiN} and from Fig. 6.2a we see that it will not be a big change in the performance of the device. Finally, the metallic layer thickness is within the value we expected, around 500 nm. The quality of the adhesion to the surface cannot be commented because this layer was damaged after the cleaving.

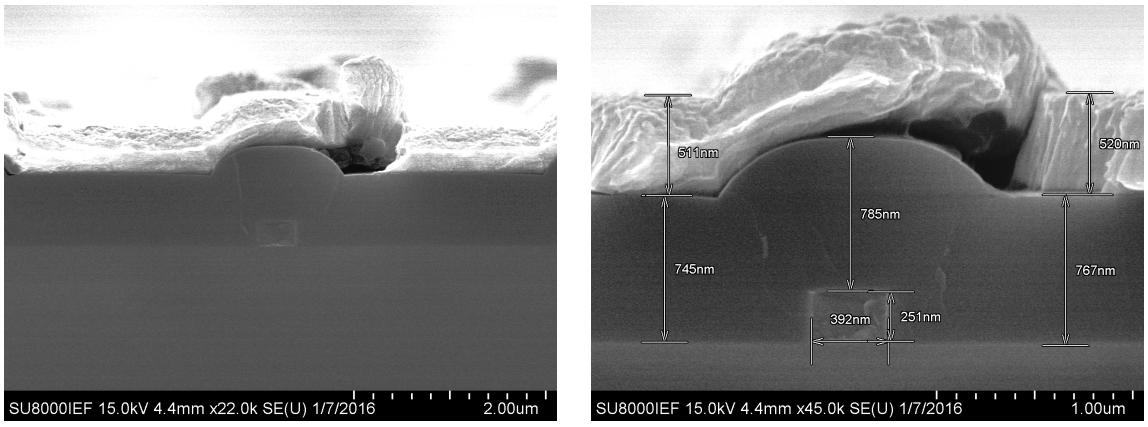

(a) (b)

Fig. 7.12 (a) The cross-section of Device 0 (b) Zoom into the waveguide with corresponding dimensions.

Figure 7.12 can be compared with those of Devices 250 and 500, shown in Fig. 7.13 taken in the taper region.The separation between the SiN and SiO_2 layers is not very clear, but it can be identified with the help of the drawn dimensions.

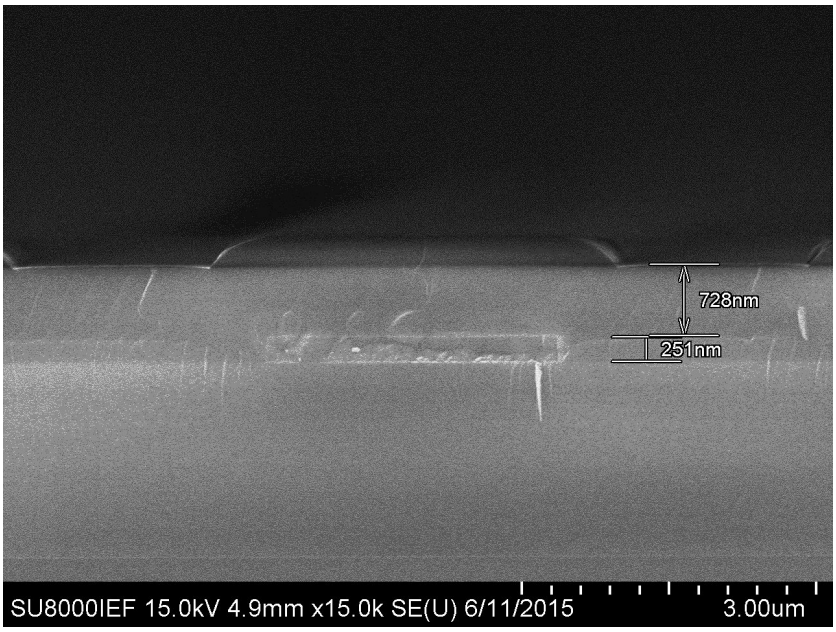

(a) Device 250

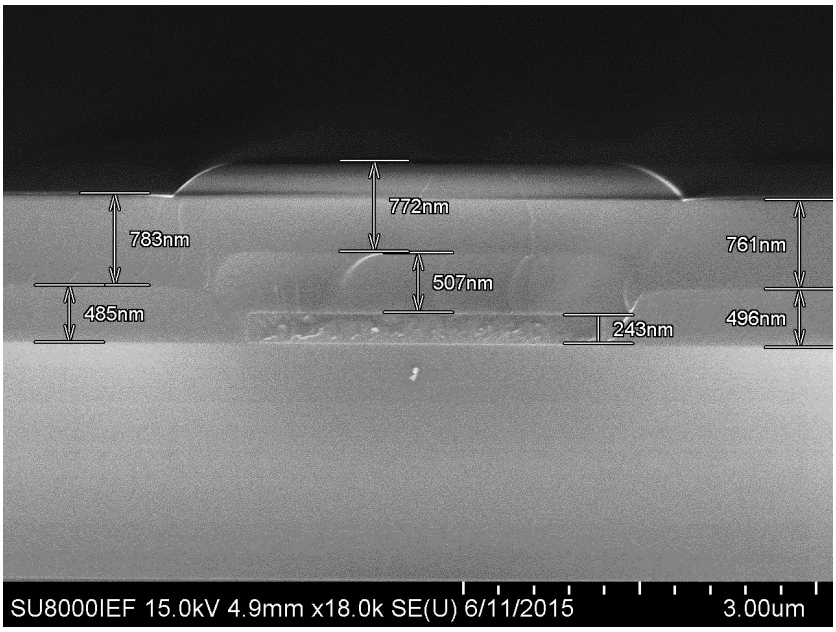

(b) Device 500

Fig. 7.13 Cross-section of Devices 250 and 500 with corresponding dimensions.

In Fig. 7.13a, showing the cross section of Device 250, we see that the thickness of the PECVD SiO_2 layer is the desired value of 251 nm and the SiN layer is also close to the expected thickness (700 nm). Fig. 7.13a shows the cross section for device Device 500. All the dimensions have an uncertainty around 20 nm due to the SEM measuring system at this resolution. Therefore, the dimensions all very close to those of the original design discussed in the previous chapter.

We should also point out that the small defects seen in Fig. 7.13a are attributed to the cleaving of the sample which generates some cracks in the layers. In general, there are no critical defects worth of mention and there are no particular reasons to not have the expected performance of these devices.

In Fig. 7.14 are shown some pictures of the top view of the sample. In Fig. 7.14a and 7.14b we focus on one of the MZI splitter before the deposition of the cladding, because it is one of the most sensitive features of our design. As we can see, the splitter is very symmetric and show good quality. In most of the devices this resulted in a very clean transmission spectrum, as we shall see in the next chapter. In these pictures we can also see the waveguide and the etched pad alongside to it.

In Fig. 7.14c and 7.14d we show microscope photos of the top view of the sample for the reader to have a clear view of the whole structure. The electrodes, that follow the path of the MZI, are also shown. In Fig. 7.14c we show the tapering system we used to make a smooth transition between the external electrical probes (connected to the electrostatic signal generator) and the electrodes of the sample. This is particularly important in order to ensure a good adaptability in high-frequency signals and avoid reflections at the input. In Fig. 7.14d we show an example of the splitter in a angled MZI with $\varphi = 30°$.

7.4 Final Remarks

The fabrication procedure described in the last pages and the resulting samples was the culmination of numerous tests, techniques and fabrication procedures. For that to be achieved, an enormous number of samples were fabricated during this research work, not only for the development of the specific chips presented in this manuscript, but also for other tests, approaches, configurations and devices. All in all, a lot of time was spent in the clean room towards the optimization of the fabrication processes. The result of that effort are the devices presented here which were very close to the design we aimed for, as shown in the SEM pictures presented throughout this chapter, validating the fabrication methods implemented.

Once the samples were fabricated, they were cleaved along the cleaving line shown in Fig. 7.5 exposing the taper through which we couple the light during the experimental

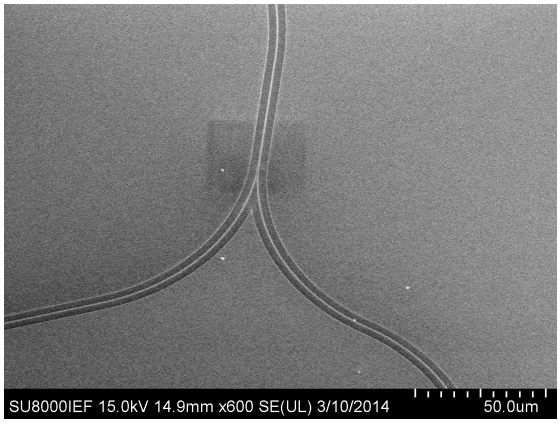

(a) MZI splitter

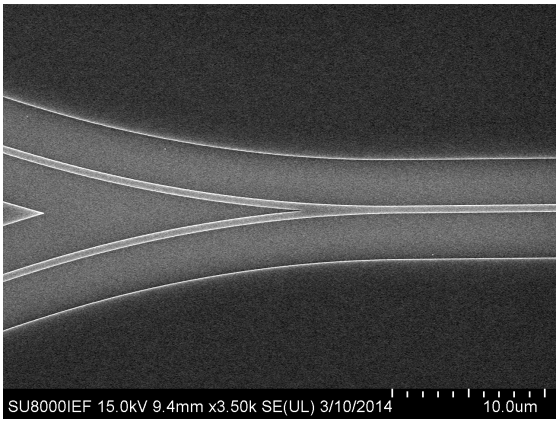

(b) MZI splitter

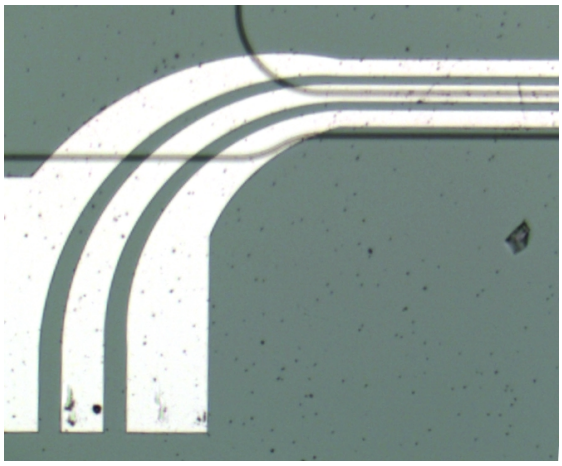

(c) The electrodes tapering system.

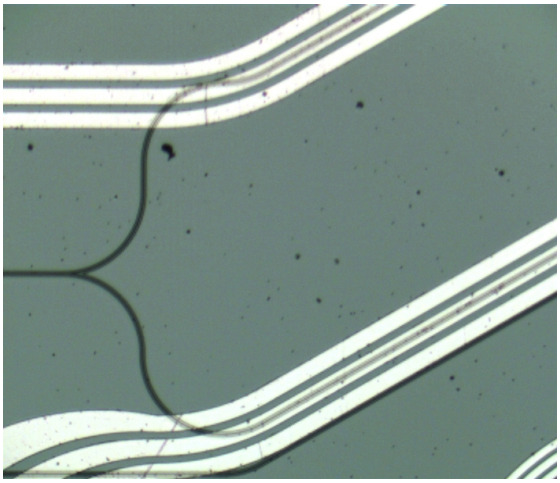

(d) An example of an angled MZI splitter.

Fig. 7.14 SEM and microscopic pictures of the top-view of the sample.

measurements. At that moment, the samples are ready to be characterized. That is the subject of the next chapter.

Chapter 8

Experimental characterization and results

The experimental results presented in this chapter are concentrated on the devices described in the previous chapter. However, these were not the only experiments we performed during this research work. In fact, our first approach to the strain-induced Pockels effect measurement consisted on Mach-Zehnder Interferometer structures, disposed in a push-pull configuration, to detect the linear Pockels effect. This approach was referred in Chapter 2 and are shown in Fig. 2.7. We characterized those devices in a wide range of wavelengths, from 1.3 μm to 1.63 μm and reported the "$\chi^{(2)}$ " dependence in that range of wavelengths, shown in Fig. 2.7a, which culminated with the highest value reported thus far: $\chi^{(2)}_{xxy} = 336\,\mathrm{pm/V}$, obtained for $\lambda = 1.63\,\mu$m and waveguide width 385 nm.

Nonetheless, these results were erroneously analysed because we did not take into account any carriers effects which led to an over-estimation of $\chi^{(2)}$. In fact, the growing trend of $\chi^{(2)}$ with λ we obtained can be explained by the plasma-dispersion effect, because Soref equations presents the same kind of wavelength dependence (compare eqs. 1.3 and 1.5).

Once we discovered that carriers effects ought to be considered, we changed our approach and modified the design of the samples. The resulting devices, designed and fabricated as described in the previous chapters, were characterized in an optical bench designed to measure the transmission spectrum as a function of an applied electrostatic field. This allows characterizing the electro-optic effect of the samples and in this chapter we concentrate on describing the process and the results of the characterization of $\Delta n_{eff}(V_s)$. The final goal is to identify both the strain-induced Pockels and plasma-dispersion effects in the Devices 0, 250 and 500 and compare $\Delta n_{eff}(V_s)$ in different crystal orientations in order to detect a dependence in crystallographic angle.

Moreover, as referred many times throughout this thesis, one of main particularities of Pockels effect is its intrinsic high speed which enables ultrafast modulation beyond 1 THz. This characteristic is not share by carrier effects which are limited in the $1-5$ GHz range. Therefore, by making a high speed characterization of the electro-optic response of the strained-silicon device we may be able to discriminate between Pockels and carriers effects.

This chapter is separated in two different parts: one for the DC characterization, which is longer and explained in more detailed and one for the high-speed RF modulation. In both of these parts we start by introducing the optical bench and the different considerations in its implementation for the right characterization of the devices. Then, we describe the characterization method, the considerations to take into account and finish by presenting the results, their interpretation and conclusions.

8.1 The experimental DC characterization set-up

The optical bench used in this research work was set with the purpose of coupling TE-polarized light into the devices and then collect the transmitted light into a photodetector for the acquisition of the transmission spectrum over the wavelength range between 1520 nm and 1640 nm. The schematic representation of the experimental set-up we used is shown in Fig. 8.1. To simplify, we separate the description into three separated parts: the input (the light path before the light enters in the sample), the output (the light path done by the light transmitted from the sample) and the electrical system used to induce an electrostatic field.

The light input part

The light source of the system is a "Yenista Optics TUNICS-PLUS" *Laser source* (represented as a green box in Fig. 8.1) capable of generating light in the wavelength window from 1520 nm to 1640 nm. The source is connected to the "Yenista Optics CT400" *Component Tester* (represented as a purple box), which controls the wavelength scan of the sample, by comparing the light input and output, with a resolution reaching the pico-meter. This system is very efficient as it is able to scan the full 1520 nm to 1640 nm range in just a few seconds.

The CT-400 component tester is connected to a *polarization rotator* which defines the polarization of the laser beam. The light then goes through a *polarizer*. This device is set to filter the TM components of light and let through only TE-polarized light. The light is then guided through an optical fibre which maintains the light polarization.

The light is injected into the waveguide by a lensed fibre placed on the Sample Holder. The position of the fibre can be controlled by 3 piezoelectric motors that can make submicron displacements of the fibre in the X, Y and Z directions. This is helpful for the optimization

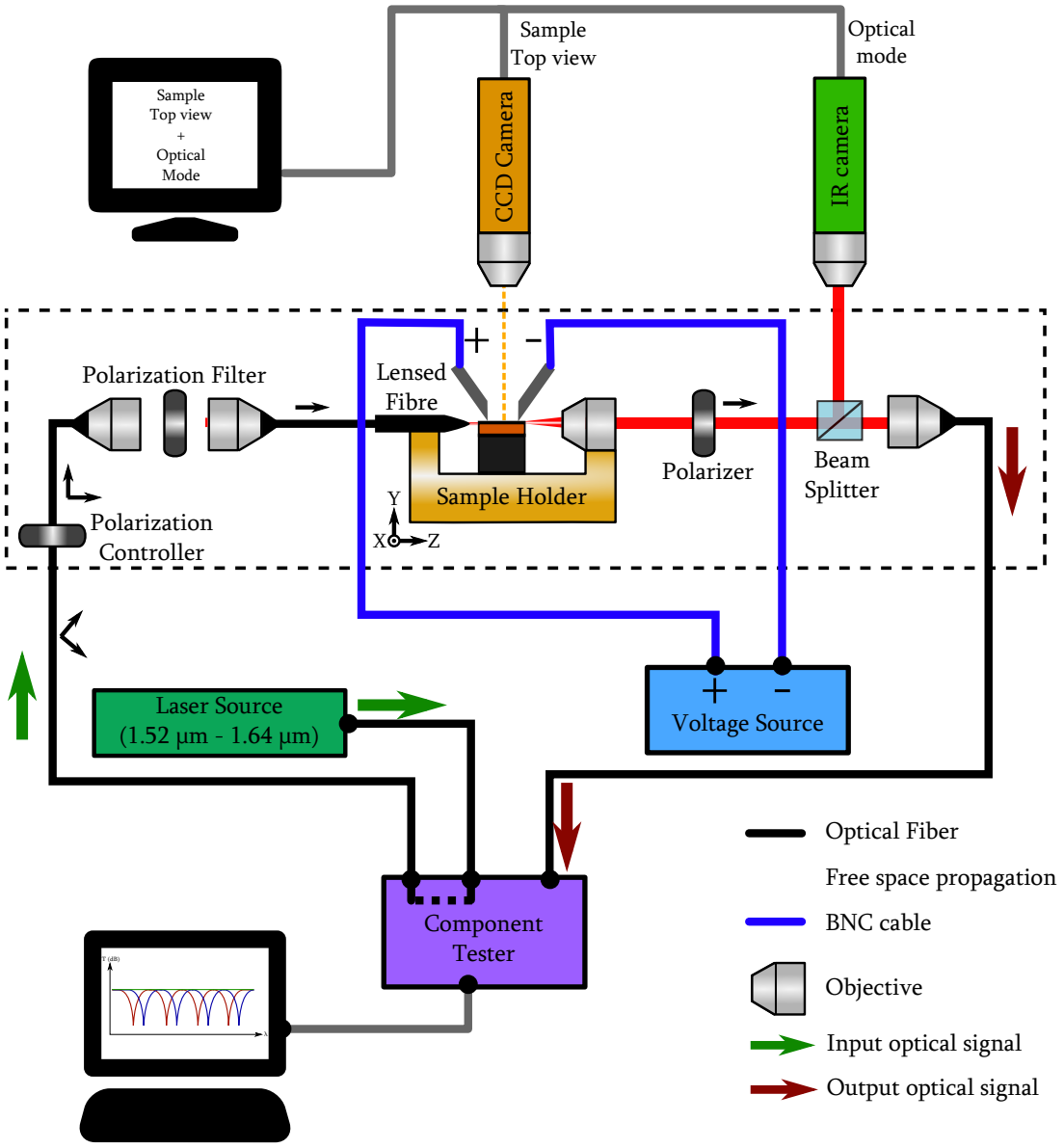

Fig. 8.1 Schematic representation of the experimental set-up. The light path starts at the green arrow and it ends in the red arrow. This set-up allows the characterization of the transmission spectrum the TE-polarized light whose wavelength is between 1.52 μm and 1.64 μm. The small black arrows represent the polarization of light)

of the light coupling into edge of the chip. The movement of the fibre can be visualized by a backlit *CCD camera* placed over the sample holder which illuminates its surface. This system has an objective Mitsutoyo with $10\times$ zoom and 0.35 Numerical Aperture (N.A.) which allows to control the position of the fibre with a submicron precision.

The sample itself is glued to a sample holder which can move in the X and Z directions and rotate in the Y and Z axis. This makes it possible to move the sample while keeping everything else in the set-up untouched, which is particularly useful to keep the alignment while changing the waveguide to be characterized.

The light output part

The sample output light is collected by an objective (N.A. 0.26) whose goal is collimating the beam that goes through another TE polarizer and then through a prism which separates the beam in two. One of these two beams is sent to an infra-red camera Hamamatsu capable of imaging the optical mode exiting the sample. The other beam is directed into an objective (N.A. 0.26) that focus the light into an optical fibre. The prism is used during the coupling and alignment processes and removed during the measurements.

The output fibre is connected to the photo-detector in the CT400 and everything in the components analyser is controlled by a computer through a GPIB interface.When performing a wavelength scan, the CT400 changes the λ of the laser source and compares the intensity of the input with the output signals for each wavelength. The result is the transmission spectra of the device and it can be visualized in the computer.

The electrical system

The DC signal is generated by a "Ketley 2400 Source Meter" *Voltage Source* which is capable of generating electrical signals with voltages in the range $\pm 200\,\mathrm{V}$. The Ground (represented by $-$, with $V = 0\,\mathrm{V}$) and the Signal (represented by $+$, with $V = V_s$) are connected to the corresponding probes by regular BNC cables.

The electrostatic signal is transmitted to the sample by placing the electrical probes in physical contact with the input pads of the electrodes.The signal voltage of the electrodes is then controlled by manually changing the output of the electrical source. This process allows the generation of stable electrostatic signals in the devices for a wide range of voltages.

8.2 DC Characterization of the transmission spectrum

In all measurements describe next, we used the laser source at 1 mW power, to ensure stability of the wavelength scans in the components analyser. At this power, by optimizing the alignment of all the components in the set-up, we can achieve a fibre to fibre transmission of around -15 dB.

8.2.1 Transmission spectrum of the reference waveguide

As referred in the previous chapter, we placed reference waveguides besides every MZI line. These structures are used to help during the coupling and alignment processes and to evaluate the quality of the passive transmission, thus they were the first to be characterized. A typical transmission spectrum of a fully working reference waveguide is shown in Fig. 8.2 in black. We see that the transmission is considerably flat in the whole spectrum with an average transmission around -38 dB.

The facets of the chip, obtained by cleaving the sample, expose the cross-section of the SOI adiabatic taper (see Fig. 7.13 for the cross-section view). This abrupt termination of the silicon waveguide creates a Fabry-Perot cavity with the length of the whole waveguide, creating an interference pattern in the spectrum. This interference makes a high contribution for the visible noise in the transmission spectrum of the waveguide, as shown in the inset of Fig. 8.2. The Free Spectral Range (FSR) of the Fabry-Perot interference fringes is smaller than the nanometer, corresponding to a cavity some millimetres long, in agreement with the actual length of the sample.

8.2.2 Transmission spectrum of the Mach-Zehnder Interferometer

Once the alignment to the reference waveguide is optimized, we couple the light into the MZI line and measure its transmission spectrum. The typical transmission spectrum of an undamaged, fully working MZI, is shown in Fig. 8.2 in Blue (obtained for Device 0- MZI1). The resonances are very well defined, are evenly spread in the whole wavelength range, presenting an extinction ratio (ER) of 23 dB. The Insertion Loss (IL), obtained by making the difference between the waveguide and the MZI transmission levels, is seen to be less than 3 dB.

However, some MZI do not have a transfer function as perfect as that shown in Fig. 8.2. To exemplify this, in Fig. 8.3 we present a MZI output spectrum that is not as neat, whose resonances are not as defined as the previous one, obtained for Device0-MZI3. In Fig. 8.3a is presented the full transmission spectrum and we can see a strong background noise in

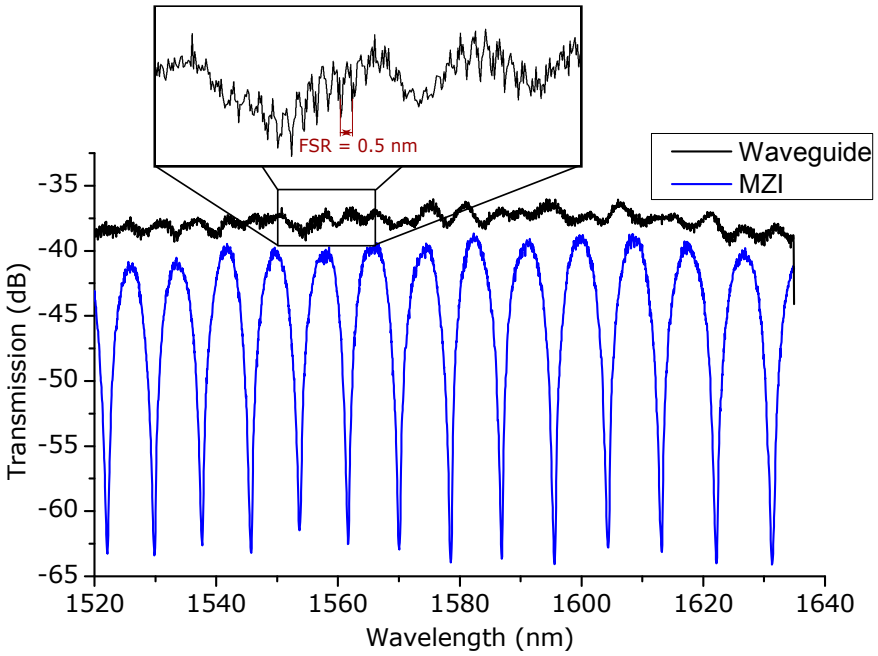

Fig. 8.2 Transmission spectrum of well functioning straight waveguide (black) and a MZI (blue), obtained for Device0-MZI1.

the MZI transmission spectrum. We were not able to identify the exact origin of this noise, but we attribute it to either some defects in the arms or in the splitter of the MZI. Defects in the arms can induce wavelength dependent phase shifts which create new resonances when interfering with the light coming from the other arm; defects in the splitter can create additional features in the spectra by separating the light unevenly to the arms.

Regardless, of their origin, the noise shown in Fig. 8.3a affects deeply the precision of the electro-optic measurements. In fact, when a voltage is applied to the system, the resonances in the MZI move and the superposition with the noise changes, modifying the overall shape of the resonance and masking the real position of the resonance wavelengths (λ_r) which we intend to measure precisely. This situation is exemplified in Fig. 8.3b and for sensitive measurements required in the measurement of a weak electro-optic effect, we can see that it introduces high uncertainties in the real position of λ_r, on the order of magnitude of the resonance shift itself. This is one of the reasons why we used two identical MZI for angles 0º and 30º, so that in case one of the MZI is damaged and the spectrum is imperfect, we have a second one available for a precise measurement and achieve more confidence in the results.

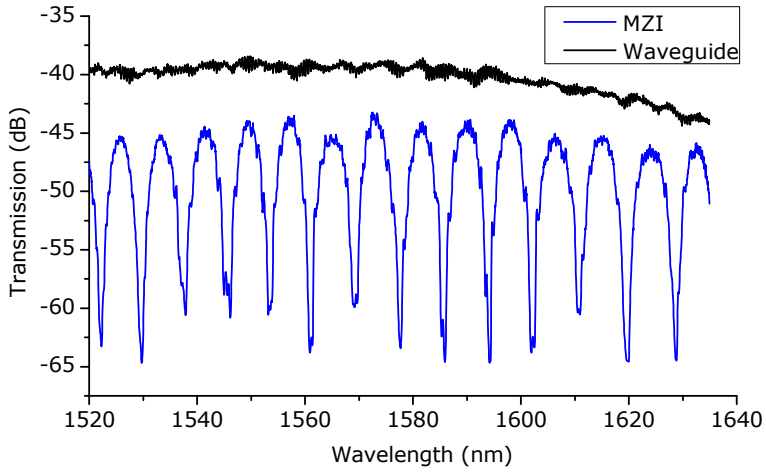

(a)

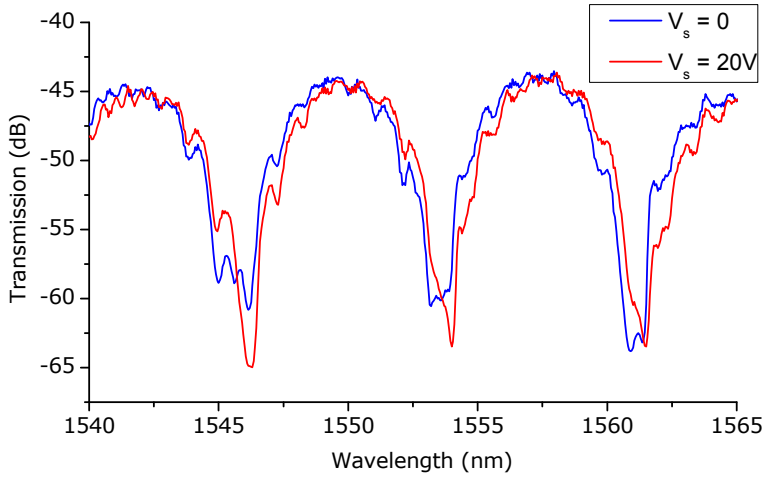

(b)

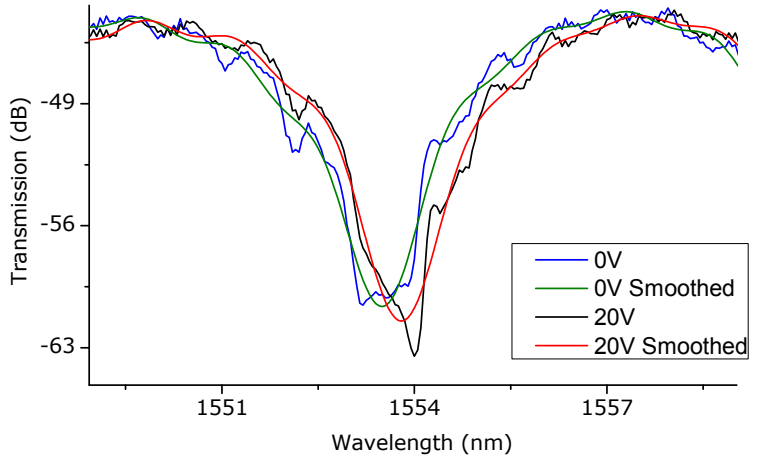

(c)

Fig. 8.3 (a) Example of the transmission spectrum of damaged MZI, obtained for Device0-MZI3. (b) The modification of the resonance shape due to the application of a 20 V voltage. (c) The smoothing process for the resonances in the spectra presented in (b).

The method of analysing the resonances

When a voltage is applied to the electrodes, we induce a shift $\Delta\lambda_r$ in the transmission spectrum due to the electro-optic effect, as shown in Fig. 8.4a. The curve we want to characterize is $\Delta n_{eff}(V_s)$ and the measurement of the resonance shift for each V_s provides us that information through (see eq. 7.4)

$$\Delta n_{eff}(V_s) = \frac{\lambda_r \cdot \Delta\lambda_r(V_s)}{\mathrm{FSR}(\lambda_r) \cdot L} \,. \tag{8.1}$$

The value of λ_r is defined by the resonance wavelength which corresponds to the minimum of the transmission spectrum. However, as referred before, the noise generally present in the transmission spectrum makes it sometimes difficult to clearly identify λ_r because finding the minimum of the transmission spectrum may not be clear (see Fig. 8.3b for instance). From eq. 8.1 we see that the precision of the experimental value of Δn_{eff} is defined by the precision of the $\Delta\lambda_r$ measurement and in order to have precise measurements, a method that determines λ_r with the least uncertainty possible is required.

To overcome this problem, we developed an algorithm that detects the resonances of the transmission spectrum of a MZI with the highest precision possible. The method consists of three sequential steps:

1. **Perform a FFT smooth of the spectrum** As we can see from the previous figures, the noise of the transmission spectrum is composed by high frequency oscillations. Thus we take the Fourier Transform of the original spectrum, we neglect all the frequencies above a specific cut-off frequency (chosen depending on the noise) and make an inverse Fourier transform back to the original λ domain. The result is a smoothed spectrum without the high frequency noise, where the resonances minima are much better defined. This is shown in Fig. 8.3c for the referred damaged MZI and in Fig. 8.4 for a very well performing MZI.

2. **Fit the minimum with a parabola** The algorithm automatically detects the minimum in the smoothed spectrum and fits it by a 2^{nd} order polynomial $f(\lambda) = a\lambda^2 + b\lambda + c$.

3. **Find the analytical minimum** Once the resonance is fitted by a parabola, we can determine the resonance position analytically by $\lambda_r = -b/2a$. This allows the automatic and precise detection of very small resonance shifts, in the order of the 0.2 nm.

Once the value λ_r is determined, it is then recorded as a function of V_s and by taking $\Delta\lambda_r(V_s) = \lambda_r(V_s) - \lambda_r(0)$ we can calculate $\Delta n_{eff}(V_s)$ through equation 8.1.

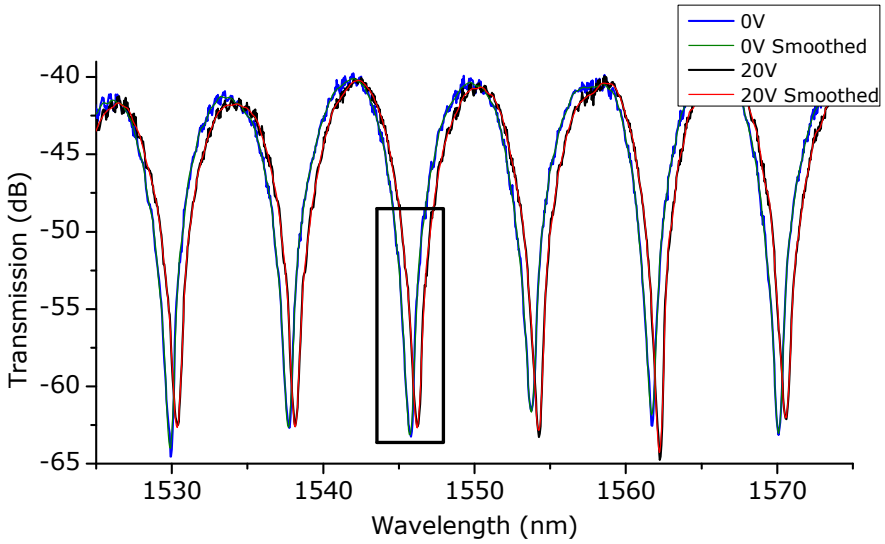

(a)

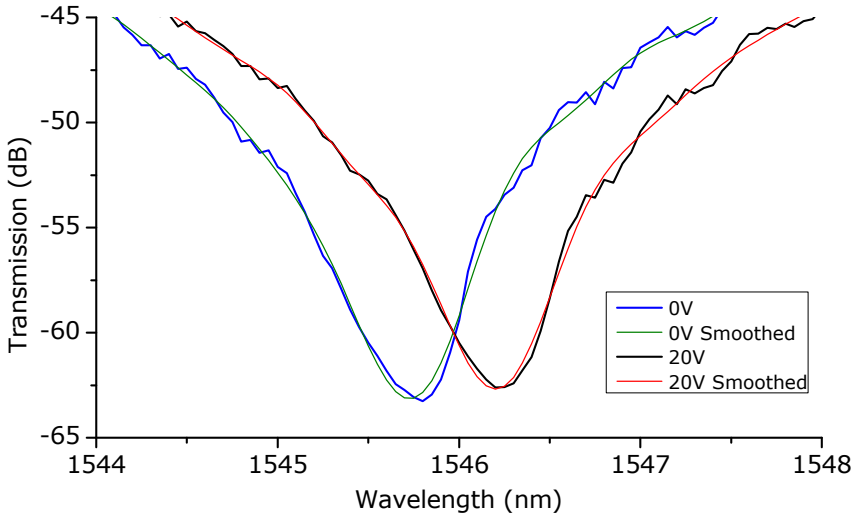

(b)

Fig. 8.4 (a) An example of the output spectrum of a very good MZI (Device 0 - MZI1) in a wide range of wavelengths. (b) The result of the smoothing process for detection of the resonance minima, for the highlighted region of the spectrum.

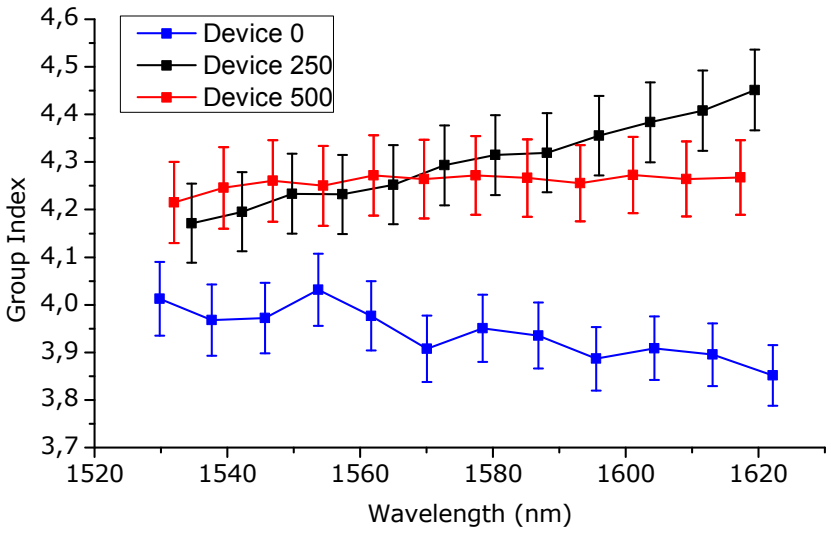

Fig. 8.5 The group index (n_g) as a function of the wavelength for the different Devices 0, 250 and 500.

Equation 8.1, however, depends on the value of the MZI's FSR which depends on λ_r because the group index of the guided mode is wavelength dependent (see eq. 7.3). For a given λ_r the FSR is determined by

$$\mathrm{FSR}(\lambda_r) = \frac{\lambda_{r+1} - \lambda_{r-1}}{2} \,. \tag{8.2}$$

The group index n_g can be experimentally obtained by (see eq. 7.2)

$$n_g = \frac{\lambda_r^2}{\Delta L \cdot \mathrm{FSR}} \,, \tag{8.3}$$

with $\Delta L = 70\,\mu$m. The result of n_g as a function of the wavelength for all Devices 0, 250 and 500 is shown in Fig. 8.5. We can clearly see the differences in the dispersion curves due to the different claddings. The simulation of the dispersion of the corresponding waveguides at $\lambda = 1550\,$nm, resulted in $n_g = 3.92$, 4.2 and 4.3 for Device 0, 250 and 500, respectively, showing a very good agreement with the experimental values presented in Fig. 8.5. This information together with $\Delta\lambda_r(V_s)$ allows us to determine $\Delta n_{eff}(V_s)$ for every device in the whole wavelength range.

8.3 Temporal considerations during the DC characterization

Although so far we have not approached the time dependences of any of the effects we have been describing, the response of the device to the applied voltage is not instantaneous. In fact, experimentally, we detect a time dependent behaviour of $\Delta\lambda_r(V_s)$ which enormously complicates the electrostatic characterization of the samples. In this section we present the analysis of temporal response of the devices and explain the methods we adopted to characterize the samples in DC when considering that temporal behaviour.

8.3.1 Sources of time dependence

As studied in both Chapter 4 and 5, under a voltage the concentration of free-carriers change and they move inside the silicon waveguide. These processes are characterized by time constants on the nanosecond range and even though they can be a limiting factor in high speed modulation of light in silicon, they are much faster than the time scale involved in a DC characterization. Therefore, they are not detectable during the DC experiments and can be considered instantaneous in this case, just like Pockels effect. Therefore, neither of these electro-optics effects are expected to contribute to any measurable temporal dependence of Δn_{eff} in the DC characterization experiments. However, the processes involving trap filling by free carriers or the possible movement of ionic charges in the cladding can be considerably slower than the fast carrier motion inside the waveguide and they may play a visible role when we apply a voltage to the device.

In general, the slow time-dependent processes that may take place when an electric field is applied to the device shown in Fig. 6.6 are in some way related to the cladding. One possible effect is the motion of ionic charges inside the SiN layer itself. Because a$-SiN_x$:H tends to generate K and N centres with very particular charging properties (which we have discussed in detail in section 5.3), we should not exclude the possibility that mobile charges exist in the SiN film, which can move under a voltage [168]. This motion, may naturally change the distribution of charges in the cladding which will modify the response of the waveguide to the applied electrostatic field.

The most important, however, involves the capturing processes of free carriers by the K-centres in the SiN layer, described by equation 5.13. The electronic processes involving Si dangling bonds were thoroughly described in section 5.3.3 and were experimentally analysed specifically for the electro-optic effects in strained silicon waveguides by Azadeh et al. in [66]. In this work, the authors studied the electro-optic response of a silicon waveguide to

a varying strong electrostatic field and they detected different behaviours when the devices were soaked at different voltages prior to the characterization. This suggests that under a high voltage, the K-centers capture positive or negative charges which modify the charge properties of the cladding, thus changing the performance of the device. When the voltage is changed, the K-centers tend to adapt to the new conditions by changing their charging state (by releasing or capturing charges).

This situation interferes with the characterization of the samples in two different ways: on the one hand, trap charging and de-charging are slow dynamical processes, with time constants on the order of seconds [181] and it can take several minutes or even hours to achieve a stationary behaviour [66, 181], introducing a time constant to the overall process of measurement. On the other hand, the charge characteristics of the cladding itself is not voltage independent, but it may change as a function of V_s by capturing carriers from silicon or by the motion of ionic charges. This situation was not assumed in our simulations, as we considered Q_f to be constant.

8.3.2 Hysteresis and charge build-up

From the previous discussion, when V_s changes the charge state of the K centres also changes, but it does not change instantaneously and takes some time to reach a stationary state, i.e. there is a time constant in the system. The signal voltage acts like a dragging force towards the build up of a stationary charging state in the cladding.

One immediate consequence of this process is the appearance of hysteretic behaviours of Δn_{eff} on the applied voltage. To exemplify this situation, consider that we are changing the voltage V_s of the system in time intervals $\Delta t < \tau$, τ being the stabilization time of the system (which can be several minutes or hours). In this case, the system never reaches a stationary state and it is always reacting to the voltages applied previously. The result is then different when the voltage was goes up and down because the state of the system is not the same and the result is an hysteretic behaviour. This process was also described and detected by Azadeh and co-workers in [66] and in other studies related with traps in SiN [174].

Although we have put a SiO_2 layer separating the SiN layer and the silicon waveguide, hysteresis can still happen for two main reasons. The first is that the SiO_2 layer is also known to possess interface traps which can induce an hysteretic behaviour [173, 175, 176]. The second, is that under a sufficiently high voltage, the carriers in silicon may be able to *tunnel* through the potential barrier created by the SiO_2 layer and go into the SiN layer to charge the K-centers. This process was commonly used several years ago in SiN based devices for charge retention in SiN for memory systems and its detailed description can be found elsewhere [180]. Obviously, the voltage required to achieve tunnelling of the electrons

depends on t_{SiO_2} and we expect to detect different hysteretic behaviours in the Devices 0, 250 and 500.

8.3.3 Time behaviour of the Devices

The processes described above lead to a dependence of the measurements on the time interval Δt waited between two consecutive measurements of V_s. In order to know what is the time response of the samples and adapt the characterization method to it, we measured the time dependence of Δn_{eff} for different applied voltages sequentially:

$$0\,\mathrm{V} \rightarrow 10\,\mathrm{V} \rightarrow 20\,\mathrm{V} \rightarrow 0\,\mathrm{V} \rightarrow -10\,\mathrm{V} \rightarrow -20\,\mathrm{V} \rightarrow -30\,\mathrm{V}\,. \tag{8.4}$$

This measurement consisted of measuring the resonance position every 10 s for a given applied voltage. The results are shown in Fig. 8.6 for all Devices where we have placed small circles at the times the voltage changed. The experiments for Device 0 and Devices 250 and 500 were not carried out for the same period of time. In Devices 250 and 500 we did for a longer period (1h:25min), whereas Device 0 we did it for just 13 min because we confirmed the same trends we had detected in the other two Devices. This is the reason for the different Time axis in the graph, for Device 0 and for the other two.

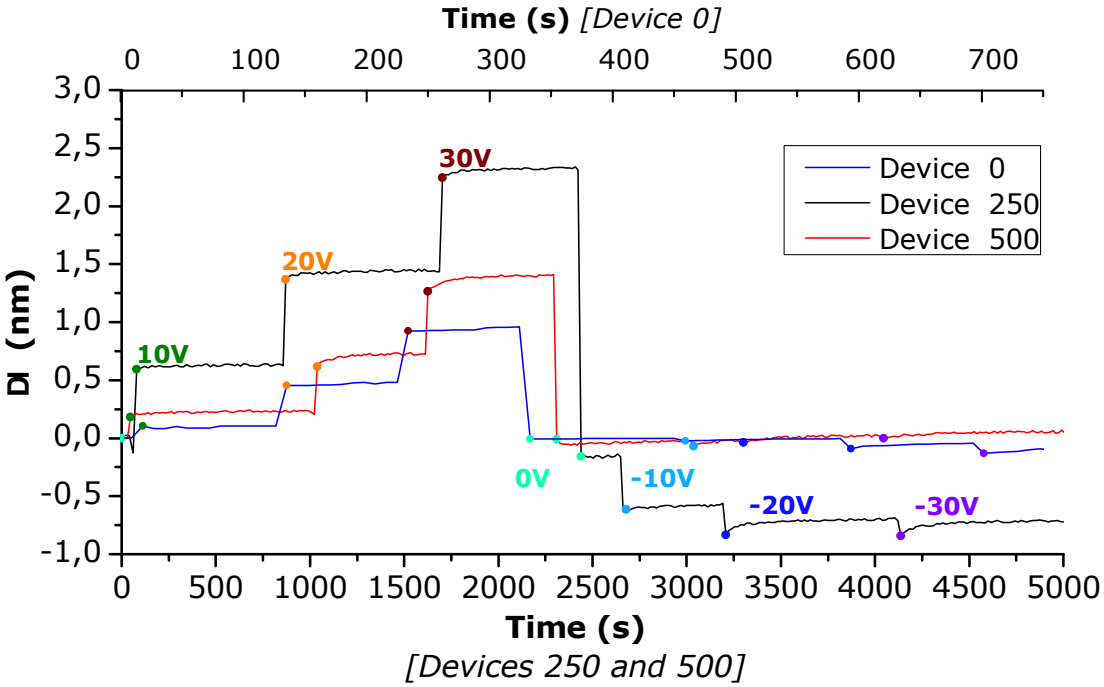

Fig. 8.6 Time dependence of $\Delta\lambda$ for the three Devices 0, 250 and 500 and for different applied voltages.

From Fig. 8.6 we can identify different behaviours depending on the absolute value of the applied voltage. While for $V_s = \pm 10\,\mathrm{V}$ the response is immediately stabilized, $V_s = \pm 30\,\mathrm{V}$ the $\Delta\lambda$ takes some time to reach a stationary state (some tens of seconds).This is compatible with the idea that for low voltages the electrons in the waveguide do not enough energy to fill the traps in the cladding. For higher voltages, though, the electrons are able to fill the traps in the cladding and thus a time dependence appears and a slow change in $\Delta\lambda$ is detected.

In addition to high / low voltages difference, we can also see a difference in the time dependence for positive and negative voltages. In the case of a positive voltage, for 30 V, the curves present a typical shape of a charging capacitor, before it stabilizes. This could correspond to a charging process of the traps in the cladding. For negative voltage, however, the shape is opposite, i.e. looks like a discharging process tending to $\Delta\lambda = 0$.

The shape of the curves presented in Fig. 8.6 are compatible with the existence of three different time scales in the electro-optic effect: Pockels effect, with time constants on the fentosecond [27]; a fast motion of free-carriers inside the waveguide, with time constants on the nanosecond [71]; a slow motion of free-carriers involving trap filling processes inside the cladding, which affects the carrier concentration in the waveguide and with time constants on the second scale [181]. As a result, we can write the total electro-optic effect as:

$$\Delta n_{eff} = \Delta n_{eff_P} + \Delta n_{eff_{c-Fast}} + \Delta n_{eff_{c-Slow}} \,. \tag{8.5}$$

What we see in Fig. 8.6 is the interplay of these effects: while the two fast effects contribute for the abrupt change in $\Delta\lambda$, the slow carrier effects contribute for the slow change occurring during the following seconds, which is more important under high voltages.

In order to be consistent in the experimental procedure, we decided to apply the same time step Δt to all the samples and in all types of measurements. Since our focus is not studying the trap filling processes, but mainly the fast effects occurring in the device, the optimal time step Δt should be sufficiently fast so that the influence of $\Delta n_{eff_{c-Slow}}$ is as little as possible. This speed is constraint by the time required for manually change V_s and acquire the transmission spectrum, which take some seconds. Under these considerations, the selected time step was $\Delta t = 15\,\mathrm{s}$, which by looking at Fig. 8.6 we consider it is fast enough to prevent a strong effect of $\Delta n_{eff_{c-Slow}}$, even though these effects are practically impossible to avoid, in particular when high voltages are involved.

8.3.4 The characterization procedure

The characterization procedure we used in our experiments was chosen to take into account all the considerations described above in terms of voltage and time scale. For these reasons

we separated the characterization into four independent experiments performed in each device:

- **Experiment 10 V:** In this experiment we limit the maximum absolute voltage to 10 V with the purpose of avoiding the contribution from traps in the cladding and concentrate only on the fast effects from Pockels and plasma-dispersion. In addition, after applying a voltage, we grounded the system by setting $V_s = 0$ and confirming that the measured position of the studied resonance λ_r was the same as the one measured initially, before any voltage was applied. By doing so, we force the system to come back to equilibrium and thus revert any charging process that occurred under $V_s \neq 0$.

  In this experiment, the voltage change in each step was $\Delta V_s = \pm 2\,\mathrm{V}$, resulting in the following "voltage sequence":

$$0\,\mathrm{V} \to 2\,\mathrm{V} \to 0\,\mathrm{V} \to 4\,\mathrm{V} \to 0\,\mathrm{V} \to \cdots \to 10\,\mathrm{V} \to 0\,\mathrm{V} \to \tag{8.6}$$

$$\to -2\,\mathrm{V} \to 0\,\mathrm{V} \to -4\,\mathrm{V} \to 0\,\mathrm{V} \to \cdots \to -10\,\mathrm{V} \to 0\,\mathrm{V}\,. \tag{8.7}$$

- **Experiment 20 V:** In this case,we increase the voltage until $V_s = \pm 20\,\mathrm{V}$, then decrease it until $V_s = -20\,\mathrm{V}$ and bring it back to $V_s = 0\,\mathrm{V}$, all in steps of $\Delta V_s = 5\,\mathrm{V}$. The voltage sequence can be written as:

$$0\,\mathrm{V} \to 5\,\mathrm{V} \to \cdots \to 15\,\mathrm{V} \to 20\,\mathrm{V} \to 15\,\mathrm{V} \to \cdots \to 5\,\mathrm{V} \to 0\,\mathrm{V} \to \tag{8.8}$$

$$\to -5\,\mathrm{V} \to \cdots \to -15\,\mathrm{V} \to -20\,\mathrm{V} \to -15\,\mathrm{V} \to \cdots \to -5\,\mathrm{V} \to 0\,\mathrm{V} \to\ . \tag{8.9}$$

  This type of experiment allow us to see the behaviour of Δn_{eff} for $V_s = \pm 20\,\mathrm{V}$ and measure the hysteretic behaviour of the sample for relatively low voltages.

- **Experiment 40 V:** This measurement is exactly the same as the previous one but for higher voltages, i.e. $\Delta V_s = \pm 40\,\mathrm{V}$ with $\Delta V_s = 10\,\mathrm{V}$. The purpose of this measurement is not only increasing the voltage range of the $\Delta n_{eff}(V_s)$ curve, but also, because of the higher voltage, detect a stronger effect of the cladding like hysteresis.

- **Experiment 100 V:** In this case we increase the voltage in steps of $\Delta V_s = 10\,\mathrm{V}$ until $V_s = 100\,\mathrm{V}$ and bring it back to $V_s = 0\,\mathrm{V}$. Then we wait until the resonances reach the same position as in beginning of the experiment, i.e. the system is back to the initial state, before decreasing the voltage until $V_s = -100\,\mathrm{V}$ in the same voltage step. In this case, the effects of the charging and de-charging of the cladding is very high and the $\Delta n_{c_{Slow}}$ contribution is very high.

The previous 4 types of experiments were performed in the order referred above so that the lower voltages are applied to the devices before the higher ones so that the initial state of the device is not highly perturbed by voltage soaking effects, like those reported and described in [66]. Furthermore, all these experiments were done on the two arms of the 5 MZI for the 3 samples. This corresponds to a total of 30 different devices and more than 100 measurements. In what follows we present the selected results and the analysis of the data obtained by the characterization method described above.

8.4 DC characterization results

The results presented in this section were obtained by carefully considering all the data acquired during the high number of measurements performed. For identical devices, we computed the average of the experimental results and the uncertainties are given by the standard deviation of that calculation. All the measurements were done around $\lambda_r = 1.55\,\mu$m.

In what follows we show the most relevant information and graphs to provide an informative view on the results of the DC characterization of the samples presented in this thesis. In addition, we try to match the experimental data with the models developed and presented before in this manuscript and from that make as many conclusions as possible. Nonetheless, some open questions will be raised which we were not capable of answering and could be approached in further developments in a future work.

8.4.1 Comparison of different voltage measurements

In this section we compare the results obtained from the 4 different measurements we made in order to see to what extent the voltage influences the response of the system. To start with, we compare the experiments 10V, 20V, 40V and 100V for the 3 samples. The results are shown in Fig. 8.7 where we present three figures (one for each device) with the Δn_{eff} curves obtained in each one of the measurements. The curves plotted in this figure show that the response of the devices is very different. Nevertheless, the results of the 4 experiments in the same device are consistent: the curves for lower voltages are in general included in the curves for higher voltages.

From Fig. 8.7, it is clear that, even though the curves show a linear regime in a narrow voltage range, the nonlinear voltage dependence and the asymmetry of the curves (the different response for positive and negative voltages) are clearly seen in a wider voltage window. This is expected, because from the analysis made in Chapter 6, both plasma-

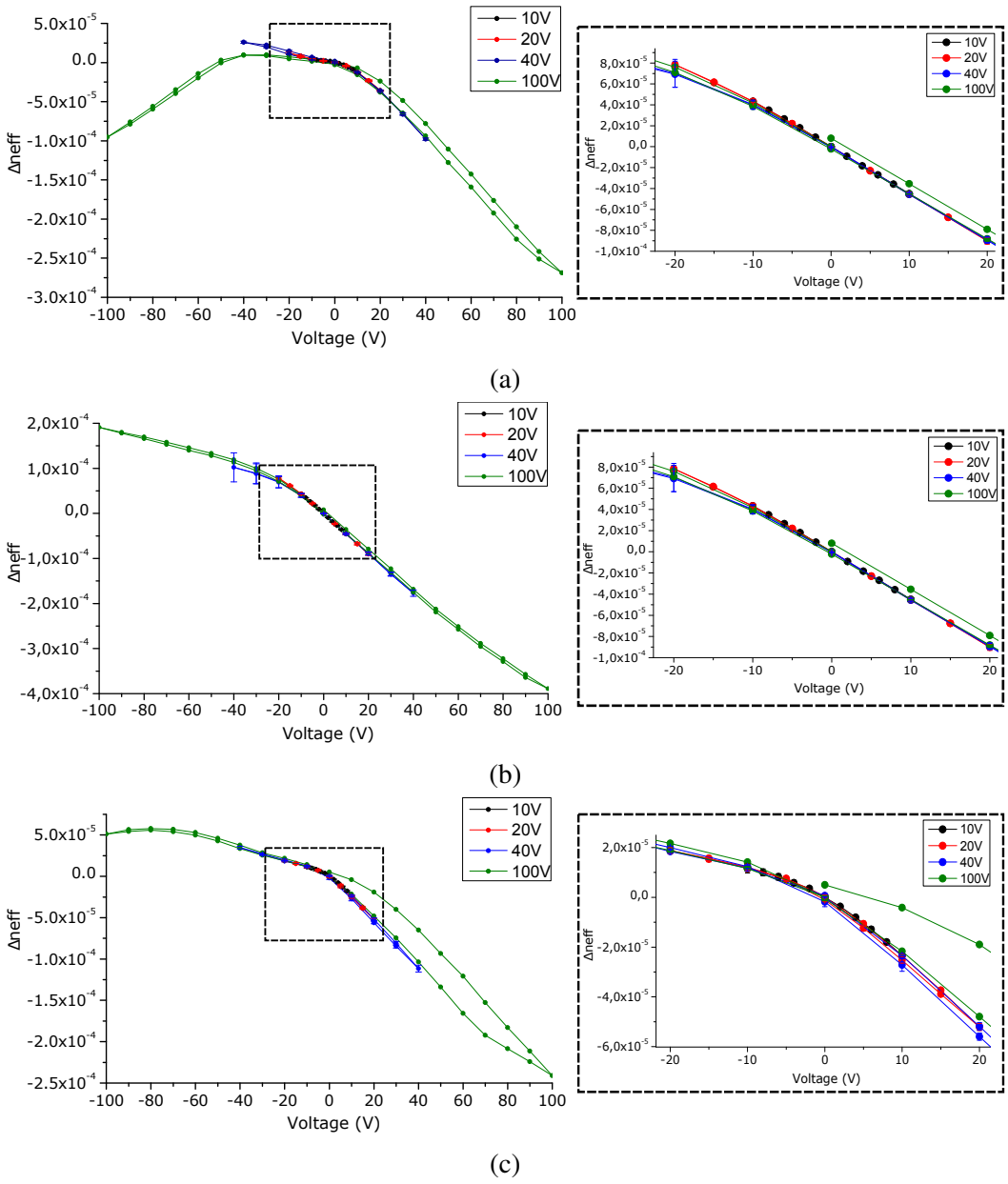

Fig. 8.7 The experimentally detected Δn_{eff} response as a function of V_s for the three devices n the different types of experiments described in the text. (a) Device 0. (b) Device 250. (c) Device 500.

dispersion and Pockels effects are neither linear nor symmetric as a functions of V_s. Yet, it is not straightforward to explain the exact shape of the curves.

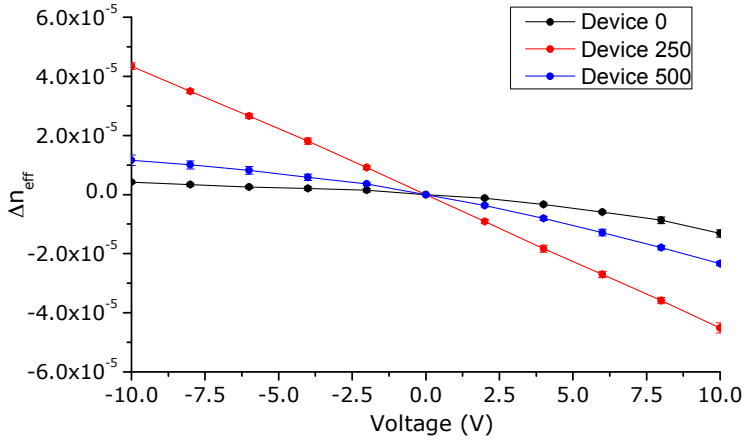

(a)

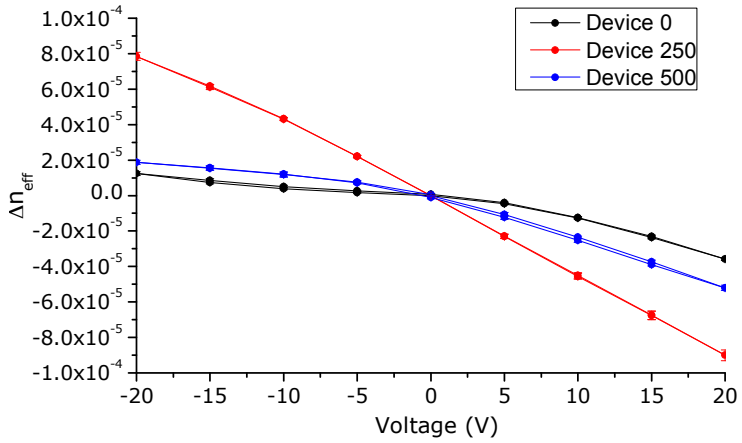

(b)

Fig. 8.8 The voltage dependent Δn_{eff} for the three Devices in experiments 10V (a) and 20V (b).

In order to make a clear comparison between the stacks, we plot in the same graph the response of the 3 Devices, for each type of experiment. In Fig. 8.8 we show the results for the two low voltage experiments: 10V and 20V. In the graphs shown in this figure it is clear that the most efficient is Device 250, where a variation of the applied voltage results in a higher change of Δn_{eff}. For the 10V experiment, there is a high linearity of the Δn_{eff} curve, which is in line with the results reported for this kind of measurements in previous publications [67]. In experiment 20V, however, we start to see both a drift from the linear behaviour close to ± 20 V and also the appearance of a very small hysteretic behaviour, particularly in Devices

0 and 500. The analysis of the low voltage behaviour will deepened in section 8.4.2, where we compare with simulated results.

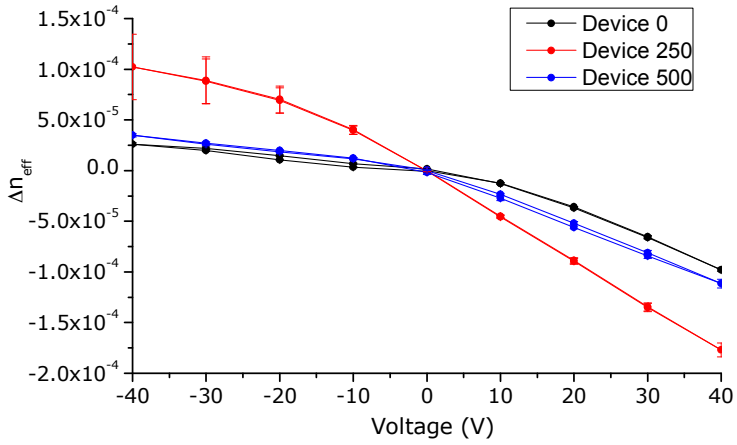

(a)

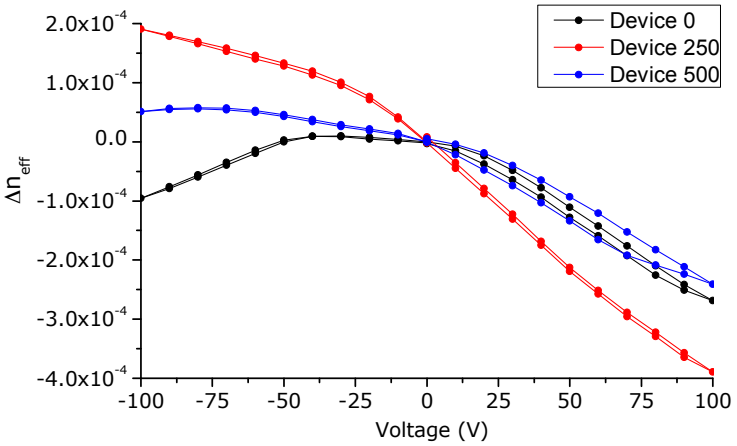

(b)

Fig. 8.9 The voltage dependent Δn_{eff} for the three Devices in experiments 20V (a) and 40V (b).

The high voltage behaviour is presented in Fig. 8.9 and it shows that for higher voltage both hysteresis and nonlinearity increase. The analysis of the high voltage response is not straightforward because we do not know exactly which effects are playing the biggest role, the slow or the fast electro-optic effects. Nevertheless, we can make a qualitative comment on the shape of the curves. The $n_{eff}(V_s)$ curve for Device 0 shows a maximum at $V_s \sim -20\,\mathrm{V}$ which could correspond to the depletion regime of the waveguide, as obtained in Fig. 6.7, even though the experimental results present a much flatter maximum than those simulated. The same phenomenological feature is not found in Devices 250 and 500, which do not present a clear inversion point. By considering only the effects of the plasma dispersion

effect (which we consider to be the strongest effect), the only justification we could find for th e absence of an inversion point requires the existence of a very high value of Q_f in the cladding, which "pushes" the inversion point very far from $V_s = 0$ (see for instance Fig. 6.7a), farther than the voltage range we used experimentally. However, this is not compatible with the assumption that SiO_2 has a smaller value of Q_f than SiN, otherwise Device 0 would present the highest linearity for the widest voltage range.

Nevertheless, if we compare only the results for Device 250 and 500, they show an explainable trend: the overall Q_f of Device 250 is expected to be higher than that of Device 500, because of the higher proximity to the waveguide of the Q_f-rich SiN layer, which justifies a linear behaviour for a wider range of V_s. In fact, unlike Device 250, the curve for Device 500 shows a tendency to go down at $V_s \sim -80\,\mathrm{V}$, due to a lowe value of Q_f in the latter. This reasoning could explain, qualitatively, the behaviour of the curves. Of course, in all of this we assume that Pockels effect is not strong enough to induce a drastic change in the shape of the curves, but could only be capable of perturbing it.

Regarding the hysteretic behaviour, from both Figs. 8.9a and 8.9b we clearly see that the hysteresis increases in the following order: Device 500, Device 0 and Device 250. This trend is strange and from these results it is not clear how the trap filling process, which is responsible for the hysteretic behaviour, takes place and which traps are being filled. The fact that the highest hysteretic behaviour is detected in Device 500 is not in line with the assumption that the traps are mainly located in SiN because the material surrounding the waveguide in this case is SiO_2. Therefore, this could mean that the traps leading to the hysteretic behaviour are not in SiN, but preferably in the SiO_2. In fact, this material is known to possess some traps [67, 173] but by assuming that the hysteresis is caused by traps in the SiO_2, it does not explain why the Device 250 does not possess the same kind of hysteretic behaviour, while presenting even lower hysteresis than Device 0, with no SiO_2 layer (excluding the thin thermally grown silica).

On the other hand, if we consider that the electrons can tunnel through the SiO_2 layer and reach the SiN layer for such high voltage, the higher hysteresis detected for the thickest t_{SiO_2} can be possibly explained due to a higher resistance of the electrons to return to their initial state in the silicon waveguide once the electrostatic field is inverted due to the presence of the SiO_2 layer. These are the different possible situations that we could find to explain the detected hysteretic behaviours. However, it is very hard to find a clear answer to this problem with the available data and its complete understanding is not the purpose of the present research work and it would require specific research and further investigations.

Finally, it is also interesting to notice that the hysteresis occurs preferably for $V_s > 0$. This may give information on the type of traps and their energy levels because it means that

only by applying a positive voltage we move the Fermi level (E_F) closer to the trap filling level, which does not occur for $V_s < 0$.

8.4.2 Fitting with the electro-optic simulations with the experiment

In this section we make an attempt o merge quantitatively the experimental results with the analysis we have done in Chapter 6 for the total electro-optic effect. However, before starting this study, some comments should be done in advance to advert the reader for the difficulty of this analysis and the numerous possible sources of uncertainties during this process.

From the discussion made in Chapter 6, the total electro-optic effect can be given by[1]:

$$\Delta n_{eff} = \Delta n_{eff_c} + \Delta n_{eff_P} = \tag{8.10}$$

$$= \Delta n_{eff_c} + \Gamma_{xxy,xxy}\left(\widehat{\eta_{xxy}^{xxy}} + \zeta\,\widehat{\eta_{yyy}^{xxy}}\right) . \tag{8.11}$$

The dependencies of Δn_{eff_c}, $\widehat{\eta_{xxy}^{xxy}}$ and $\widehat{\eta_{yyy}^{xxy}}$ on the voltage are found by performing FEM simulations using COMSOL, as thoroughly discussed in section 6.5. Therefore, the goal of the present section is the following: find the parameters $\Gamma_{xxy,xxy}$ and ζ that, by using the simulated curves, result in the best fit of eq. 8.10 with the obtained experimental results.

However, there many sources of possible errors in this approach. In order to find the correct fit it would be required that the simulation results for $\Delta n_{eff_c}(V_s)$, $\widehat{\eta_{xxy}^{xxy}}(V_s)$ and $\widehat{\eta_{yyy}^{xxy}}(V_s)$ describe *exactly* the real response of the device. Yet, it is not easy to ensure this for different reasons. On the one hand, even though the plasma-dispersion simulation results we obtained and described in section 6.5 were in line with the main publications on this topic [66–68], these results may possibly not quantitatively describe the sample response perfectly, as also acknowledged and reported in Ref. [68]. In order ensure that, separate and independent experiments designed specifically to validate the plasma-dispersion simulations quantitatively would be required. Without that, even though the simulated $\Delta n_{eff_c}(V_s)$, $\widehat{\eta_{xxy}^{xxy}}(V_s)$ and $\widehat{\eta_{yyy}^{xxy}}(V_s)$ curves may present the correct trends, if the numerical values are not *exactly* those of the real experiment, it will considerably compromise the fitting process.

On the other hand, as it was referred many times throughout this manuscript, a complete knowledge of the trapping and charging mechanism is required to properly simulate the structure. By complete knowledge, we mean not only the numerical value of Q_f and D_{it}, but also their spatial distribution inside the cladding, because the waveguide can be considered a 2D object and the distribution of charges and traps in both x and y direction are equally important. Furthermore, it is also relevant to know how the charges are located inside the

[1] Recall that $\zeta = \Gamma_{xxy,xxy}/\Gamma_{xxy,yyy}$ from eq. 6.15.

SiO_2 and SiN layers, because different distributions in the stacks result in different electro-optic behaviours. Since the experiments to know *exactly* the referred distribution of the charges and traps in the cladding are still on-going (being performed by Mathias Berciano, a PhD student involved in this research project), we do not have all the information required to properly simulate the structures correctly, which can be a major source of errors.

With the previous considerations in mind, in the simulations performed in this section we used the information available in the literature for the Q_f distribution in the cladding, particularly that reported in [67]. The reported values are $Q_f = 3 \times 10^{12}\,\mathrm{cm}^{-2}$ for the Si/SiN interface and $Q_f = 1 \times 10^{12}\,\mathrm{cm}^{-2}$ for the Si/SiO_2 interfaces. These values, however, do not provide information about the charge distribution over the whole cladding and represent only an effective value at the interface. Therefore, we may question whether there is an effective Q_f in the SiN/SiO_2 interface resulting from the bulk charge inside the SiN layer. From the analysis made in section 5.3 (and this is why that section is so relevant) we may expect a volume fixed charge ($Q_{f_{vol}}$) distribution inside the SiN layer because of the spread distribution of the K centres inside the SiN bulk. This will inevitably correspond to an effective Q_f distribution in the SiN/SiO_2 interface. For that reason, we considered $Q_f = 2 \times 10^{12}\,\mathrm{cm}^{-2}$ in the SiN/SiO_2 interface (for Devices 250 and 500), as shown in Fig. 8.10. In fact, we found that only by considering this effective interface charge in the SiN/SiO_2 layer, we could find a relevant match between simulations and the experiment, confirming that this kind of information is essential for properly simulate the devices performance and it can make all the difference when comparing experiment with simulations.

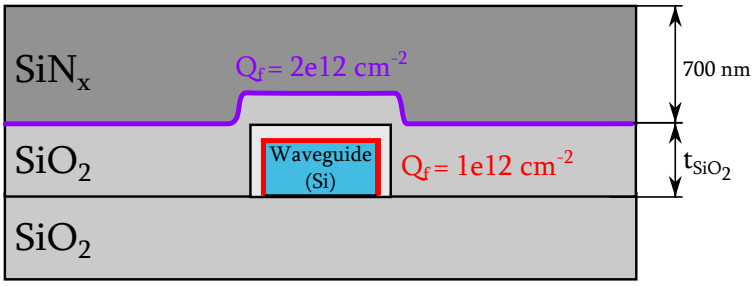

Fig. 8.10 Configuration of fixed carriers assuming different Q_f at both SiO_2 interfaces: with the Si and with SiN.

In the fitting process we only considered the 10V experiment because the contribution from $n_{eff_{c-Slow}}$ is considerably smaller in this case. Thus, the fitting process consists of finding the best $\Gamma_{xxy,xxy}$ and ζ parameters that result in the best fit between the measured experimental values (in the 10V Experiment) and eq. 8.10, using the curves Δn_{eff_c}, $\widehat{\eta_{xxy}^{xxy}}$ and $\widehat{\eta_{yyy}^{xxy}}$ simulated as described above. These two fitting parameters, however, should be the

same for all the experiments because, as we discussed in Chapter 3, the Γ coefficients depend only on the crystal itself, which is the same for all experiments.

In Fig. 8.11 we present, for each one of the 3 Devices, the three simulated curves together with the corresponding experimental data and the best fitting curve, with the respective $\Gamma_{xxy,xxy}$ and ζ. The curves in Fig. 8.11 show that, the results of Device 0 are not as good as those of Devices 250 and 500: not only the fitting parameters are considerably different for these two sets of devices, but also Devices 250 and 500 present a much better fitting than the Device 0. The difference we detected experimentally (consistently) for Devices 0 and Devices 250 and 500 in almost every experiment is attributed to the fact that these two sets of devices were fabricated with a time gap of some months. Because the charging conditions of the cladding is so dependent on the deposition conditions and because the PECVD system we had available is susceptible to undergo some changes over a time period of months, we suspect that the electronic properties of the cladding is not exactly the same in Device 0, which can justify such a big different behaviour in respect to the other two samples. For this reason and because we cannot establish a consistent relation with all the 3 Devices, in what follows we concentrate only on the comparison and analysis of Devices 250 and 500.

The results shown in Fig. 8.11 show that the best fitting correspond to

$$\Gamma_{xxy,xxy} = -2.2 \times 10^{-13}\,\mathrm{m}^2/\mathrm{V} \quad \text{and} \quad \zeta = 1.3\,, \quad \text{for Device 250} \tag{8.12}$$

$$\Gamma_{xxy,xxy} = -2.2 \times 10^{-13}\,\mathrm{m}^2/\mathrm{V} \quad \text{and} \quad \zeta = 1.1\,, \quad \text{for Device 500.} \tag{8.13}$$

Since these parameters should be the same for all the samples, we found that the combination

$$\Gamma_{xxy,xxy} = -2.2 \times 10^{-13}\,\mathrm{m}^2/\mathrm{V} \quad \text{and} \quad \zeta = 1.18 \tag{8.14}$$

resulted in the a good fitting for both experiments, as shown in Fig. 8.12. The fact that the data for both Device 250 and 500 presents a reasonable match with experiment for the same values of $\Gamma_{xxy,xxy}$ and ζ is a very positive sign to support the model suggested throughout this thesis. These results correspond to the following values of the corresponding Γ coefficients:

$$\Gamma_{xxy,xxy} = -2.2 \times 10^{-13}\,\mathrm{m}^2/\mathrm{V} \tag{8.15}$$

$$\Gamma_{xxy,yyy} = -3.74 \times 10^{-13}\,\mathrm{m}^2/\mathrm{V}\,. \tag{8.16}$$

The first noticeable thing about these values is their order of magnitude, which is almost 3 orders higher than our first rough estimates for the Γ coefficients back in eq. 3.99. This is the reason why we stated very clearly in that analysis that our purpose was not to find a very good theoretical estimation of Γ but only the physical properties could provide viable results.

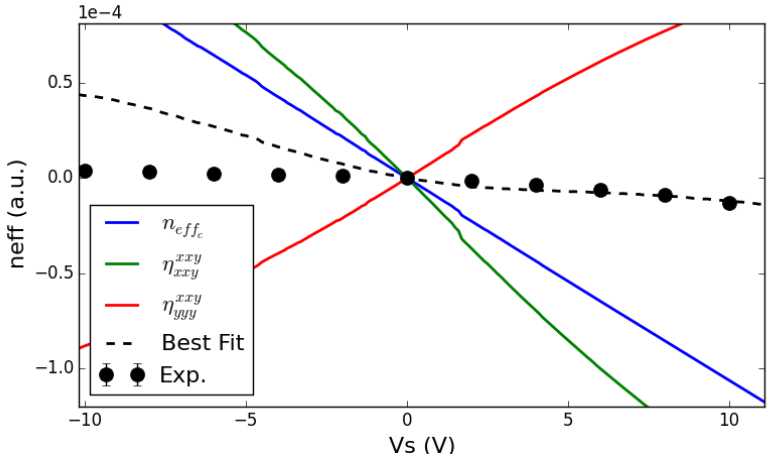

(a) Device 0: $\Gamma_{xxy,xxy} = -2 \times 10^{-13}\,\mathrm{m}^2/\mathrm{V}$ and $\zeta = 1.4$.

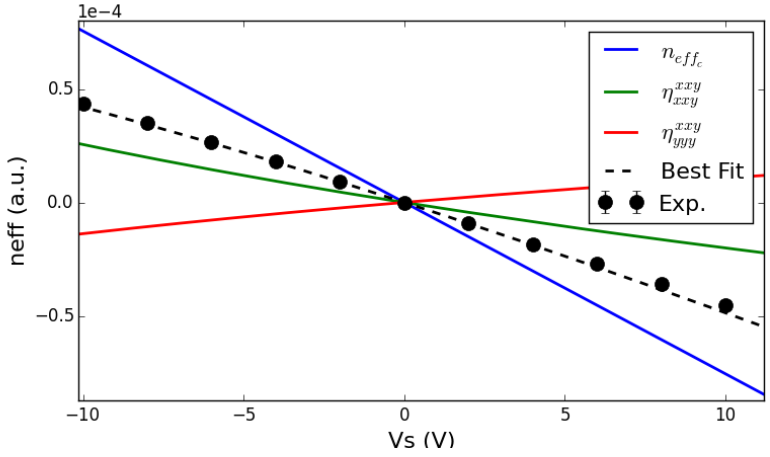

(b) Device 250: $\Gamma_{xxy,xxy} = -2.2 \times 10^{-13}\,\mathrm{m}^2/\mathrm{V}$ and $\zeta = 1.3$.

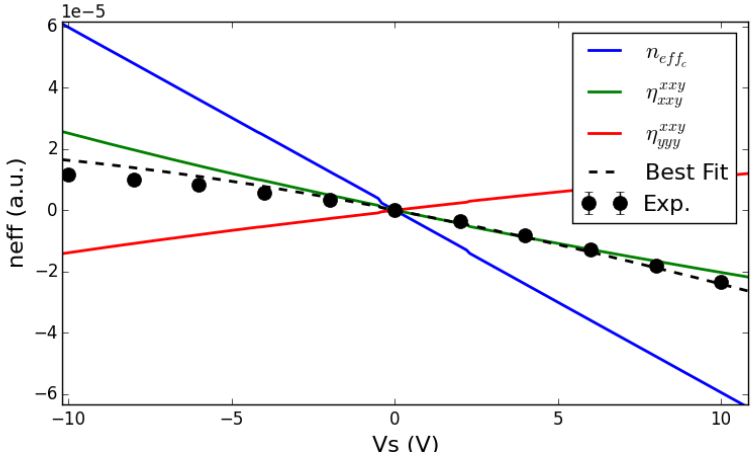

(c) Device 500: $\Gamma_{xxy,xxy} = -2.2 \times 10^{-13}\,\mathrm{m}^2/\mathrm{V}$ and $\zeta = 1.1$.

Fig. 8.11 The voltage dependent curves of Δn_{eff_c}, $\widehat{\eta^{xxy}_{xxy}}$ and $\widehat{\eta^{xxy}_{yyy}}$ considering $Q_f = 3 \times 10^{12}\,\mathrm{cm}^{-2}$, $Q_f = 2 \times 10^{12}\,\mathrm{cm}^{-2}$ and $Q_f = 1 \times 10^{12}\,\mathrm{cm}^{-2}$ for the Si/SiN, SiN/SiO_2 and Si/SiO_2 interfaces respectively. The best fitting curve, using the fitting parameters in the corresponding caption are also represented. All the curves were offset so that $n_{eff} = 0$ for $V_s = 0\,\mathrm{V}$.

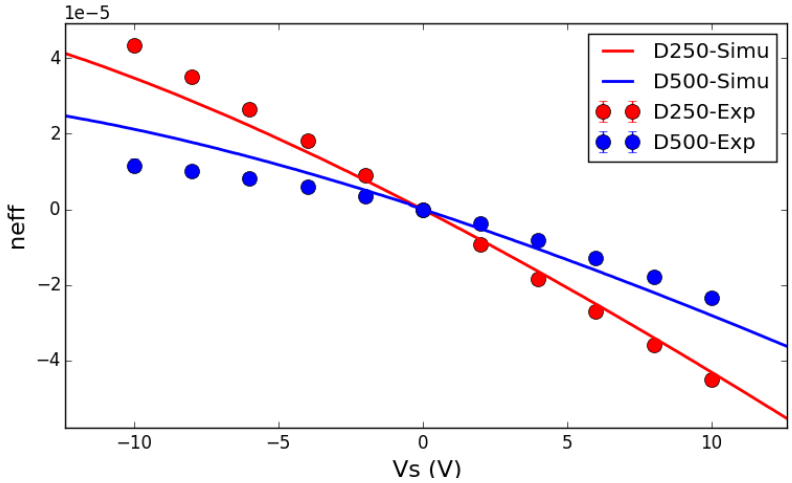

Fig. 8.12 Comparison between experiment and simulations for $\Gamma_{xxy,xxy} = -2.2 \times 10^{-13}\,\mathrm{m}^2/\mathrm{V}$ and $\zeta = 1.18$ for Devices 250 and 500.

The parameters should be determined experimentally because the approximate method we used to make a numerical estimation does not take into account many potential contributions that could and should play an important role in the results. Furthermore, as reported in Ref. [94], the higher the order of the nonlinearity, the more sensitive is the corresponding susceptibility to the numerical values of the Bond Orbital Model, so it is not surprising that an over simplification in the theoretical analysis of $\chi^{(2)}$ can result in a drastic difference in the comparison with experiments. Nonetheless, this value is much higher than what we could possibly estimate with our theoretical model, which can raise questions about the viability of the theory developed so far. For that reason a commentary will be made about that in section 8.4.4.

Finally, the two Γ parameters can be used to calculate both α and β parameters (defined in Chapter 3) through equation 3.92 for $\varphi = 0$ and this results in

$$\alpha = 4.31 \times 10^7\,\mathrm{J/m^2} \quad \text{and} \quad \beta = -6.45 \times 10^7\,\mathrm{J/m^2}\,. \tag{8.17}$$

The analysis performed in this section can be tested by comparing the experimental results obtained for the crystal orientation dependence with the theory developed in 3.92 using these values of α and β.

8.4.3 The effect of crystallographic direction on the electro-optic effect

In this section we analyse the effect of the crystal orientation of the waveguides on the electro-optic response, limiting the analysis to the 10V measurements because the results

should be valid for lower voltages where n_{eff_P} is not as affected by the cladding effects. The results for the three angles we measured $\varphi = 0°$, 15° and 30° for the three Devices are shown in the Fig. 8.13.

The curves shown in Fig. 8.13 show a clear angle dependence of Δn_{eff}. By comparing the values of Δn_{eff} at $V_s = 10\,\mathrm{V}$ as a function of the 3 angles, as shown in Fig. 8.14, we see that the Δn_{eff} is an increasing function with the angle, except for Device 500. However, we could not find a physical reason for the strange behaviour of this particular device and could be due to experimental errors.

From the discussion made in Chapter 6, we expect the strain applied to the silicon waveguide to decrease with the SiO_2 thickness (t_{SiO_2}). Therefore, we also expect the dependence of Δn_{eff} on the angle φ to increase from Device 500 to Device 0. Since the dependence on φ should depend on the relative change of Δn_{eff} with the angle, we define the following relative quantity

$$\Theta(\varphi) = \left| \frac{\Delta n_{eff}(\varphi) - \Delta n_{eff}(0°)}{\Delta n_{eff}(0°)} \right| , \tag{8.18}$$

to compare the relative change in angle with the applied strain between Devices.

The results for $\Theta(30°)$ as a function of the Device number are shown in Fig. 8.15. We were expecting this to be a decreasing function of the device number, but that is not what the graphs show, where Device 250 presents a higher $\Theta(30°)$ than Device 0. Once again, just like what we described in the previous section, the results from Device 0 are not in line with those of the other two devices and we will concentrate on Devices 250 and 500 for the exact same reasons discussed before.

In fact, if we concentrate only on Devices 250 and Device 500, we find a promising agreement with the experimental curves and the simulations, using the α and β parameters obtained in the previous section. To check that, we inserted the corresponding values obtained in eq. 8.17 into eq. 3.92, given by

$$\Gamma_{xxy,xxy}(\varphi) = \frac{d^6 k}{27\epsilon_0} \left[(5\beta - 3\alpha - (\alpha + \beta)\cos(4\varphi)) \right] \tag{8.19}$$

$$\Gamma_{xxy,yyy}(\varphi) = -\frac{d^6 k}{27\epsilon_0} \left[2(\alpha - 3\beta) \right] \tag{8.20}$$

in order to determine the angle dependence of the Γ coefficients. Since the only relevant angle dependence of eq. 8.10 are in the coefficients $\Gamma_{xxy,xxy}$ and ζ, we use the previous set of equations to calculate the expected angle dependence of Δn_{eff}. The results are shown in Fig. 8.16, for both Device 250 and Device 500. We can see that there is a considerable agreement in this voltage range, particularly for the curve of Device250. For Device500,

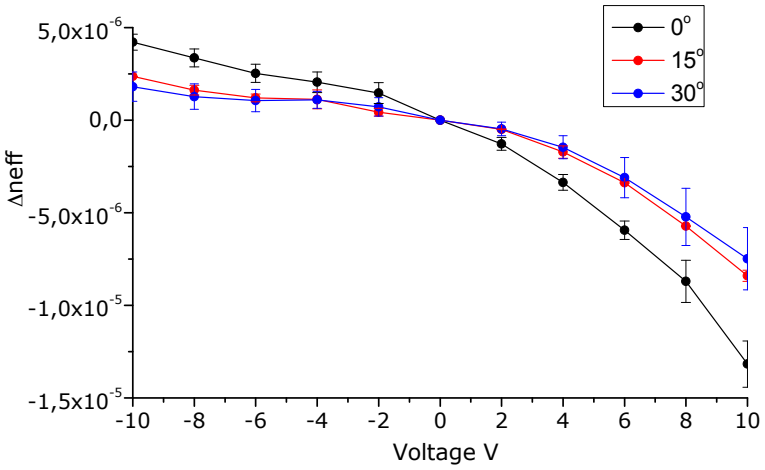

(a) Device 0

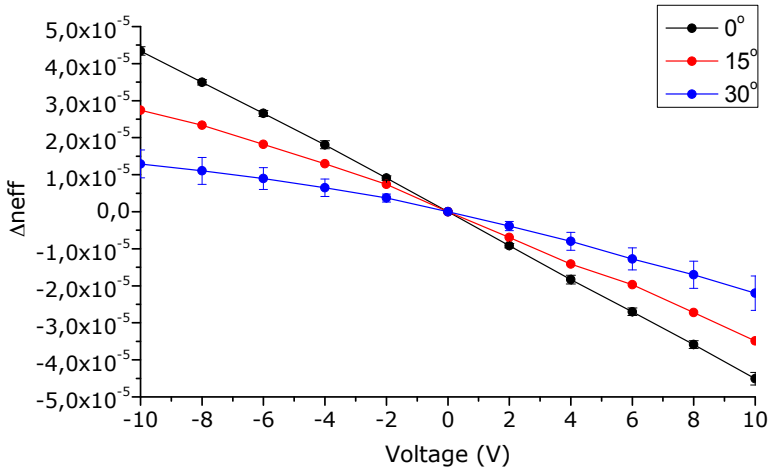

(b) Device 250

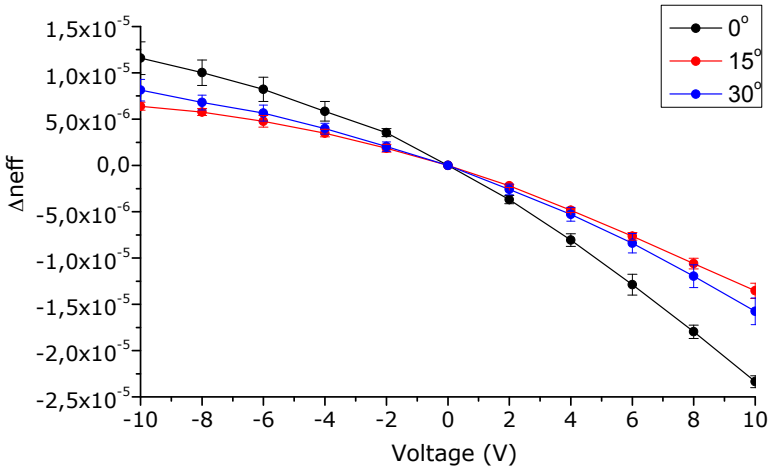

(c) Device 500

Fig. 8.13 The angle dependence of the Δn_{eff} curves for the three devices in the 10V measurements.

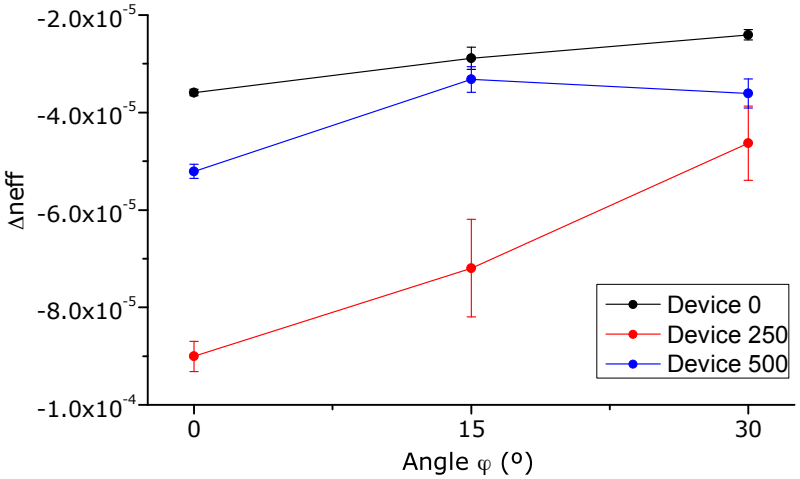

Fig. 8.14 The value of Δn_{eff} at $V_s = 20\,\mathrm{V}$ as a function of the angle for the tree devices.

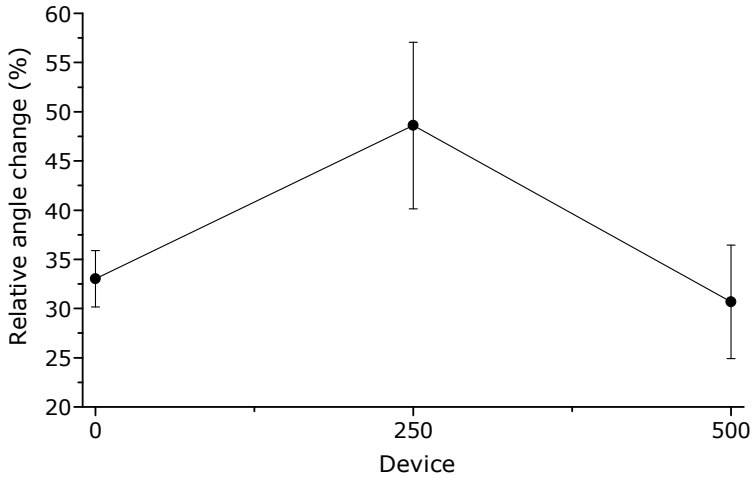

Fig. 8.15 The relative angle change at $\varphi = 30°$, defined by $\Theta(30°)$ in eq. 8.18 as a function of the device number.

however, the agreement is not as good, but it matches the trends of both the curve shape and in the angle dependence trend. Furthermore, it is remarkable that a single set of α and β can actually explain the Δn_{eff} response for 2 different devices and 3 different angles, in agreement with the theoretical model used throughout this thesis.

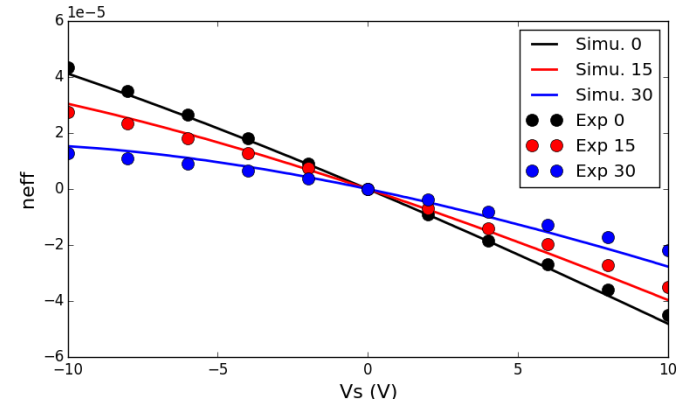

(a)

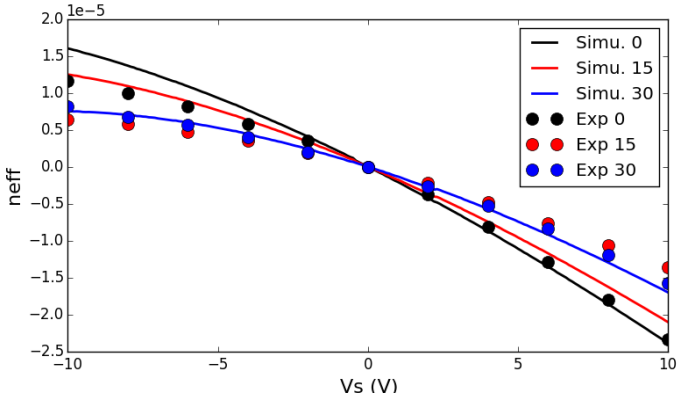

(b)

Fig. 8.16 Comparison between experiment and simulations for $\alpha = 4.31 \times 10^7\,\mathrm{J/m^2}$ and $\beta = -6.45 \times 10^7\,\mathrm{J/m^2}$ as defined in eq. 8.17 for the three angle orientations and for Devices 250 (a) and Device 500 (b).

8.4.4 Comment on the obtained results

The treatment performed above showed considerable agreement with the data for Device 250 and also (even though not as good) for Device 500, for the 10V experiment and a single set of the α and β coefficients. This is a interesting fact because it shows that the models developed throughout this thesis can actually be applied to explain some trends in the Δn_{eff} curves and other phenomena like the crystal orientation dependence.

However, it is also true that there is too much flexibility in the approach we used, i.e. the parameters $\Gamma_{xxy,xxy}$ and ζ were allowed to change freely and without any restriction. By doing that, the fitting problem is not a problem with a single and unique solution and there may be several combinations of parameters that fit curves in such a short voltage range. Moreover, the fact that the Device 0 did not match the results like the other two devices can contribute to the question our methods.

In fact, our results for Devices 250 and 500 were only achievable when a higher concentration of charges was considered (in the interface SiN/SiO_2). As we see from the simulations presented throughout this thesis, the dependence on the Q_f value is enormous. Thus, in order to be sure of the charge state of the SiN and SiO_2 layers, the Q_f in the stack must be determined experimentally with high precision. Furthermore, a good understanding of how free-carriers interact with these charges is required to have complete control over the problem. This information could possibly be acquired by measuring the capacitance (C) vs V_s curves of the different stacks in a MIS configuration to determine Q_f and D_{it}, but an even deeper analysis would be required to determine their distribution.

Finally, we should comment on the numerical values obtained. The Γ parameters we have found in eq. 8.15 can be used to calculate $\chi^{(2)}$ in the sample:

$$\chi^{(2)}_{xxy}(\boldsymbol{r}) = \Gamma_{xxy,xxy} \cdot \eta_{xxy}(\boldsymbol{r}) + \Gamma_{xxy,yyy} \cdot \eta_{yyy}(\boldsymbol{r}) \, . \tag{8.21}$$

The distribution of $\chi^{(2)}_{xxy}$ in the waveguide is computed by summing the distributions of η_{xxy} and η_{yyy} (presented in Fig. 6.9), weighted by the coefficients Γ in eq. 8.15. The result is shown in Fig. 8.17. That picture, shows that $\chi^{(2)}$ may vary immensely from positive to negative inside the waveguide and its highest values are located close to the borders. This is due to a variable strain gradient direction throughout the waveguide and the average $\chi^{(2)}$ inside the waveguide is calculated to be $-120\,\mathrm{pm/V}$. This value can be considered very high, particularly when we compare with the predictions made back in Chapter 3 and with the experimental results reported recently [34, 71].

However, it must be referred that this average means very little in a Pockels effect point of view. In fact, the local Pockels change of refractive index in the waveguide (Δn_P) is given by

$$\Delta n_P = \epsilon_0 \, n_{\mathrm{Si}} \, \chi^{(2)} \cdot \Delta F \, , \tag{8.22}$$

and if ΔF is very small, $\chi^{(2)}$ must be high to compensate, so that Δn_P remains relevant. In fact, ΔF varies very little inside the silicon waveguide because its free carriers and the charges in the cladding screen the electrostatic field for a change in applied voltage. This

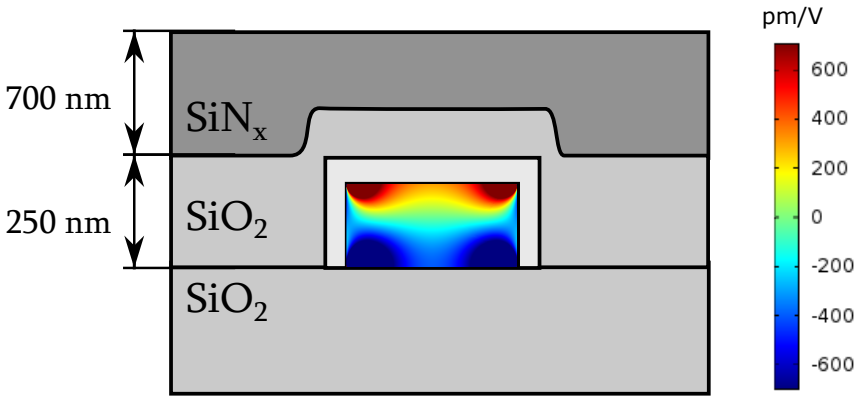

Fig. 8.17 Distribution of $\chi^{(2)}$ in the Device 250 structure ($t_{SiO_2} = 250\,\text{nm}$ assuming the fitting paramters $\Gamma_{xxy,xxy} = -2.2 \times 10^{-13}\,\text{m}^2/\text{V}$ and $\zeta = 1.18$.

small variation can be seen by the profile of the simulated F_y distribution in the waveguide shown in Fig. 5.16[2].

All in all, the mentioned high value of $\chi^{(2)}$ results from a measured experimental value of $\Delta n_{eff_P} \sim 1 \times 10^{-5}$ for a variation of $\Delta V_s \sim 10\,\text{V}$, which is a rather small value, as expected. This also means that under these conditions, if $\chi^{(2)}$ was considerably smaller (as one could expect), the variation of the $n_{eff} \sim 1 \times 10^{-5}$ with the crystal orientation achieved for $\Delta V_s \sim 10\,\text{V}$ could not be explained by a Pockels effect variation and it could only mean that there was some other unknown contribution that we did not take into account.

Finally, it should also be mentioned that the estimation of the value of $\chi^{(2)}$ is extremely sensitive to the Γ coefficients, which means that unless we make a precise and correct experimental determination of these parameters, we cannot have a sure knowledge of the $\chi^{(2)}$ distribution.

To sum up, we can wrap up the experimental results of this section as follows:

1. The results for Devices 250 and 500 follow the expected trends, but Device 0 does not;
2. We have found that

$$\alpha = 4.31 \times 10^7\,\text{J/m}^2 \quad \text{and} \quad \beta = -6.45 \times 10^7\,\text{J/m}^2\,. \tag{8.23}$$

   was the set of parameters that ensured the best match between experimental results and simulations, when considering a cladding charge distribution as shown in Fig. 8.10.
3. The resulting values of Γ could explain both the behaviour of the curves for Devices 250 and 500 for low voltages, but it had it could not lead to an agreement with the

[2]Similar results were also reported by Sharma *et al.* in [67]

results from Device 0. This could mean that the simulations are not replicating the real situation, or that the device is not working as we suppose and further studies are required.

4. The values of α and β obtained were capable of explaining the numerical variation of Δn_{eff} with the angle for Devices 250 and 500.

5. The same values of Γ predict a distribution of $\chi^{(2)}$ given in Fig. 8.17, which present very high values of $\chi^{(2)}$. However, if we consider that the crystal orientation dependence is due to Pockels effect alone, only Γ values on these orders of magnitude can explain a variation $n_{eff} \sim 1 \times 10^{-5}$ for $\Delta V_s \sim 10\,\mathrm{V}$, as we have detected experimentally.

It is clear that the presented study is not sufficiently conclusive for a strong validation of the models presented in this thesis, but the results shown in this section and the reasonable fitting of the curves for the crystal orientation dependence and for the Devices 250 and 500 with a single set of α and β coefficients are very promising and encouraging. This suggests that the theory we presented in this work may indeed be capable of explaining the strain-induced Pockels effect in silicon. Lastly, it is worth to stress that the high angle dependence we have detected could mean that, after-all, the strain-induced Pockels effect in silicon can be indeed a considerably stron and that strain can efficiently generate second order nonlinear effects in this material.

8.5 Characterization of the high speed response of the devices

In this section we make the analysis of the high speed characterization of the strained silicon devices. In this study we considered only the Device 0, because it was the device expected to possess higher levels of strain and thus stronger Pockels effect. Finally, we only present the results for devices oriented with $\varphi = 0°$ because the measurement of the other orientations did not show any considerable difference. Therefore, all the data presented in this section is referred to Device 0 oriented in the $[110]$ direction of the crystal.

8.5.1 The experimental set-up and methodology for RF characterization

The RF characterization of the devices consisted in measuring the *S* parameters of the whole system. The S_{21} parameter corresponds to the transmission, i.e. the optical modulation,

whereas the S_{11} parameter corresponds to the reflection, i.e. the RF signal reflected and detected in the input port. A deeper analysis on these phenomena can be found elsewhere [203].

In order to measure the RF response of the Device (the S_{21} parameter) some changes needed to be made to the set-up presented in Fig. 8.1 and configuration for the high speed characterization is shown in Fig. 8.18. The working principle is similar to the DC characterization set-up, so we refer the reader to the description of the DC optical bench, for more detailed explanations. However, some critical modifications were made in the optical and electrical parts of the bench to adapt to the high frequency modulator, which are described below.

RF set-up changes to the optical part

The optical response detected from the modulation, depends on the power of the optical signal which must be high enough so that the modulation is detected. With the configuration presented in Fig. 8.1 the optical signal did not have enough power. Therefore, we introduced two Erbium-Doped Fiber Amplifiers (EDFA) optical amplifiers, both operating in the wavelength window from 1535 nm to 1570 nm, in the input and in the output of the set-up. With the introduction of these two optical amplifiers, we could amplify the optical signal enough to detect a modulated optical signal.

The amplifiers, however, introduced some noise to the optical spectrum and this was particularly relevant in the output because it introduces noise to the modulated signal. In order to reduce the noise, we placed a narrow band optical filter after the output EDFA to filter the noise introduced by the amplifier and pass wavelengths in a narrow spectrum around the operating wavelength. This cleaner signal was then guided into the photo-detector located in the Network Analyser.

A 90/10 splitter was also introduced so that a small fraction of the signal was sent to the CT400 which allowed for the control of the output intensity during alignment. In addition, we could also analyse the transfer function of the MZI, useful to select the operating wavelength.

RF set-up differences: electrical part

The electrical part was drastically changed to accommodate high frequency signals. All the optoelectronic analysis was done using an "Agilent Lighwave Component Analyser". This machine generated the RF signal which was then compared with the optical signal detected in its integrated photo-detector to measure the frequency dependent optical response of the device under test.

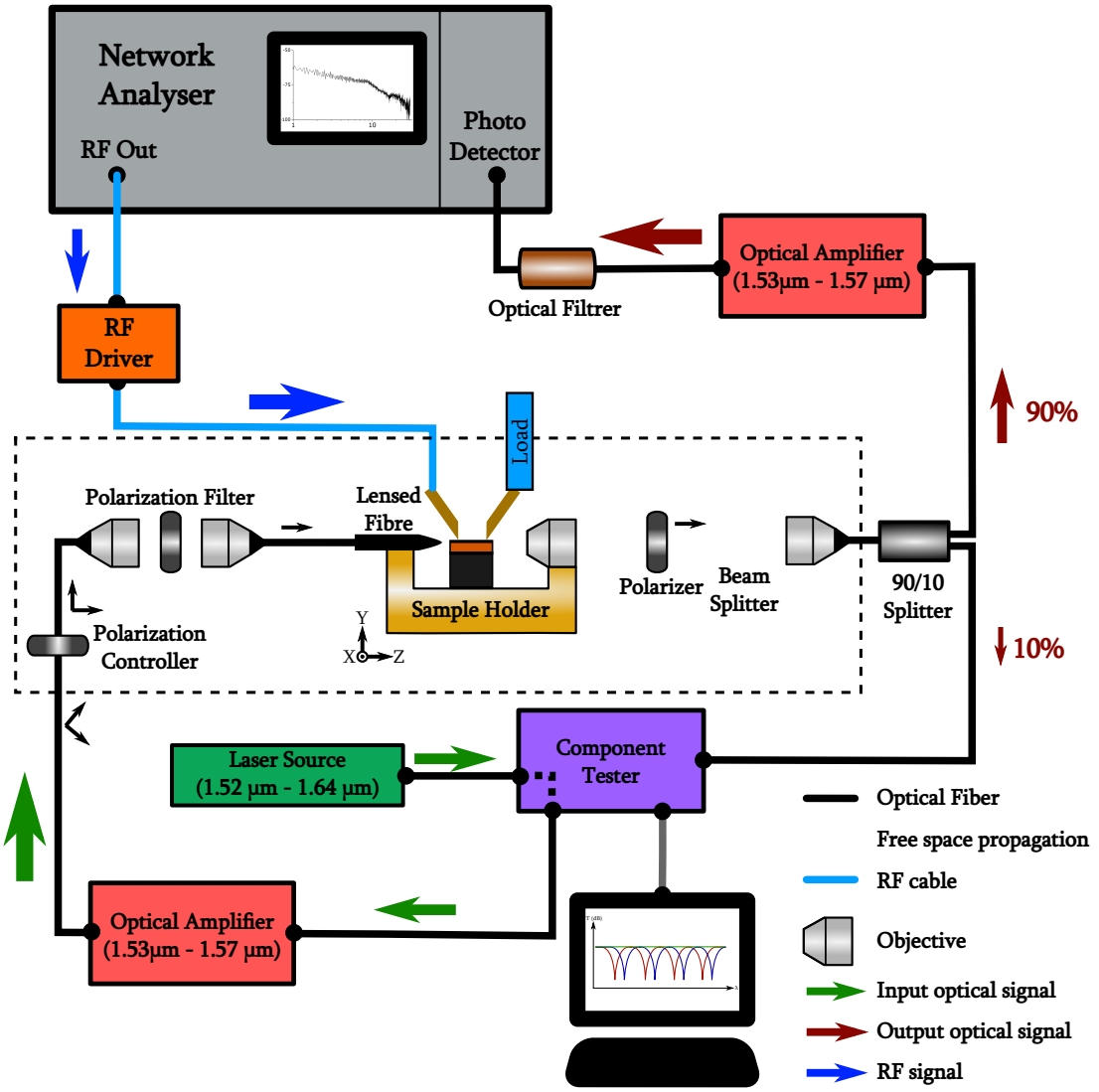

Fig. 8.18 Schematic representation of the optical and electrical set-up to characterize the devices driven by a RF electrical signal. For simplicity reasons, we did not present the parts corresponding to the CCD and IR cameras, which can be seen in Fig. 8.1 for the DC set-up.

The RF signal generated in this machine was directed into an RF driver capable of amplifying the RF signal by ∼27 dB up to 38 GHz. Furthermore, the BNC cables and electrical probes were changed to their RF adaptable counterparts (compatible with frequencies up to 50 GHz), so that they do not limit the performance of the system. The complete electrical set-up built in this way is capable to accommodate frequencies until ∼35 GHz, which was largely enough for our purposes.

8.5.2 The electrical response to a RF signal

Before doing the optoelectronic measurement, the RF characterization system must be calibrated to the desired frequency range (100 MHz − 35 GHz). This process involved measuring the electrical response at open circuit, short circuit and 50 Ω load. Furthermore, in order to accurately describe the optoelectronic results, the spectral bandwidth of the electrical system alone should be characterized in advance. We did so by making an isolated measurement of the spectral response of the individual elements that constitute the electrical system: the "RF driver + cables" and "cables + electrodes in the sample". The results are shown in Fig. 8.19.

Firstly, we can see that the "RF driver+cables" group has a stable response up to 10 GHz, corresponding to a rather "flat" amplification of 20 dB.

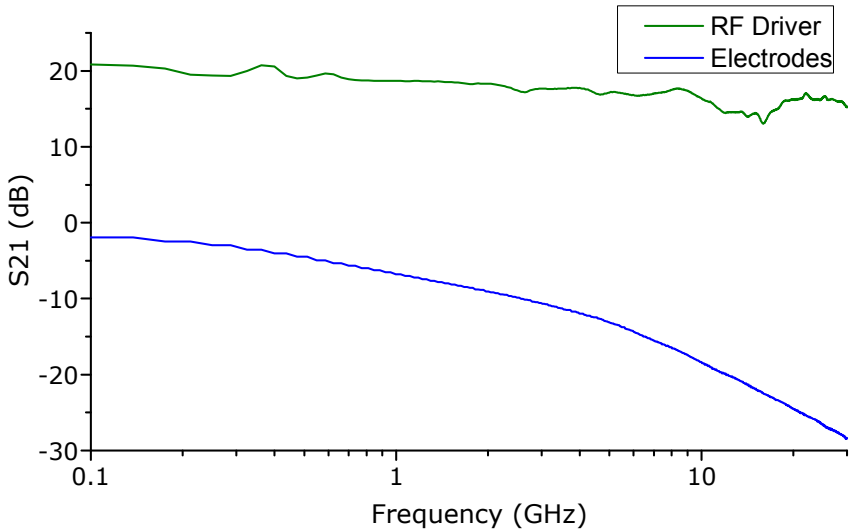

Fig. 8.19 The spectral response of the S_{21} parameter of the electrical components: the RF-Driver and the electrodes of the sample. Both plots include the cables response.

However, the response of the electrodes of the sample, in blue, is very limiting. The design of the electrodes discussed in section 6.4.3, for the adaptation to a 50 Ω line was

successfully made because the detected input reflection (S_{11} parameter) was very weak in the studied frequency range. The source of the limited spectral response of the electrodes, though, is their intrinsic loss. In fact, preliminary simulations (made by Mathias Berciano) and fruitful discussions with Professor Paul Crozat, an expert in high frequency signal communications collaborating with our group, have led to the conclusion that the coplanar configuration becomes very lossy at high frequencies. In order to overcome this limitation of the electrodes, new electrode geometries must be investigated. From the results presented in Fig. 8.19, we conclude that the optical cut-off frequency of the complete electrical line is 1.7 GHz and it is highly limited by the electrodes.

8.5.3 Characterization of the RF-driven optoelectronic response

In a MZI, optical modulation occurs because the resonances shift due to the electro-optic effect induced by the applied electric field of the RF signal. The output spectrum of Device 0 in the high speed characterisation process is shown in Fig. 8.20. The wavelength range is limited by the EDFA's, which covers $1530-1570$ nm. There is an optimal working point in the spectrum of a MZI resonance to achieve the highest modulation efficiency, which corresponds to the green wave represented in the scheme at the right side of Fig.8.20, because the same resonance shift leads to higher signal modulation. For the spectrum of our device, the selected working point was $\lambda_0 = 1551$ nm, as shown in Fig. 8.20.

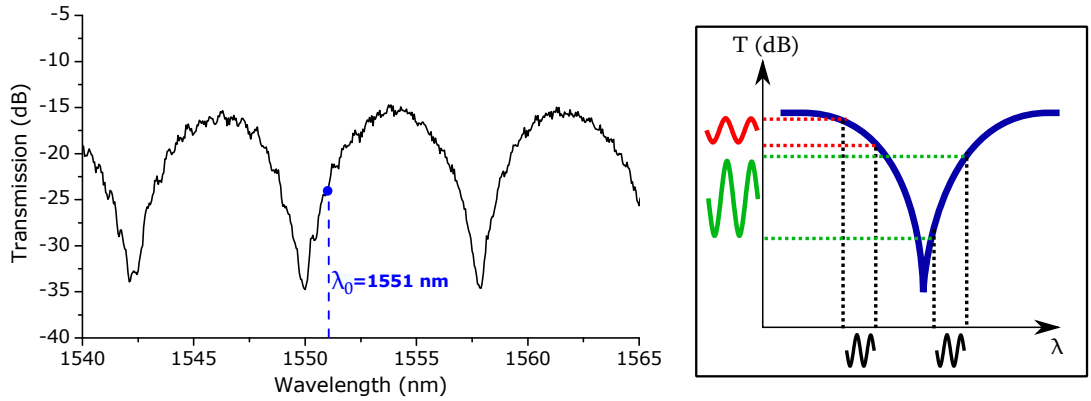

Fig. 8.20 The spectrum of the MZI used for the RF characterization with the corresponding selected operation wavelength λ_0. The wavelength range considered is the same as the input EBFA. The figure on the right shows how to choose the most efficient operation wavelength.

The optical response measured by the photo-detector in the network analyser at $\lambda_0 = 1551$ nm is presented in Fig. 8.21. This corresponds to the S_{21} parameter of the whole optoelectronic system and we can see that a clear modulation of the optical signal is detected.

Furthermore, the optical response is 10 dB above the noise level until almost 20 GHz, which means that there is a physical mechanism capable of modulating light at such high frequencies. Since the free-carrier effects are limited above the $1-5$ GHz range, the only electro-optic effect fast enough to be able to respond to such high frequencies in this particular sample is expected to be the strain-induced Pockels effect. Of course, this cannot be considered as a complete proof and further measurements would be required. Nonetheless, it is a very strong hint that Pockels effect may be in the origin of this small, but detectable modulation.

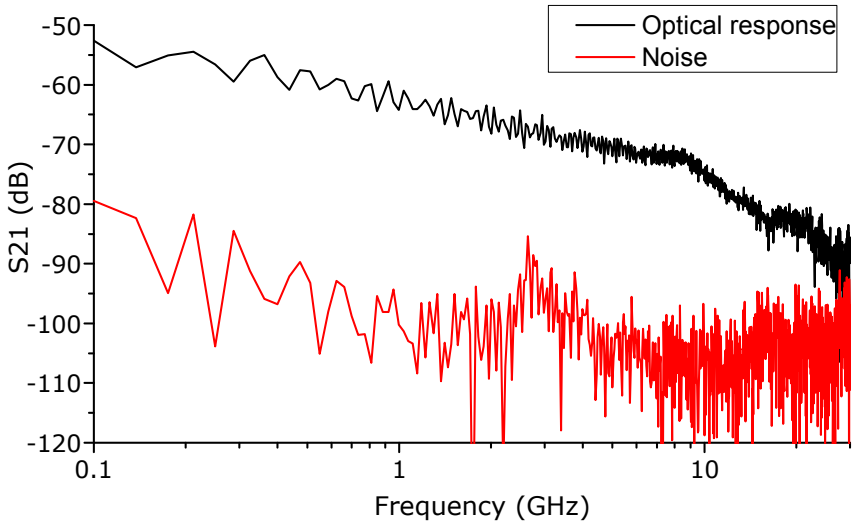

Fig. 8.21 The spectral response of the device at $\lambda_0 = 1551$ nm considering every element of the set-up, i.e. the actual data detected by the photo-detector in the Network Analyser. The noise level is also plotted.

In the spectrum of Fig. 8.21 we see a sudden drop of the optical response at $\sim$10 GHz. This feature arises from the influence of the RF driver, as we can see from its spectral response in Fig. 8.19. To remove the effect of the amplifier in order to analyse the performance of the sample alone, we subtract its response (green line in Fig. 8.19) from the optoelectronic response (black line in Fig. 8.21) and the result is represented in black in Fig. 8.22. The electrodes response is replotted in this figure to facilitate comparisons.

The similarity between the responses between the electrodes of the device and the total optoelectronic modulation is striking. In fact, the bandwidths of the two spectra are the same, as represented in Fig. 8.22 by the red dashed line, corresponding to a optoelectronic bandwidth 1.7 GHz. This essentially means that the optoelectronic modulation at high frequencies is mainly limited by the electrodes. We may then speculate that with an improvement of the electrodes performance, so that they can accommodate signals at frequencies higher than 10 GHz, the electro-optical bandwidth of this strained silicon Pockels-based modulator could

also go beyond the 10 GHz regime. These are very promising results that may open a new route in the Pockels-based high-speed modulators based on strained silicon devices.

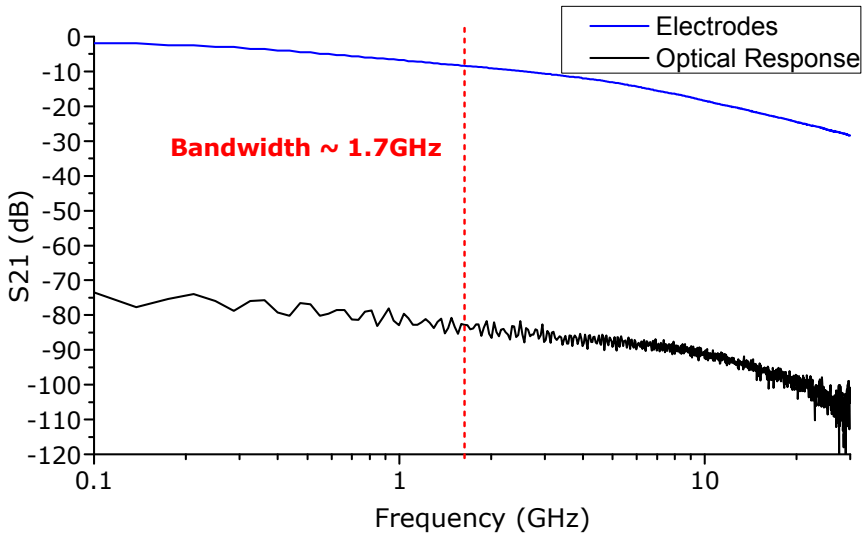

Fig. 8.22 Comparison between the electrical response of the electrodes and the optoelectronic response of the device when the contribution from the amplifier is not considered. The vertical red line represents the optical bandwidth of both responses.

8.6 Final remarks

The experimental results of this Chapter are very promising for three main reasons: we detected a clear crystal orientation dependent that we can only attribute to a Pockels effect modulation; were able to justify this crystal dependence of both Devices 250 and 500 in a method consistent with the models developed previously in this thesis; we detected RF optical modulation at high speed with a bandwidth that does not look to be limited by the electro-optic effect. The fact that we have detected such a clear dependence on the crystal orientation of the waveguides is a strong hint about the presence of strain-indeuced $\chi^{(2)}$ effects in the waveguide. In fact, there is no reason for carrier effects to present such a strong dependence on the angle of the waveguide and thus the only reason we could find for this dependence in a crystal-dependent electro-optic effect, is a crystal-dependent Pockels effect.

However, it is also clear that the results are still inconclusive and further work would be required to achieve strong conclusions about the results we obtained. The inconsistencies presented by Device 0 and the incapability of explaining them may put some question marks on our conclusions and approaches. Essential for that discussion would be samples with other

cladding stacks, namely made only of SiN or SiO_2, without any oxide layer interface. Due to lack of time and problems in the fabrication of those samples, yet, we could not fabricate those samples which could provide us useful information in every level of characterization.

Nevertheless, we believe that with the detailed knowledge about the charge properties of the cladding (which can be achieved by C vs V measurements), the strain level in the samples (which can achieved by Raman spectroscopy) and with a higher level of certainty in the simulations performed, these results can be improved and possibly to find a higher level of agreement between experiment and simulations. The results we report in this section represent some of the first steps in a long journey towards to full description of Pockels effect in strained silicon.

Chapter 9

Conclusion and future perspectives

In the present manuscript we have made an effort to approach the strain-induced Pockels effect in silicon in the most methodical way possible. We started from the very beginning, approaching the question "how does strain generate the second order nonlinear susceptibility in centro-symmetric crystals?". To look for an answer, we proposed a model that takes into account the displacements of atoms under strain and explains how that displacement induces the polar bonds required to generate second order nonlinear effects. This analysis, developed in Chapter 3, makes a natural connection between the strain-induced $\chi^{(2)}$ and the strain gradients in the crystal and forms the backbone of all the analysis performed throughout this thesis.

Those concepts were explored and naturally gave birth, in Chapter 6, to the description of the Pockels electro-optic effect in strained silicon waveguides based on the concept of *effective strain gradients*, which takes into account not only the strain gradients, but also the optical mode and the electrostatic effect in the waveguide. This description, however, is not complete if we do not include the effects of free carriers in silicon, which we explained in Chapter 5. In fact, the same electric field that generates Pockels effect, perturbs the free carriers in the silicon waveguide which, in turn, perturb the electric field. The equilibrium state of this process results in unexplored behaviours in the study Pockels effect in strained silicon and explains the nonlinear dependence of n_{eff} with the applied voltage V, a concept that may sound anti-intuitive because of the linear relation between of Pockels effect and the electrostatic field.

The generation of stress was discussed in Chapter 4 and it is achieved through the use of a highly stressed SiN cladding layer. However, everything changes when we also consider the electronic properties of the cladding itself. In both Chapters 5 and 6 we attempted an explanation for the particular charging and trapping characteristics of the SiN cladding and shown how these can deeply affect the electro-optic effect.

Based on all these discussions, we designed three different devices , with three different thicknesses of SiO_2 in the cladding (0 nm, 250 nm and 500 nm) correspondin to three different stress levels, to explore the concepts developed thus far. The fabrication process was discussed in Chapter 7 and the resulting samples were in line with the expected design. Finally, in Chapter 8 we presented the experimental results of the electro-optic effect in the samples, by characterizing both in DC electrostatic field and in high speed RF modulation. In this chapter we put modelling and experiments together: we use the models developed previously in the thesis and compare them with the experimental results under DC voltage. This analysis resulted in good fits for the devices with 250 nm and 500 nm of silicon dioxide. The same analysis was also able to explain, for the same two devices, the crystal orientation dependence predicted in the theory and detected experimentally. From the same analysis, the resulting average value of $\chi^{(2)}$ in the waveguide that could justify the detected crystal orientation dependence was determined to be $\chi^{(2)}_{xxy} \sim 120\,\mathrm{pm/V}$. This value is higher than expected but is justified because of the free carriers and charges in the cladding screen the electric field inside the waveguide: a voltage variation in the electrods results in a very low variation of electrostatic field in silicon. Because of this phenomenon, only such high value of $\chi^{(2)}$ can justify a difference of $\Delta n_{eff} \simeq 1 \times 10^{-5}$ for $\Delta V_s = 10\,\mathrm{V}$ for different angle orientations, like we have detected experimentally.

Finally, with the high speed measurements we were able to detect modulation up to 20 GHz, with a electro-optical bandwidth of 1.7 GHz. The bandwidth was clearly limited by the electrodes and the measured speed is higher than that expected from free carriers effects, so we strongly suspect this modulation to be due to Pockels effect.

However, it is also clear that many questions remain unanswered. Why could not we simulate the behaviour of the device without a SiO_2 layer, which presented the highest level of strain? Why did this same sample behave so differently from the others? Why were the simulation results only valid in a rather short voltage range? How can $\chi^{(2)}$ be so high in the waveguide? For some of these questions we may attempt an answer. For instance, when considering the carriers effect, only a high value of $\chi^{(2)}$ on the order of magnitude we detected can actually induce a visible electro-optic effect in strained silicon, even though there is a big uncertainty in this experimental value. Nonetheless, the unanswered questions we raised, show that we cannot fully explain all the processes occurring in the strained silicon waveguides. There are several reasons that can justify it, such as the lack of knowledge about the charging state of the cladding, the simulations may not describe the electro-optic state fully and need a deeper development or maybe there are other effects we did not consider at all and that also play a role.

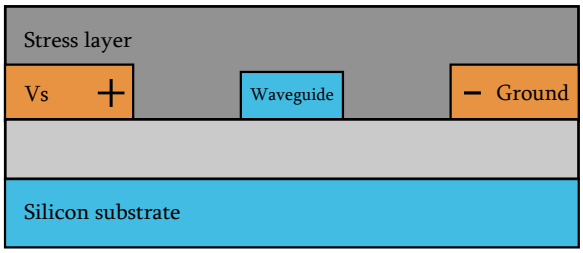

Fig. 9.1 Configuration with lateral electrodes to explore the $\chi^{(2)}_{xxx}$ and $\chi^{(2)}_{yyx}$ components of the second order susceptibility.

Regardless of these uncertainties, the consistencies we achieved with the experimental results suggest that our approach can be indeed correct and contribute for a better understanding of $\chi^{(2)}$ generation in strained silicon. Yet, that understanding can be strongly deepened by exploring other features that are open for discovery. The study of other components of $\chi^{(2)}$, namely the $\chi^{(2)}_{yyy}$, that can be explored using the TM polarized mode, and the $\chi^{(2)}_{xxx}$, which can be studied with lateral electrodes as shown in Fig. 9.1, can provide further information on the description of strain-induced $\chi^{(2)}$. From the model developed in Chapter 3, none of these components of $\chi^{(2)}$ is expected to depend on the angle φ and the confirmation of that fact may result on a major validation of the model developed in this thesis.

There are also different geometries of strained waveguides to be explored that may enhance the $\chi^{(2)}$ effects. One option is the configuration shown in Fig. 9.2, where the strain layer is only located on top of the waveguide. The strain gradients in the waveguide for such design do not have a strong sign variation between the top and the bottom of the waveguide (compare with those of Fig. 6.9) and thus contribute for a higher value of $\chi^{(2)}$ when averaged in the whole waveguide. This configuration was frequently reported in the study of Second-Harmonic Generation in strained silicon [30], but it is unexplored in the study of Pockels effect and may contribute for the enhancement of the results.

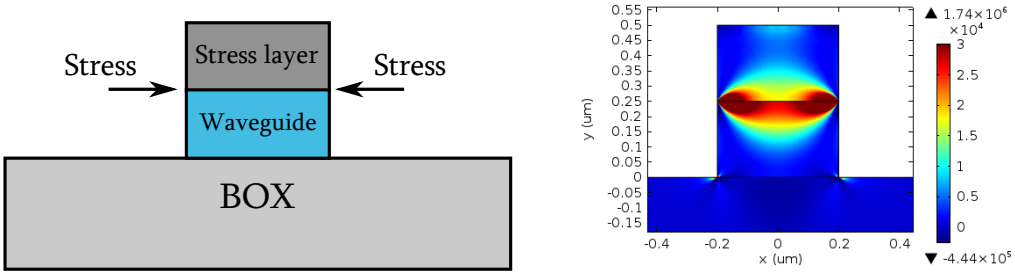

Fig. 9.2 Configuration with the stress layer placed on top. On the right we can see the simulation of the η_{xxy} component of the strain gradient tensor, which is positive almost everywhere.

Another subject that can be widely explored in the future is how to generate strain in silicon. The method commonly used is by depositing a highly stressed layer, generally SiN, deposited by a CVD process, which strains the waveguide underneath. This approach is not optimal for different reasons. For once, the layers deposited by these processes can support limited stress levels, on the 1 GPa to 2 GPa range and cannot be improved much higher than this. Moreover, the process is highly inefficient in straining the silicon waveguide because only a part of this stress is transmitted to the waveguide. On the other hand, from the discussions made in Chapter 4, one of the most efficient ways to induce stress in a crystalline micro structure is by epitaxially grow a crystal with different lattice parameter than Si.

The epitaxial stress in silicon can be studied by exploring different materials that are compatible with this platform. The obvious candidate is germanium, which is CMOS compatible and is known to induce stress in silicon. However, its integration is not straightforward and some precautions must be taken because it can generate misfit dislocations in the waveguide and its higher refractive index tend to move the light away from the silicon waveguide and confine it in the germanium layer.

Other promising candidates are functional oxides. These materials are compatible with the silicon technology, are deposited by epitaxial growth (using for example *Pulsed Laser Deposition*) and naturally induce strong strain in the Si structure due to lattice parameter mismatch between the oxides and silicon. Furthermore, the difference between their thermal expansion coefficients with that of silicon is more than 5 times higher than the difference we can obtain with Si_3N_4, corresponding to 5 times higher thermal stress.

There is a huge potential in this very promising approach and the first studies have started to be carried out in our group in this direction, using Yttria-Stabilized Zirconia (YSZ). In fact, we have successfully grown this oxide epitaxially on a Si waveguide, as shown in Fig. 9.3, but further developments are still required for an efficient implementation of YSZ into strained silicon waveguides. Nonetheless, the successful development of this technology for strained silicon applications may represent a big breakthrough with unprecedent highly controlled levels of strain.

Finally, we must comment on the future perspectives of highly efficient RF modulation. The measurements at high speed we have reported in this thesis are extremely promising. The results we presented are very close to correspond to the first demonstration of high bandwidth modulation in strained silicon, but the device performance was clearly limited by the bandwidth of the electrodes, despite their good adaptation to the 50 Ω line. The underperformance of the electrodes is mainly attributed to their coplanar configuration which tend to be very lossy at high frequencies.

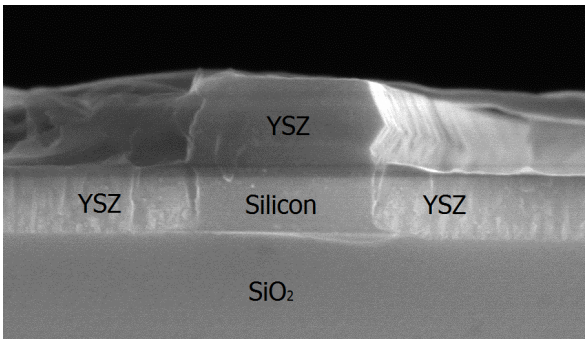

Fig. 9.3 SEM picture of the cross-section of a silicon waveguide covered by epitaxially grown YSZ. The angled feature in the YSZ film on top of silicon shows the crystalline nature of the YSZ film.

One possible solution to overcome this problem is using strip electrodes disposed as shown in Fig. 9.4. Preliminary results have shown that electrodes in this configuration can enlarge the bandwidth in comparison to the coplanar design, possibly reaching the 20 GHz range. Furthermore, this configuration is much more efficient at generating a highly intense and homogeneous vertical electric field in the waveguide because of the short distance between the electrodes in the vertical direction. As a result, this is a very encouraging approach and first developments have started to be made in our group towards its implementation in a near future.

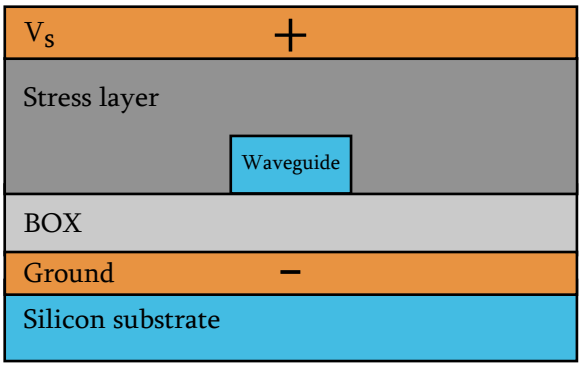

Fig. 9.4 Suggested configuration to make strip RF electrodes which considerably increase the bandwidth of the electrodes and generate higher electric field in the waveguide.

All in all, it is clear that there is an enormous room for improvement and exploration of the strain-induced $\chi^{(2)}$ effects in silicon. Big progress has been achieved in the past years towards a better understanding of this effect but this is only the beginning of a long journey towards a fully physical understanding of the strain-induced second order nonlinear effects in silicon. With the research work presented in this thesis we believe we have contributed with some important steps on that road. That road leads to a fully operating device based on

Pockels effect for high speed and low power consumption optical modulation in the silicon platform and it is our belief that with the right improvements and developments that device can indeed become a reality.

References

[1] Ian M. Ross. The invention of the transistor. *Proceedings of the IEEE*, 86(1):7–28, 1998.

[2] The chip that jack built. http://www.ti.com/corp/docs/kilbyctr/jackbuilt.shtml. Accessed: 24-04-2016.

[3] Gordon E Moore. Cramming more components onto integrated circuits. *Electronics*, 38(8):114, 1965.

[4] H G Grimmeiss and E Kasper. Today's mainstream microelectronics - A result of technological, market and human enterprise. *Materials Science Forum*, 608:1–16, 2009.

[5] E G Friedman, Mikhail Haurylau, Associate Member, Guoqing Chen, Hui Chen, Jidong Zhang, Eby G Friedman, and Philippe M Fauchet. Challenges and critical directions On-Chip Optical Interconnect Roadmap : Challenges and Critical Directions. 12(OCTOBER):1699–1705, 2005.

[6] H. O. Ron, Kenneth W. Mai, and A. Fellow. The future of wires. *Proceedings of the IEEE*, 89(4):490–504, 2001.

[7] D Miller. Device Requirements for Optical Interconnects to Silicon Chips, 2009.

[8] Pierre Delforge. America ' s Data Centers Are Wasting Huge Amounts of Energy. *Natural Resources Defense Council (NRDC)*, IB:14-08-A(August):1–5, 2014.

[9] Roger Dangel, Jens Hofrichter, Folkert Horst, Daniel Jubin, Antonio La Porta, Norbert Meier, Ibrahim Murat Soganci, Jonas Weiss, and Bert Jan Offrein. Polymer waveguides for electro-optical integration in data centers and high-performance computers. *Optics Express*, 23(4):4736, 2015.

[10] David A B Miller. Physical Reasons for Optical Interconnection. *Journal of Optoelectronics*, 11:155–168, 1997.

[11] Laurent Vivien and Lorenzo Pavesi, editors. *Handbook of Silicon Photonics*. CRC Press, 2013.

[12] Ibm's silicon photonics technology ready to speed up cloud and big data applications. https://www-03.ibm.com/press/us/en/pressrelease/46839.wss. Accessed: 24-04-2016.

[13] Bahram Jalali and Sasan Fathpour. Silicon Photonics. *J. Lightwave Technol.*, 24(12):4600–4615, 2006.

[14] R.A. Soref and J.P. Lorenzo. Single-crystal silicon: a new material for 1.3 and 1.6 μm integrated-optical components. *Electronics Letters*, 21(21):953, 1985.

[15] R. Soref and B. Bennett. Electrooptical effects in silicon. *IEEE Journal of Quantum Electronics*, 23(1):123–129, jan 1987.

[16] Harish Subbaraman, Xiaochuan Xu, Amir Hosseini, Xingyu Zhang, Yang Zhang, David Kwong, and Ray T. Chen. Recent advances in silicon-based passive and active optical interconnects. *Optics Express*, 23(3):2487, 2015.

[17] G. T. Reed, G. Mashanovich, F. Y. Gardes, and D. J. Thomson. Silicon optical modulators. *Nature Photonics*, 4(8):518–526, jul 2010.

[18] David J. Lockwood and Lorenzo Pavesi, editors. *Silicon Photonics II*. Springer, 2011.

[19] Diego Galacho. *To confirm title*. PhD thesis, Universite Paris Sud, 09/2016 2016.

[20] Jifeng Liu, Mark Beals, Andrew Pomerene, Sarah Bernardis, Rong Sun, Jing Cheng, Lionel C. Kimerling, and Jurgen Michel. Waveguide-integrated, ultralow-energy GeSi electro-absorption modulators. *Nature Photonics*, 2(7):433–437, 2008.

[21] Ning-Ning Feng, Dazeng Feng, Shirong Liao, Xin Wang, Po Dong, Hong Liang, Cheng-Chih Kung, Wei Qian, Joan Fong, Roshanak Shafiiha, Ying Luo, Jack Cunningham, Ashok V. Krishnamoorthy, and Mehdi Asghari. 30GHz Ge electro-absorption modulator integrated with 3μm silicon-on-insulator waveguide. *Optics Express*, 19(8):7062, apr 2011.

[22] Papichaya Chaisakul, Delphine Marris-Morini, Giovanni Isella, Daniel Chrastina, Xavier Le Roux, Eleonora Gatti, Samson Edmond, Johann Osmond, Eric Cassan, and Laurent Vivien. Quantum-confined Stark effect measurements in Ge/SiGe quantum-well structures. *Optics letters*, 35(17):2913–2915, 2010.

[23] Papichaya Chaisakul, Delphine Marris-Morini, Jacopo Frigerio, Daniel Chrastina, Mohamed-Said Rouifed, Stefano Cecchi, Paul Crozat, Giovanni Isella, and Laurent Vivien. Integrated germanium optical interconnects on silicon substrates. *Nat Photon*, 8(6):482–488, 2014.

[24] Ansheng Liu, Richard Jones, Ling Liao, Dean Samara-Rubio, Doron Rubin, Oded Cohen, Remus Nicolaescu, and Mario Paniccia. A high-speed silicon optical modulator based on a metal-oxide-semiconductor capacitor. *Nature*, 427(6975):615–8, feb 2004.

[25] Ching Eng Png, Seong Phun Chan, Soon Thor Lim, and Graham T. Reed. Optical phase modulators for MHz and GHz modulation in silicon-on-insulator (SOI). *Journal of Lightwave Technology*, 22(6):1573–1582, 2004.

[26] D J Thomson, F Y Gardes, Y Hu, G Mashanovich, M Fournier, P Grosse, J-M Fedeli, and G T Reed. High contrast 40Gbit/s optical modulation in silicon. *Optics express*, 19(12):11507–11516, 2011.

[27] Hongtao Lin, Student Member, Okechukwu Ogbuu, Jifeng Liu, Lin Zhang, and Jurgen Michel. Breaking the energy - bandwidth limit of electro - optic modulators : theory and a device proposal. *Journal of Lightwave Technology*, 31(24):4029–4036, 2013.

[28] Rune S Jacobsen, Karin N Andersen, Peter I Borel, Jacob Fage-Pedersen, Lars H Frandsen, Ole Hansen, Martin Kristensen, Andrei V Lavrinenko, Gaid Moulin, Haiyan Ou, Christophe Peucheret, Beáta Zsigri, and Anders Bjarklev. Strained silicon as a new electro-optic material. *Nature*, 441(7090):199–202, may 2006.

[29] Bartos Chmielak, Michael Waldow, Christopher Matheisen, Christian Ripperda, Jens Bolten, Thorsten Wahlbrink, Michael Nagel, Florian Merget, and Heinrich Kurz. Pockels effect based fully integrated, strained silicon electro-optic modulator. *Optics express*, 19(18):17212–9, aug 2011.

[30] M Cazzanelli, F Bianco, E Borga, G Pucker, M Ghulinyan, E Degoli, E Luppi, V Véniard, S Ossicini, D Modotto, S Wabnitz, R Pierobon, and L Pavesi. Second-harmonic generation in silicon waveguides strained by silicon nitride. *Nature materials*, 11(2):148–54, feb 2012.

[31] Bartos Chmielak, Christopher Matheisen, Christian Ripperda, Jens Bolten, Thorsten Wahlbrink, Michael Waldow, and Heinrich Kurz. Investigation of local strain distribution and linear electro-optic effect in strained silicon waveguides. *Optics Express*, 21(21):25324, oct 2013.

[32] Pedro Damas, Xavier Le Roux, David Le Bourdais, Eric Cassan, Delphine Marris-Morini, Nicolas Izard, Thomas Maroutian, Philippe Lecoeur, and Laurent Vivien. Wavelength dependence of Pockels effect in strained silicon waveguides. *Optics Express*, 22(18):22095, sep 2014.

[33] Matthew W Puckett, Joseph S T Smalley, Maxim Abashin, Andrew Grieco, and Yeshaiahu Fainman. Tensor of the second-order nonlinear susceptibility in asymmetrically strained silicon waveguides: analysis and experimental validation. *Optics letters*, 39(6):1693–6, mar 2014.

[34] Clemens Schriever, Federica Bianco, Massimo Cazzanelli, Mher Ghulinyan, Christian Eisenschmidt, Johannes de Boor, Alexander Schmid, Johannes Heitmann, Lorenzo Pavesi, and Jörg Schilling. Second-Order Optical Nonlinearity in Silicon Waveguides: Inhomogeneous Stress and Interfaces. *Advanced Optical Materials*, 3(1):129–136, 2015.

[35] T. H. Maiman. Stimulated Optical Radiation in Ruby. *Nature*, 187(4736):493–494, 1960.

[36] Manfred Wohlecke, Klaus Betzler, and Mirco Imlau. *Nonlinear Optics*. Fachbereich Physik, Universitat Osnabruck, 2003. Lecture notes for graduate school.

[37] Robert W. Boyd. *Nonlinear Optics*. Academic Press, second edition edition, 2003.

[38] Y. R. Shen. *The Principles of Nonlinear Optics*. John Wiley and Sons, 1984.

[39] Richard C. Powell. *Symmetry, Group Theory and the Physical Properties of Crystals*. LectureNotes in Physics. Springer, Heidelberg Germany, 2010.

[40] Amnon Yariv and Pochi Yeh. *Optical Waves in Crystals: Propagation and control of Laser Radiation*. John Wiley and Sons, 1984.

[41] M Izdebski, W Kucharczyk, and R E Raab. On relationships between electro-optic coefficients for impermeability and nonlinear electric susceptibilities. *Journal of Optics A: Pure and Applied Optics*, 6(4):421–424, apr 2004.

[42] Lorenzo Pavesi and Gerard Guillot, editors. *Optical Interconnects: The Silicon Approach*. Springer, 2006.

[43] EL Wooten and KM Kissa. A review of lithium niobate modulators for fiber-optic communications systems. *Selected Topics in ...*, 6(1):69–82, 2000.

[44] H. M. Manasevit, I. S. Gergis, and A. B. Jones. Electron mobility enhancement in epitaxial multilayer Si-Si/1-x/Ge/x/ alloy films on /100/Si. *Applied Physics Letters*, 464(100):25–28, 1982.

[45] R. People, J. C. Bean, D. V. Lang, A. M. Sergent, H. L. Störmer, K. W. Wecht, R. T. Lynch, and K. Baldwin. Modulation doping in GexSi1-x/Si strained layer heterostructures. *Applied Physics Letters*, 45(11):1231–1233, 1984.

[46] W. Shockley and J. Bardeen. Energy bands and mobilities in monatomic semiconductors [12]. *Physical Review*, 77(3):407–408, 1950.

[47] J Bardeen and W Shockley. Deformation potentials and mobilities in non-polar crystals. *Physical Review*, 549(1948), 1950.

[48] C K Maiti, L K Bera, and S Chattopadhyay. Strained-Si heterostructure field effect transistors. *Semiconductor Science and Technology*, 13:1225–1246, 1999.

[49] Friedrich Schäffler. High-mobility Si and Ge structures. *Semiconductor Science and Technology*, 12(12):1515–1549, 1999.

[50] S. Thompson, N. Anand, M. Armstrong, C. Auth, B. Arcot, M. Alavi, P. Bai, J. Bielefeld, R. Bigwood, J. Brandenburg, M. Buehler, S. Cea, V. Chikarmane, C. Choi, R. Frankovic, T. Ghani, G. Glass, W. Han, T. Hoffmann, M. Hussein, P. Jacob, A. Jain, C. Jan, S. Joshi, C. Kenyon, J. Klaus, S. Klopcic, J. Luce, Z. Ma, B. Mcintyre, K. Mistry, A. Murthy, P. Nguyen, H. Pearson, T. Sandford, R. Schweinfurth, R. Shaheed, S. Sivakumar, M. Taylor, B. Tufts, C. Wallace, P. Wang, C. Weber, and M. Bohr. A 90 nm logic technology featuring 50 nm strained silicon channel transistors, 7 layers of Cu interconnects, low k ILD, and 1 μm/sup 2/ SRAM cell. In *Digest. International Electron Devices Meeting,*, pages 61–64. IEEE, 2002.

[51] M. Huang. Stress effects on the performance of optical waveguides. *International Journal of Solids and Structures*, 40(7):1615–1632, apr 2003.

[52] David K. Biegelsen. Photoelastic tensor of Silicon and the volume dependence of the average gap. *Physical Review Letters*, 32(21):1196–1199, 1974.

[53] Qianfan Xu, Vilson R Almeida, Roberto R Panepucci, and Michal Lipson. Experimental demonstration of guiding and confining light in nanometer-size low-refractive-index material. *Optics letters*, 29(14):1626–1628, 2004.

[54] D.-X. Xu, P. Cheben, D. Dalacu, A Delage, S. Janz, B. Lamontagne, M.-J. J Picard, and W. N. Ye. Eliminating the birefringence in silicon-on-insulator ridge waveguides by use of cladding stress. *Optics letters*, 29(20):2384–6, oct 2004.

[55] Winnie N. Ye, Dan-Xia Xu, Siegfried Janz, Pavel Cheben, Marie-Josée Picard, Boris Lamontagne, N. Garry Tarr, and Silicon-on-insulator S O I Waveguides. Birefringence Control Using Stress Engineering in Silicon-on-Insulator (SOI) Waveguides. *Journal of Lightwave Technology*, 23(3):1308–, mar 2005.

[56] MM Milo*s*eviü, PS Matavulj, and GZ Mashanovich. Stress-induced characteristics of silicon-on-insulator rib waveguides. *Telecommunications forum TELFOR 2007*, (2):401–404, 2007.

[57] Kevin K. Tsia, Sasan Fathpour, and Bahram Jalali. Dynamic tuning of birefringence in silicon waveguides. *2008 Conference on Quantum Electronics and Laser Science Conference on Lasers and Electro-Optics, CLEO/QELS*, 061109(2008):12–15, 2008.

[58] Kevin K Tsia, Sasan Fathpour, and Bahram Jalali. Electrical control of parametric processes in silicon waveguides. *Optics express*, 16(13):9838–9843, 2008.

[59] S. V. Govorkov, V. I. Emel'yanov, N. I. Koroteev, G. I. Petrov, I. L. Shumay, V. V. Yakovlev, and R. V. Khokhlov. Inhomogeneous deformation of silicon surface layers probed by second-harmonic generation in reflection. *Journal of the Optical Society of America B*, 6(6):1117, jun 1989.

[60] JY Huang. Probing Inhomogeneous Lattice Deformation at Interface of Si (lll)/Si02 by Optical Second-Harmonic Reflection and Raman Spectroscopy. *Jpn. J. Appi. Phys. Vol*, 33:3878–3886, 1994.

[61] Nick K. Hon, Kevin K. Tsia, Daniel R. Solli, and Bahram Jalali. Periodically poled silicon. *Applied Physics Letters*, 94(9):091116, mar 2009.

[62] Clemens Schriever, Christian Bohley, and Ralf B Wehrspohn. Strain dependence of second-harmonic generation in silicon. *Optics letters*, 35(3):273–5, feb 2010.

[63] F. Bianco, E. Borga, A. Yeremian, B. Dierre, K. Fedus, P. Bettotti, A. Pitanti, R. Pierobon, M. Ghulinyan, G. Pucker, M. Cazzanelli, and L. Pavesi. Second-order susceptibility chi(2) in Si waveguides. *IEEE International Conference on Group IV Photonics GFP*, (2):27–29, 2011.

[64] Pedro Damas, Xavier Le Roux, Eric Cassan, Delphine Marris-morini, Nicolas Izard, Alain Bosseboeuf, Thomas Maroutian, Philippe Lecoeur, and Laurent Vivien. Analysis of second order nonlinear effects in strained silicon. In *Asia Communications and Photonics Conference 2013*, page AF2B.8, 2013.

[65] Jeremy Witzens. Ab initio calculation of the deformation potential and photoelastic coefficients of silicon with a non-uniform finite-difference solver based on the local density approximation. *Computer Physics Communications*, 185(8):2221–2231, aug 2014.

[66] S Sharif Azadeh, F Merget, M P Nezhad, and J Witzens. On the measurement of the Pockels effect in strained silicon. *Optics letters*, 40(8):1877–1880, 2015.

[67] Rajat Sharma, Matthew W. Puckett, Hung-Hsi Lin, Felipe Vallini, and Yeshaiahu Fainman. Characterizing the effects of free carriers in fully etched, dielectric-clad silicon waveguides. *Applied Physics Letters*, 106(24):241104, 2015.

[68] Rajat Sharma, Matthew W Puckett, Hung-Hsi Lin, Andrei Isichenko, Felipe Vallini, and Yeshaiahu Fainman. The effect of dielectric claddings on the electro-optic behavior of silicon waveguides. *Opt. Lett.*, 41(6):1185–1188, 2016.

[69] Costanza Lucia Manganelli, Paolo Pintus, and Claudio Bonati. Modeling of strain-induced Pockels effect in Silicon. *Optics Express*, 23(22):28649–28666, 2015.

[70] Eleonora Luppi, Elena Degoli, Matteo Bertocchi, Stefano Ossicini, and Valérie Véniard. Strain-designed strategy to induce and enhance second-harmonic generation in centrosymmetric and noncentrosymmetric materials. *Physical Review B*, 92(7):075204, 2015.

[71] M Borghi, M Mancinelli, F Merget, J Witzens, M Bernard, M Ghulinyan, G Pucker, and L Pavesi. High-frequency electro-optic measurement of strained silicon racetrack resonators. *Optics Letters*, 40(22):5287—-5290, 2015.

[72] Pedro Damas, Delphine Marris-Morini, Eric Cassan, and Laurent Vivien. Bond orbital description of the strain-induced second-order optical susceptibility in silicon. *Physical Review B*, 93(16):165208, apr 2016.

[73] Viktor Sverdlov. *Strain-Induced Effects in Advanced MOSFETs*. SpringerWienNewYork, 2011.

[74] L. D. Landau and E. M. Lifshitz. *The Theory of Elasticity*, volume 7. Pergamon Press, Oxford, 1970.

[75] P M Gullett, M F Horstemeyer, M I Baskes, and H Fang. A deformation gradient tensor and strain tensors for atomistic simulations. *Modelling and Simulation in Materials Science and Engineering*, 16(1):015001, 2008.

[76] A. Stukowski and A. Arsenlis. On the elastic–plastic decomposition of crystal deformation at the atomic scale. *Modelling and Simulation in Materials Science and Engineering*, 20(3):035012, 2012.

[77] Peter H. Mott, Ali S. Argon, and Ulrich W. Suter. The atomic strain tensor. *Journal of Computational Physics*, 101(1):140–150, 1992.

[78] Yu. A. Amenzade. *The Theory of Elasticity*. MIR Publishers Moscow, 1979.

[79] N. I. Muskhelishvili. *Some Basic Problems of Mathematical Theory of Elasticity*. Noordhoff International Publishing, 1977.

[80] G. L. Bir and G. E. Pieu. *Symmetry and Strain-Induced Effects in Semiconductors*. John Willey and Sons, New York/Toronto, 1972.

[81] Toshikazu Nishida Yongke Sun, Scott E. Thompson. *Strain Effect in Semiconductors*. Springer, 2010.

[82] JL Birman. Theory of the piezoelectric effect in the zincblende structure. *Physical Review*, 1955(1951):0–4, 1958.

[83] Richard M Martin. Piezoelectricity. *Physical Review B*, 5(4), 1972.

[84] P V Yudin and a K Tagantsev. Fundamentals of flexoelectricity in solids. *Nanotechnology*, 24(43):432001, oct 2013.

[85] A. K. Tangantsev. Piezoelectricity and flexoelectricicty in crystalline dielectrics. *Physical Review B*, 34(8):5883, 1986.

[86] L. Eric Cross. Flexoelectric effects: Charge separation in insulating solids subjected to elastic strain gradients. *Journal of Materials Science*, 41(1):53–63, jan 2006.

[87] Raffaele Resta. Towards a bulk theory of flexoelectricity. *Physical review letters*, (3):1–5, 2010.

[88] Sergei V. Kalinin and Anna N. Morozovska. Multiferroics: Focusing light on flexoelectricity. *Nat Nanotechnol*, 10(November):16–17, aug 2015.

[89] Umesh Kumar Bhaskar, Nirupam Banerjee, Amir Abdollahi, Zhe Wang, Darrell G. Schlom, Guus Rijnders, and Gustau Catalan. A flexoelectric microelectromechanical system on silicon. *Nature Nanotechnology*, (November):2–6, 2015.

[90] Zachary H. Levine, Hua Zhong, Siqing Wei, Douglas C Allan, and John W Wilkins. Strained silicon: A dielectric-response calculation. *Physical Review B*, 45(8):4131–4140, feb 1992.

[91] Min Huang. The influence of light propagation direction on the stress-induced polarization dependence of silicon waveguides. *Photonics Technology Letters, IEEE*, 18(12):1314–1316, 2006.

[92] NK Nick K. Hon, Kevin. K. KK Tsia, Daniel R. DR Solli, Bahram Jalali, and Jacob B. Khurgin. Stress-induced $\chi(2)$ in silicon — Comparison between theoretical and experimental values. In *2009 6th IEEE International Conference on Group IV Photonics*, pages 232–234, San Francisco, CA, USA, sep 2009. IEEE.

[93] Patricia Eldredge Bruce A. Averill. *Principles of General Chemistry*. LardBucket, 1.0 edition, 2012.

[94] Walter A. Harrison. *Electronic Structure and the Properties of Solids*. Dover Books on Physics. Dover Publications, New York, 1989.

[95] WA Harrison. Bond-orbital model and the properties of tetrahedrally coordinated solids. *Physical Review B*, 8(10):4487–4498, 1973.

[96] D. E. Aspnes. Bond models in linear and nonlinear optics. *Physica Status Solidi (B)*, 247(8):1873–1880, jun 2010.

[97] Zachary H. Levine. Optical second-harmonic susceptibilities: Frequency-dependent formulation with results for GaP and GaAs. *Physical Review B*, 49(7):4532–4538, 1994.

[98] Jian Chen, Z H Levine, and J W Wilkins. Calculated second-harmonic susceptibilities of BN, AlN, and GaN. *Applied Physics Letters*, 66(September 1994):1129–1131, 1995.

[99] D.A. Kleinman. Nonlinear optical susceptibilities of covalent crystals. *Physical Review B*, 2(8), 1970.

[100] SS Jha and N Bloembergen. Nonlinear optical susceptibilities in group-IV and III-V semiconductors. *Physical Review*, 171(3), 1968.

[101] BF Levine. Bond-charge calculation of nonlinear optical susceptibilities for various crystal structures. *Physical Review B*, 7(6):2600–2627, 1973.

[102] G. D. Powell, J.-F. Wang, and D. E. Aspnes. Simplified bond-hyperpolarizability model of second harmonic generation. *Physical Review B*, 65(20):205320, 2002.

[103] WA Harrison and JC Phillips. Angular Forces in Tetrahedral Solids. *Physical Review Letters*, 33(7):410–411, 1974.

[104] WA Harrison and S Ciraci. Bond-orbital model. II. *Physical Review B*, 10(4):1516–1527, 1974.

[105] BF Levine. Electrodynamical bond-charge calculation of nonlinear optical susceptibilities. *Physical Review Letters*, 22(15):787–790, 1969.

[106] WA Harrison. Orbital-Correction Method. *Physical Review A*, 7:1876, 1973.

[107] Chuping Huang, John A. Moriarty, A. Sher, and R. A. Breckenridge. Two-electron bond-orbital model I. *Physical Review B*, 12(12):5395–5406, 1975.

[108] M. E. Lines. Photoelastic trends from halides to pnictides by a bond-orbital method. *Journal of Applied Physics*, 60(4):1472–1478, 1986.

[109] Timothy B. Boykin, Mathieu Luisier, Mehdi Salmani-Jelodar, and Gerhard Klimeck. Strain-induced, off-diagonal, same-atom parameters in empirical tight-binding theory suitable for [110] uniaxial strain applied to a silicon parametrization. *Physical Review B - Condensed Matter and Materials Physics*, 81(12):1–9, 2010.

[110] M. Zieliński. Including strain in atomistic tight-binding Hamiltonians: An application to self-assembled InAs/GaAs and InAs/InP quantum dots. *Physical Review B - Condensed Matter and Materials Physics*, 86(11):1–9, 2012.

[111] M. H. Grimsditch and A. K. Ramdas. Brillouin scattering in diamond. *Physical Review B*, 11(8):3139–3148, 1975.

[112] L. S. Hounsome, R. Jones, M. J. Shaw, and P. R. Briddon. Photoelastic constants in diamond and silicon. *Physica Status Solidi (A) Applications and Materials Science*, 203(12):3088–3093, 2006.

[113] A. Feldman, R. M. Waxler, and D. Horowitz. Photoelastic constants of germanium. *Journal of Applied Physics*, 49(4):2589–2590, 1978.

[114] Clemens Schriever, Christian Bohley, Jörg Schilling, and Ralf B. Wehrspohn. Strained Silicon Photonics. *Materials*, 5(5):889–908, may 2012.

[115] J. R. Chelikowsky, K. M. Glassford, and J. C. Phillips. Interatomic force fields for silicon microclusters. *Physical Review B*, 44(4):1538–1545, 1991.

[116] H Wendel and R. M. Martin. Charge Density and Structural Properties of Covalent Semiconductors. *Physical Review Letters*, 40(14):950–953, 1978.

[117] Chen Huang and Emily a Carter. Transferable local pseudopotentials for magnesium, aluminum and silicon. *Physical Chemistry Chemical Physics : PCCP*, 10(47):7109–7120, 2008.

[118] P. J. Burnett and T. F. Page. An investigation of ion implantation-induced near-surface stresses and their effects in sapphire and glass. *Journal of Materials Science*, 20(12):4624–4646, 1985.

[119] H. Hora. Stresses in silicon crystals from ion-implanted amorphous regions. *Applied Physics A Solids and Surfaces*, 32(4):217–221, 1983.

[120] R Koch. The intrinsic stress of polycrystalline and epitaxial thin metal films. *Journal of Physics: Condensed Matter*, 9519, 1994.

[121] WD Nix. Mechanical properties of thin films. *Metallurgical transactions A*, 20(November), 1989.

[122] J.A. Sue and G.S. Schajer. Stress determination for coatings. *Surface Engineering*, 5 ASM Handbok:647, 1994. ASM International.

[123] Ch. Hollauer, H. Ceric, G. van Barel, A. Witvrouw, and S. Selberherr. Investigation of Intrinsic Stress Effects in Cantilever Structures. *2007 2nd IEEE International Conference on Nano/Micro Engineered and Molecular Systems*, pages 151–154, jan 2007.

[124] P Paduschek, C Höpfl, and H Mitlehner. Hydrogen-related mechanical stress in amorphous silicon and plasma-deposited silicon nitride. *Thin Solid Films*, 110:291–304, 1983.

[125] J.-h. Jeong, D. Kwon, W.-S. Lee, and Y.-J. Baik. Intrinsic stress in chemical vapor deposited diamond films: An analytical model for the plastic deformation of the Si substrate. *Journal of Applied Physics*, 90(3):1227, 2001.

[126] Xiaolin Chen and Yijun Liu. Thermal stress analysis of multi-layer thin films and coatings by an advanced boundary element method. *CMES- Computer Modeling in Engineering ...*, 2001.

[127] Eric Johlin, Nouar Tabet, Sebastián Castro-Galnares, Amir Abdallah, Mariana I. Bertoni, Tesleem Asafa, Jeffrey C. Grossman, Syed Said, and Tonio Buonassisi. Structural origins of intrinsic stress in amorphous silicon thin films. *Physical Review B*, 85(7):075202, feb 2012.

[128] E. Kobeda. SiO2 film stress distribution during thermal oxidation of Si. *Journal of Vacuum Science & Technology B: Microelectronics and Nanometer Structures*, 6(2):574, 1988.

[129] Haruna Tada, Amy E. Kumpel, Richard E. Lathrop, John B. Slanina, Patricia Nieva, Paul Zavracky, Ioannis N. Miaoulis, and Peter Y. Wong. Thermal expansion coefficient of polycrystalline silicon and silicon dioxide thin films at high temperatures. *Journal of Applied Physics*, 87(9):4189–4193, 2000.

[130] Chuen-Lin Tien and Tsai-Wei Lin. Thermal expansion coefficient and thermomechanical properties of SiN(x) thin films prepared by plasma-enhanced chemical vapor deposition. *Applied optics*, 51(30):7229–35, 2012.

[131] H. Ceric, C. Hollauer, and S. Selberherr. Three-Dimensional Simulation of Intrinsic Stress Build-Up in Thin Films. *2006 International Conference on Simulation of Semiconductor Processes and Devices*, pages 192–195, sep 2006.

[132] CA Davis. A simple model for the formation of compressive stress in thin films by ion bombardment. *Thin solid films*, 226(1993):30–34, 1993.

[133] S. Mayr and K. Samwer. Model for Intrinsic Stress Formation in Amorphous Thin Films. *Physical Review Letters*, 87(3):036105, jul 2001.

[134] H Ceric, A Nentchev, E Langer, and S Selberherr. Intrinsic Stress Build-Up During Volmer-Weber Crystal Growth. . . . *of Semiconductor Processes* . . . , 12(September):37–40, 2007.

[135] Carl V Thompson and Roland Carel. Stress and Grain growth in thin films. *J. Mech. Phys. Solids*, 44(5):657–673, 1996.

[136] H Ceric, R Heinzl, and Ch Hollauer. Microstructure and stress aspects of electromigration modeling. *AIP Conference* . . . , pages 262–268, 2006.

[137] V. Au, C. Charles, and R. W. Boswell. Interface creation and stress dynamics in plasma-deposited silicon dioxide films. *Applied Physics Letters*, 88(23):234103, 2006.

[138] Liang Dong, Jurgen Schnitker, Richard W. Smith, and David J. Srolovitz. Stress relaxation and misfit dislocation nucleation in the growth of misfitting films: A molecular dynamics simulation study. *Journal of Applied Physics*, 83(1):217, 1998.

[139] Jon Parsons. *Relaxation of strained silicon on virtual substrates*. PhD thesis, University of Warwick, 2007.

[140] Fredric Ericson and Jan ??ke Schweitz. Micromechanical fracture strength of silicon. *Journal of Applied Physics*, 68(11):5840–5844, 1990.

[141] Taeko Ando, Xueping Li, Shigeki Nakao, Takashi Kasai, Mitsuhiro Shikidd, and Kazuo Sato. Effect of Crystal Orientation on Fracture Strength and Fracture Toughness of Single Crystal Silicon. *17th International Conference on Micro Electro Mechanical Systems*, pages 177–180, 2004.

[142] John Robertson. Electronic structure of silicon nitride. *Philosophical Magazine Part B*, 63(1):47–77, 1991.

[143] J. Robertson. Defects and hydrogen in amorphous silicon nitride. *Philosophical Magazine Part B*, 69(2):307–326, 1994.

[144] a Stoffel, A Kovács, W Kronast, and B Müller. LPCVD against PECVD for micromechanical applications. *Journal of Micromechanics and Microengineering*, 6(1):1–13, 1999.

[145] Sinje Keipert-colberg, Nadine Barkmann, Christian Streich, Andreas Schütt, Dominik Suwito, Stefan Müller, and Dietmar Borchert. Investigation of a PECVD silicon oxide / silicon nitride passivation system concerning process influences. *26th European Photovoltaic Solar Energy Conference and Exhibition*, (September):1770–1773, 2011.

[146] Y. Mańglia, F. Rahmoune, and D. Bauza. On the Si-Si O2 interface trap time constant distribution in metal-oxide-semiconductor transistors. *Journal of Applied Physics*, 97(2005), 2005.

[147] a G Aberle. Overview on SiN surface passivation of crystalline silicon solar cells. *Solar Energy Materials and Solar Cells*, 65:239–248, 2001.

[148] Yvete Toivola, Jeremy Thurn, Robert F. Cook, Greg Cibuzar, and Kevin Roberts. Influence of deposition conditions on mechanical properties of low-pressure chemical vapor deposited low-stress silicon nitride films. *Journal of Applied Physics*, 94(10):6915, 2003.

[149] A Sherman. Plasma-assisted chemical vapor deposition processes and their semiconductor applications. *Thin Solid Films*, 3:135–149, 1984.

[150] W. a. P. Claassen. Influence of Deposition Temperature, Gas Pressure, Gas Phase Composition, and RF Frequency on Composition and Mechanical Stress of Plasma Silicon Nitride Layers. *Journal of The Electrochemical Society*, 132(4):893, 1985.

[151] Masahiko Maeda and Koichi Ikeda. Stress evaluation of radio-frequency-biased plasma-enhanced chemical vapor deposited silicon nitride films. *Journal of Applied Physics*, 83(7):3865, 1998.

[152] M. S. Haque, H. a. Naseem, and W. D. Brown. Correlation of stress behavior with hydrogen-related impurities in plasma-enhanced chemical vapor deposited silicon dioxide films. *Journal of Applied Physics*, 82(6):2922, 1997.

[153] Frank Engel Rasmussen. *Electrical Interconnections Through CMOS Wafers PhD Thesis*. PhD thesis, Technical University of Denmark, 2003.

[154] H Bertin, A Bosseboeuf, P Coste, M Péalat, and N Roux. Large area and broadband semi-reflective Bragg mirror membrane manufactured by PECVD. *Journal of Micromechanics and Microengineering*, 23(7):074005, jul 2013.

[155] L. Vanzetti, M. Barozzi, D. Giubertoni, C. Kompocholis, A. Bagolini, and P. Bellutti. Correlation between silicon-nitride film stress and composition: XPS and SIMS analyses. *Surface and Interface Analysis*, 38(4):723–726, apr 2006.

[156] Federica Bianco. *Second order nonlinear optical phenomena in strained silicon waveguides*. PhD thesis, Universita degli Studi di Trento, 2012.

[157] Eddy Romain-latu. *Mesures de contraintes par spectroscopie et imagerie Raman dans des dispositifs micro-électroniques*. Phd, Institut National Polytechnique de Grenoble, 2006.

[158] F Bianco, K Fedus, F Enrichi, R Pierobon, M Cazzanelli, M Ghulinyan, G Pucker, and L Pavesi. Two-dimensional micro-Raman mapping of stress and strain distributions in strained silicon waveguides. *Semiconductor Science and Technology*, 27(8):085009, aug 2012.

[159] P F Fewster and N L Andrew. Strain analysis by X-ray diffraction. *1997 ICAME/E-MRS Spring Conference, Symposium C; Related Developments in Electron Microscopy and X-Ray Diffraction of Thin Film Structures, 16-20 June 1997*, 319:1–8, 1998.

[160] Me Fitzpatrick, At Fry, P Holdway, Fa Kandil, J Shackleton, and L Suominen. Determination of Residual Stresses by X-ray Diffraction - Issue 2. *Measurement Good Practice Guide*, (52):74, 2005.

[161] King-Ning Tu. *Electronic Thin Film Reliability*. Cambridge University Press, 2011.

[162] Shusen Huang and Xin Zhang. Extension of the Stoney formula for film–substrate systems with gradient stress for MEMS applications. *Journal of Micromechanics and Microengineering*, 16(2):382–389, feb 2006.

[163] Xue Feng, Yonggang Huang, Hanqing Jiang, Duc Ngo, and Ares J. Rosakis. The effect of thin film/substrate radii on the Stoney formula for thin film/substrate subjected to nonuniform axisymmetric misfit strain and temperature. *Journal of Mechanics of Materials and Structures*, 1(6):1041–1053, oct 2006.

[164] Zhe-chuan Feng and Hong-du Liu. Generalized formula for curvature radius and layer stresses caused by thermal strain in semiconductor multilayer structures. *Journal of Applied Physics*, 54(1):83, 1983.

[165] B.G.R. van Schaik. *Deformation in thin SiN membranes due to residual stresses*. Phd thesis, École Polytechnique Féféral Lausanne, 2005.

[166] Patrick Waters. *Stress analysis and mechanical characterization of thin films for microelectronics and MEMS applications*. Phd, University of South Florida, 2008.

[167] Matthew a. Hopcroft, William D. Nix, and Thomas W. Kenny. What is the Young's Modulus of Silicon? *Journal of Microelectromechanical Systems*, 19(2):229–238, apr 2010.

[168] S. M. Sze and Kwog K. Ng. *Physics of Semiconductor Devices*. Wilew-Interscience, college edition edition, 1976.

[169] Donald A. Neamen. *Semiconductor Physics and Devices*. Mc Graw Hill, 3rd edition, 2003.

[170] Neil W. Ashcroft and N. David Mermin. *Solid state physics*. Harcourt College Publishers, 3 edition, 2007.

[171] Walter Frei. Solving nonlinear static finite element problems. http://www.comsol.com/blogs/solving-nonlinear-static-finite-element-problems/, 2013. Accessed: 2016-02-22.

[172] N Endo. Charge distributions in silicon nitride of MNOS devices. *Solid-State Electronics*, 21(9):1153–1156, 1978.

[173] F.P. Heiman and G. Warfield. The effects of oxide traps on the MOS capacitance. *IEEE Transactions on Electron Devices*, 12(4), 1965.

[174] G. Beylier, S. Bruyere, P. Mora, and G. Ghibaudo. New Characterization Methodology of Borderless Silicon Nitride Charge Kinetics Using C-V Hysteresis Loops. *Journal of The Electrochemical Society*, 155(5):H273, 2008.

[175] Horng-Chih Lin, Cheng-Hsiung Hung, Wei-Chen Chen, Zer-Ming Lin, Hsing-Hui Hsu, and Tiao-Yuang Hunag. Origin of hysteresis in current-voltage characteristics of polycrystalline silicon thin-film transistors. *Journal of Applied Physics*, 105(5):054502, 2009.

[176] I Lundstrom, S Christensson, and C Svensson. Carrier Trapping Hysteresis in MOS Transistorsl). *Most*, 395:395–407, 1970.

[177] W. L. Warren, J. Kanicki, F. C. Rong, E. H. Poindexter, and P. J. McWhorter. Charge trapping centers in N-rich silicon nitride thin films. *Applied Physics Letters*, 61(1992):216–218, 1992.

[178] R. Castagne and A. Vapaille. Apparent interface state density introduced by the spatial fluctuations of surface potential in an m.o.s. structure. *Electronics Letters*, 6(22):691, 1970.

[179] Jan Schmidt and Armin G Aberle. Carrier recombination at silicon – silicon nitride interfaces fabricated by plasma-enhanced chemical vapor deposition Carrier recombination at silicon – silicon nitride interfaces fabricated by plasma-enhanced chemical vapor deposition. *Journal of Applied Physics*, 3626(7):3626–3633, 1999.

[180] V. J. Kapoor and R A Turi. Charge storage and distribution in the nitride layer of the metal-nitride-oxide semiconductor structures. *Journal of Applied Physics*, 52(1):311, 1981.

[181] Yang Yang and Marvin H. White. Charge retention of scaled SONOS nonvolatile memory devices at elevated temperatures. *Solid-State Electronics*, 44(January):949–958, 2000.

[182] P. C. Arnett and B. H. Yun. Silicon nitride trap properties as revealed by charge-centroid measurements on MNOS devices. *Applied Physics Letters*, 26(3):94, 1975.

[183] Vivek Sharma, Clarence Tracy, Dieter Schroder, Stanislau Herasimenka, William Dauksher, and Stuart Bowden. Manipulation of K center charge states in silicon nitride films to achieve excellent surface passivation for silicon solar cells. *Applied Physics Letters*, 104(2014), 2014.

[184] Machteld W.P.E. Lamers, Keith T. Butler, John H. Harding, and Arthur Weeber. Interface properties of a-SiNx:H/Si to improve surface passivation. *Solar Energy Materials and Solar Cells*, 106:17–21, 2012.

[185] K. J. Weber and H. Jin. Improved silicon surface passivation achieved by negatively charged silicon nitride films. *Applied Physics Letters*, 94(2009):12–15, 2009.

[186] a. El amrani, I. Menous, L. Mahiou, R. Tadjine, A. Touati, and A. Lefgoum. Silicon nitride film for solar cells. *Renewable Energy*, 33:2289–2293, 2008.

[187] Susanne Helland. *Electrical Characterization of Amorphous Silicon Nitride Passivation Layers for Crystalline Silicon Solar Cells*. PhD thesis, 2011.

[188] J Robertson. The electronic properties of silicon nitride. *Philos. Mag. B*, 44(January 2015):215, 1981.

[189] J. Robertson, W.L. Warren, and J. Kanicki. Nature of the Si and N dangling bonds in silicon nitride. *Journal of Non-Crystalline Solids*, 187:297–300, 1995.

[190] W. L. Warren, J. Robertson, and J. Kanicki. Si and N dangling bond creation in silicon nitride thin films. *Applied Physics Letters*, 63(1993):2685–2687, 1993.

[191] L. E. Hintzsche, C. M. Fang, M. Marsman, G. Jordan, M. W. P. E. Lamers, a. W. Weeber, and G. Kresse. Defects and defect healing in amorphous Si3N4-xHy: An ab initio density functional theory study. *Physical Review B*, 88(15):1–6, 2013.

[192] W. L. Warren, P. M. Lenahan, and J. Kanicki. Electrically neutral nitrogen dangling-bond defects in amorphous hydrogenated silicon nitride thin films. *Journal of Applied Physics*, 70(4):2220–2225, 1991.

[193] H. MäcKel and R. Lüdemann. Detailed study of the composition of hydrogenated SiN x layers for high-quality silicon surface passivation. *Journal of Applied Physics*, 92(2002):2602–2609, 2002.

[194] John Robertson and Martin J. Powell. Gap States in Silicon Nitride. *Applied Physics Letters*, 44:415–417, 1984.

[195] P. M. Lenahan, D T Krick, and J Kanicki. The nature of the dominant deep trap in amorphous silicon nitride films: Evidence for a negative correlation energy. *Applied Surface Science*, 39(1-4):392–405, 1989.

[196] D. T. Krick, P. M. Lenahan, and J. Kanicki. Nature of the dominant deep trap in amorphous silicon nitride. *Physical Review B*, 38(12):8226–8229, 1988.

[197] J. R. Elmiger and M. Kunst. Investigation of charge carrier injection in silicon nitride/silicon junctions. *Applied Physics Letters*, 69:517, 1996.

[198] L. E. Hintzsche, C. M. Fang, M. Marsman, M. W. P. E. Lamers, A. W. Weeber, and G. Kresse. The formation of the positive, fixed charge at c-Si(111)/a-Si$_3$N$_{3.5}$:H interfaces. (111):2–6, jan 2015.

[199] F Duerinckx and J Szlufcik. Defect passivation of industrial multicrystalline solar cells basedon PECVD silicon nitride. *Solar Energy Materials and Solar Cells*, 72:231–246, 2002.

[200] S. D. Tzeng and S. Gwo. Charge trapping properties at silicon nitride/silicon oxide interface studied by variable-temperature electrostatic force microscopy. *Journal of Applied Physics*, 100(2), 2006.

[201] S. L. Miller, D. M. Fleetwood, P. J. McWhorter, R. A. Reber, and J. R. Murray. A general centroid determination methodology, with application to multilayer dielectric structures and thermally stimulated current measurements. *Journal of Applied Physics*, 74(8):5068, 1993.

[202] K. Lehovec and A. Fedotowsky. Charge centroid in MNOS devices. *Journal of Applied Physics*, 48(7):2955, 1977.

[203] Thomas H. Lee. *The degign of CMOS radio-frequency integrated circuits*. Cambridge University Press, Cambridge, 1998.

[204] LJR Pinky, Shakila Islam, and MNK Alam. Modeling of Orientation-Dependent Photoelastic Constants in Cubic Crystal System. *Materials Sciences and . . .* , (March):223–230, 2014.

[205] W. Bogaerts, P. de Heyn, T. van Vaerenbergh, K. de Vos, S. Kumar Selvaraja, T. Claes, P. Dumon, P. Bienstman, D. van Thourhout, and R. Baets. Silicon microring resonators. *Laser and Photonics Reviews*, 6(1):47–73, 2012.

[206] Otto Schwelb. Transmission, group delay, and dispersion in single-ring optical resonators and add/drop filters - A tutorial overview. *Journal of Lightwave Technology*, 22(5):1380–1394, 2004.

[207] Yunfei Fu, Tong Ye, Weijie Tang, and Tao Chu. Efficient adiabatic silicon-on-insulator waveguide taper. *Photonics Research*, 2(3):A41, 2014.

[208] F. H. Groen, A. H. de Vreede, M. K. Smit, and B. H. Verbeek. Mach-Zehnder Interferometer Polarization Splitter in InGaAsP/InP. *IEEE Photonics Technology Letters*, 6(3):402–405, 1994.

[209] Lucas B. Soldano, Frank B. Veerman, Meint K. Smit, Bastiaan H. Verbeek, Alain H. Dubost, and Erik C M Pennings. Planar Monomode Optical Couplers Based on Multimode Interference Effects. *Journal of Lightwave Technology*, 10(12):1843–1850, 1992.

[210] Maria Stepanova and Steven Dew, editors. *Nanofabrication - Techniques and Principles*. Springer, 2012.

[211] ZEONREX Electronic Chemicals. *ZEP520A Technical Report*.

[212] Charles Caer. *Cristaux photoniques a fente: vers une photonique silicium huybride a exaltation localiseee du champ electromagnetique*. PhD thesis, Universite Paris Sud, September 2013.

[213] EM Resist Ltd.

[214] EM Resist Ltd, Unit 3, Hayloft, Normans Hall Farm, Shrigley Road, Macclesfield, SK10 5SE, UK. *SML Resis - Product Information*.

[215] Allan W. Snyder and John D. Love. *Optical Waveguide Theory*. Chapman and Hall Ltd., 1983.

Appendix A

Calculations of the bond mode theory

A.1 Relation

We start by comparing the two hybrids, schematically represented in Fig. 3.8. From the definition of these two hybrids, $h_\xi^{B'}$ is obtained after h_ξ^A by making a translation and a reflection. Thus:

$$h_\xi^{B'}(\boldsymbol{r}) = h_\xi^A(\boldsymbol{R}_B - \boldsymbol{r}) \,. \tag{A.1}$$

In addition, we make use of the central properties of the potential $V(\boldsymbol{r}) = V(r)$. Because it is central, it is an even function of the argument its derivative is an odd function of the argument. Therefore, we have the following relationships:

$$V(\boldsymbol{r}) = V(-\boldsymbol{r}) \quad \text{and} \quad \nabla V(\boldsymbol{r}) = -\nabla V(-\boldsymbol{r}) \tag{A.2}$$

With these relations between these quantities, we are in conditions to prove the desired the results between V_B and V_A.

We start by analysing the term the form of the potentials $V(\boldsymbol{r} - \boldsymbol{R}'_{A_i})$ after a displacement of the atoms. Because $\boldsymbol{R}'_{A_i} = \boldsymbol{R}_{A_i} + \boldsymbol{u}_{A_i}$, applying a first order Taylor expansion to the potentials we have:

$$V(\boldsymbol{r} - \boldsymbol{R}'_{A_i}) \simeq V(\boldsymbol{r} - \boldsymbol{R}_{A_i}) - \nabla V(\boldsymbol{r} - \boldsymbol{R}'_{A_i}) \cdot \boldsymbol{u}_{A_i} \,. \tag{A.3}$$

Therefore, the term $\left\langle h_\xi^A \middle| V'_{A_i} \middle| h_\xi^A \right\rangle$ becomes:

$$\left\langle h_\xi^A \middle| V'_{A_i} \middle| h_\xi^A \right\rangle \simeq \int_\infty |h_\xi^A(\boldsymbol{r})|^2 \cdot V(\boldsymbol{r} - \boldsymbol{R}'_{A_i}) dV - \int_\infty |h_\xi^A(\boldsymbol{r})|^2 \cdot \nabla V(\boldsymbol{r} - \boldsymbol{R}_{A_i}) dV \cdot \boldsymbol{u}_{A_i} \tag{A.4}$$

Identifying the second term by

$$\left\langle h_\xi^A \right| \Delta V_{A_i} \left| h_\xi^A \right\rangle = - \left\langle h_\xi^A \right| \nabla V_{A_i} \left| h_\xi^A \right\rangle \cdot \boldsymbol{u}_{A_i} \, , \tag{A.5}$$

immediately proves eq. 3.56.

We now turn into the potential in $\boldsymbol{R}'_{B_i}$. Using the relationship A.1 and the central properties of the bond, we can do the following:

$$\begin{aligned}
\left\langle h_\xi^{B'} \right| V'_{B_i} \left| h_\xi^{B'} \right\rangle &= \int_\infty |h_\xi^{B'}(\boldsymbol{r})|^2 \cdot V(\boldsymbol{r} - \boldsymbol{R}'_{B_i}) dV = && \text{(A.6)} \\
&= \int_\infty |h_\xi^A(\boldsymbol{R}'_B - \boldsymbol{r})|^2 \cdot V(\boldsymbol{r} - \boldsymbol{R}'_{B_i}) dV = && \text{(A.7)} \\
&= \int_\infty |h_\xi^A(\boldsymbol{r})|^2 \cdot V(\boldsymbol{R}'_B - \boldsymbol{r} - \boldsymbol{R}'_{B_i}) dV && \text{(A.8)}
\end{aligned}$$

The same type of Taylor expansion can be done for $\bar{\boldsymbol{R}}'_B = \bar{\boldsymbol{R}}_B + \boldsymbol{u}_B$ and $\bar{\boldsymbol{R}}'_{B_i} = \bar{\boldsymbol{R}}_{B_i} + \boldsymbol{u}_{B_i}$, so that

$$V(\boldsymbol{R}'_B - \boldsymbol{r} - \boldsymbol{R}'_{B_i}) \simeq V(\boldsymbol{R}_B - \boldsymbol{r} - \boldsymbol{R}_{B_i}) + \nabla V(\boldsymbol{R}_B - \boldsymbol{r} - \boldsymbol{R}_{B_i}) \cdot (\boldsymbol{u}_B - \boldsymbol{u}_{B_i}) \tag{A.9}$$

Replacing A.9 into A.8, we deduce:

$$\begin{aligned}
\left\langle h_\xi^{B'} \right| V'_{B_i} \left| h_\xi^{B'} \right\rangle &= \int_\infty |h_\xi^A(\boldsymbol{r})|^2 \cdot V(\boldsymbol{R}_B - \boldsymbol{r} - \boldsymbol{R}_{B_i}) dV + \\
&+ \int_\infty |h_\xi^A(\boldsymbol{r})|^2 \cdot \nabla V(\boldsymbol{R}_B - \boldsymbol{r} - \boldsymbol{R}_{B_i}) dV \cdot (\boldsymbol{u}_B - \boldsymbol{u}_{B_i}); .
\end{aligned}$$

We identify the first and second terms as being $\left\langle h_\xi^B \right| V_{B_i} \left| h_\xi^B \right\rangle$ and $\left\langle h_\xi^{B'} \right| \Delta V_{B_i} \left| h_\xi^{B'} \right\rangle$ respectively. We now treat them separately.

$$\begin{aligned}
\left\langle h_\xi^B \right| V_{B_i} \left| h_\xi^B \right\rangle &= \int_\infty |h_\xi^A(\boldsymbol{r})|^2 \cdot V(\boldsymbol{R}_B - \boldsymbol{r} - \boldsymbol{R}_{B_i}) dV = \\
&= \int_\infty |h_\xi^A(\boldsymbol{r})|^2 \cdot V(-\boldsymbol{\xi}_{B_i} - \boldsymbol{r}) dV = \\
&= \int_\infty |h_\xi^A(\boldsymbol{r})|^2 \cdot V(\boldsymbol{\xi}_{A_i} - \boldsymbol{r}) dV = \\
&= \int_\infty |h_\xi^A(\boldsymbol{r})|^2 \cdot V(\boldsymbol{r} - \boldsymbol{\xi}_{A_i}) dV \\
&= \left\langle h_\xi^A \right| V_{A_i} \left| h_\xi^A \right\rangle \, ,
\end{aligned}$$

and thus we have deduced that

$$\left\langle h_\xi^B \right| V_{B_i} \left| h_\xi^B \right\rangle = \left\langle h_\xi^A \right| V_{A_i} \left| h_\xi^A \right\rangle \tag{A.10}$$

which is the reason behind $\epsilon_A = \epsilon_B$, as used in section 3.4.3.

Regarding the second term:

$$\begin{aligned}
\left\langle h_\xi^{B'} \middle| \Delta V_{B_i} \middle| h_\xi^{B'} \right\rangle &= \int_\infty |h_\xi^A(\boldsymbol{r})|^2 \cdot \nabla V(\boldsymbol{R}_B - \boldsymbol{r} - \boldsymbol{R}_{B_i}) dV \cdot (\boldsymbol{u}_B - \boldsymbol{u}_{B_i}) = \\
&= \int_\infty |h_\xi^A(\boldsymbol{r})|^2 \cdot \nabla V(-\boldsymbol{\xi}_{B_i} - \boldsymbol{r}) dV \cdot (\boldsymbol{u}_B - \boldsymbol{u}_{B_i}) = \\
&= \int_\infty |h_\xi^A(\boldsymbol{r})|^2 \cdot \nabla V(\boldsymbol{\xi}_{A_i} - \boldsymbol{r}) dV \cdot (\boldsymbol{u}_B - \boldsymbol{u}_{B_i}) = \\
&= \int_\infty |h_\xi^A(\boldsymbol{r})|^2 \cdot \nabla V(\boldsymbol{r} - \boldsymbol{\xi}_{A_i}) dV \cdot (\boldsymbol{u}_{B_i} - \boldsymbol{u}_B) \,,
\end{aligned}$$

resulting in

$$\left\langle h_\xi^{B'} \middle| \Delta V_{B_i} \middle| h_\xi^{B'} \right\rangle = \left\langle h_\xi^A \middle| \nabla V_{A_i} \middle| h_\xi^A \right\rangle \cdot (\boldsymbol{u}_{B_i} - \boldsymbol{u}_B) \tag{A.11}$$

which is eq. 3.57.

A.2 Average position of the electron in the bond

The average position of the electron in the bond is simply given by

$$\langle \boldsymbol{r} \rangle = \langle b | \boldsymbol{r} | b \rangle \,. \tag{A.12}$$

Since the bond function $|b\rangle$ is given by

$$|b\rangle = v_A \left| h_\xi^A \right\rangle + v_B \left| h_\xi^{B'} \right\rangle \tag{A.13}$$

then we can write

$$\langle b | \boldsymbol{r} | b \rangle = v_A^2 \left\langle h_\xi^A \middle| \boldsymbol{r} \middle| h_\xi^A \right\rangle + v_B^2 \left\langle h_\xi^{B'} \middle| \boldsymbol{r} \middle| h_\xi^{B'} \right\rangle + 2 v_A v_B \left\langle h_\xi^A \middle| \boldsymbol{r} \middle| h_\xi^{B'} \right\rangle \,. \tag{A.14}$$

In order to evaluate the previous expressions, we define $\boldsymbol{\kappa}$ as the position of the "center of gravity" of the hybrids in respect to the atom, so that

$$\left\langle h_\xi^A \middle| \boldsymbol{r} \middle| h_\xi^A \right\rangle = \boldsymbol{R}_A + \boldsymbol{\kappa} \quad \text{and} \quad \left\langle h_\xi^{B'} \middle| \boldsymbol{r} \middle| h_\xi^{B'} \right\rangle = \boldsymbol{R}'_B - \boldsymbol{\kappa} \,. \tag{A.15}$$

By defining $\boldsymbol{\gamma}$ as the vector connecting the two centres of gravity of both hybrids h_ξ^A and $h_\xi^{B'}$, then

$$\boldsymbol{R}_A + 2\boldsymbol{\kappa} + \boldsymbol{\gamma} = \boldsymbol{R}'_B \Longrightarrow \boldsymbol{\gamma} = \boldsymbol{\xi}' - 2\boldsymbol{\kappa} \,, \tag{A.16}$$

where $\boldsymbol{\xi}'$ is the bond vector, given by $\boldsymbol{\xi}' = \boldsymbol{R}'_B - \boldsymbol{R}_A$.

Finally, we define the constant γ so that[1]

$$\boldsymbol{\kappa} = \left(\frac{1-\gamma}{2}\right)\boldsymbol{\xi}\ , \tag{A.17}$$

where $\boldsymbol{\xi}$ corresponds to the unstrained bond vector. In this case, the $\boldsymbol{\gamma}$ vector can be written as

$$\begin{aligned}\boldsymbol{\gamma} &= \boldsymbol{\xi}' - (1-\gamma)\,\boldsymbol{\xi} = && \text{(A.18)}\\ &= \boldsymbol{\xi}' - \boldsymbol{\xi} + \gamma\boldsymbol{\xi} = && \text{(A.19)}\\ &= \boldsymbol{u}_B + \gamma\boldsymbol{\xi}\ , && \text{(A.20)}\end{aligned}$$

which in the case of an unstrained crystal $\boldsymbol{u}_B = 0$ and we recover $\boldsymbol{\gamma} = \gamma\boldsymbol{\xi}$, as reported by Harrison *et al.* in [94, 104].

The term $\left\langle h_\xi^A \middle| \boldsymbol{r} \middle| h_\xi^{B'} \right\rangle$ in equation A.14 is the exact midpoint between atoms A and B, because of the symmetry of the problem. By taking this as the origin of the coordinates, i.e. considering the average position in respect to this point, this term vanishes:

$$\left\langle h_\xi^A \middle| \boldsymbol{r} \middle| h_\xi^{B'} \right\rangle = 0 \tag{A.21}$$

and in respect to the midpoint of the bond, equation A.14 becomes

$$\begin{aligned}\langle b|\,\boldsymbol{r}\,|b\rangle &= -v_A^2\frac{\boldsymbol{\gamma}}{2} + v_B^2\frac{\boldsymbol{\gamma}}{2} = && \text{(A.22)}\\ &= \left(v_B^2 - v_A^2\right)\frac{\boldsymbol{\gamma}}{2} = && \text{(A.23)}\\ &= \frac{v_B^2 - v_A^2}{2}\left(\boldsymbol{u}_B + \gamma\boldsymbol{\xi}\right)\ , && \text{(A.24)}\end{aligned}$$

which is the result shown in equation 3.46.

[1] This is the definition given by Harrison *et al.* in [94, 104], where it is defined γd as the distance between the center of gravity of the two hybrids in the unstrained crystal.

Appendix B

Important photonics considerations

Consider a general electro-magnetic wave, whose electric and magnetic fields are given, respectively, by:

$$\boldsymbol{E}(\boldsymbol{r},t) = \boldsymbol{E}(\boldsymbol{r})e^{-i\omega t} \tag{B.1}$$

$$\boldsymbol{H}(\boldsymbol{r},t) = \boldsymbol{H}(\boldsymbol{r})e^{-i\omega t} \tag{B.2}$$

By inserting these fields $\boldsymbol{E}$ and $\boldsymbol{H}$ in Maxwell equations, after some manipulations and bearing in mind that $\omega = ck = k/\sqrt{\epsilon_0\mu_0}$ we get:

$$\nabla \cdot [\epsilon_0 \overline{\epsilon}(\boldsymbol{r}) \cdot \boldsymbol{E}(\boldsymbol{r})] = 0 \tag{B.3}$$

$$\nabla \cdot \boldsymbol{H}(\boldsymbol{r}) = 0 \tag{B.4}$$

$$\nabla \times \boldsymbol{E}(\boldsymbol{r}) = ik\sqrt{\frac{\mu_0}{\epsilon_0}}\boldsymbol{H}(\boldsymbol{r}) \tag{B.5}$$

$$\nabla \times \boldsymbol{H} = -ik\sqrt{\frac{\epsilon_0}{\mu_0}}\overline{\epsilon}(\boldsymbol{r}) \cdot \boldsymbol{E}(\boldsymbol{r}) \, . \tag{B.6}$$

In order to explore the propagation of the guided modes inside the waveguide, consider two completely different electromagnetic fields $(\boldsymbol{E}_0, \boldsymbol{H}_0)$ and $(\boldsymbol{E}_1, \boldsymbol{H}_1)$, propagating in a media with dielectric permittivity $\overline{\epsilon}_0(\boldsymbol{r})$ and $\overline{\epsilon}_1(\boldsymbol{r})$ respectively. We now define the second auxiliary field $\boldsymbol{F}_c$ which uses the two different electro-magnetic fields by

$$\boldsymbol{F}_c = \boldsymbol{E_0} \times \boldsymbol{H}_1^* + \boldsymbol{E}_1^* \times \boldsymbol{H_0} \, . \tag{B.7}$$

The divergence of $\boldsymbol{F}_c$ can be calculated to hold:

$$\nabla \cdot \boldsymbol{F}_c = \nabla \cdot (\boldsymbol{E}_0 \times \boldsymbol{H}_1^*) + \nabla \cdot (\boldsymbol{E}_1^* \times \boldsymbol{H}_0) = \tag{B.8}$$

$$= -ik\sqrt{\frac{\epsilon_0}{\mu_0}} [\boldsymbol{E}_0 \cdot \overline{\epsilon}_1 \cdot \boldsymbol{E}_1^* - \boldsymbol{E}_1 \cdot \overline{\epsilon}_0 \cdot \boldsymbol{E}_0^*] \tag{B.9}$$

The two auxiliary field $\boldsymbol{F}_c$ is so relevant because it can be shown that for any combination $(\boldsymbol{E}, \boldsymbol{H}, \overline{\epsilon})$ for cases 0 and 1, the following relationship is valid [215]:

$$\frac{\partial}{\partial z} \int_\infty \boldsymbol{F}_c \cdot \hat{\boldsymbol{z}} dS = \int_\infty \nabla \cdot \boldsymbol{F}_c dS \,. \tag{B.10}$$

This relation is the key to deduce the change in effective index of a mode in an electro-optical effect. Consider now that 0 and 1 are two different guided modes propagating in the z direction in two different waveguides, so that

$$\boldsymbol{E}_0(\boldsymbol{r}) = \boldsymbol{A}_0(x,y) e^{i\beta_0 z} \quad , \quad \boldsymbol{H}_0(\boldsymbol{r}) = \boldsymbol{B}_0(x,y) e^{i\beta_0 z} \tag{B.11}$$

$$\boldsymbol{E}_1(\boldsymbol{r}) = \boldsymbol{A}_1(x,y) e^{i\beta_1 z} \quad , \quad \boldsymbol{H}_1(\boldsymbol{r}) = \boldsymbol{B}_1(x,y) e^{i\beta_1 z} \tag{B.12}$$

where $\boldsymbol{A}_j$ and $\boldsymbol{B}_j$ are the electric and magnetic mode profiles and $\beta_j = k n_{eff_j}$ is the propagation constant of the mode, for cases $j = 0, 1$ respectively. With these definitions, the field $\boldsymbol{F}_c$ is given by

$$\boldsymbol{F}_c = [\boldsymbol{A}_1 \times \boldsymbol{B}_0^* + \boldsymbol{A}_0^* \times \boldsymbol{B}_1] \, e^{i(\beta_1 - \beta_0) z} \,. \tag{B.13}$$

By explicitly taking the divergence and the temporal derivative of $\boldsymbol{F}_c$, equation B.10 becomes leads to

$$(\beta_1 - \beta_0) \int [\boldsymbol{A}_1 \times \boldsymbol{B}_0 + \boldsymbol{A}_0 \times \boldsymbol{B}_1] \, dxdy = -ik\sqrt{\frac{\epsilon_0}{\mu_0}} \int [\boldsymbol{A}_1 \cdot \overline{\epsilon}_0 \cdot \boldsymbol{A}_0^* - \boldsymbol{A}_0 \cdot \overline{\epsilon}_1 \cdot \boldsymbol{A}_1^*] \, dxdy \tag{B.14}$$

which with some manipulations and using $\beta = k n_{eff}$ the finally leads to

$$n_{eff_1} - n_{eff_0} = c\epsilon_0 \frac{\int \boldsymbol{A}_0 \cdot \overline{\epsilon}_1 \cdot \boldsymbol{A}_1^* - \boldsymbol{A}_1 \cdot \overline{\epsilon}_0 \cdot \boldsymbol{A}_0^* \, dS}{\int \boldsymbol{A}_1 \times \boldsymbol{B}_0^* + \boldsymbol{A}_0^* \times \boldsymbol{B}_1 \, dS} \,. \tag{B.15}$$

This is the general formula that allows us to calculate the difference in effective index n_{eff} of two different modes in terms of their electric and magnetic field profiles.

The previous equation can be applied to the case of an electro-optic effect. In such effect, the application of an electric field changes the permittivity of the media from $\overline{\epsilon}_0 = \overline{\epsilon}$ to $\overline{\epsilon}_1 = \overline{\epsilon} + \Delta\overline{\epsilon}$, which from Maxwell equations lead to two different mode profiles $\boldsymbol{E}_0$ and $\boldsymbol{E}_1$.

However, in an electro-optic effect the change in permittivity is usually much smaller than the original one. Therefore, the electro-magnetic state of the mode will be slightly perturbed in respect to the original case and we can assume that in the perturbed state we have:

$$\overline{\epsilon}_1 = \overline{\epsilon} + \Delta\overline{\epsilon} \tag{B.16}$$

$$\beta_1 = \beta_0 + \Delta\beta \tag{B.17}$$

$$\boldsymbol{A}_1 = \boldsymbol{A}_0 + \Delta\boldsymbol{A} \tag{B.18}$$

$$\boldsymbol{B}_1 = \boldsymbol{B}_0 + \Delta\boldsymbol{B}\,, \tag{B.19}$$

where all the variations Δ are assumed to be small. Therefore, by applying the previous set of definitions to eq. B.15 and keeping only first order terms in Δ, that equation is reduced to:

$$\Delta n_{eff} = c\epsilon_0 \frac{\int \boldsymbol{A}_0 \cdot \Delta\overline{\epsilon} \cdot \boldsymbol{A}_0^* \, dS}{\int \boldsymbol{A}_0 \times \boldsymbol{B}_0^* + \boldsymbol{A}_0^* \times \boldsymbol{B}_0 \, dS}\,. \tag{B.20}$$

Finally, because the previous integration is done over x and y, the previous equation can be written in terms of the electromagnetic fields in the unperturbed waveguide $\boldsymbol{E}$ and $\boldsymbol{H}$ as:

$$\Delta n_{eff} = \frac{1}{N} \int \boldsymbol{E} \cdot \Delta\overline{\epsilon} \cdot \boldsymbol{E}^* \, dS\,, \tag{B.21}$$

where N is the active power in the waveguide, given by

$$N = \frac{1}{c\epsilon_0} \int (\boldsymbol{E} \times \boldsymbol{H}^* + \boldsymbol{E}^* \times \boldsymbol{H}) \cdot \hat{\boldsymbol{z}} \, dS\,. \tag{B.22}$$

This is the general form to describe the change of effective index of a mode under an electro-optic (or other type) effect. The permittivity variation $\Delta\overline{\epsilon}$ will then depend on the electro-optic effect itself and below we apply it to the specific cases of Pockels and plasma-dispersion effects.

B.1 Pockels effect refractive index change

In Pockels effect, the change in dielectric permittivity is given by (eq. 6.2):

$$\Delta\overline{\epsilon}) = 2\overline{\overline{\boldsymbol{\chi}}}^{(2)} \cdot \boldsymbol{F}\,. \tag{B.23}$$

where vF is the applied electrostatic field. By replacing it into eq. B.21, we get the change in effective index due to Pockels effect:

$$\Delta n_{eff_P} = \frac{1}{N} \int_{wg} 2\boldsymbol{E} \cdot \overline{\overline{\boldsymbol{\chi}}}^{(2)} : \boldsymbol{F}\boldsymbol{E}\, dS\,, \tag{B.24}$$

which is equation 6.3.

B.2 Plasma-dispersion effect refractive index change

The refractive index change due to plasma dispersion effect (Δn_c), is given by eq. 6.8. Because this electro-optic effect is isotropic, the permittivity ϵ of silicon is given by

$$\epsilon = n^2 = (n_{\mathrm{Si}} + \Delta n_c)^2 \simeq n_{\mathrm{Si}}^2 + 2n_{\mathrm{Si}}\Delta n_c\,. \tag{B.25}$$

Therefore, $\Delta\epsilon = 2n_{\mathrm{Si}}\Delta n_c$ and by replacing this into eq. B.21, we get the change in effective index due to plasma-dispersion effect

$$\Delta n_{eff_c} = \frac{2n_{\mathrm{Si}}}{N} \int_{wg} \boldsymbol{E}^2 \cdot \Delta n_c\, dS\,, \tag{B.26}$$

which is equation 6.9.